An investigation of the hydration history of chondrites and search for their asteroidal parent bodies

Jolantha Eschrig

THÈSE

Pour obtenir le grade de

DOCTEUR DE L'UNIVERSITÉ GRENOBLE ALPES

École doctorale : STEP - Sciences de la Terre de lEnvironnement et des Planètes
Spécialité : Sciences de la Terre et de l'Univers et de l'Environnement
Unité de recherche : Institut de Planetologie et dAstrophysique de Grenoble

Etude de l'évolution de l'hydratation des chondrites et recherche de leurs corps parents

An investigation of the hydration history of chondrites and search for their asteroidal parent bodies

Présentée par :

Jolantha ESCHRIG

Direction de thèse :

Lydie BONAL astronome-adjoint, Université Grenoble Alpes	Directrice de thèse
Pierre BECK Enseignant-chercheur, Université Grenoble Alpes	Co-directeur de thèse

Rapporteurs :

Pierre VERNAZZA
CHARGE DE RECHERCHE HDR, CNRS délégation Provence et Corse
Conel ALEXANDER
CHARGE DE RECHERCHE, Carnegie Institution for Science

Thèse soutenue publiquement le **19 octobre 2022**, devant le jury composé de :

Lydie BONAL ASTRONOME ADJOINT, Université Grenoble Alpes	Directrice de thèse
Pierre BECK PROFESSEUR DES UNIVERSITES, Université Grenoble Alpes	Co-directeur de thèse
Bertrand DEVOUARD PROFESSEUR DES UNIVERSITES, Aix-Marseille Université	Examinateur
Laurent TRUCHE PROFESSEUR DES UNIVERSITES, Université Grenoble Alpes	Président
Pierre VERNAZZA CHARGE DE RECHERCHE HDR, CNRS délégation Provence et Corse	Rapporteur
Conel ALEXANDER CHARGE DE RECHERCHE, Carnegie Institution for Science	Rapporteur
Francesca DeMeo CHARGE DE RECHERCHE, Massachusetts Institute of Technology	Membre invité
Sean Raymond CHARGE DE RECHERCHE, Universite de Bordeaux	Membre invité

"The only fight that is lost is the one that is abandoned."

Ernesto (Che) Guevara

Résumé

Les astéroïdes font partie des objets les plus importants dont nous disposons pour étudier l'histoire de la formation du système solaire. Certains d'entre eux ont échappé à de grandes quantités de chauffage et de différenciation, ce qui a permis la préservation de matériaux primitifs. Les missions spatiales étant rares, ils sont le plus souvent étudiés par spectroscopie de réflectance. Étant donné que les spectres de réflectance acquis pour les astéroïdes ne montrent que deux caractéristiques d'absorption, parfois faibles, l'interprétation des spectres de réflectance des astéroïdes peut être améliorée par des mesures en laboratoire des météorites. Elles sont utilisées pour contraindre l'histoire post-accrétion des astéroïdes, comme l'altération aqueuse, le métamorphisme thermique et les impacts, afin de trouver la composition des corps parents astéroïdaux. Cette information peut être utilisée pour contraindre la région de formation des astéroïdes. Enfin, en comparant les spectres de réflectance des astéroïdes et des météorites, un lien génétique entre eux peut être recherché.

Au cours de cette thèse, j'ai analysé un total de 132 chondrites, dont 46 chondrites carbonées (CCs) (23 CVs, 15 COs, 8 CRs) et 86 chondrites ordinaires (OCs) (47 chondrites non équilibrées (UOCs) et 39 chondrites ordinaires équilibrées (EOCs)), en utilisant différentes techniques de mesure. Les spectres de réflectance ont été obtenus pour étudier la variation spectrale entre et au sein des groupes de chondrites. La pétrographie, les mesures magnétiques, l'analyse thermogravimétrique (TGA) et la spectroscopie FTIR ont été utilisées pour contraindre l'histoire de l'hydratation des UOCs.

La comparaison des caractéristiques spectrales de réflectance a montré des variations entre et au sein de chaque groupe de chondrites. Les OCs se distinguent des CCs en montrant des bandes d'absorption plus profondes. Les UOCs et les EOCs ne peuvent pas être bien distingués sur la base des seuls spectres de réflectance. Il en va de même pour les CV et les CO. Les CR présentent des bandes d'absorption 1 µm à des longueurs d'onde plus faibles, ce qui les distingue des chondrites de type pétrographique (PT) 3. En ce qui concerne les OC dont le PT ≥ 4, LL peut être distingué de H et L sur la base des profondeurs de bande à 2 µm et des positions à 1 µm. Plusieurs caractéristiques spectrales semblent être contrôlées par le métamorphisme thermique, notamment la bande 1 µm pour les CV et la pente visible pour les CO. La recherche d'un lien génétique basé sur la comparaison des caractéristiques spectrales de réflectance des chondrites avec les classes d'astéroïdes suggère une bonne correspondance des UOC avec le type S, des CV et des CO avec les types L et des CK avec les Eos et les types K. La comparaison directe des caractéristiques spectrales de 466 astéroïdes de type S avec celles des UOC et des EOC montre que des degrés inconnus d'altération spatiale et de granulométrie du régolithe empêchent la distinction entre les surfaces de type S équilibrées et non équilibrées. Ces résultats soulignent le potentiel de la bande d'hydratation 3 µm pour contraindre davantage les liens astéroïde-météorite. L'étude approfondie de l'histoire de l'hydratation des UOC à l'aide de la pétrographie, de la TGA et de la spectroscopie FTIR a tout d'abord montré que 74 % des UOC antarctiques avaient été mal classés. En outre, elle a montré que les UOC ne sont pas sèches. En me basant sur la spectroscopie TGA et FTIR, j'ai montré que l'hydratation

des UOC, une fois normalisée par rapport à l'abondance de la matrice, est comparable à celle des CV avec des grades métamorphiques équivalents. J'ai montré que l'hydratation des UOCs est contrôlée par leur température métamorphique maximale, la corrélation prolongeant celle observée précédemment pour les CVs. Cela signifie que le système solaire interne n'était pas sec et que la ligne de neige au moment de l'accrétion devait être située à l'intérieur de la région de formation des UOCs.

Abstract

Asteroids are some of the most important objects available to us for investigating the formation history of the Solar System. Some of them escaped large amounts of heating and differentiation which allowed for the preservation of primitive material. With space missions being rare, they are most commonly studied using reflectance spectroscopy. Since the reflectance spectra acquired for asteroids show only two, sometimes faint absorption features, the interpretation of asteroid reflectance spectra can be improved through laboratory measurements of chondrites. They are used to constrain the post-accretion history of asteroids such as aqueous alteration, thermal metamorphism and shock metamorphism to find the initial composition of the asteroidal parent bodies. This information can be used to constrain the formation region of asteroids. Lastly, by comparison of asteroid and chondrite reflectance spectra a genetic link between them can be searched.

During this PhD, I analyzed a total of 132 chondrites, including 46 carbonaceous chondrites (CCs) (23 CVs, 15 COs, 8 CRs) and 86 ordinary chondrites (OCs) (47 unequilibrated (UOCs) and 39 equilibrated ordinary chondrites (EOCs)), using varying measuring techniques. Reflectance spectra were obtained to investigate spectral variation between and within chondrite groups. Petrography, magnetic measurements, Thermogravimetric analysis (TGA) and FTIR spectroscopy were used to constrain the hydration history of UOCs.

The comparison of reflectance spectral features showed variations between and within each chondrite group. OCs are distinguished from CCs by showing deeper absorption features. UOCs and EOCs cannot be well distinguished based on reflectance spectra alone. The same is true for CVs and COs. CRs show 1 µm absorption features at lower wavelengths distinguishing them from the petrographic type (PT) 3 chondrites. For OCs with PT $\geq$ 4, LL can be distinguished from H and L based on 2 µm band depths and 1 µm positions. Several spectral features seem to be controlled by thermal metamorphism, including the 1 µm band for CVs and the visual slope for COs. Searching for a genetic link based on the comparison of reflectance spectral features of chondrites with asteroid end members suggests a good match of UOCs with S-type, CVs and COs with L-type and CKs with Eos and K-type. The direct comparison of the spectral features of 466 S-type asteroids with those of UOCs and EOCs shows that unknown degrees of space weathering and regolith grain size hinder the distinction between equilibrated and unequilibrated S-type surfaces. These results underline the potential of the 3 µm hydration band to further constrain asteroid–meteorite links. The in-depth study of the hydration history of UOCs that I performed using petrography, TGA and FTIR spectroscopy firstly showed that 74 % of Antarctic UOCs were previously misclassified. Furthermore, it showed that UOCs are not dry. Based on TGA and FTIR spectroscopy, I showed that the UOC hydration, once normalized to the matrix abundance, is comparable to that of CVs with equivalent metamorphic grades. I showed that the hydration of UOCs is controlled by their peak metamorphic temperature with the correlation extending the one previously observed for CVs. This means that the inner Solar System was not dry and that the snowline at the time of accretion must have been located inward of the UOC formation region.

Acknowledgments

When I started the journey of my PhD I knew it would be hard. But I think nothing could have prepared me for how hard it actually was. Besides the everyday challenges of finally having reached the stage in my career where there are no clear answers to the questions you have in any textbooks anymore, the list of additional challenges that I did not anticipated is long. To name just a few: I lived alone for the first time in my life, in a foreign country, with a foreign language that I did not know well when I arrived; I injured my knee (twice) while living alone for the first time; I lived through a global pandemic, month long lockdowns and isolation while still trying to be productive and work on my PhD and lost loved ones without the chance of saying goodbye due to the pandemic.

When I look at that list, I cannot help but feel proud that despite everything I made it. And I cannot help but feel thankful to all the lovely people who have kept me sane, helped me and supported me through the most difficult time of my life. I am confident that I would not have been able to finish my thesis without them.

Firstly, I would like to thank my supervisors. Lydie, you were one of the main reasons I chose my PhD at IPAG. Knowing you from my Master thesis made me confident that I could trust in your guidance and I am very grateful for everything that you have done and made possible for me. Pierre, you were always there for me when I had any questions and always took time for me when I needed it. Thank you both very much. I would also like to thank the other members of the Planeto team as well as the IPAG staff for all the help they gave me during this thesis. Special thanks also to my collaborators, Jérôme Gattacceca, Lisa Krämer-Ruggiu, Max Mahlke and Benoit Carry. Working with you was immensely enriching to my PhD and you have all significantly contributed to getting me to the end of my PhD. Thank you very much.

Of course, I also owe a special thanks to all of my friends, those that I had the honor to meet along the way, and those that I have known for most of my life. The list is long, most of you hopefully know how much you mean to me. Linda, du bist eine der wichtigsten Personen in meinem Leben. Vielen Dank, dass du immer für mich da bist egal was kommt. Danke auch dir Maike für deine Freundschaft. To my friends that I met along the way: Ricardo, Junko, Aina, Pedro, Mathilde, Marta, Joan, Trygve, Van, Robin, Kana, Jian, Aymane, Hawraa, Lisa, Lorenzo, Eleonora, André, Tai, Simon and Marie: thank you for your wonderful friendship, for the fun we had together and the many helpful discussions. My heart is full knowing I got to meet and befriend so many amazing people during my time in Grenoble. Thank you also to my wonderful pet rats: Tato, Georgie, Chaz, Billy, Ash and Yuppy. It might seem silly, but without you I would have not survived the quarantine. You will forever be in my heart.

And last but not least, of course, I would like to thank my family, who have always supported, loved and inspired me throughout any of my life choices. You are the reason why I never questioned that I could do a PhD in the first place. From the bottom of my heart, Ute, Matthias, Hannes, Immanuel, Anna, Angela and Rosi: Thank you. In loving memory of my grandparents: Helmut Eschrig, Günter Stejskal and Eva Stejskal.

Contents

List of Figures

List of Tables

List of Abbreviations

AMM	Antarctic Micrometeorite
AOA	Amoeboid Olivine Aggregate
BD	Band Depth
CAI	Calcium-Aluminum-rich Inclusion
CC	Carbonaceous Chondrite
CCAM	Carbonaceous Chondrite Anhydrous Mineral
DTG	Derivative Thermogravimetry
EMG	Exponentially Modified Gaussian
EOC	Equilibrated Ordinary Chondrite
FTIR	Fourier Transform Infrared
HED	Howardite-Eucrite-Diognite
IBD	Integrated Band Depth
IDP	Interplanetary Dust Particle
ITL	Induced Thermoluminescence
MS	Magnetic Susceptibility
NC	Non-carbonaceous
NEO	Near Earth Object
NIR	Near Infrared
OC	Ordinary Chondrite
PCA	Principle Component Analysis
PDF	Planar Deformation Feature
PT	Petrologic Type
RMS	Root Mean Square
SEM	Scanning Electron Microscopy
SHADOWS	Spectrophotometer with cHanging Angles for the Detection Of Weak Signals
SMOW	Standard Mean Ocean Water

SW	Space Weathering
TEM	Transmission Electron Microscopy
TFL	Terrestrial Fractionation Line
TGA	Thermogravimetric Analysis
UOC	Unequilibrated Ordinary Chondrite

1 Asteroids and meteorites as constraints of the early Solar System

Investigating the formation history of the Solar System is a longstanding endeavor. Understanding its exact evolution from Solar Nebula to Protoplanetary Disk to Planetary system is a major driver of current Solar System exploration. In doing so, we also open the door to gaining insight into other planetary systems and possibly finding other habitable Earth-like planets.

Solar System small bodies include asteroids, comets, trojans, centaurs and trans-Neptunian objects. However, during this PhD the focus will be on asteroids only. Asteroids are some of the most important materials available to us for learning about the Solar System history. It is believed that the majority of the asteroid population today are "second generation asteroids". They are thought to have formed from a few, large "primary parent bodies" that were broken apart during collisions (e.g. Greenwood et al. (2020)). In the following, when referring to "asteroids" and "asteroidal parent body" the former is meant. Being small in size, some of these asteroids escaped large amounts of heating and differentiation which allowed for the preservation of primitive material, some of which can date back to the Solar Nebula. Therefore, Asteroids are of great interest for answering some fundamental questions about the formation history of the Solar System. Which asteroid groups might have contributed to the building blocks of terrestrial planets? Could they have contributed to delivering water and other volatiles to Earth? We know that the majority of meteorites in our collection are of asteroidal origin, but which group of meteorites samples which group of asteroids? During this thesis I tried to contribute to answering some of the questions above.

1.1 Asteroids

1.1.1 Classification

Today, the majority of Asteroids are located in the main Asteroid belt in-between the orbit of Mars and Jupiter. Since space missions (sample return missions or asteroid approaches) are expensive and rare, ground-based reflectance spectroscopy is the main tool for investigating asteroid surfaces. Therefore, asteroids are classified into different types based on reflectance spectral properties. The classification used most widely at the time of writing, called the Bus-DeMeo taxonomy (DeMeo et al., 2009), is based

on the Bus taxonomy (Bus and Binzel, 2002) but extends the original classification from only the visible to the near-IR range. It includes three main asteroid complexes: The S-complex characterized by the presence of silicate absorption features at 1 µm and 2 µm, the C-complex characterized by flat, low slope spectra with small or no absorption bands, and the X-complex characterized by high slope spectra with little or no absorption features. A fourth category includes asteroid spectra that do not fit in any of the above-mentioned complexes. They are distributed among 9 classes (D-, A-, K-, L-, T-, O-, Q-, V- and R-types). Figure 1.1a summarizes all these classes with example spectra. As can be seen, each of the three main complexes can be further sub-divided to account for spectral variations within one complex. For the S-complex this includes S-, Sa-, Sq-, Sr-, and Sv-types. For the C-complex it includes C-, Cb-, Cg-, Cgh- and Ch-types. Lastly, for the X-complex it includes X-, Xc-, Xe-, Xk-, and T-types.

A recent study on improving this classification was presented by Mahlke et al. (2022). In this work, the visual albedo is re-introduced into the classification process, the classification of incomplete spectra (only in the visible or only in the NIR) is made possible and a probability for belonging to a certain class is given by applying a clustering analysis on dimensionally reduced spectra. Mahlke et al. (2022) find three main complexes including the previously mentioned S- and C-complex and a third M-complex. 17 sub-classes are defined. The C-complex includes B-, C- and Ch-types as well as P-types which were previously included in the X-complex (Tholen and Barucci, 1989). The S-complex includes S- and Q-type and the M-complex, which replaces the X-complex, includes K-, L- and M-types. Lastly, seven end members are defined including A-, D-, E-, O-, R-, V- and Z-types.

Within the large data set of more than 700,000 Asteroids (status 2015, Asteroids IV, Michel et al. (2015a)) whose orbits have been observed, several groups have been identified with similar orbital and compositional characteristics. These groups are called asteroid families or dynamical families. Each dynamical family is believed to originate from a single, large parent asteroid which was violently destroyed by catastrophic high velocity collisions during the dynamical evolution of the asteroid belt (Nesvorný et al. (2015), Masiero et al. (2015), Michel et al. (2015b)). The debris of these collisions (family members) could then gravitationally re-accumulate, explaining the existence of some larger family members today (Nesvorný et al., 2015). This formation process could also be reproduced for asteroid families using numerical simulations (Michel et al., 2015b). Since asteroid families are dynamically active areas it is probable that they are major contributors to the flux of meteorites to Earth. Over 100 Asteroid families have been identified to date and can contain up to several hundred identified family members (Michel et al., 2015b). Examples of prominent asteroid families are the Eos, Eunomia and Flora families (S-complex), the Hygiea and Themis families (C-complex), the Hungaria family (X-complex) and the Vesta family (V-type) (e.g. Masiero et al. (2015)).

Studies on the heliocentric distance distribution of the different asteroid complexes throughout the asteroid belt today have been performed. X-complex asteroids dominate in the 1.8-2.0 au Hungaria region. The inner region around 2.0-2.5 au is dominated by (4) Vesta and large (D $>$ 100 km) S-complex objects, but C-type also show a sig-

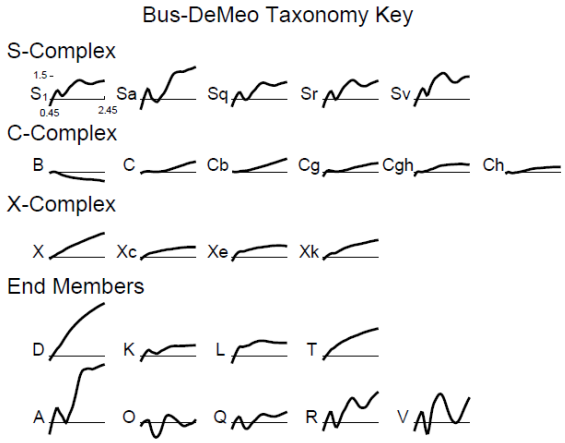

(a) Summary of the different asteroid complexes and the corresponding sub-classes based on the Bus-Demeo taxonomy. Image was taken from DeMeo et al. (2015).

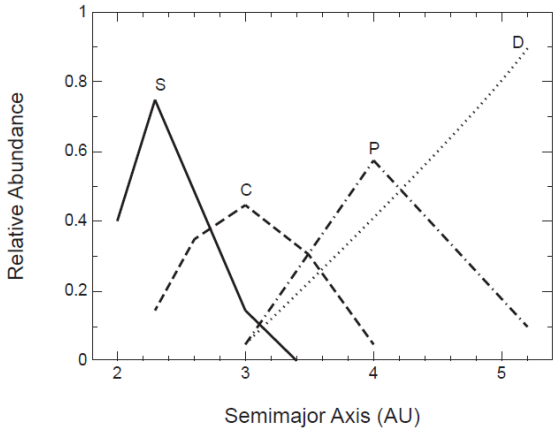

(b) Mixing between the positions of different asteriod types throughout the Solar Disk. Image was taken from (Morbidelli et al., 2015).

Figure 1.1: Asteroid spectra and distribution

nificant contribution for medium (20 km < D < 100 km) and small (5 km < D < 20 km) sized objects. The two C-complex asteroids (1) Ceres and (2) Pallas dominate by mass in the 2.5-2.82 au middle region of the asteroid belt. The outer main asteroid belt between 2.82 – 3.3 au is dominated by C-complex asteroids but S-complex also show a significant contribution (DeMeo et al., 2015). The abundance of large asteroids (D > 50 km) of different complexes as a function of their heliocentric distance summarized in Figure 1.1b (Gradie and Tedesco (1982) and Morbidelli et al. (2015)) shows how mixing between different asteroid complexes is indeed taking place between the regions of the asteroid belt. This mixing is even more prominent when looking at smaller sized Asteroids (DeMeo et al., 2015). Furthermore, large Asteroids (D > 100 km) show large eccentricities and inclinations, ranging from 0 – 0.30 and 0° – 30°, respectively (e.g. Morbidelli et al. (2015) and references therein). The present structure of the asteroid belt clearly witnessed the dynamical past of the early Solar System.

The goal of dynamical models is to explain how Solar System objects formed and ended up at the positions we see today. A complete model is faced with several obstacles such as the condensation-line problem (snow line and silicate line) to explain the small size of Mars in comparison to Earth and the depletion in volatiles in the inner Solar System (Morbidelli et al., 2016) or the missing mantel problem to explain the lack of olivine and pyroxene dominated mantles in differentiated asteroids (DeMeo et al. (2015) and references therein). Some of them will be discussed below. The goal of this chapter is to give an overview of what the most promising and accepted theories for the formation and evolution of our Solar System currently are. Special emphasis is placed on the stages after the gravitational collapse of the Solar Nebula and the formation of the protostar and protoplanetary disk, since this is what is most important for the present work.

1.1.2 Dynamical processes

Three main observational constraints of Asteroids helped develop the basis of the solar evolution models used today. The first one is the large eccentricity and inclination of Asteroid orbits, which stands in contrast to the expected Keplerian plane orbit of planetesimals (Petit et al., 2002). The second is the low mass of the present asteroid belt, which is estimated to be around 4.5×10^{-4} Earth masses (Morbidelli et al. (2015) and references therein, Krasinsky et al. (2002), Kuchynka and Folkner (2013) and Somenzi et al. (2010)). For the formation of the terrestrial planets and Jupiter's core a larger mass in the order of 1 Earth mass is needed (Weidenschilling, 1977). Therefore, the asteroid belt seems to have been depleted by 3 orders of magnitude (Morbidelli et al. (2015) and references therein). Lastly, as mentioned before, while there is a taxonomic structure to the asteroid belt, with S-type asteroids more represented in the inner asteroid belt and C-type in the outer Gradie and Tedesco (1982), a certain degree of taxonomic mixing throughout the orbital semi-axis took place (Morbidelli et al. (2015) and references therein). With temperatures decreasing in the protoplanetary disk with increasing distance from the central star, a more sorted distribution could be expected. These three observations all point towards a dynamically disruptive period during the protoplanetary disk which lead to the depletion in mass, partial mixing of taxonomic classes and miss-alignment of asteroid orbits.

The Wetherill's Methode was first proposed in 1992 (Wetherill, 1992). In this model the inner protoplanetary disk was populated by planetesimals and planet embryos. Perturbations between these bodies and the resonances of Jupiter emptied the asteroid belt region and led to collisions between embryos at lower radii leading to the formation of the terrestrial planets. In the asteroid belt region, the embryos are excited and ejected from the disk leading to a depletion in the overall mass of the asteroid belt. Any remaining asteroids are scattered changing their major semi-axis, eccentricities and inclinations. Simulations of such a scenario indeed reproduced similar conditions as are observed today (Morbidelli et al. (2015) and references therein, O'Brien et al. (2006), O'Brien et al. (2007)). Only the inclination of the asteroids seems to be higher than what we observe in the present asteroid belt. The extent of scattering along the semi-axis of the asteroids is on the order of 0.5 au (O'Brien et al., 2007). Looking at Figure 1.1b this implies that the S-complex formed around 2 au and the C-complex around 3 au in this scenario.

While the Wetherill model reproduces the asteroid distribution we see today quite well, it does not explain the small size of Mars in comparison to Earth or the large semi-major axis of Jupiter today especially with the the inward migration of planets. A more recent model that additionally tries to tackle these two obstacles is the Grand Tack Model first suggested by Walsh et al. (2011). It is based on the gas driven migration of the giant planets within the gas dominated protoplanetary disk (during 10,000 y). Several different migration schemes were attempted by Walsh et al. (2011) including the migration of only Jupiter, Jupiter and Saturn or Jupiter, Saturn as well as Neptune and Uranus. All showed similar results. Here we present one possible scheme also presented by Morbidelli et al. (2015) (see Figure 1.2). The position of Jupiter close to the snowline (around 3.5 au) allowed it to grow fast and large in the

gas disk (few Myr), leading to its inward motion towards the Sun through gas drag. Jupiter and Saturn start an inward migration until Saturn reaches its final size. This is expected to happen when Jupiter reaches a heliocentric distance of 1.5 au, which is the distance at which simulations best reproduce terrestrial planet formation since the formation region is truncated at 1 au on its outer edge. At this point Saturn is large enough to trigger an outwards motion by "tacking" onto Jupiter. The planets migrate out until Jupiter reaches about 5.5 au which is when the gas in the disk is removed. In the next 30 Myr the terrestrial planets form. During the inward migration, the giant planets pass through the initial inner planetesimal and planet embryo material pushing it inwards and scattering parts of it outwards beyond 3 au. This inner disk material is expected to be S-type, because volatile-poor material (S-type material) is expected to have formed in the inner disk and volatile-rich material (C-type) in the outer disk. Once the giant planets migrate back out they pass through this scattered (S-type) material and scatter some of it back to the asteroid belt region. They then continue migrating outwards scattering more material (presumably C-type) to the asteroid belt region from further out in the disk as well. Since the region in which the material is scattered into is dependent of its initial position of the disk, this process leads to a similar distribution of S- and C-complex material as observed in the asteroid belt today, with S-type material dominating in the inner asteroid belt and C-type in the outer asteroid belt. A schematic summary of the Grand Tack model is given in Figure 1.2. The total mass of the asteroid belt after the Grand Tack exceeds that of today by a factor of four. The Grand Tack model succeeds to reproduce the inclination distribution of the asteroid belt. The eccentricity distribution is slightly higher than observed today. The orbits of the giant planets after the end of the Grand Tack were most probably not the final ones we see today.

It is expected that a second dynamical phase took place due to the interaction of the giant planets with planetesimals located between the orbit of Neptune and 30 au (Morbidelli et al. (2015) and references within). This is simulated in the Nice Model. Thereafter, the resonances of the giant planets are disturbed which leads to an instability in the Solar System presumably 450 Myr after the gas removal. The interaction between the giant planets scatters them into the separated orbits they are in today. Jupiter and Saturn initially "jump" apart before further drifting smoothly. This allows for the secular resonance to jump over the asteroid belt and the terrestrial planet region, thus preserving their orbital structure. However, the change in Jupiter's eccentricity leads to a re-adjustment of the asteroids eccentricities and depletion of the asteroid belt by approximately 50 % leading to a distribution similar to the one seen today Deienno et al. (2016). A schematic summary of the Nice Model is given in Figure 1.2 as well.

After the giant planets become stable, the asteroid belt continues to evolve by depletion of regions with unstable resonances and collisional breakups. The Yarkowski effect leads to the drift of bodies in the Solar Disk due to re-emission of radiation previously absorbed from the sun (e.g. Bottke et al. (2002) and Bottke et al. (2006)). It is size dependent, with smaller sized objects drifting faster, and leads to the drift of small bodies like asteroids into resonances (DeMeo et al. (2015) and references therein). This process is believed to help deliver Asteroids into a near earth orbit (NEO) (Bottke

et al., 2002) from where it is possible for them to reach Earth.

1.2 Meteorites

The collection of extraterrestrial materials we have on Earth includes various types such as meteorites, Interplanetary Dust Particles (IDPs), Antarctic Micrometeorites (AMMs) or cometary grains (e.g. Grady and Wright (2006) and references therein). While in terms of mass, meteorites do not dominate the flux of extraterrestrial material to Earth (micrometeorites deliver $\sim$ 2000 time more material than meteorites (e.g. Engrand and Maurette (1998) and references therein), their larger sizes present a real advantage in comparison to dust for laboratory measurements. Here we focus on the analysis of meteorites only.

Meteorites are pieces of extraterrestrial material that are ejected from their parent bodies (e.g. through collision processes), find their way to Earth's orbit and survive the passage through Earth's atmosphere. While meteorites can come for several different types of parent bodies (including martian or lunar meteorites) the majority ($>$ 99 % Scott and Krot (2003)) have asteroidal origins. Once on Earth, they can be found, collected and analyzed in the laboratory. Meteorites for which the fall was observed (falls) and those for which it was not (finds) are distinguished. Besides the remote analysis of asteroids through reflectance spectroscopy and sample return missions, meteorites are the main means for investigating asteroids and their formation history.

Generally, a distinction is made between differentiated meteorites (achondrites, stony irons and iron meteorites) and undifferentiated meteorites (chondrites). The latter contain some of the most primitive material in our Solar System some of which can date back to the Solar Nebula. Thus, chondrites are of great importance for the investigation of the origin and formation history of the Solar System and are the main focus of this dissertation.

Chondrites show a large variety of chemical and mineralogical properties allowing for the identification of different chondrite classes. The main classes are carbonaceous (CCs), ordinary (OCs) and enstatite chondrites as well as R (Rumuruti-like) and K (Kakangari-like) chondrites. Each class was initially sub-divided into different groups based on their chemical and stable isotopic compositions, petrographies and mineralogies (primary classification, see Section 1.2.1). Later, petrology was taken into account for the classification as well (secondary classification, see Section 1.2.2). A summary of all classes and their corresponding groups is given in Figure 1.3.

1.2.1 Primary classification

Petrography

Chondrites consist of four main components which are chondrules, refractory inclusions, metal and matrix material (Krot et al., 2014). The modal abundances and sizes of these different components vary between chondrite groups as summarized in Table 1.4.

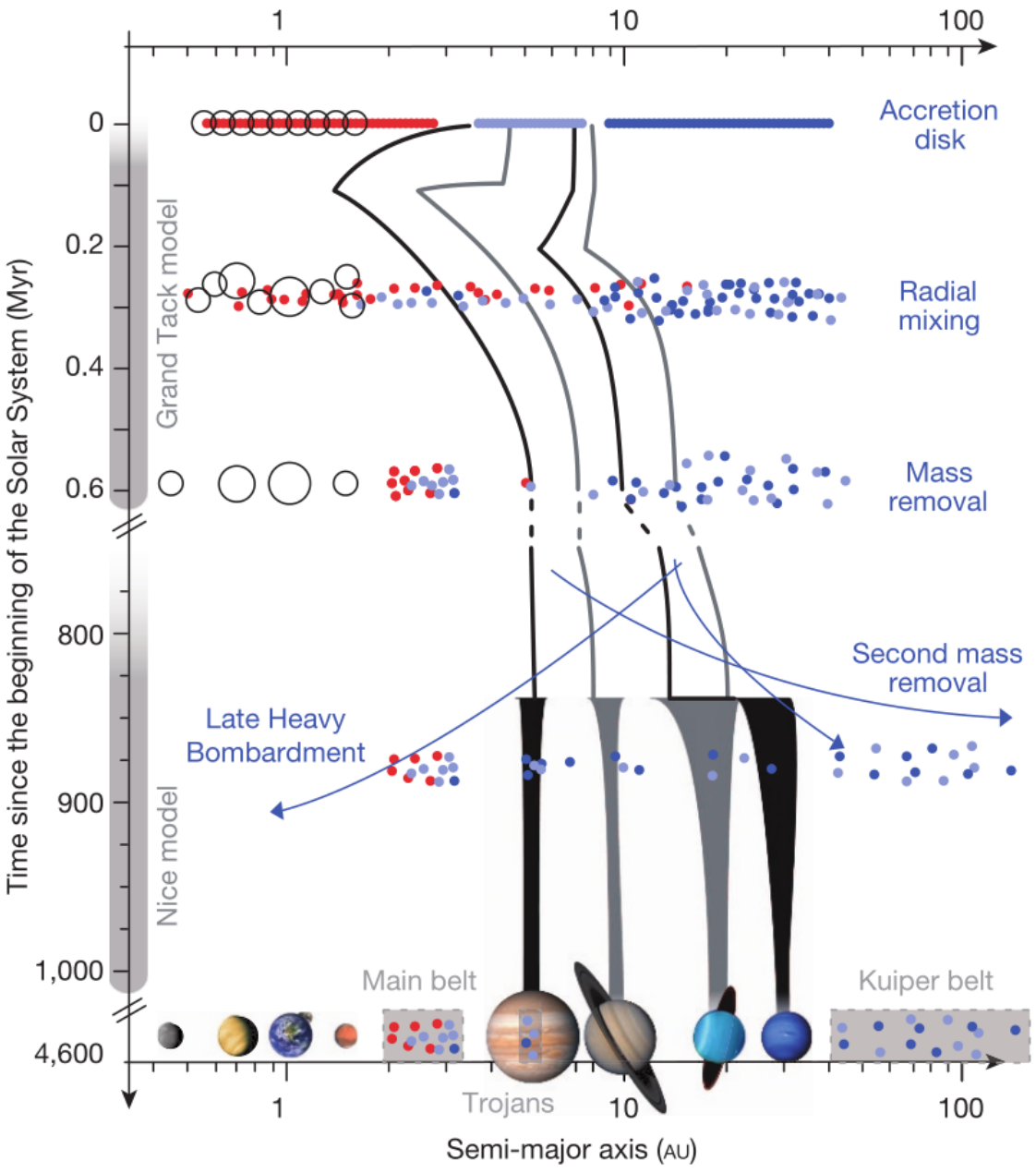

Figure 1.2: Schematic summary of the dynamical history of early Solar System assuming the Grand Tack and Nice model. Shown are the different dynamical stages of these models as a function of time since the beginning of the Solar System. The image was taken from DeMeo and Carry (2014).

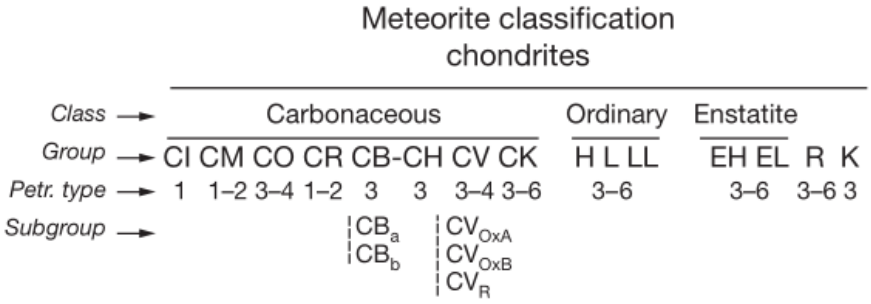

Figure 1.3: Summary of the different chondrite classes and their sub-groups. Image was taken from Scott and Krot (2003).

Chondrules are spherical silicate (mainly olivine and low-calcium pyroxene (Scott and Krot, 2003)) droplets that vary in size and abundance between chondrite groups (Table 1.4). They are thought to have formed as melts in the Solar Nebula and as such are some of the oldest material from the early Solar System. It is believed that most of the material that accreted in the inner Solar System came from chondrules (Scott and Krot (2003). and references therein). They contribute up to 80 % to the total volume of chondrites (Table 1.4).

Refractory inclusions are less abundant than chondrules but of great importance due to their age. Generally, refractory inclusions are either Calcium-Aluminum-rich inclusions (CAIs) or Amoeboid Olivine Aggregates (AOAs). Specifically, CAIs are the oldest material in chondrites (besides presolar grains). Dating of CAIs in the famous CV chondrite Allende was used to estimate the age of the Solar System, that is the time of first condensation of matter, at 4567.18 ± 0.50 billion years (Amelin et al., 2010). CAIs are very diverse with mineralogical and isotopic differences between different CAI groups. The most common CAI groups found in chondrites are spinel-rich, pyroxene-rich and melilite-rich CAIs (Lin et al., 2006). CAIs are believed to have formed through high-temperature (> 1300 K) condensation, evaporation or a mixture of both. AOAs are small (< 5 mm) irregularly shaped inclusions that are found in CCs. As some CAIs, they most likely formed through high-temperature condensation in the Solar Nebula (Ruzicka et al., 2012).

Metals in chondrites are either refractory elements associated with CAIs Schwander et al. (2011) or iron, troilite, cobalt and nickel associated with chondrules. (Scott and Krot (2003) and references therein). Through melting processes some of the iron in the chondrules can be released into the surrounding matrix material.

Lastly, the fine-grained, porous matrix material can be found in between the other chondrite components, holding them together. It is made of silicates (e.g. olivine, pyroxene and amorphous silicates), oxides, sulfides (e.g. pyrrhotite or troilite), iron-nickle, carbonates and in some cases phyllosilicates (such as saponite, cronstedtite or smectite) (Scott and Krot (2003) and references therein). The matrix is richer in volatiles than the other chondrite components and its fine grained texture makes it especially susceptible for secondary processes.

			Carbonaceous						*Ordinary*			*Enstatite*		*Additional*	
	CI	CM	CO	CR	CH	CB	CV	CK	H	L	LL	EH	EL	K	R
CAI + AOA (vol%)	«1	5	13	0.5	0.1	<0.1	10	4	<0.1	<0.1	<0.1	<0.1	<0.1	<0.1	<0.1
chd (vol%)	«1	20	48	50–60	~70	30–40	45	15	60–80	60–80	60–80	60–80	60–80	27	>40
matrix (vol%)	>99	70	34	30–50	5	<5	40	75	10–15	10–15	10–15	<0.1	<0.1	60	30
metal (vol%)	0	0.1	1–5	5–8	20	60–70	0–5	<0.01	8.4	4.1	2.0	10.1	10.2	7.4	<0.1
chd, mean diam. (mm)		0.3	0.15	0.7	0.02	0.1–20	1	0.7	0.3	0.7	0.9	0.2	0.6	0.6	0.4

Figure 1.4: Summary of the average modal abundances of the different petrographic components for different chondrite groups. Chondrite groups that I worked on during this PhD are highlighted in grey. Table was taken and adapted from Krot et al. (2014).

Oxidation state and oxygen isotopic composition

The oxidation state between different chondrite groups can vary greatly as shown in the Urey-Craig diagram in Figure 1.5a. It depicts the iron in metal and sulfides over the iron in silicates and oxides. As can be seen, the CCs are the most oxidized, followed by the OCs and lastly the enstatite chondrites (Krot et al., 2014). Within the different chondrite groups, the oxidation state decreases from LL to L to H for OCs and from CI to CM to CK to CV to CO to CR to CH to CB for CCs and from EH to EL for enstatite chondrites.

Differences in oxygen isotopic compositions are observed between chondrite groups. By comparing the ratio of ^{17}O and ^{18}O over ^{16}O in the sample with each other (with both ratios normalized to the ratio of ^{17}O and ^{18}O over the ^{16}O of Standard Mean Ocean Water (SMOW)) different trends can be seen (Figure 1.5b) (e.g. Clayton (1993), Krot et al. (2014) and references therein). Terrestrial samples plot along the terrestrial fractionation line (TFL). The CCs plot along the carbonaceous chondrite anhydrous mineral (CCAM) line which is located underneath the TFL. The OCs and enstatite chondrites plot above the TFL in a cluster.

1.2.2 Secondary classification

Petrologic type

While chondrites are primitive, they experience a range of secondary processes in their asteroidal parent bodies. This includes aqueous alteration, thermal metamorphism and shock metamorphism. Therefore, an additional classification scheme was introduced by Van Schmus and Wood (1967) to give a measure of the alteration state of each chondrites. It assigns a petrologic type (PT), ranging from type 1-7, to each chondrite. Type 1 and 2 indicate aqueous alteration with type 1 being the most aqueously altered. In some studies, these two groups are summarized in 10 sub-categories ranging from type 2.0-2.9 (e.g. Alexander et al. (2013), Harju et al. (2014),Kimura et al. (2020), Rubin et al. (2007), Howard et al. (2015) and Prestgard et al. (in prep.)). Types 4-6 (sometimes uo to 7) indicate an increase of metamorphic grade, with type 7 being the most metamorphosed. Type 3 chondrites are the most primitive. They are further subdivided into 10 sub-categories ranging from type 3.0-3.9 with metamorphic grade increasing with increasing type (Sears et al., 1995). These classifications are

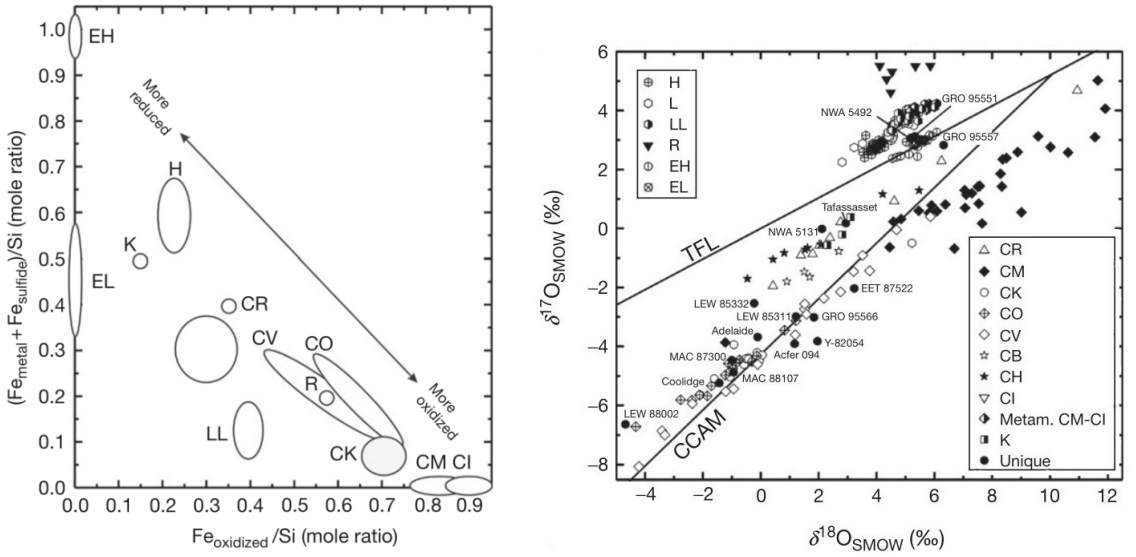

(a) Urey-Craig diagram comparing the iron in metal and sulfates with the iron in sulfides and oxides. Image was taken from Krot et al. (2014).

(b) Comparison of the oxygen isotopic composition between chondrite groups. Image was taken from (Krot et al., 2014).

Figure 1.5: Summary of the oxidation state and oxygen isotopic composition of different chondrite groups.

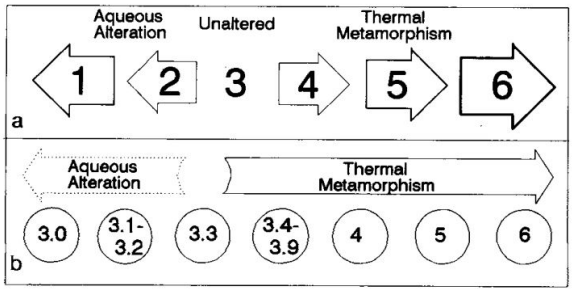

Figure 1.6: Summary of the petrologic types of chondrites. Image was taken from Sears et al. (1995).

summarized in Figure 1.6.

Secondary processes

Identifying the secondary processes and quantifying the amount experienced by each chondrite is an important but not easy task. In order to acquire the original composition of the asteroidal parent bodies it needs to be understood in which way the material has been altered since formation. By constraining the post-accretion history of each chondrite, we can start to build up a picture of which components are original to the initial asteroid and which were altered. In the following, a summary on each of the aforementioned secondary processes is given.

Thermal metamorphism is the process of heating of small bodies. Several heating mechanisms have been proposed including short-lived (e.g. ^{60}Fe, ^{26}Al Urey (1955))

and/or long-lived radionuclides (e.g. ^{238}U, ^{235}U, ^{232}Th and ^{40}K Yomogida and Matsui (1984)) or electromagnetic induced heating (Sonett et al., 1968). However, it has been shown that the latter could not have been the sole heating source (e.g. Ciesla et al. (2013)). Similar cosmic-ray exposure ages between OCs of different PTs (e.g. Thomas and Kurt (1995)) argue against long-lived radionuclides. Therefore, the most widely accepted heating mechanism for small bodies is the radioactive decay of short-lived radionuclides such as ^{26}Al (first suggested by Urey (1955)) or ^{60}Fe. Depending on the time of accretion as well as the size of the small body, different amounts of thermal metamorphism are experienced with varying peak metamorphic temperatures ((Bonal et al., 2016), Huss et al. (2006)). Timescales of thermal metamorphism can be estimated from radiometric age dating. Based on such measurements done on a few OCs, the OC parent bodies accreted about 2 Myr after CAI formation. The thermal metamorphism experienced by PTs 3.0-3.2 then took place until 2 - 4 Myr after CAI formation, for PTs 3.7-4 it took place until 6 Myr later and for PT 6 it took place until more than 7 Myr later (Huss et al., 2006).

In the laboratory, different techniques can be used to determine the extent of metamorphism experienced by type 3 chondrites. Induced thermoluminescence (ITL) of feldspar in the chondrites is a widely used method (e.g. Sears et al. (1980)). However, the PTs determined by ITL were found to often be erroneous (e.g. Bonal et al. (2006)). Therefore, Raman spectroscopy of polyaromatic carbonaceous matter (Bonal et al., 2016) is a preferred method. With Ramam spectroscopy, the width of the D band ($FWHM_D$) is given as a measure of the peak metamorphic temperature experienced and, thus, the PT. The $FWHM_D$ is a spectral parameter derived from the Raman spectra of matrix fragments. It reflects the structural order of the polyaromatic carbon matter in the matrix which in return reflects the metamorphic history of the whole rock. It is particularly sensitive to the experienced peak metamorphic temperature (Bonal et al., 2016).

Aqueous alteration is the process of hydration and hydroxylation of minerals in the chondrite components. Different aqueous alteration processes have been proposed including aqueous alteration of Solar Nebula grains from water vapor and icy regions (e.g. Lawrence and W. (1974), Ciesla et al. (2003)) and alteration on protoplanetary bodies (e.g. Bischoff (1998)). However, for most chondrite groups that show traces of hydration, aqueous alteration in the asteroidal parent bodies seems most probable (e.g. Brearley (2003)). During the accretion process icy particles can be accumulated onto the parent body from the formation reservoir. Defining the start and duration of the parent body aqueous alteration is difficult. Based on thermal models and short-lived radionuclide chronometers, aqueous alteration should have started within 0.03-0.6 Myr after accretion when the melting temperature of water ice was reached. Assuming that the initial ^{26}Al/^{27}Al ratios were high enough to ensure melting temperatures of water ice but not so high that all water was lost early on, aqueous alteration could have lasted several million years (Brearley (2006), Krot et al. (2006)). Evidence for extraterrestrial sources of hydration in the early inner Solar System exists as well (e.g. McCubbin and Barnes (2019)).

The amount of hydration each chondrite experienced can be constrained with vary-

ing measuring techniques. For the detection of secondary hydration minerals such as phyllosilicates, carbonates, magnetite and sulfides (Krot et al., 2015), X-ray microscopy, transmission electron microscopy (TEM) or scanning electron microscopy (SEM) are widely used (e.g. Brearley (2006) and references therein, Dobrică and Brearley (2020), Abreu and Brearley (2010), Tomeoka et al. (1989)). Besides these mineralogical studies, elemental analysis, Fourier transform infrared (FTIR) spectroscopy of matrix fragments and Thermogravimetric analysis (TGA) of bulk powders are also suitable for the detection of hydration. The latter two will be discussed in more detail during this dissertation (see Sections 2.2.3 and 2.2.4).

Shock metamorphism is the result of collisions between bodies. The impact can heat up the impacted region locally (e.g. Davison et al. (2012)). This elevation of temperature and pressure can lead to the dehydration of the material around it (e.g. Jewitt (2012)). Depending on the size and velocity of the impactor (relative to the given body), varying degrees of shock are measured in different chondrite samples. The shock states, which can range from S1 for unshocked chondrites to S6 for very strongly shocked chondrites, are determined e.g. by petrographic measurements using shock indicators (Bennett and McSween, 1996, Scott et al., 1992, Stöffler et al., 1991) (see Section 2.2.5).

1.2.3 Terrestrial modification

Once the chondrites have reached Earth, they will interact with its environment to varying degrees, a process called terrestrial weathering. The amount of weathering experienced is dependent on when and where they land as well as the composition and texture of the chondrite. For falls, the terrestrial weathering can be minimal if they are found quickly and stored appropriately. However, only 1.95 % of chondrites in our collection are falls, the remaining are finds (based on the Meteoritical Bulletin Database (2022)). Many of the finds in our meteorite collection (about 57 %, based on the Meteoritical Bulletin Database (2022)) come from very cold (mainly Antarctica) or hot, dry deserts environments (e.g. Atacama or Sahara). The extreme conditions in these specific environments allow for the preservation of the chondrites over thousands or even millions of years after their fall (e.g. Bland et al. (2006)). Nonetheless, some modification induced by terrestrial weathering are found in most chondrites. Typical weathering products are iron oxides and oxy-hydroxides (such as goethite, ferrihydrite, magnetite or maghemite) (Bland et al., 2006).

Weathering products can be identified e.g. through the inspection of thin or thick sections under a microscope (see Section 2.2.5). The weathering scale most widely used ranges from W0 to W6, with W0 being almost unaltered and W6 showing alteration to most silicates (Wlotzka, 1993).

1.2.4 Carbonaceous versus ordinary chondrites

During the course of this three year PhD I have worked both on a large set of CCs as well as a large set of OCs (see Chapter 2). More specifically, I focused on CV, CO

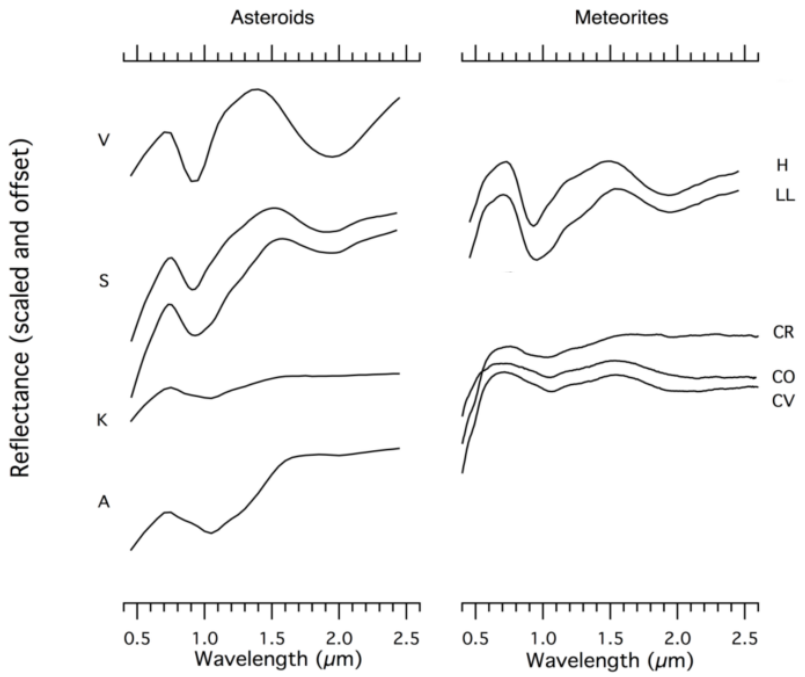

Figure 1.7: Comparison of several end member main-belt asteroid reflectance spectra with those of OCs, CVs, COs, and CRs. The end member asteroid spectra come from DeMeo et al. (2009). The S-type spectra are average spectra of H-like and LL-like S-type spectra from Vernazza et al. (2014). The H, LL, CV, CO and CR spectra are averages group spectra taken from the RELAB (2022) database. Plot was taken and adapted from Vernazza and Beck (2016).

and CR chondrites for CCs. As shown in Figure 1.7 the reflectance spectra of CVs, COs and CRs are quite similar but do not seem to have an immediate equivalent among the asteroid end member spectra taken from DeMeo et al. (2009). This makes them interesting chondrite groups to study. For OCs, I worked both on equilibrated (EOCs) and unequilibrated ordinary chondrite (UOCs). While the characteristics of each of these chondrite groups will be discussed in Section 2.1, in this Section, the focus will be on the differences between the CC and OC groups.

Hydration history

Hydrated minerals are detected to varying degrees in almost all chondrite groups besides enstatite chondrites. Within the CC group, varying amounts of hydration are observed. CIs, CMs and CRs are characterized by PTs 1-2, indicating an elevated amount of aqueous alteration in their asteroidal parent bodies (Figure 1.3). Being the most aqueously altered chondrites, hydrated minerals such as phyllosilicates, magnetites, sulfides, carbonates and sulfates can be found in their matrices, CAIs and chondrules (Brearley, 2003, Scott and Krot, 2003). For CVs and COs, which are PT 3, aqueous alteration seems to be mainly confined to their matrices. Their matrices contain hydrated minerals such as phyllosilicates (e.g. Brearley (2003) and Bonal et al. (2020)).

In contrast, OCs, originating from inner Solar System bodies (S-type asteroids), are traditionally believed to be dry. However, traces of hydration have been previously detected in some OCs (Brearley, 2006). Based on X-ray microscopy, SEM and TEM, hydrated minerals due to aqueous alteration have been detected in a few, most primitive UOCs such as Semarkona (LL3.09) and Bishunpur (LL3.15) (e.g. Alexander et al. (1989), Alexander et al. (2010), Dobrică et al. (2019) or Brearley (2006)). Even for EOCs signatures of aqueous alteration have been detected (e.g. Grossman et al. (2000), Rubin et al. (2002), Lewis and Jones (2016), Lewis et al. (2018), Lewis and Jones (2019), Lewis et al. (2022)). Contributing to the existing knowledge on hydration in OCs is one of the main goals of this PhD (Chapter 5).

As explained in Section 1.2.2 aqueous alteration is the process of hydration in asteroids. However, the final hydration measured in a chondrite is not only dependent on extraterrestrial hydration processes. It is determined by a combination of terrestrial and extraterrestrial hydration episodes as well as heating processes. Terrestrial weathering will increase the hydration of a chondrite while thermal metamorphism and shock metamorphism lead to dehydration. To assess the initial hydration experienced on the asteroidal parent body, all of these processes and their influence on the mineralogy of the chondrites need to be taken into account.

Stable isotope anomalies

When comparing stable-isotope anomalies (e.g. ϵ^{50}Ti versus ϵ^{54}Cr, Figure 1.8) of different Solar System bodies, two distinct groups can be observed (Trinquier et al. (2007), Warren (2011)). The first group, called the carbonaceous (C) group, includes CCs, and shows higher percentage of ϵ^{50}Ti and ϵ^{54}Cr. The second group, called the non-carbonaceous (NC) group, includes terrestrial planets, OCs and enstatite chondrites and several non-chondritic meteorites. For this group the ϵ^{50}Ti and ϵ^{54}Cr abundances are lower. The existence of two distinct groups indicates two genetically distinct nebular formation reservoirs that were spatially separated (e.g. Warren (2011)). Constraining the exact location of these reservoirs in the disk as well as the start and duration of their existence is subject of many studies. Warren (2011) suggested that the two reservoirs could have been initially separated by Jupiter, subsequently being mixed by a process such as the Grand Tack model (Walsh et al., 2011) (see Section 1.1.2). With the objects in the NC group generally being depleted in volatiles, including water, in comparison to the C group (Morbidelli et al. (2015) and references therein) this suggests that OCs formed in the inner Solar System inside of the snowline, while CCs formed in the outer Solar System beyond the snowline.

While previously studied iron meteorite groups were comparable to those of the NC group only, Kruijer et al. (2017) showed that the tungsten (W) and molybdenum (Mo) isotope signatures of some iron meteorite groups plot with those of the C group. This indicates the existence of NC and C iron meteorites. Using the ^{182}Hf–^{182}W chronometer on iron meteorites Kruijer et al. (2017) was able to conclude that the accretion in the NC and C reservoirs took place at different times. The oldest iron meteorites in the C reservoir accreted around 0.2 Myr after CAI formation. This is before OCs in the NC reservoir which accreted around 2 Myr after CAIs and the youngest CCs which

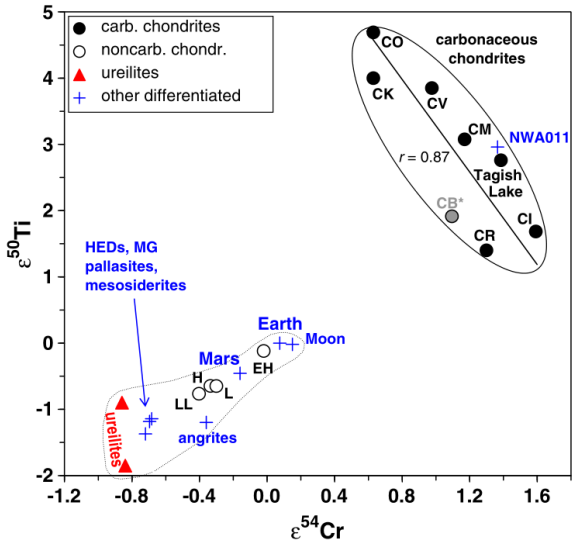

Figure 1.8: Comparison of stable isotope anomalies between different Solar System bodies. Show is ϵ^{50}Ti versus ϵ^{54}Cr. Two distinct groups can be seen: a non-carbonacous and carbonaceous group.

accreted around 3-4 Myr after CAI formation. This also indicated that the dichotomy in the disk must have existed at least until 3-4 Myr after CAI formation (Kruijer et al. (2017), Scott et al. (2018)). Recently these accretion ages have been reviewed (Spitzer et al., 2021) and found to have taken place within about 1 Myr after CAI formation for both NC and CC iron meteorites.

1.3 Asteroid-Meteorite connection

With the majority of our meteorite collection being of asteroidal origin (Section 1.2) the question of how well it samples the asteroid belt arises. Most of the information we have on asteroids is limited to ground based observations such as reflectance spectroscopy of asteroid surfaces. By combining these studies with the analysis of meteorites in the laboratory we can increase our understanding of asteroids but is it possible to find a genetic link between meteorites and their asteroidal parent bodies? While many matches have been suggested, only a few have been confirmed so far.

1.3.1 Space missions

Flyby missions and sample return missions allow for the combination of space observations and laboratory measurements, making the direct comparison of asteroid material with meteorite samples on Earth possible. For example, the Dawn mission which was launched in 2007 by NASA reached (4) Vesta in 2011 and (1) Ceres in 2015. It allowed for identifying (4) Vesta as the parent body of differentiated meteorites, more specifically Howardite-Eucrite-Diogenite (HED) (Coradini et al., 2011, McSween et al., 2011).

The Near Earth Asteroid Rendezvous-Shoemaker (NEAR Shoemaker) mission vis-

ited the S-type asteroid Eros in 2000 and confirmed the link between OCs and S-type asteroids (e.g. Trombka et al. (2000)). Similarly, the Hayabusa space mission, launched in 2003 by the Japanese Aerospace Exploration Agency (JAXA) to orbit the S-type asteroid (25143) Itokawa, touched down in 2005 and returned to Earth with asteroid samples in 2010. It allowed for the confirmation of a genetic link between S-type asteroids and OCs. More specifically, it was found that Itokawa is made of thermally metamorphosed (PT 4-6) LL OCs (Nakamura et al., 2011). Since then, a second mission, Hayabusa 2 has been launched in 2014 and reached the surface of the C-type asteroid (162173) Ryugu in 2018. It returned to Earth in December 2020 and the analysis of the asteroid samples are currently ongoing. Preliminary results suggest that Ryugu is most similar to CI chondrites (e.g. Yada et al. (2022)).

The Origins Spectral Interpretation Resource Identification Security – Regolith Explorer (OSIRIS-REx) was launched in 2016 by NASA to analyze the low-albedo B-type asteroid (101955) Bennu (e.g. Hergenrother et al. (2013) and Lauretta et al. (2019)). It successfully touched down in 2020 and will return with the collected samples in 2023.

1.3.2 Spectral comparison

Besides space missions, reflectance spectroscopy is a key tool for linking meteorites to their asteroidal parent bodies. This is not an easy task. As shown in Figure 1.1a the average reflectance spectra of asteroids show often faint spectral features between 0.45 and 2.45 µm. The main spectral features that can be distinguished between different types are the 1 µm and 2 µm absorption bands and the spectral slopes.

Several factors play into the comparability of asteroid and meteorite reflectance spectra. The measuring geometry and grain size can influence band depths and slopes. Temperature differences can have an influence on the mafic mineral bands but the effects are generally negligible in comparison to grain size and geometry effects (e.g. Cloutis et al. (1986)). In fact, an increase in reflectance and a decrease in band depths can be observed with decreasing grain size (e.g. Mustard and Hays (1997), Sultana et al. (2021)). Therefore, when studying asteroid surfaces and comparing them with meteorites, grain size is of importance (e.g. Krämer Ruggiu et al. (2021)).

Environmental factors further change the shape of reflectance spectra. For meteorite spectra, terrestrial weathering products can change the spectral region below 600 nm (e.g. Cloutis et al. (2012a)) and increase the size of the 3 µm hydration band. For Asteroids, which are exposed to the space environment, space weathering (SW) plays an important role. SW is the bombardment of the asteroid surface by micrometeorites and the irradiation by cosmic-ray ions and solar winds (e.g. Brunetto et al. (2015)). This leads to a change in their composition and physical properties (e.g Pieters and Noble (2016)) and thus influences their reflectance spectra. Since SW only affects the most upper surface layer of asteroids, any signature of it is erased during the high temperature entry of meteors into Earths atmosphere. To be able to compare between asteroid and meteorite spectra, the effects SW has on asteroid spectra needs to be taken into account.

To better understand and quantify SW, irradiation experiments are used to artificially space weather chondrites. Irradiation experiments using N^+, Ar^+ and Ar^++ ion

beams on orthopyroxene, olivine and bulk silicate-rich rocks to represent silicate-rich (S-type) asteroids revealed reddening and darkening of the reflectance spectra (Marchi et al., 2005). The effects of SW on dark (low-albedo) surfaces such as carbonaceous asteroids (C-Type) seem to be more variable than for S-types. Ion irradiation of the CV chondrite Allende led to a reddening and darkening of its reflectance spectrum (Brunetto et al., 2014). The same is found for CM, CV and CO chondrites by Lazzarin et al. (2006) and Moroz et al. (1996a). For the ungrouped CC (C-ung.) Tagish Lake, irradiation experiments lead to spectral flattening (Vernazza et al., 2013). Laser pulse irradiation (to simulate micrometeorite bombardment) of CM chondrite Murchison resulted in spectral flattening, darkening and a decrease of the 0.7 µm and 3 µm band depths (Matsuoka et al., 2020). Lantz et al. (2017) performed ion irradiation experiments on CV, CO, CM, CI and Tagish Lake samples. They observe spectral darkening and reddening for the CV and CO chondrites and a spectral brightening and blueing of the CM, CI and Tagish Lake. chondrites. On the basis of all these works, SW models have been developed (e.g. Brunetto et al. (2006), see Section 2.3.1) which were used during this PhD (see Chapter 4).

Nonetheless, attempts to identify asteroidal parent bodies based on reflectance spectra have previously been made (e.g. Cloutis et al. (2012c), Cloutis et al. (2012a), Cloutis et al. (2012b), Vernazza et al. (2014)). Indeed, the link between S-type asteroids and OCs had been suggested based on reflectance spectroscopy before it was confirmed by the samples returned by the Hayabusa space mission. More specifically, it was found that the silicate bands as well as olivine to ortho-pyroxene ratios and spectral slopes of OCs are comparable to S-type asteroids after laser treatment (e.g. Chapman and Salisbury (1973) and Moroz et al. (1996b)).

For the CCs various asteroidal parent bodies were suggested although the majority are expected to come from C-complex asteroids (e.g. (Bell et al., 1989), DeMeo et al. (2015), Vernazza and Beck (2016) and references therein). Several works have suggested a link between L-type asteroids and CAI-rich material such as CV and CO chondrites Burbine et al. (1992), Devogèle et al. (2018), Sunshine et al. (2008). Bell et al. (1988a) suggested that Eos family members (K-type) are linked to CV and CO chondrites while Vernazza et al. (2015) suggests that K-type are linked to CV, CO, CK and CR chondrites. Others indicated that the C-types are the asteroidal parent bodies to CKs (Gaffey and McCord, 1978) and CRs (Hiroi et al., 1996).

1.4 Objectives of this dissertation

This Section will summarize the main objectives of this dissertation. The first objective is to improve our understanding of asteroid reflectance spectra. As discussed in Section 1.3 measuring and analyzing chondrite reflectance spectra is a great tool for doing so. What are the spectral variations within the same chondrite group as well as between different chondrite groups? Which spectral features might be controlled by post-accretion processes? How do terrestrial processes influence the reflectance spectra? To answer these questions I focus on the acquisition and analysis of a large set of CC (Chapter 3) and OC reflectance spectra (Chapter 4). Constraining the variation in

spectral features of chondrites then has direct implications on variations in asteroid spectra.

Furthermore, constraining the reflectance spectral features of chondrite and asteroid groups, will allow for the direct comparison between the two. By doing so, the second objective of this dissertation is to refine the genetic link between type 3 chondrites and their asteroidal parent bodies. As discussed in Section 1.3.2 this is not an easy task. In Chapter 3 I focus on the search for the asteroidal parent bodies of the CCs. In Chapter 4 an attempt is made to further constrain the already established link between S-type asteroids and OCs.

The last objective of this three year PhD is to help constrain the place of formation of different asteroid groups within the protoplanetary disk. As explained in Section 1.2.4, we expect separate formation reservoirs for the CCs and OCs based on stable isotope anomalies. However, the exact location of these reservoirs is not well known. The in-depth analysis of the post-accretion history of chondrites can help constrain their locations. Therefore, in Chapter 5 I will present an in-depth study of the hydration history of a larger set of UOCs. The detection of hydration in UOCs has implications on the position of the snowline in the protoplanetary disk at the time of accretion.

2 Samples and Measuring techniques

2.1 Samples

During the course of this three year PhD, I have worked on over 130 chondrites by measuring them with various analytical techniques, which will be discussed in detail in Section 2.3. More specifically, I measured 47 UOCs, 39 EOCs, 28 CVs, 15 COs and 8 CRs and reduced and interpreted the resulting data. Due to varying sample masses, metamorphic grades and weathering degrees, not every chondrite was measured with each technique. Tables 2.1, 2.2 and 2.3 lists all the considered chondrites and indicate which techniques were applied to which sample. It also includes the various sources of the bulk samples and thin/thick sections.

Additionally, I obtained the reflectance spectra of 9 CKs (RELAB, 2022), 24 Eos family members (RELAB, 2022), 466 S-type asteroids (Mahlke et al., 2022) and 17 asteroidal end members (DeMeo et al., 2009) from various databases and treated them in as I did for chondrites, for comparison.

2.1.1 Ordinary chondrites

The OCs are the most abundant chondrite group in our collections (about 85 % Meteoritical Bulletin Database (2022)). They are characterized by a large range of metamorphic grades. Therefore, the OCs are sub-divided into UOCs for PTs 3.0-3.9 and EOCs for PTs 4-7. Furthermore, UOCs and EOCs are sub-divided into H, L and LL based on their total abundance of iron and its oxidation state. The abundance of metal decreases (Table 1.4) and the oxidation state increases from H to L to LL (Figure 1.5a). As shown in Table 1.4, the OCs are characterized by high abundances of chondrules (60-80 vol%), 10-15 vol% matrix and little or no CAIs and AOAs (< 0.1 vol%). The metal abundance (8.4 vol% for H, 4.1 vol% for L and 2.0 vol% for LL) and chondrule size (0.3 mm for H, 0.7 mm for L and 0.9 mm for LL) varies between H, L and LL.

Of the 85 OCs I studied, 46 were UOCs and 39 EOCs. A list of all UOCs and EOCs considered during my PhD is given in Tables 2.1 and 2.2.

Table 2.1: List of all UOCs I measured. Listed are their: names, $FWHM_D$ values, type (as re-classified during this PhD) and PT. For UOCs where the PT and/or Type are italic, Raman spectroscopy was unsuccessful or not performed and/or the classification was not verified here. For these UOCs, the PT and Type were taken from the Meteoritical Bulletin Database (2022). For each UOC the used measuring technique (TGA, FTIR spectroscopy (IR Spectr.), Reflectance spectroscopy (Refl. spectr.) or Petrography) is marked. "y" stands for "yes", "-" stands for "no". "(y)" means that TGA was measured at 3 min instead of 10 min isotherm (see Section 2.3.3). "y*" means measurements were done at ambient temperature and pressure. The source of the bulk samples and thin sections are: ASU: Arizona State University (USA), CRPG: Centre de Recherches Pétrographiques et Géochimiques (Nancy, France), MNHN: Museum National d'Histoire Naturelle (Paris – France), MWG: Meteorite Working Group, NASA Johnson Space Center (Houston – USA), NHM: National History Museum (Vienna, Austria)

Samples	$FWHM_D$ (cm-1) (Bonal et al. 2016)	Type (Eschrig et al. 2022)	PT (Bonal et al. 2016)	TGA	FTIR spectr.	Refl. spectr.	Petr.	Source bulk samples	Source thin sections
ALH 76004	158.9 ± 19.7	L(LL)	3.1–3.4	y	y	y	y	MWG	MWG
ALH 77216	-	*L*	*3.7-3.9*	(y)	-	-	-	MWG	-
ALH 78119	47.4 ± 3.7	LL(L)	-	y	-	y	y	MWG	MWG
ALH 82110	-	*H*	*3.6*	(y)	-	-	-	MWG	-
ALH 83007	154.6 ± 15.3	LL	3.4	-	-	y*	y	MWG	MWG
ALH 83008	115.1 ± 9.4	LL	>3.6	y	-	y*	y	MWG	MWG
ALH 83010	200.4 ± 7.5	LL	3.6	(y)	-	-	y	MWG	MWG
ALH 84086	-	LL	3.8	y	-	y*	y	MWG	MWG
ALH 84120	-	L	3.8	y	-	y*	y	MWG	MWG
Bishunpur	174.1 ± 12.9	L/LL	3.15	y	-	y	y	ASU	MNHN
Bremervörde	50 ± 0	H/L	3.9	y	-	y	y	ASU	MNHN
BTN 00302	159.3 ± 16.8	LL	3.1–3.4	y	y	y	y	MWG	MWG
Chainpur	147.8 ± 7.2	LL	3.4	y	-	y	y	ASU	MNHN
Dhajala	-	H	3.8	y	-	y	y	ASU	MNHN
DOM 03287	122 ± 13	LL	3.6	y	-	y	y	MWG	MWG
DOM 08468	122 ± 6.2	H	3.6	y	-	y	y	MWG	MWG
EET 83248	110.6 ± 13	H	>3.6	(y)	y	y	y	MWG	MWG
EET 87735	192.1 ± 21.8	LL	3.05–3.1	y	-	y	y	MWG	MWG
EET 90066	182.2 ± 9.3	LL	3.1	y	y	y	y	MWG	MWG
EET 90628	254.2 ± 19.7	LL	3	y	y	y	y	MWG	MWG
EET 96188	167.6 ± 11.4	LL	3.1-3.4	(y)	y	y	y	MWG	MWG
GRO 06054	225.2 ± 18.6	LL	3.05	y	y	y	y	MWG	MWG
GRO 95504	149.1 ± 7.3	*L*	3.4	-	y	-	-	MWG	-
Hallingeberg	115.33 ± 0	L	3.4	y	-	y	y	ASU	MNHN
Kymka	173 ± 9.8	LL	3.2	y	-	y	y	MNHN	MNHN
LAR 04382	168.8 ± 22	LL	3.1–3.4	y	-	y	y	MWG	MWG
LAR 06279	208.5 ± 27.6	LL	3.05-3.1	(y)	-	y	y	MWG	MWG
LAR 06469	105.4 ± 7.7	L	>3.6	y	-	y	y	MWG	MWG
LEW 87248	248.7 ± 12.9	L(LL)	3	(y)	y	y	y	MWG	MWG
LEW 87284	167.3 ± 46	LL	3.1–3.4	y	y	y	y	MWG	MWG
LEW 88617	133.7 ± 17.6	LL	3.6	y	-	y	y	MWG	MWG
LEW 88632	151.5 ± 11.1	LL	3.4	y	-	y	y	MWG	MWG
MAC 88174	105.1 ± 6.7	H	>3.6	y	-	y	y	MWG	MWG
MCY 05218	198.5 ± 16.7	L	3.05-3.1	(y)	y	y	y	MWG	MWG
MET 00489	204.2 ± 10.7	LL	3.05–3.1	y	-	y	y	MWG	MWG
MET 00506	179.5 ± 7.1	LL	3.1	y	-	y	y	MWG	MWG
Mezö-Madaras	70 ± 0	L	3.7	y	-	y	y	NHM	NHM
MIL 05050	174.5 ± 9.8	LL	3.1	y	-	y	y	MWG	MWG
MIL 05076	148.4 ± 17.2	LL	3.4	y	-	y	y	MWG	MWG
Parnallee	74.7 ± 5.3	LL	3.7	y	-	y	y	NHM	MNHN
Piancaldoli	173.4 ± 20.2	LL	3.1	y	-	y	y	CRPG	CRPG
QUE 97008	222.4 ± 13.4	*L*	3.05	-	y	-	-	MWG	-
RBT 04251	144.4 ± 9	LL	3.4	y	y	y	y	MWG	MWG
Tieschitz	125.9 ± 4.5	H(L)	3.6	y	-	y	y	NHM	MNHN
TIL 82408	208.4 ± 9	LL	3.05–3.1	y	y	y	y	MWG	MWG
WIS 91627	111.3 ± 25.7	H	>3.6	(y)	-	y	y	MWG	MWG
WSG 95300	146.2 ± 8.8	H	3.4	y	-	y	y	MWG	MWG

Table 2.2: List of all EOCs I measured during this three year PhD. Listed are their names, their type and their PT. Additionally, it is marked for each EOC if it was measured using Reflectance spectroscopy. "y" stands for "yes", "-" stands for "no". The source of the bulk samples are: MNHN: Museum National d'Histoire Naturelle (Paris – France), CEREGE (Aix-en-Provence – France)

Samples	Classification	Reflectance spectroscopy	Source bulk samples
Bandong	LL6	y	MNHN
Beni M'hira	L6	y	CEREGE
Bensour	LL6	y	CEREGE
Catalina 024	H4	y	CEREGE
Catalina 309	L5	y	CEREGE
Coya Sur 001	H6	y	CEREGE
El Medano 378	L6	y	CEREGE
Forest Vale	H4	y	MNHN
Iran 009	LL5	y	CEREGE
Iran 011	L6	y	CEREGE
Kernouve	H6	y	MNHN
Lançon	H6	y	MNHN
Limon Verde 004	L6	y	CEREGE
Los Vientos 083	H4	y	CEREGE
Los Vientos 147	L6	y	CEREGE
Los Vientos 155	H5	y	CEREGE
Los Vientos 416	L4	y	CEREGE
Los Vientos 423	H6	y	CEREGE
Los Vientos 432	H5	y	CEREGE
Monte Das Forte	L5	y	MNHN
Moshampa	LL5	y	CEREGE
MountTazerzait	L5	y	MNHN
NWA 12475	LL6	y	CEREGE
NWA 12546	LL7	y	CEREGE
NWA 12556	LL5	y	CEREGE
NWA 12961	L7	y	CEREGE
NWA 13838	L5	y	CEREGE
NWA 7283	LL6	y	CEREGE
NWA 8268	L4	y	CEREGE
NWA 8275	LL7	y	CEREGE
NWA 8477	L5	y	CEREGE
Paposo 012	H6	y	CEREGE
Saint Severin	LL6	y	MNHN
Soko Banja	LL4	y	MNHN
Ste Marguerite	H4	y	MNHN
Tamdakht	H5	y	CEREGE
Taqtaq-e Rasoul	H5	y	CEREGE
Tuxtuac	LL5	y	MNHN
Viñales	L6	y	CEREGE

Table 2.3: List of all CCs I measured during this three year PhD. Listed are their groups and names, their $FWHM_D$ values as determined by Raman spectroscopy and their PT. If no $FWHM_D$ value is given it means that either Raman spectroscopy was unsuccessful, or not performed for this sample. For these samples, the PT values taken from the Meteoritical Bulletin Database (2022) and marked italic. Additionally, it is marked for each CC if it was measured using TGA, FTIR spectroscopy (IR Spectr.) and Reflectance spectroscopy (Refl. spectr.). "y" stands for "yes", "-" stands for "no". The source of the bulk samples are: FMNH: Field Museum of Natural History (Chicago – USA), MWG: Meteorite Working Group at NASA Johnson Space Center (Houston – USA), MNHN: Museum National d'Histoire Naturelle (Paris – France), CEREGE (Aix-en-Provence – France), NHM: National History Museum (Vienna, Austria).

	Samples	$FWHM_D$ (cm^{-1})	PT	TGA	FTIR spectr.	Refl. spectr.	Source bulk samples
CV_{OxA}	**ALH 81003**	70 ± 3.3	>3.6	y	y	y	MWG
	Allende	73.99 ± 4.31	>3.6	y	y	y	MNHN
	Axtell	72 ± 4	>3.6	y	-	y	FMNH
	GRA 06101	71.6 ± 3.2	>3.6	y	y	y	MWG
	LAP 02206	54.1 ± 8.3	>3.7	y	-	y	MWG
	MIL 07002	68.8 ± 9.2	3.7	y	-	y	MWG
	MIL 07671	68.8 ± 7.6	3.1	y	y	y	MWG
	MIL 091010	75.5 ± 5.8	>3.6	y	y	y	MWG
	QUE 94688	75.7 ± 5.5	>3.6	y	y	y	MWG
CV_{OxB}	**ALH 85006**	121.3 ± 33	3.6	y	y	y	MWG
	Bali	98.56 ± 7.39	>3.6	-	y	-	CEREGE MNHN
	Grosnaja	112.74 ± 6.16	3.6	y	y	y	FMNH
	Kaba	161.85 ± 6.34	3.1	y	y	y	MNHN
	LAR 06317	130.8 ± 26.9	3.4-3.6	y	y	y	MWG
	MCY 05219	93 ± 6.9	>3.6	y	y	y	MWG
	MET 00430	113.2 ± 4.8	3.6	y	y	-	MWG
	MET 00761	117.8 ± 7.9	3.6	y	y	y	MWG
	MET 01074	112.5 ± 4.9	3.6	y	y	y	MWG
	Mokoia	97.14 ± 7.99	3.6	y	y	y	NHM
CV_{Red}	**Efremovka**	159.6 ± 16.6	3.1–3.4	y	y	y	MNHN
	GRO 95652	119.7 ± 8.6	3.6	y	y	y	MWG
	Leoville	173.2 ± 10.4	3.1-3.4	y	y	y	MNHN
	MIL 07277	131.3 ± 24.7	3.4-3.6	y	y	y	MWG
	QUE 97186	116.8 ± 14.0	3.4-3.6	-	y	-	MWG
	RBT 04133	154.8 ± 27.1	>3.6	-	-	y	MWG
	RBT 04302	154.8 ± 27.1	3.1-3.4	y	y	y	MWG
	RBT 04143	144.2 ± 19.4	3.4	-	y	-	MWG
	Vigarano	162.8 ± 5.8	3.1-3.4	y	y	y	MNHN
CO	**ALH 77003**	89 ± 4.3	>3.6	y	-	y	MWG
	ALH 83108	-	*3.5*	-	-	y	MWG
	ALH 85003	-	*3.5*	-	-	y	MWG
	DOM 03238	185.8 ± 6.8	3.1	-	-	y	MWG
	DOM 08006	250.4 ± 13.1	3	y	-	y	MWG
	EET 92126	-	*3*	-	-	y	MWG
	Kainsaz	117 ± 5	3.6	-	-	y	MNHN
	LAP 031117	213.8 ± 5.1	3.05	-	-	y	MWG
	MET 00737	-	*3.6*	-	-	y	MWG
	MIL 05024	170 ± 6.2	3.1	y	-	y	MWG
	MIL 05104	172.3 ± 6.1	3.1	-	-	y	MWG
	MIL 07193	170.6 ± 10.1	3.1	-	-	y	MWG
	MIL 07709	65.5 ± 9.7	3.7	-	-	y	MWG
	Moss	79 ± 2	3.6	y	-	y	MNHN
	QUE 97416	-	3	-	-	y	MWG
C-ung.	***MIL 07687***	*250.0 ± 9.3*	*2*	-	-	*y*	MWG
CR	**EET 92042**	-	2	-	-	y	MWG
	EET 92159	-	2.7	-	-	y	MWG
	GRA 06100	-	2-T	-	-	y	MWG
	GRA 95229	-	2.6	-	-	y	MWG
	GRO 95577	-	1	-	-	y	MWG
	GRO 03116	-	2-T	-	-	y	MWG
	LAP 04720	-	2.6	-	-	y	MWG
	MIL 090657	-	2.6	-	-	y	MWG

UOCs

Ten of the UOCs I considered are falls (Bishunpur, Bremervörde, Chainpur, Dhajala, Hallingeberg, Krymka, Mezö-Madaras, Parnallee, Piancaldoli and Tieschitz), the remaining 36 are Antarctic finds. Because there are many misclassifications in the Meteoritical Bulletin Database (2022), I verified the classification of the UOCs into H, L an LL through petrography (see Section 4 for details). Table 2.1 summarizes the classification found for each UOC. The exception to this are ALH 77216, ALH 82110, GRO 95504 and QUE 97008 for which no thin sections were acquired, thus no petrographic measurements were performed. For these four UOCs, the classifications from the Meteoritical Bulletin Database (2022) were taken. In summary, out of the 46 UOCs I considered, 8 are classified as H or in between H and L, 8 are classified as L, 4 are classified in between L and LL and 26 are classified as LL.

Furthermore, Table 2.1 lists the $FWHM_D$ value previously determined through Raman spectroscopy of polyaromatic carbonaceous matter (taken from Bonal et al. (2016) for Antarctic UOCs, adapted from Quirico et al. (2003) for non-Antarctic UOCs and taken from Marrocchi et al. (2020) for Piancaldoli) as well as the corresponding PT. For UOCs where this value is not given in Table 2.1, either Raman spectroscopy was not done or was not successful. For these six UOCs (ALH 77216, ALH 82110, ALH 84086, ALH 84120 and Dhajala) only the PT as given in the Meteoritical Bulletin Database (2022) is listed. As can be seen, the UOCs I studied during this thesis range from 3.0 - 3.7, thus, including a wide range of PTs.

During this thesis, I studied UOCs through TGA, FTIR spectroscopy, reflectance spectroscopy and petrography. As mentioned before, not every chondrite was measured with each measuring technique. TGA was performed on 43 of the 46 UOCs (not enough sample mass was available for ALH 83007, GRO 95504 and QUE 97008). However, due to an inconsistency in the measurement settings of the TGA instrument between measurements done in 2019 and those done after, only 35 of these 43 UOCs could be used for further analysis (see Section 2.3.3). UOCs for which TGA measurements were acquired but that were excluded from further analysis are ALH 77216, ALH 82110, ALH 83010, EET 83248, EET 96188, LAR 06279, LEW 87248 and MCY 05218 (Table 2.1).

FTIR spectroscopy was successfully performed on 14 of the 46 UOCs. These 14 samples are ALH 76004, BTN 00302, EET 83248, EET 90066, EET 90628, EET 96188, GRO 06054, GRO 95504, LEW 87248, LEW 87284, MCY 05218, QUE 97008, RBT 04251 and TIL 82408. These UOCs were picked based on having a low metamorphic grade, which eases the sample preparation (see Section 2.2.3). Due to a lack of time, no further FTIR measurements could be performed.

Reflectance spectroscopy and petrography were performed on all but 4 UOCs (ALH 77216, ALH 82110, GRO 95504 and QUE 97008, Table 2.1) for which no thin sections and no sufficient sample mass were available. For ALH 83010 a thin section was available but no bulk powder. Thus, petrographic measurements were possible but not reflectance measurements.

EOCs

Out of the 39 EOCs that I considered during this PhD, 16 are falls (Bandong, Beni M'hira, Bensour, Forest Vale, Kernouve, Lançon, Monte das Forte, Moshampa, Mount Tazerzait, Saint-Séverin, Soko-Banja, Ste. Marguerite, Tamdakht, Taqtaq-e Rasoul, Tuxtuac and Viñales) and the remaining 23 are finds from hot deserts (Atacama and Sahara) and from Iran.

The classification and PT of the EOCs were taken from the Meteoritical Bulletin Database (2022) and are listed in Table 2.2. 13 of the EOCs are classified as H, 14 as L and 12 as LL. PT range from 4 - 7 covering the full range of metamorphic grades for EOCs. During this thesis, I studied all EOCs listed in Table 2.2 with reflectance spectroscopy.

2.1.2 Carbonaceous chondrites

CV chondrites

CV (Vigarano-like) chondrites are characterized by a moderate number (45 vol%) of large (1 mm sized) chondrules, a large matrix abundance (40 vol%), a high abundance of CAIs and AOAs (10 vol%) and little to no metal (0-5 vol%) (Table 1.4).

Based on the modal abundance of metal, the average Ni content of sulfide and the abundance of magnetite, CVs can further be sub-divided into oxidized Allende-like (CV_{OxA}), oxidized Bali-like (CV_{OxB}) and reduced CVs (CV_{Red}). An in-depth study in classifying CVs and constraining their post-accretion history was recently performed by Bonal et al. (2020) (in which I contributed the FTIR spectra). In their work they showed, that based on petrographic measurements CV_{Red} can be distinguished from CV_{Ox} based on lower matrix abundances, higher metal abundances and by containing Ni-poor metal and sulfides. CV_{OxA} and CV_{OxB} show similar matrix and metal abundances with the metal content in CV_{OxB} being slightly lower. They can be distinguished based on CV_{OxA} having lower Ni content in sulfides, lower saturation remanence and lower magnetic susceptibility (MS) than CV_{OxB}. All three subgroups experienced aqueous alteration with the degree of hydration being controlled by their peak metamorphic temperature. CV_{OxA} show higher degrees of thermal metamorphism and therefore, lower amounts of hydration than CV_{OxB}. It was suggested that CV_{OxA} might be thermally metamorphosed CV_{OxB} material. CV_{Red} seem to show larger abundances of oxy-hydroxides than CV_{Ox}.

All 28 CVs that I considered during this PhD are listed in Table 2.3. Of these 28 CVs, 9 are classified as CV_{Red}, 9 as CV_{OxA} and 10 as CV_{OxB} (Bonal et al., 2020). With the exception of the well-known non-Antarctic samples Allende, Axtell, Bali, Efremovka, Grosnaja, Kaba, Leoville, Mokoia and Vigarano, all CVs considered in this work are Antarctic finds. In addition, Allende, Bali, Grosnaja, Kaba, Mokoia and Vigarano are falls. As for UOCs, the metamorphic grade of all CVs considered here were previously constrained by Raman spectroscopy. The $FWHM_D$ values as well as the PT as determined by Bonal et al. (2016) and Bonal et al. (2020) for Antarctic CVs and adapted from Bonal et al. (2006) for non-Antarctic CVs are listed in Table 2.3. As can be seen, PT range from 3.1 to >3.7. Furthermore, TGA measurements were

available for 24 of the 28 CVs from previous studies (Bonal et al., 2020). The 4 CVs without TGA data are Bali, QUE 97186, RBT 04133 and RBT 04143.

During this thesis, CVs were analyzed using FTIR spectroscopy. As can be seen in Table 2.3. FTIR spectroscopy was successfully done for all but 4 CVs. For Axtell, MIL 07002 and RBT 04133 no sample mass was available for the measurement. For LAP 02206 the sample preparation was attempted but because this sample is highly metamorphosed (PT > 3.7, Table 2.3) it was unsuccessful (see Section 2.2.3 for details).

Reflectance spectroscopy was also done for all but 4 CVs. For CVs Bali, MET 00430, QUE 97186 and RBT 04143 no bulk powders were available to perform the measurement.

CO chondrites

CO (Ornans-like) chondrites are similar in mineralogical composition to CV chondrites (Krot et al., 2014). They show abundant chondrules (48 vol%) which are small in size (0.15 mm), moderate abundance of matrix (34 vol%), abundant CAIs and AOAs (13 vol%) and some metal (1-5 vol%) (Table 1.6). Their PT ranges from 3-4 (Figure 1.3). Aqueous alterations seem to have mainly effected their matrix material during parent body process that took place after thermal metamorphism (Brearley, 2003).

The 15 COs that I considered during this PhD are listed in Table 2.3. With the exception of Kainsaz and Moss, which are non-Antarctic falls, all COs considered are Antarctic finds. Based on the classification given in the Meteoritical Bulletin Database (2022), sample MIL 07687 was initially measured and considered as a CO. However, as explained in great length in Prestgard et al. (2021), MIL 07687 was re-classified as a C2-ung. (ungrouped type 2 carbonacous chondrite). Therefore it is listed as such in Table 2.3 and was not used for the further analysis in Chapter 3. Raman spectroscopy result ($FWHM_D$ and PT) allowing for the determination of the metamorphic grade of the COs were available in previous works (Bonal et al. (2016) for Antarctic COs, adapted from Bonal et al. (2007) for non-Antarctic COs) and are listed in Table 2.3. For COs ALH 83108, ALH 85003, EET 92126, MET 00737 and QUE 97416 Raman spectroscopy measurements were attempted but unsuccessful (Bonal et al., 2016). For these 5 COs, the PT was taken from the Meteoritical Bulletin Database (2022). As can be seen, PTs range from 3.0 to >3.6, covering a large range of the metamorphic grades of COs.

COs were studied by reflectance spectroscopy during this PhD. All 15 COs as well as the re-classified C2-ung. MIL 07687 were measured.

CR chondrites

CR (Renazzo-like) chondrites show many large (0.7 mm) FeNi-metal-rich chondrules (50-60 vol%), moderate amounts of matrix (30-50 vol%), very few CAIs and AOAs (0.5 vol%) and a good amount of metal (5-8 vol%) (Krot et al. (2014) and references therein, Table 1.6). With PT raging from 1-2 (Figure 1.3), they show signs of aqueous alteration in their components, e.g. phyllosilicates, calcium carbonates, sulfides and magnetite in their matrix (Brearley, 2003). They are some of the least altered type 2 chondrites

making them important for the analysis of Solar Nebula components (Scott and Krot (2003) and references therein).

All 8 CRs considered during this PhD are Antarctic finds (Table 2.3). Their PTs are currently being determined (Prestgard et al., in prep.) and range from 1-2.7. CRs were not studied as in-depth as type 3 CCs during this PhD. However, I obtained reflectance spectra for all 8 CRs for comparison purposes. Furthermore, I applied a leaching protocol which was developed in Krämer Ruggiu et al. (2021) to all 8 CRs and measured reflectance spectra of the leached CRs as well. The results of these measurements are currently being interpreted and discussed in Prestgard et al. (in prep.).

2.2 Experimental procedures

2.2.1 Spectral analysis of chondrites

During the course of this PhD I conducted an extensive spectral analysis of several large sets of chondrites. The main spectral tools used for this were reflectance spectroscopy and FTIR spectroscopy. Here, a short summary of the basic theory behind these spectroscopic measurements is given based on Clark (1999).

Reflectance and FTIR spectroscopy are based on the interaction of light with matter. More specifically, spectroscopy allows to analyze the light emitted, reflected or scattered off a material as function of the wavelength. When photons encounter a medium with a different refraction index, they are either reflected by the surface or refracted into the medium where they can encounter secondary scattering. Within the medium the photons can be absorbed by electronic or vibrational processes. For the former, a photon of a specific wavelength can be absorbed when encountering atoms and ions, which have discrete energy states, and exciting an electron to a higher energy level. As a result, a photon is emitted at a lower-wavelength that can be detected. During vibrational processes the electron bonds between atoms in a molecule can absorb a photon. The bonds between atoms are comparable to springs, leading to the vibration of the whole molecule. The vibrational frequency is dependent on the bonding strength and mass of the element in the molecule. Since the excitation energies in atoms and vibrational modes in molecules are dependent on the composition of the medium they result in specific absorption bands in the spectra.

Reflectance spectroscopy, thus, measures the intensity of the light reflected back by a certain material into a specific direction compared to incident intensity of the light (Hapke, 2012). Depending on the composition of the material, different absorption bands are seen in the reflectance spectra. For FTIR spectroscopy the intensity of light after passing through a medium in comparison of the intensity of the incident light is measured. Depending on the frequencies of the different vibrational modes of the molecules in the medium absorption bands are seen.

During this PhD, reflectance spectra were measured in the 0.34 µm to 4.2 µm wavelength range and FTIR spectra in the 2.5 µm to 16 µm wavelength range (Section 2.2.2 and 2.2.3). Figure 2.1 shows an example of a FTIR spectrum of a chondrite. As can be seen, the FTIR spectra are characterized by two main absorption band regions in this

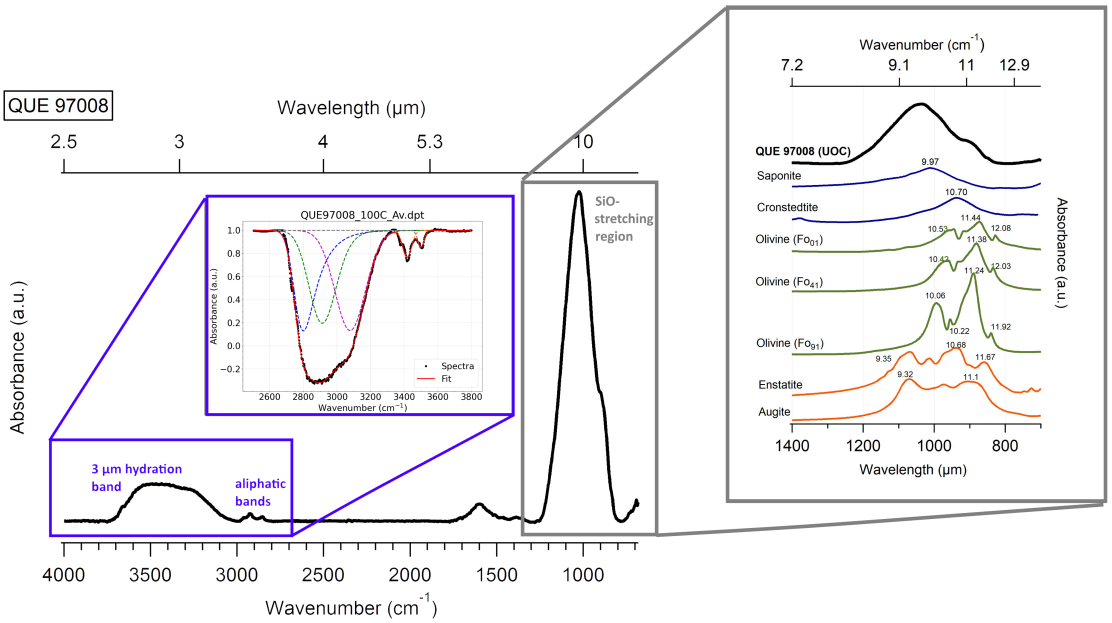

Figure 2.1: Example of a FTIR spectrum of QUE 97008 (UOC). Shown is the 3 µm hydration band as well as an example of a fit of this band, using three fitting curves corresponding to the OH-groups in hydrated minerals at 2.8 µm, the adsorbed H_2O at 2.9 µm and the interlayer H_2O molecules and oxy-hydroxides at 3.1 µm. At 10 µm the SiO-streching region is shown. For comparison it is plotted with various reference mineral spectra which were taken from Salisbury (1991).

range. One related to hydration around 3 µm and another related to anhydrous (and hydrous) silicates around 10 µm. The latter, is related to vibrational modes of SiO_4 as well as stretching modes of Si-O (Beck et al., 2014). Examples of minerals contributing in this region are olivine, pyroxene (such as enstatite or augite) and phyllosilicates (such as saponite and cronstedtite) which are plotted in Figure 2.1 as well. The 3 µm band is a superposition of the stretching modes of hydroxyl groups in hydrated minerals (around 2.8 µm), the symmetric and asymmetric stretching modes of weakly bound adsorbed H_2O molecules (around 2.9 µm), and stretching modes of strongly bound H_2O molecules to interlayer cations and oxy-hydroxides (such as goethite) (around 3.1 µm) (e.g. Frost et al. (2000) and Potin et al. (2020b), see Figure 2.1). The exact size and shape of the the 3 µm band then depends on the amount of water and -OH mineral carriers.

An example of a reflectance spectrum of a chondrite is shown in Figure 2.2. Three main absorption bands are visible. The first two located around 1 µm and 2 µm are related to the electron transitions in the Fe^{2+} of olivine and pyroxene. More specifically, olivine has one broad, asymmetric absorption band around 1 µm while pyroxene shows two absorption bands, one at 1 µm and one at 2 µm (Cloutis et al., 1986). For CCs, spinel ($MgAl_2O_4$) can also contribute in the 2 µm range (e.g. Cloutis et al. (2012b), Cloutis et al. (2012c)). The third band located at 3 µm is related to the hydration of the sample (as explanation above).

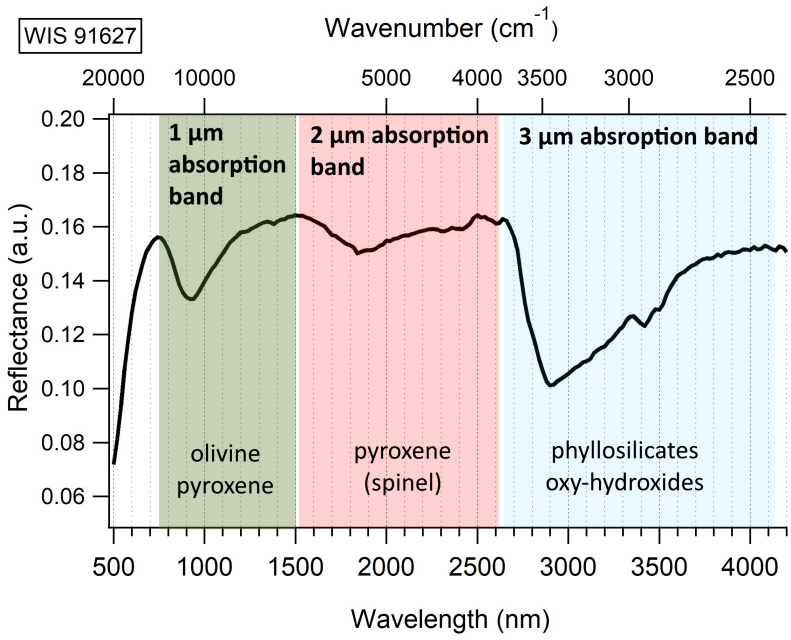

Figure 2.2: Example of reflectance spectrum of WIS 91627 (UOC). Shown are the three spectral bands at 1 µm due to olivine and pyroxene, at 2 µm due to pyroxene (and for CCs spinel) and at 3 µm due to hydrated minerals.

2.2.2 Reflectance spectroscopy

Reflectance spectroscopy measurements were performed using the Spectrophotometer with cHanging Angles for the Detection Of Weak Signals (SHADOWS) instrument (Figure 2.3a) (Potin et al., 2018), a spectro-radio goniometer available at IPAG (Grenoble, France). For this, the bulk chondrites were first carefully crushed into a fine powder by hand using a mortar and pestle. To ensure the representativity of all chondrite components, at least 50 mg of bulk sample were crushed per chondrite. Subsequently, the powder was transferred into a round (d = 7 mm) sample holder which holds about 35 mg of chondrite powder.

The surface of the powder was smoothed out and flattened using a spatula and the sample was transferred into an environmental cell (Figure 2.3b). This cell, which was closed off with a sapphire window, allowed for measurements under vacuum ($P < 10^{-4}$ mbar) and at 80 °C. Increasing the temperature and measuring under vacuum allowed for a minimization of ambient water contamination leaving the hydration feature of the spectra predominantly due to chondritic hydration. Each chondrite powder was then measured between 340 nm and 4200 nm using an integration time of 40 s and a spectral sampling of 20 nm. The diameter of the incident illumination beam was 5.2 mm. The measuring geometry was set to i = 0° and e = 30° which is used as a standard for good comparability between measurements of different laboratories. To normalize the spectra to the Lambertian surface, two reference spectra were measured using a Spectralon™ standard between 340 nm and 2100 nm and an Infragold™ between 2000 nm and 4200 nm. Lastly, a photometric correction was performed for each spectrum to account for any reflectance effects introduced by the sapphire window clos-

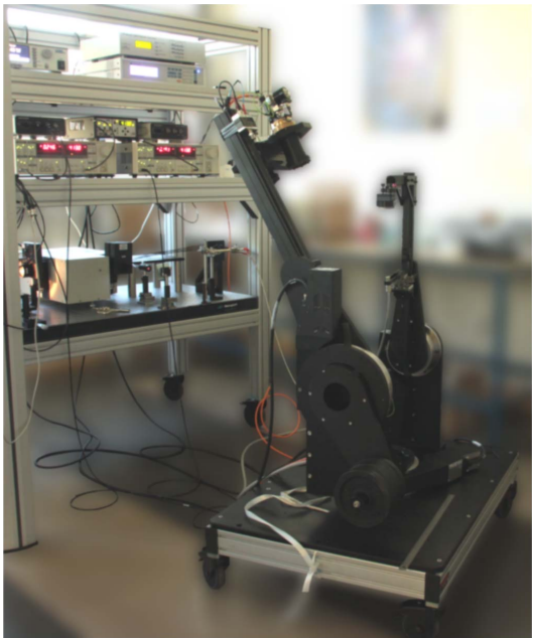

(a) The SHADOWS instrument at IPAG (France). Image was take from Potin et al. (2018)

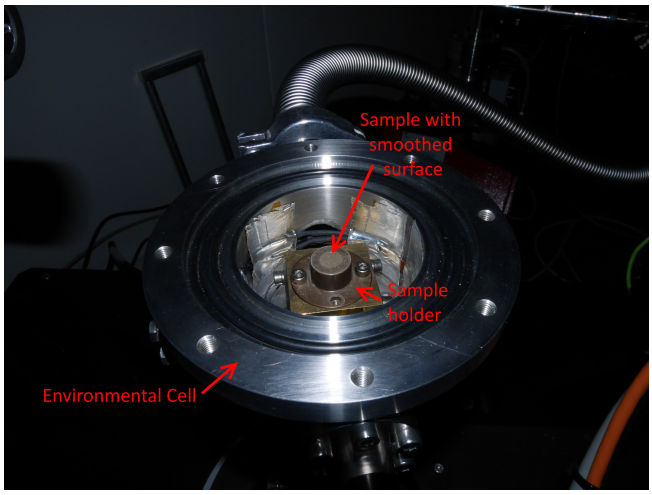

(b) Close-up of the environmental cell. Shown is also the sample holder with a smoothed out, powdered sample inside.

Figure 2.3: Overview of the SHADOWS instrument and its components.

ing the cell (Potin et al., 2020a). All spectra measured during this dissertation were uploaded online to the GhoSST/SSHADE spectral database (for CVs (Eschrig et al., 2019b), for COs (Eschrig et al., 2019d), for CRs (Eschrig et al., 2019a), for UOCs (Eschrig et al., 2019c) and for EOCs (Eschrig et al., 2020)).

2.2.3 FTIR spectroscopy

The sample preparation of the matrix fragments measured by FTIR spectroscopy is challenging and delicate. Working in a clean room, the bulk chondrites were first carefully crushed using a mortar and pestle until they resembled a fine powder. Subsequently, a fine layer of powder was dusted onto a microscope slide and carefully inspected using an optical binocular under a laminar flow at IPAG (France). Matrix fragments were selected based on their dark color and fluffy, porous texture. This selection process is made more difficult, the lower the abundance of matrix in the chondrite and the higher the metamorphic and terrestrial weathering grade. The latter can change the color of the matrix material, turning it whitish or grayish and therefore making it hard to distinguish from other chondrite components. With increasing metamorphic grade the chemical equilibration process of the chondrite components can also lead to a change in texture of the matrix.

Once identified, each matrix grain was carefully picked using a tungsten needle and transferred onto a d = 3.5 mm diamond window (Figures 2.4a and 2.4b). This was repeated until a total of 15-20 matrix fragments no bigger than 30 µm - 90 µm were picked (Figure 2.4e). The diamond window with the matrix fragments was then carefully transferred into a press (Figures 2.4c and 2.4d) using tweezers and gently covered

with a second diamond window. The matrix fragments were then manually pressed in-between the two diamond windows and one or both diamond windows were subsequently inserted into a sample holder, depending on which side the matrix fragments stuck to after separation (Figure 2.4f).

The sample holder containing the pressed matrix fragments was then inserted into an environmental cell which allowed for measurements under vacuum ($P < 10^{-4}$ mbar) and temperatures up to 300 °C. The cell was closed off with a ZnS window. The usage of diamond and ZnS windows allowed for measurements between 4000 cm^{-1} and 600 cm^{-1} (2.5 µm and 16 µm) in transmitted light. Matrix fragments were then measured using a BRUKER Vertex 70 FTIR spectrometer equipped with a HYPERION 3000 IR microscope at the IPAG (France) (Figure 2.5). Spectra were acquired with 200 scans and a spectral resolution of 4 cm^{-1}. Each matrix fragment was measured at 100 °C, 200 °C and 300 °C and under vacuum. The acquired spectra of each matrix fragment was checked for aliphatic bands between 2855 cm^{-1} and 2955 cm^{-1} (Kebukawa et al., 2011) which indicate that the fragment measured was indeed matrix material. Given the difficulty of the sample preparation, in some cases only 3 to 10 good spectra of matrix fragments could be successfully acquired per chondrite.

2.2.4 Thermogravimetric analysis (TGA)

TGA measurements were done using a Mettler-Toledo TGA-DSC3+ instrument at the Institut des Sciences de la Terre (ISTerre, France). For this, each bulk chondrite was ground by hand using a mortar and pestle until a fine powder. To ensure the representability of all chondrite components a minimum of 50 mg of bulk sample were ground per chondrite. Subsequently, 35 mg of powder were weighed out for the measurement. The powders were transferred into a 70 µL aluminum crucible and then placed into the TGA instrument where they were heated from ambient temperature up to 1075 °C at a heating rate of 10 °C min^{-1}. The mass loss was measured at a 50 mL min^{-1} inert N_2 atmosphere. To be able to account for any mass loss contributions from the aluminum crucible, an empty crucible measurement was performed. Due to time constraints, this was not done before each chondrite but rather one empty crucible was measured per measuring set.

The gas evolved from the TGA-DSC instrument was transferred from the outlet of the TGA-DSC instrument to an IS50 FTIR instrument from Thermo Scientific, using a heated transfer line (300 °C). A FTIR spectrum of the evolved gas was measured every 23s.

2.2.5 Petrography

Petrographic measurements were performed at the Centre Européen de recherche et d'Enseignement des Géosciences de l'Environnement (CEREGE, Aix-en-Provence). For this a thin and/or thick section was acquired for each chondrite from various origins (see Table 2.1) and analyzed using a Leica DM2500P petrographic optical microscope. Point counting was used to determine the modal abundance of the different chondrite components. For this, each section was scanned at ×50 magnification along the full

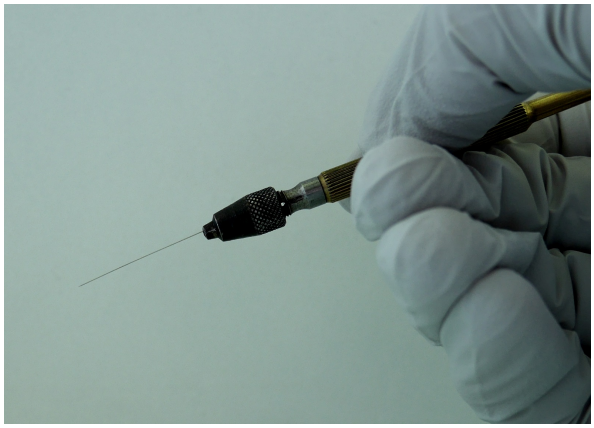

(a) Tungsten needle that was used to pick the matrix fragments.

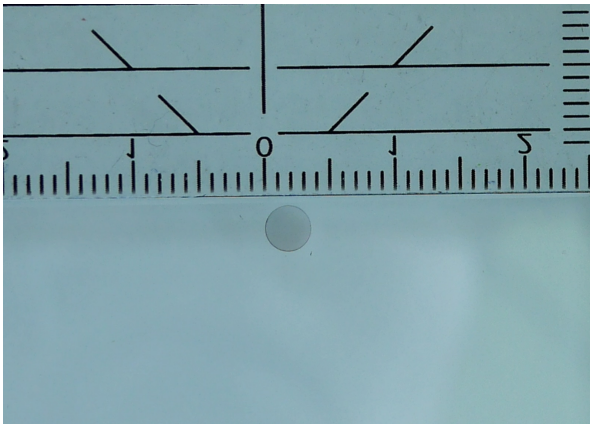

(b) Diamond window on which the matrix fragments are placed with a ruler for scale.

(c) Top view of the custom press made to press the grains

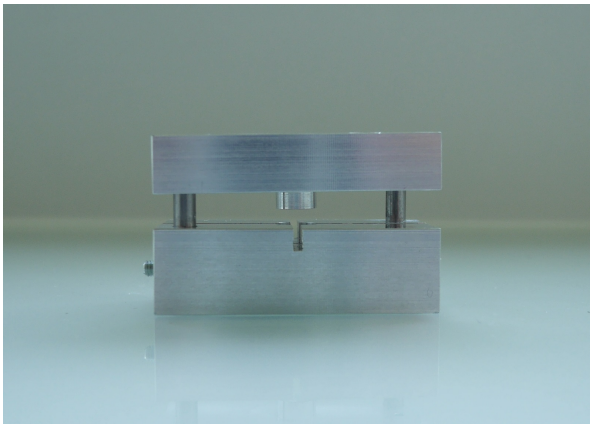

(d) Side view of the custom press made to press the grains.

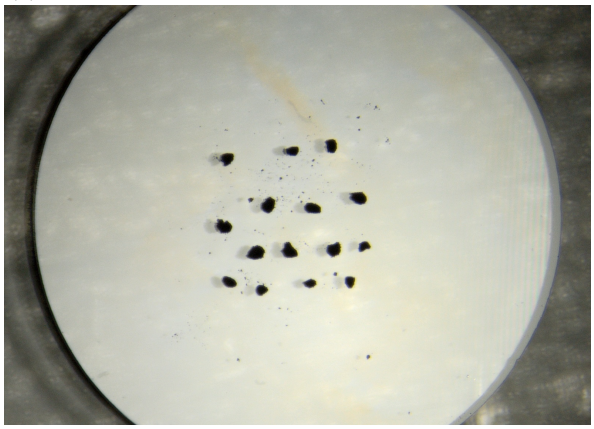

(e) Matrix fragments picked for CV GRA 06101 before pressing.

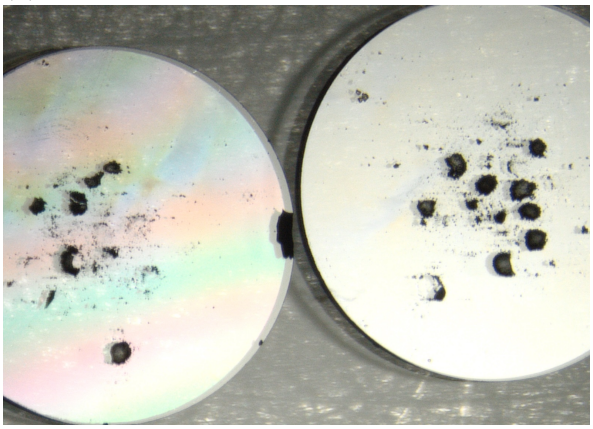

(f) Matrix fragments picked for CV GRA 06101 after pressing.

Figure 2.4: Overview of the different steps necessary for the sample preparation for FTIR spectroscopy.

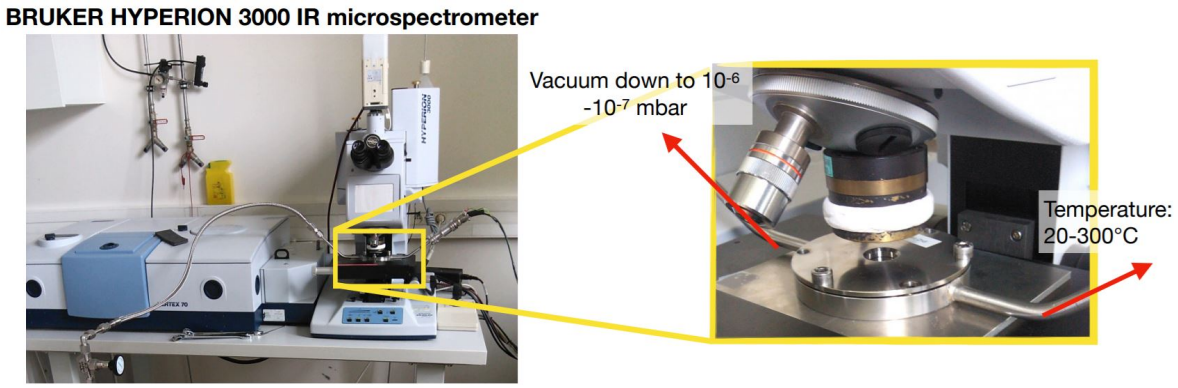

Figure 2.5: Overview of the FTIR spectroscopy experimental set up. Shown is the FTIR spectroscope, the IR microscope as well as the closed environmental cell.

range of the section using the set step increments of the microscope table. At each point, the type of chondrite component was identified (metal, matrix, sulfides (troilite), magnetite/weathering products or chondrules/chondrule fragments) and counted. This was repeated until a minimum of 500 points were counted. Lastly, the upper and lower bounds of the modal abundance values were calculated by determining the two-sided confidence bounds following Howarth (1998) and then subtracting them from the total phase abundance values.

The initial classification of UOCs into H, L and LL given in the Meteoritical Bulletin Database (2022) was checked using MS measurements, average chondrule size measurements and modal metal abundance values. The combination of these three indicators allows for a robust classification of UOC material. The metal modal abundance, determined by point counting as described above, was compared to the average abundance values in Hs of (7.80 ± 0.62) vol% (n = 25), in Ls of (3.54 ± 0.34) vol% (n = 53) and in LLs of (1.16 ± 0.59) vol% (n = 14). These reference values were computed by Gattacceca et al. (2014) using meteorite densities from Consolmagno et al. (2008).

The MS was measured at CEREGE (France) on bulk UOCs using an Agico MFK1 instrument operating with a field of 200 A/m and a frequency of 976 Hz. The resulting MS values were normalized to the sample mass and then compared to the reference values of $\log(\chi) = 5.24 \pm 0.08$ ($n = 10$) for H3, $\log(\chi) = 4.79 \pm 0.11$ ($n = 11$) for L3 and $\log(\chi) = 4.41 \pm 0.16$ ($n = 14$) for LL3, with χ in $10^{-9}\,\mathrm{m^3\,kg^{-1}}$ (unpublished updated version of Rochette et al. (2003)).

The average chondrule size was determined from mosaic pictures of the sections in reflected and/or transmitted light. Each chondrule was manually outlined using a graphics editor (Figure 2.6a), the outlined curve was fitted with an ellipse (Figure 2.6b) and the diameter of each ellipse was determined as follows

$$d = \sqrt{d_{major} \cdot d_{minor}} \tag{2.1}$$

with d_{major} and d_{minor} being the major and minor axis of the ellipse. Subsequently, the average chondrule apparent diameter was determined for each chondrite. This value was then compared to the average diameter reference values of 450 µm for H, 500 µm for L and 690 µm for LL (Metzler, 2018).

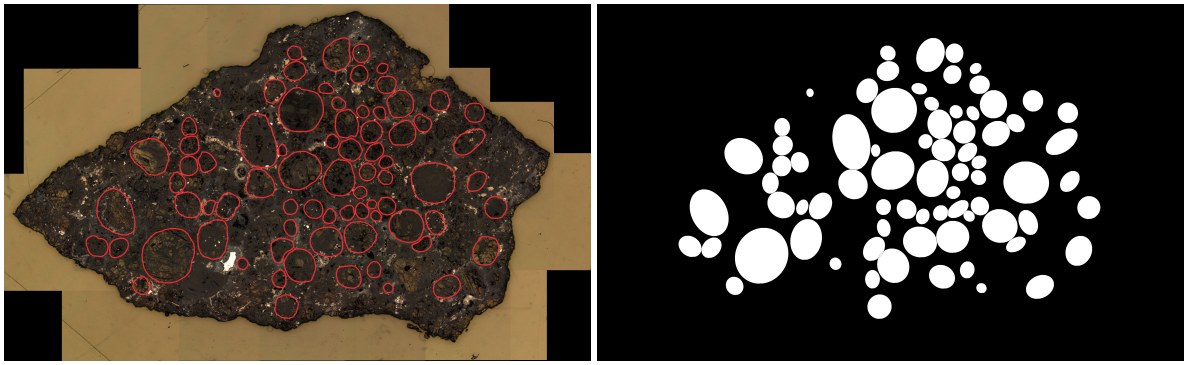

(a) UOC MET 00506 with outlined chondrules. **(b)** Elliptical fit to the outlined chondrules.

Figure 2.6: Determination of the chondrule diameter from outlined chondrules in thin and/or thick sections. The outline is fit with an ellipse and the average apparent diameter is determined.

To determine the terrestrial weathering degree of each chondrite, the thin/thick sections were analyzed under reflected light. The percentage of weathering products (iron oxides and oxy-hydroxides) was estimated by eye at 4-5 different regions of the section (see examples Figure 2.7). Finally, the weathering scale of Wlotzka (1993) (see also Section 1.2.3) was used to determine the terrestrial weathering stage of each chondrite.

To identify the shock stages of each chondrite the shock indicators introduced by Bennett and McSween (1996), Scott et al. (1992) and Stöffler et al. (1991) were used. They can be summarized as follows:

- S1: sharp optical extinction and irregular fractures of olivine
- S2: Undulatory extinction and irregular fractures of olivine
- S3: planar fractures, undulatory extinction and irregular fractures of olivine as well as polycrystalline troilite
- S4: mosaicism and planar fractures of olivine as well as existence of melt pockets and polycrystalline troilite
- S5: strong mosaicism, planar fractures and planar deformation features (PDFs) of olivine as well as polycrystalline troilite

Thus, a total of 10-20 olivine grains were examined under transmitted light for irregular fractures, the extent of undulatory extinction, planar fractures, and mosaicism (see examples in Figure 2.8). Subsequently, the thin sections were examined for polycrystalline troilite under reflected light.

2.3 Analytical procedures

2.3.1 Treatment of reflectance spectra

The reflectance spectra of chondrites are characterized by three main absorption bands in the 0.34 µm to 4.2 µm range: two at 1 µm and 2 µm due to olivine (*Ol*) and

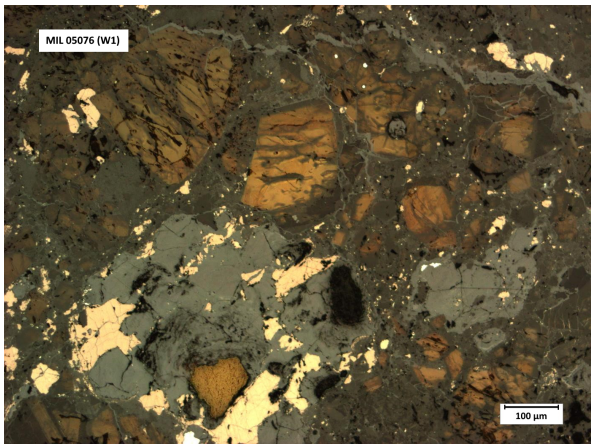

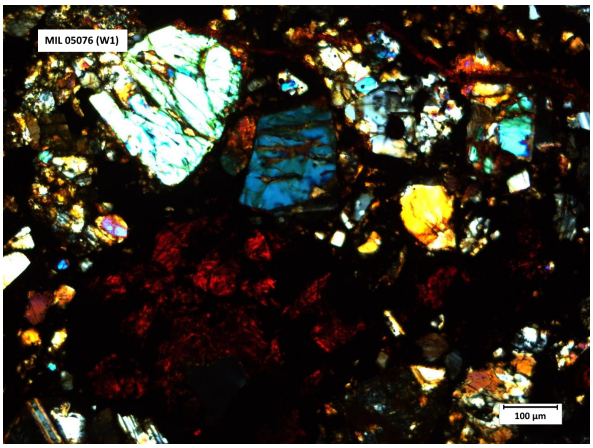

(a) Weathering products in UOC MIL 05076 (W1) in reflected (left) and transmitted light (right). The weathering products show up red in transmitted light.

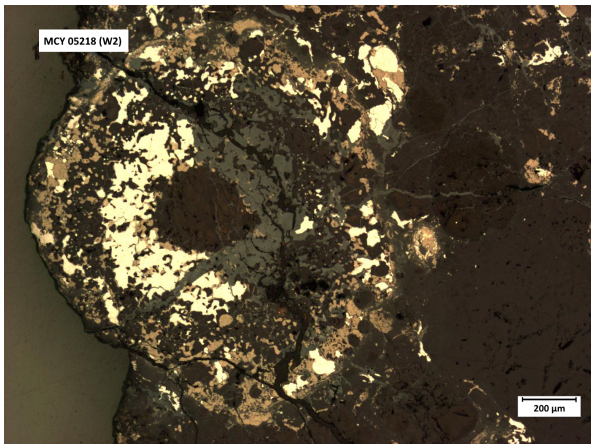

(b) Corroded metal and weathering products in UOC MCY 05218 (W2). About 30 % of the metal grains are weathered.

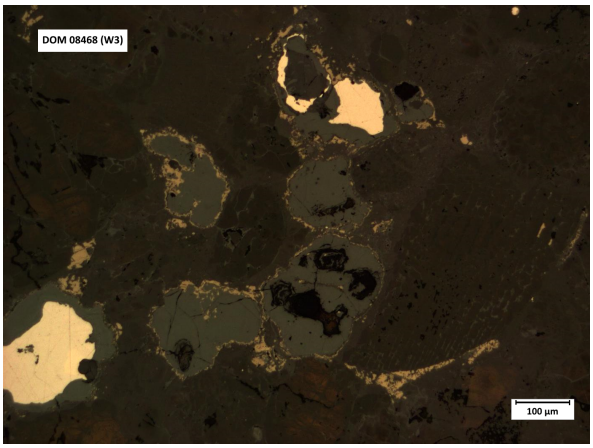

(c) Weathered metal grains in DOM 08468 (W3). Almost all the metal is weathered.

Figure 2.7: Examples for weathering products and veins observed in some of the UOCs considered in the present dissertation. Grayish material are weathering products. They often replace metal and sulfide grains. They can also be seen in transmitted light.

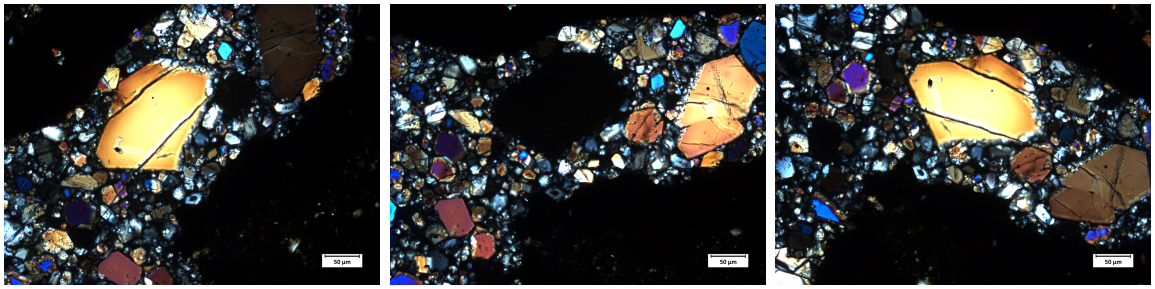

(a) Example of sharp extinction of an olivine grain in UOC ALH 78119.

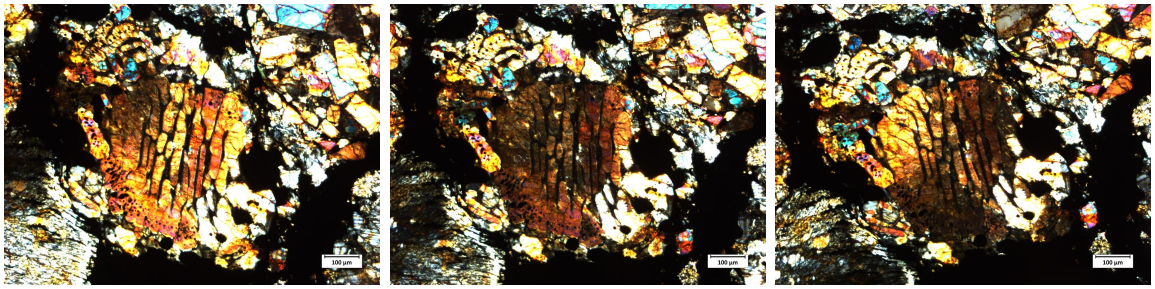

(b) Example of ondulatory extinction in an olivine grain of UOC ALH 83007.

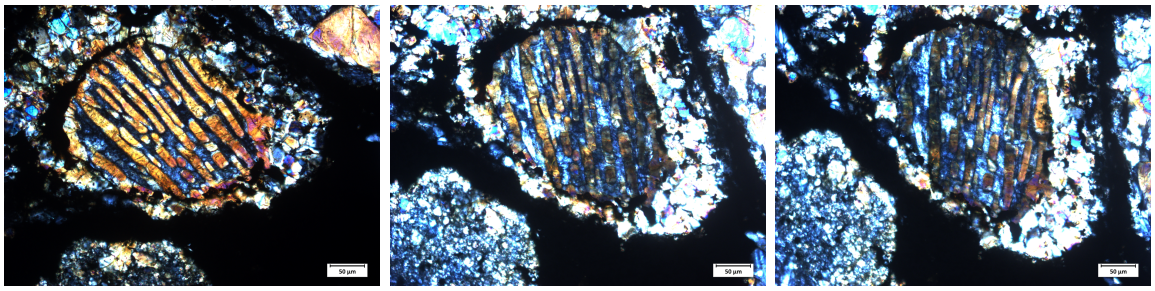

(c) Example of mosaicism in a barred olivine chondrule of UOC ALH 83010.

Figure 2.8: Examples for sharp extinction, undulatory extinction and mosaicism in olivine grains under transmitted light. The same grain is shown slightly rotated from left to right for each scenario. For sharp extinction the grain completely disappears when rotated. For undulatory extinction the grain is extinguished by sections while rotating. For mosaicism, small pockets distributed across the grain are extinguished at a time in a random pattern.

pyroxene (Px) and one at 3 µm related to hydration (see Section 2.2.1, Figure 2.2). To ease the comparison between spectra of different chondrites and between chondrite and asteroid spectra, a set of spectral features was defined following previous work by Cloutis et al. (2012c). These spectral features include: the 1 µm and 2 µm band depths and positions, the spectral slopes in the 1 µm and 2 µm region, the overall spectral slope, the peak reflectance values around 700 nm, the visual slope at wavelengths shorter than 700 nm and the Integrated Bans Depth (IBD_{Hyd}) of the 3 µm band (see Figure 2.9).

The determination of the properties of these spectral features was done using a python program I specially developed during this PhD with a user interface (Figure 2.9). To determine the 1 µm and 2 µm absorption band depths, a linear baseline was fit to the regions. The left and right bounds of the baseline fit were determined at the maximum on either side of the bands. Sliders in the user interface allowed for manual correction of these bounds, if necessary. Subsequently, the 1 µm and 2 µm bands were fit with a Gaussian by determining their minimum and then fitting the points around it. The amount of points fitted can be adjusted using sliders in the user interface. Lastly, the band depths (BD) can be determined following Clark (1999)

$$BD = 1 - \frac{R_b}{R_c} \tag{2.2}$$

with R_b the reflectance at the minimum of the Gaussian fit and R_c the reflectance of the continuum fit to the band at the same wavelength. The band positions then corresponds to R_b. The spectral slopes in the 1 µm and 2 µm band areas correspond to the slopes of the baseline fits. The peak reflectance value around 700 nm corresponds to the reflectance value of the left bound of the baseline fit to the 1 µm absorption band (see Figure 2.9). The visual slope is determined by calculating the steepest slope in the 340 nm to 520 nm range and linearly fitting the points around this area. The number of points fitted can be adjusted using sliders in the user interface. To characterize the 3 µm band, the IBD_{Hyd} is calculated. For this, firstly, the organic bands at approximately 3500 nm are excluded by linearly fitting this region. Subsequently, the IBD_{Hyd} is calculated between 2550 nm and 4000 nm following Milliken and Mustard (2005)

$$IBD_{Hyd} = \int_{\lambda_{min}}^{\lambda_{max}} \frac{BD(\lambda)\, d\lambda}{\lambda_{max} - \lambda_{min}} \tag{2.3}$$

Lastly, the Ol/(Ol + Px) ratio is determined to assess the relative abundance of olivine to pyroxene. This is done following Dunn et al. (2010)

$$\frac{\mathrm{Ol}}{(\mathrm{Ol} + \mathrm{Px})} = -0.424 \cdot BAR + 0.728 \tag{2.4}$$

with BAR being the band area ratio of the IBD of 2 µm over that of the 1 µm band. Each spectrum is fitted using this program while adjusting the sliders until the best visual fit is achieved. Finally, the spectral values are extracted.

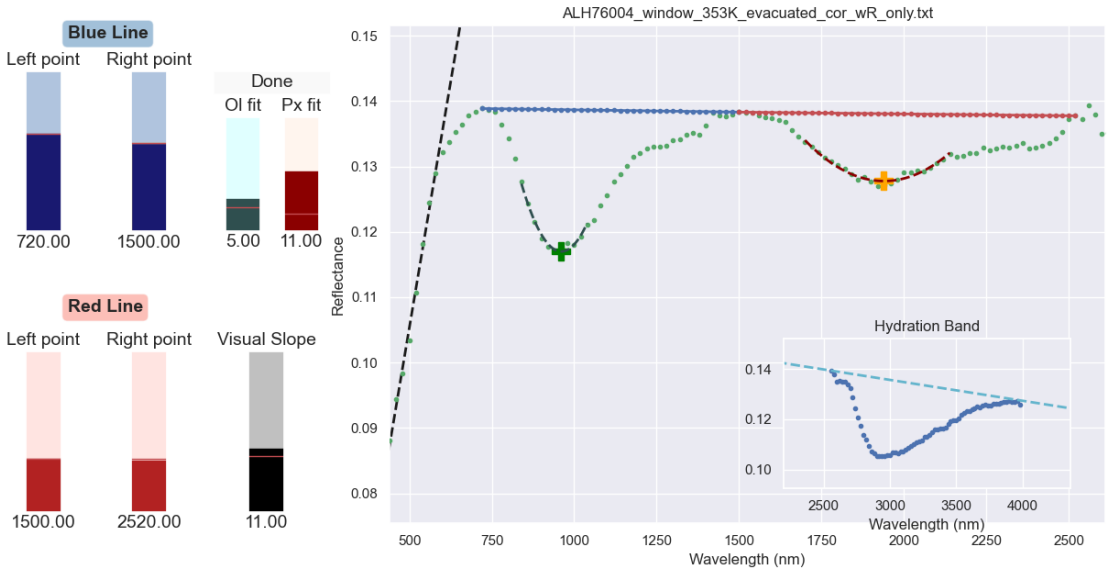

Figure 2.9: Spectral features determined for each reflectance spectrum. Shown is the user interface of the program I developed during this PhD with the spectrum of UOC ALH 74006 as an example. Shown are as a black dotted line the visual slope, as a blue dotted line the 1 nm band area slope, as a red dotted line the 2 nm band area slope, as a green cross the the 1 nm band minimum, and as an orange cross the 2 nm band minimum. On the left are the handles used to optimize the spectral value determination.

Space weathering in asteroid spectra

For the treatment of asteroid spectra, a further is necessary. As explained in Section 1.3.2, the surfaces of asteroids are exposed to SW, a process that will alter their reflectance spectra. In order to make direct comparison between chondrite and asteroid spectra possible, the asteroid first need to be analytically "de-space weathered". This is done following Brunetto et al. (2006). Through irradiation experiments on an OC and on bulk terrestrial silicates, Brunetto et al. (2006) show that the ratio of irradiated (or space weathered (sw)) to non-irradiated (or pristine (p)) spectrum can be well approximated using an exponential function

$$\frac{Spectrum_{sw}}{Spectrum_{p}} = K \cdot \exp\left(\frac{C_s}{\lambda}\right) \tag{2.5}$$

with K being a scaling factor, C_s the strength of SW and λ the wavelength. Therefore, under the assumption that SW mainly affects the slope of the spectra (see Section 1.3.2) and is the only effect influencing the spectral slope, the asteroid spectra are de-space weathered by fitting their continuum with an exponential function and then dividing them by this function. After this, the spectral features of the asteroid spectra are determined as explained above.

2.3.2 Treatment of the FTIR spectra

In a first step, the baseline is removed from each FTIR spectrum of each matrix fragment using a spline function. Then, to ensure comparability between chondrites,

all spectra are normalized to the 840 cm^{-1} band. It is important that the pressed matrix fragments are thin and flat but not too thin. If the pressed fragments are too thin, scattering artifacts can affect the spectra. If they are too thick, absorption bands can become saturated. For this reason, the 840 cm^{-1} band was chosen for the normalization, since it is not likely to be affected by either of these effects. It is worthy to mention that the normalization to this band can lead to band depth values higher than 100 %. Lastly, the average FTIR spectrum is determined from all matrix fragment spectra measured per chondrite. Since the FTIR spectra can be noisy between 2.5 µm and 2.7 µm the spectra were smoothed in this region using a Gaussian smoothing.

To quantify the different contributions of OH-groups in hydrated minerals at 2.8 µm, adsorbed H_2O at 2.9 µm and interlayer H_2O molecules and oxy-hydroxides at 3.1 µm to the overall 3 µm bands (see Section 2.2.1) a fit using exponentially modified Gaussian (EMG) profiles is done following Potin et al. (2020b). To be able to fit the aliphatic bands, two Gaussian functions (G) are used. This gives a total fit function of

$$f(\lambda) = 1 - (EMG(\lambda, h_1, \mu_1, \sigma_1, \tau_1) + EMG(\lambda, h_2, \mu_2, \sigma_2, \tau_2) + EMG(\lambda, h_3, \mu_3, \sigma_3, \tau_3) + G(\lambda, A_1, \sigma_{org,1}, \lambda_{0,1}) + G(\lambda, A_2, \sigma_{org,2}, \lambda_{0,2})) \quad (2.6)$$

With each EMG being dependent of four variables (h the amplitude, μ the mean, σ the variance of the Gaussian and τ the exponent relaxation factor), and each Gaussian function being dependent of three variable (A the amplitude, σ_{org} the width and λ_0 the center of the Gaussian function) it becomes clear that this fit is complex. To be able to easily find the best initial guess values for all 12 variables necessary to fit the 3 µm band with three EMG profiles, I developed a python program with a user interface during this PhD (Figure 2.10).

Using this program, each spectrum was first visually assessed. If the spectrum was very noisy it was smoothed. Based on the overall shape it was then decided whether one, two or three bands are needed for the overall fit. The number of bands used for the fit could be adjusted using the check boxes in the user interface (Figure 2.10). If all three bands contribute, the 3 µm band has a more symmetrical, rounded shape (as is the case for QUE 97008 in Figure 2.10). In the case of a more asymmetrical overall shape, it is expected that only one or two bands are contributing. Finally, a least square fit was performed for each 3 µm band by adjusting the sliders for the initial guess values of the variables in the user interface. The band position, depth, FWHM, and IBD_{Hyd} of the total 3 µm band as well as the individual fitting bands were determined for each spectrum.

An important thing to note here is that the comparability between the FTIR spectra of matrix fragments in this dissertation is hampered by the fact that the thickness and the measuring area of the pressed fragments were not constrained. Since measurements were performed in transmitted light, both of these factors are important for the FTIR spectroscopy to be quantitative.

The Si-O stretching region was analyzed by comparing its shape to FTIR spectra of typical silicates expected in chondrites (see Figure 2.1). This includes for example

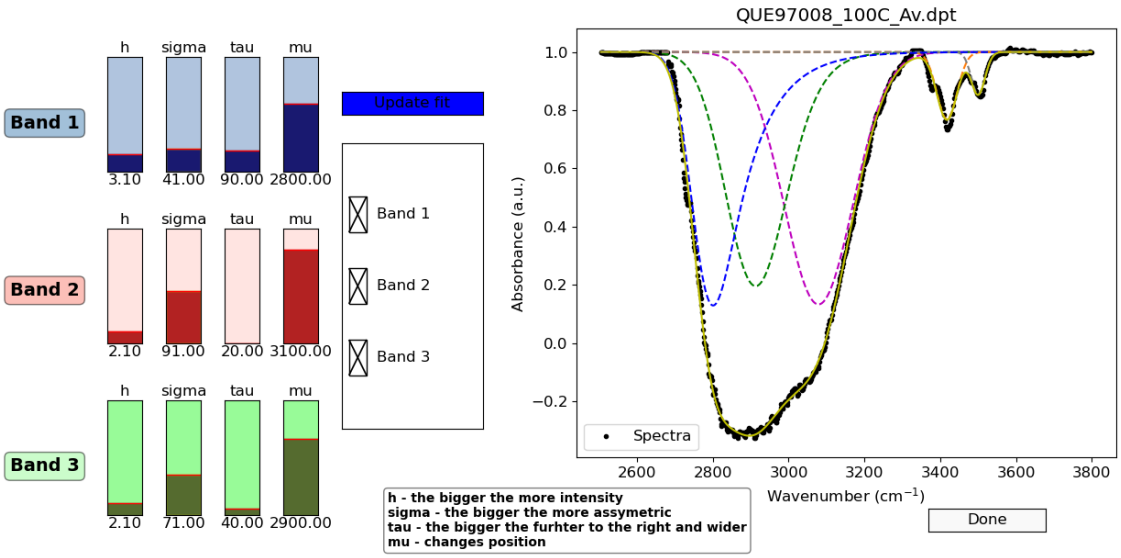

Figure 2.10: User interface of the python program used to fit the 3 µm band of the FTIR spectra, here for UOC QUE 97008. Shown on the right are the 3 µm band (black dots) with the three fitting bands in blue, magenta and green as well as the fit to the aliphatic bands in orange and grey. The total fit curve is shown in yellow. On the left, the different buttons and handles for optimizing the fit are shown. The three check boxes called "Band 1", "Band 2" and "Band 3" allow to add or remove a band from the fit. The handles allow to adapt the initial guess values of the 4 variables in the EMG profile for the fit: "h" varies the height of the EMG, "σ" influences the symmetry of the EMG, "τ" influences the width and position of the EMG and "μ" influences the position.

phyllosilicates (e.g. saponite), olivine, enstatite and magnetite. By doing so, the dominating silicates in each chondrite could be identified.

2.3.3 Treatment of TGA data

In a first step, the contribution of the empty crucible to the mass loss was corrected for by subtracting the empty crucible TGA curve from that of the chondrite. Subsequently, the first derivative of the TGA curve (DTG curve) was taken. This allows for the easy identification of temperature ranges with strong mass losses. The TGA and DTG curves could then be compared to those of mineral standards to identify the origin of the mass loss in certain temperature ranges. Often, these are similar between chondrites of the same group. By comparing the shape of the DTG curves of a given chondrite group common patterns can be recognized and mass loss ranges due to the dehydration and de-hydroxylation of different minerals can be identified. This process is not always easy. For CCs four temperature regions have previously been identified (e.g. Bonal et al. (2020), Garenne et al. (2014) and King et al. (2015)). The first one ranges from 25 °C to 200 °C mostly due to adsorbed water, the second from 200 °C to 400 °C mostly due to oxy-hydroxides, the third from 400 °C to 770 °C/850 °C mostly due to -OH groups and the fourth from 770 °C to 900 °C mostly due to carbonates (see Figure 2.12a).

For UOCs the identification of the temperature ranges was more complex. UOCs show more variable TGA curves than CCs (see Figure 2.11). When plotting all 43

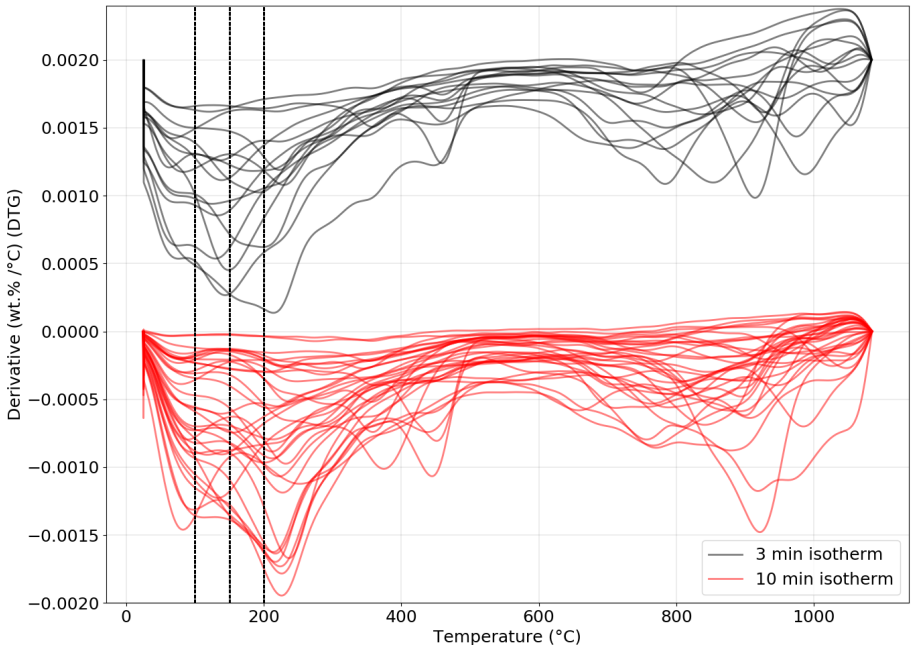

Figure 2.11: Comparison of the DTG curves measured at 3 min (black) and 10 min (red) isotherm. The positions at 100 °C, 150 °C and 200 °C are marked by vertical dashed lines.

UOCs that I measured by TGA during the course of this three year PhD together, two groups could be identified: one showing a single wide DTG peak between 25 °C and 300 °C centered around 150 °C and another showing two distinct DTG peaks one centered around 100 °C and one around 200 °C (Figure 2.11). Upon closer investigation, the difference between these two groups could be identified as a slight difference in the measuring settings for TGA done in 2019 and those done after. In 2019, the isotherm at the beginning of the TGA was set to 3 min. Later, this was changed to 10 min to allow for enough time to measure the background in the FTIR spectrometer coupled with the TGA instrument. For the 10 min isotherm measurements, the terrestrial water contamination had more time to escape before the start of the actual measurement, resulting in a smaller, narrower adsorbed water peak centered around 100 °C. For the 3 min isotherm measurements, the adsorbed water escaped during the beginning of the measurements (and not before), resulting in a wide adsorbed water peak, that merges with the second peak seen in the 10 min isotherm measurements. To ease the identification of common mass loss intervals, only the 35 UOCs which were measured with a 10 min isotherm were considered in the further discussions (see Chapter 5). Which UOCs were measured at 3 min and which at 10 min isotherm is marked in Table 2.1.

Finally, three temperature ranges were identified based on the UOCs measured at 10 min isotherm. A first one ranging from 25 °C to 150 °C mostly due to adsorbed water, a second one from 150 °C to 550 °C mostly due to oxy-hydroxides and a third ranging from 550 °C to 1000 °C mostly due to phyllosilicates and carbonates (see Figure 2.12b). Contributions due to FeS are also possible in all three temperature ranges (Yokoyama et al., 2022). The mass loss values of each of these temperature ranges are determined.

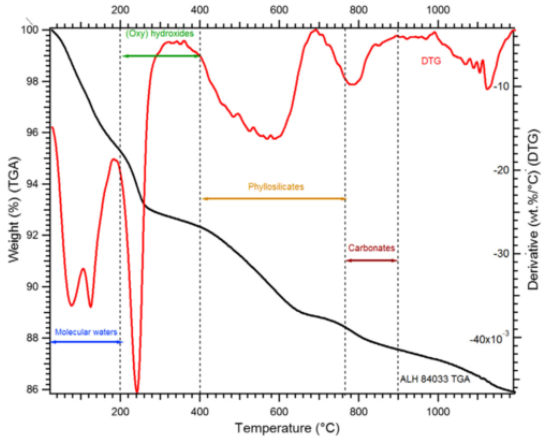

(a) Example of a TGA curve and DTG curve for the CM ALH 84033. Also shown are the four different temperature ranges identified for CCs. Image was taken from Garenne et al. (2014).

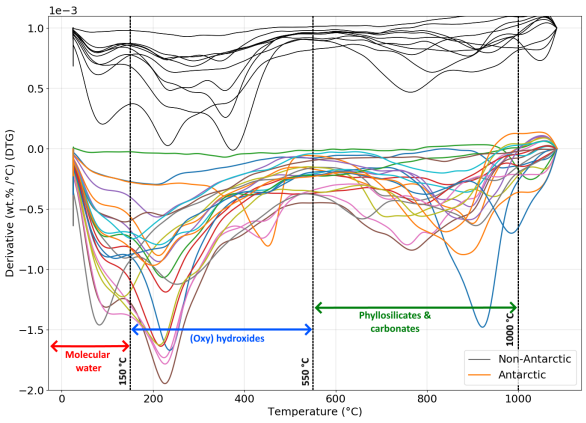

(b) DTG curves for the the UOCs considered in the present PhD. Also shown are the three different temperature ranges identified for UOCs. As can be seen, DTG curves vary between UOCs.

Figure 2.12: Examples for CC and UOC DTG curves and the corresponding mass loss regions identified for each group.

Since the hydration in UOCs is expected mainly in the fine-grained, porous matrix material, each mass loss values is normalized by the modal abundance of matrix in the chondrite (as determined though petrography (Section 2.2.5)).

Another limitation that needs to be mentioned here for the detection of hydration using TGA, is that of low matrix abundance. In comparison to CCs, UOCs show a low matrix abundance (Table 1.4). For one, this low matrix abundance induces a larger error in the matrix normalized mass loss values. For another, other thermal reactions besides dehydration and de-hydroxylation (e.g. the oxidation and reduction of organic matter and magnetite (Földvári, 2011)) can lead to a mass loss. With lower matrix abundances, the relative abundance of hydrated to non-hydrated minerals that might contribute to the mass loss becomes higher. Therefore, the total mass loss value will not only reflect the hydration of the chondrite. To overcome this, matrix enriched TGA measurements might be necessary for some chondrites (see more details in Section 5.2.1).

To analyze the FTIR spectra measured every 23 s on the gas evolved from the TGA instrument, chemigrams were retrieved. They give the integrated intensity over a certain wavelength range as a function of the temperature. For H_2O a chemigram in the 4200-3000 cm^{-1} was retrieved, for CH in the 3000-2800 cm^{-1} range, for CO_2 in the 2450-2240 cm^{-1} range and for CO in the 2240-2040 cm^{-1} range. As the results in Chapter 5 will show, unfortunately the data from the evolved gas is too noisy to be used. Due to the low abundance in matrix in UOCs the concentration of different gases at a given time in the FTIR spectrometer was too low to be detected. Additionally, it should be mentioned here that the windows used in the gas chamber of the FTIR spectrometer were made of highly hydrophilic KBr, which might have perturbed the measurements.

3 Spectral reflectance analysis of type 3 carbonaceous chondrites and search for their asteroidal parent bodies

3.1 Background and main findings

As explained in the Introduction (Chapter 1), undifferentiated asteroids are of great importance for the understanding of the formation history our Solar System. Being primitive, they contain some of the oldest and least modified material in our Solar System. While sample return missions deliver lots of information about particular asteroids, they are expensive and, therefore, rare. Therefore, another widely used tool for investigating the physical and chemical composition of asteroid surfaces is reflectance spectroscopy (e.g. Burbine et al. (2002) and Reddy et al. (2015)). A large variety of asteroid types has been identified so far (see Section 1.1.1). However, while asteroid spectra include a wide range of information, most of them show only two, sometimes faint spectral features in the 0.45 – 2.45 µm region with little variations between different asteroid types (see Figure 1.1a in Section 1.1.1).

Our understanding of the reflectance spectra of different asteroid groups can be improved by increasing our knowledge on reflectance spectra of different meteorite groups. Laboratory measurements of meteorites allow to identify spectral differences within different meteorite groups as well as between them. It enables us to analyze which spectral features are controlled by secondary processes such as thermal metamorphism and aqueous alteration and allows for the search of a genetic link between meteorites and their asteroidal parent bodies. While reflectance spectra of asteroids can only provide information on asteroid surfaces, establishing a link with meteorites makes it possible to learn about asteroid interiors. For example, analysis of chondrites showed that chondrules are a main component of their asteroidal parent bodies interiors (see Table 1.4). However, finding such a link is a difficult task.

The general hypothesis is that each meteorite group samples one asteroidal parent body (e.g. Burbine et al. (2002)). The number of such parent asteroids necessary to represent the current meteorite collection was estimated to be between 95 and 148 (Greenwood et al., 2020). Finding a genetic link between meteorites and asteroids has only been done successfully in a few cases, such as between S-type asteroid Itokawa and EOCs by the Hayabusa sample return mission (Nakamura et al., 2011). Several asteroidal parent bodies have been suggested for CCs based on reflectance spectroscopy, but the links vary between sources (e.g. Bell et al. (1988b), Vernazza et al. (2015),

Hiroi et al. (1996) or Vernazza and Beck (2016)) (see Section 1.3.2 for more details).

During the first part of this PhD I have, thus, put a focus on the analysis of a large set of reflectance spectra of type 3 CCs. I measured reflectance spectra of 23 CVs, 15 COs and 4 CRs. 9 CK spectra were taken from the RELAB (2022) database. Additionally, the work included the reflectance spectra of 31 UOCs that I measured. The novelty of this work was that all chondrites considered had well constrained post-accretion histories. The metamorphic grade of (almost) all of these chondrites was previously constrained by Bonal et al. (2016) (see Tables 2.1 and 2.3). Furthermore, the aqueous alteration history of the CVs was previously constrained by Bonal et al. (2020).
Lastly, a total of 24 Eos family member spectra (RELAB, 2022) and 17 end member asteroid spectra (including C, Cg, Cgh, Ch, B, T, X, Xc, Xe, Xk and D-type) (DeMeo et al., 2009) were included as well.

A set of spectral features was determined for each reflectance spectrum including band depths, band positions, spectral slopes and the peak reflectance value (see Section 2.3). Using these features, spectral differences between chondrite groups were studied. The main findings are the following: UOCs can clearly be distinguished from CCs by showing much deeper absorption features, located at lower wavelengths. Type 2 CR chondrites showed 1 µm absorption bands at lower wavelengths than type 3 CCs. CVs and COs on the other hand could not be distinguished based on reflectance spectral features alone, due to their similar mineralogy.

I found that the 1 µm absorption band of CVs is controlled by their metamorphic grade. Since the 1 µm band is related to the Fe^{2+} in the olivine, the increase in band depth with increasing metamorphic grade indicates the chemical modification of olivine in CVs the higher the metamorphic temperature. For COs, a correlation between the visual slope and the metamorphic grade could be observed. This indicates an increase of iron in silicates and/or oxidized iron in COs with increasing metamorphic temperature. The negative correlation of the 2 µm spectral slope with the metamorphic grade observed for all CCs and UOCs indicates a decrease in pyroxene content with increasing peak metamorphic temperature (Bonal et al., 2016).

Since end member asteroid spectra are influenced by SW, and SW mainly influences the spectral slope (Section 1.3.2), comparisons between chondrites and asteoroids are made based on the depths and positions of the 1 µm and 2 µm bands only. When comparing the spectral features of the CV, CO, UOC and CK chondrites to those of asteroidal end members and Eos family members, certain asteroid spectral features matched well with those of certain chondrite groups. Firstly, a good match between the 1 µm and 2 µm absorption band depths of S-type asteroids and UOCs could be found, which legitimized the approach (Nakamura et al., 2011). CKs matched well with K-type and Eos family members as suggested by Vernazza et al. (2015). For CO and CV chondrites a good match could be found with Eos family members, L-type and Cb-type asteroids. A link between L-type asteroids and CV, CO chondrites was previously suggested by Sunshine et al. (2008) and Devogèle et al. (2018). Besides spectral similarities, the number of asteroids in a given class, their distribution in the asteroid belt and whether or not they belong to dynamical families is also crucial for finding good asteroidal parent body candidates. As explained in Section 1.1.1 dynam-

ical family members are efficient in delivering meteorite material to Earth. Therefore, it is expected that more fragments of asteroid types that are numerous, distributed throughout the asteroid belt and are part of dynamical families are delivered to Earth. L-type asteroids are not rare and distributed throughout the asteroid belt (between 2-4 au) (DeMeo and Carry, 2013) which strengthens the link found.

The paper published in Icarus 2021, 354, 114034 on this topic is inserted at the end of this chapter after the description of some perspectives.

3.2 Linking CV/CO chondrites to L-type asteroids without anomalous enrichment of calcium-aluminum inclusions

Since the publication of this work in 2021, we made some advances in trying to find the asteroidal parent bodies of type 3 CCs. This was done in collaboration with Max Mahlke and Benoit Carry [1].

Indeed, the link between CV spectra and L-type or K-type spectra (Eos family members) has been previously suggested (Bell et al. (1988a), Sunshine et al. (2008) and Devogèle et al. (2018)) based on the existence of a strong 2 µm iron oxide–bearing aluminous spinel band (usually contained in CAIs). In particular, Sunshine et al. (2008) used a radiative transfer model to fit the spectral features of L-type asteroids based on reflectance spectra of the CV chondrite Allende, of CAIs and of MgO-rich olivine. From these models they concluded that L-type asteroids must consist of 22-39 % of CAI material. Similarly, Devogèle et al. (2018) modeled the spectra of 28 L-type spectra with spectra of the CV chondrites Allende and Y-86751 and found similarly high CAI abundance values necessary for a good fit.

However, these approaches have some weaknesses: i) L-type asteroid spectra are variable in their 2 µm band (DeMeo et al. (2009), Mahlke et al. (2022)) and so are CV spectra. Thus, using only three L-type spectra (in the case of Sunshine et al. (2008)) and only one or two CV spectra is not sufficient to represent all and ii) we do not have any meteorites in our collection that exhibit such high CAI abundances (see Table 1.4).

With the acquisition of a large set of CV and CO spectra during this PhD and the collection of a large set of L-type, K-type and Barbarian asteroid spectra in Mahlke et al. (2022) the link between CVs and COs and L-type, K-type and Barbarian asteroids was revisited. Barbarians are a smaller group of asteroids which show peculiar behavior in their polarimetric phase curves which were first observed for (234) Barbara (Cellino et al., 2006). Here, the preliminary results of this work, which are currently in preparation for publication (Mahlke et al., in prep.), are summarized. It includes all CVs and COs and a single CK spectrum that I measured during this PhD, as well as spectra of CVs Allende and Y-86751 from the RELAB (2022) database (as used by Devogèle et al. (2018)). For a more asteroid based perspective of the following analyses, the reader is referred to the PhD thesis of M. Mahlke (Mahlke, 2022).

[1] Observatoire de la Côte d'Azur, CNRS, Laboratoire Lagrange, France

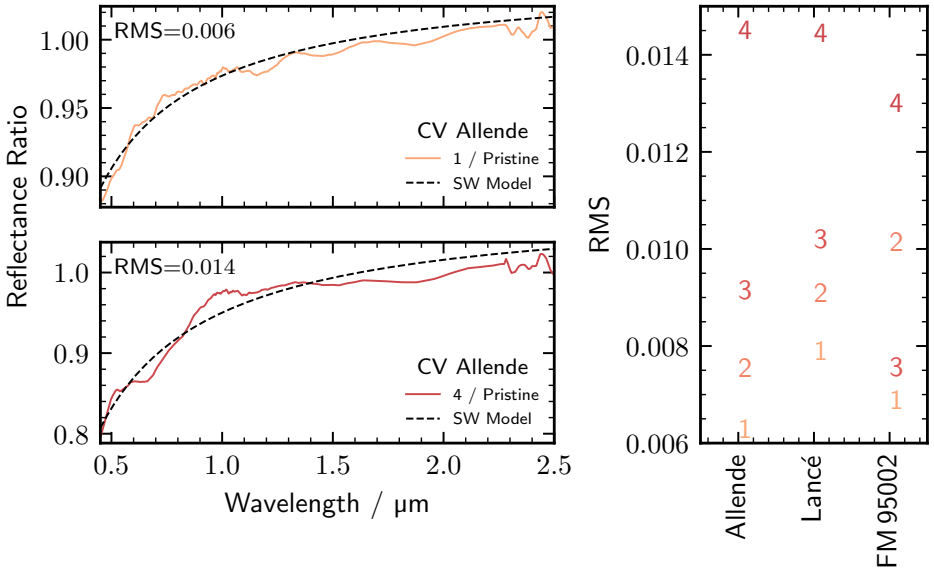

Figure 3.1: Example of the exponential SW model used on irradiated chondrite spectra (Lantz et al., 2017) to determine the RMS. *Left:* Shown on the top left is the ratio of the slightly irradiated (degree 1) to the pristine spectrum of Allende. The ratio is fit with an exponential function (dashed black line). The same is shown in the bottom left for the strongly irradiated (degree 4) Allende spectrum. *Right:* RMS determined from the fit of the irradiated to pristine spectrum ratio for Allende, Lancé and FM 95002. Shown are the RMS for four degrees of irradiation each. The average RMS is 0.0095. Data was taken from Lantz et al. (2017), plot was taken from Mahlke et al. (in prep.).

Firstly, it is assumed that asteroid surface material is equivalent to space weathered meteorite material, with no other external influences on their chemistry and mineralogy. Therefore, the approach suggested by Brunetto et al. (2006) (see also Section 2.3.1) in which the effect of SW in asteroid spectra can be approximated well with an exponential function, is justified. The chondrite spectra are divided by the asteroid spectra and the resulting curve is fit with an exponential (Figure 3.1). For each fit, the residuals and the Root mean square (RMS) are determined as follows:

$$RMS = \sqrt{\left(\frac{1}{N}\sum_{i}^{N}(x_i - y_i)^2\right)} \tag{3.1}$$

with N the number of wavelength bins. To have a comparison of what can be considered a "good match" between meteorite and asteroid spectra, the RMS is compared to the one determined for experimentally irradiated CVs taken from Lantz et al. (2017). In their work, ion irradiation experiments are performed on three CVs and COs (Allende (CV), FRO 95002 (CO) and Lancé (CO)). By dividing the spectra of the irradiated chondrites by those of the pristine chondrites for different degrees of irradiation, the RMS of each ratio fit can be determined (Figure 3.1). Subsequently, a mean RMS of 0.0095 can be determined. A "good match" is therefore found, when the difference between asteroid and meteorite spectrum can be explained by exponential SW, which is the case when the RMS is around 0.01. This procedure is repeated for all chondrite and asteroid spectra and the resulting RMS values are plotted in Figure 3.2. To highlight the best matching chondrites to specific asteroid spectra, a filled

in, white circle is plotted. The second best fit is indicated by an empty white circle. As can be seen, the spectrum of CV Allende taken from the RELAB (2022) database matches several K-type asteroids well. The spectra of CV_{OxA} QUE 94688, Axtell and Y-86751 match several L-type asteroid spectra well. The same is true for CO ALH 85003. The single CK spectrum (ALH 85002) considered here matches several K-type asteroid spectra well. In Figure 3.3 some examples of matched asteroid and chondrite spectra are shown after de-space weathering the asteroid spectra using the exponential model of Brunetto et al. (2006).

These results thus support the link between CVs and COs with K-type, L-type and Barbarian asteroids. More specifically they seem to indicate that L-type are best matched by CV_{OxA}. Note that, these results allow for a match without the need of large enrichment in CAIs in L-type asteroids as suggested by Sunshine et al. (2008) and Devogèle et al. (2018).

It should be noted here that these results are very dependent of the de-space weathering model used and therefore favors finding matches with those asteroids, for which the SW can, indeed, be well approximated by an exponential function. Previous work has shown that irradiation of carbonaceous material can have varying results (including bluing of the slopes, see Section 1.3.2). Therefore, to make this method more applicable to a wider range of asteroid spectra a more in-depth study of the effects of SW on larger data sets of carbonaceous material is necessary.

Mahlke et al. (2022) use dimensionality reduction to derive a lower-dimensional space which allows for comparison of reflectance spectra of asteroids in terms of their slopes and absorption features independently. Assuming that SW largely affects the slope of asteroid spectra, it is possible to search for asteroid-meteorite matches by projecting the meteorite spectra into the same lower-dimensional space as the asteroid spectra and emphasizing the dimensions which focus on the relevant features instead of the slope. In Figure 3.4 the different dimensions of the lower-dimensional space are plotted against each other. The Figure includes all CV, CO and CK chondrites as well as the L-, K- and M-type asteroids. In each plot, the difference in lower-dimensional space between pristine and irradiated CV and CO spectra (calculated from spectra in Lantz et al. (2017)) is indicated by a dotted arrow. It seems that chondrites and asteroids plot along the axis of this SW arrow, indicating an increase of SW from chondrites to asteroids. The solid arrow indicates the difference in the lower-dimensional space for chondrites of different grain sizes (calculated from spectra taken from Cloutis et al. (2012c)). It shows that generally, decreasing the grain size will shift chondrite spectra closer to asteroid spectra. This was also observed in Eschrig et al. (2022) for OCs and S-type asteroids (Chapter 4).

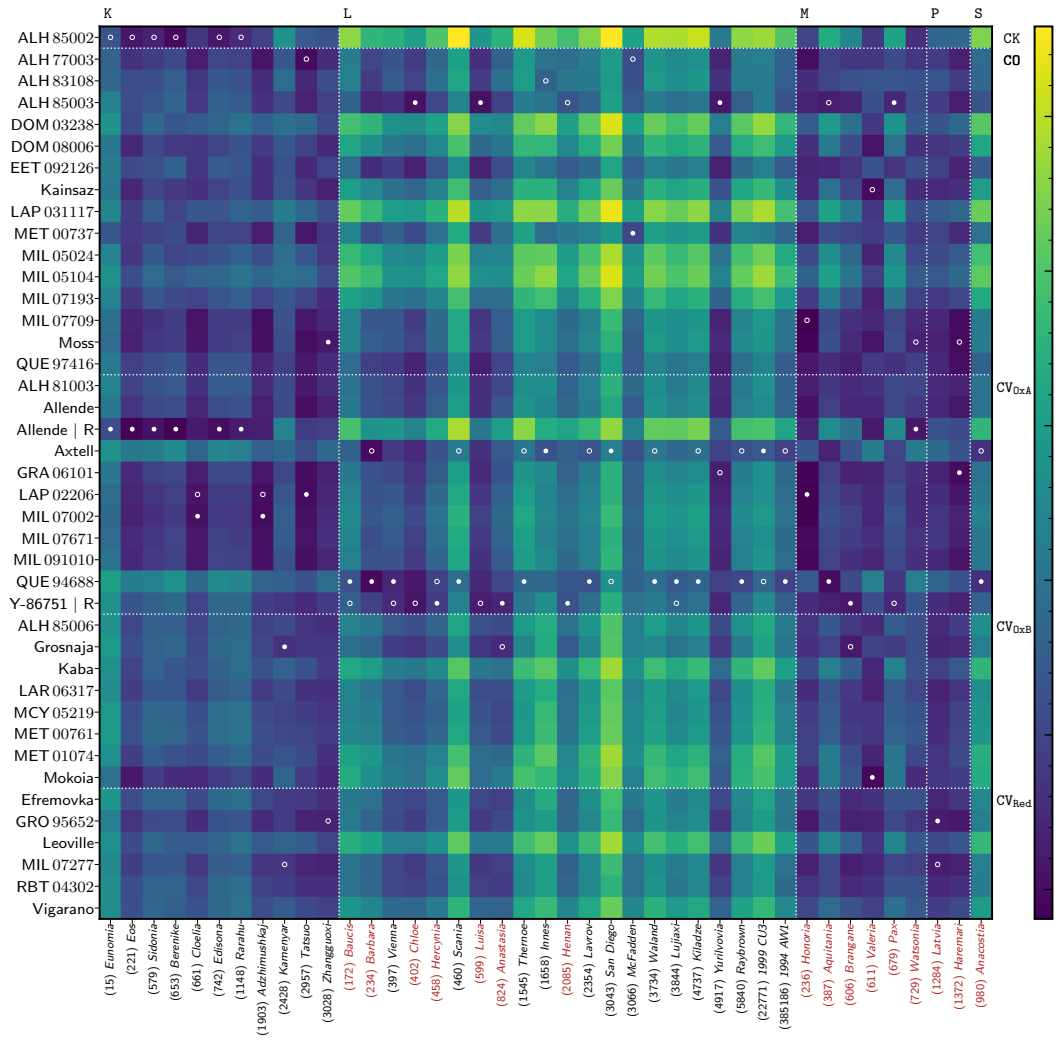

Figure 3.2: Results of the RMS values determined for all combinations of chondrite and asteroid spectral ratios. Asteroids labeled in red font are Barbarians. Filled in white circles indicated the best matching meteorite found for a given asteroid. Empty white circles give the second best fit. Plot was taken from Mahlke et al. (in prep.).

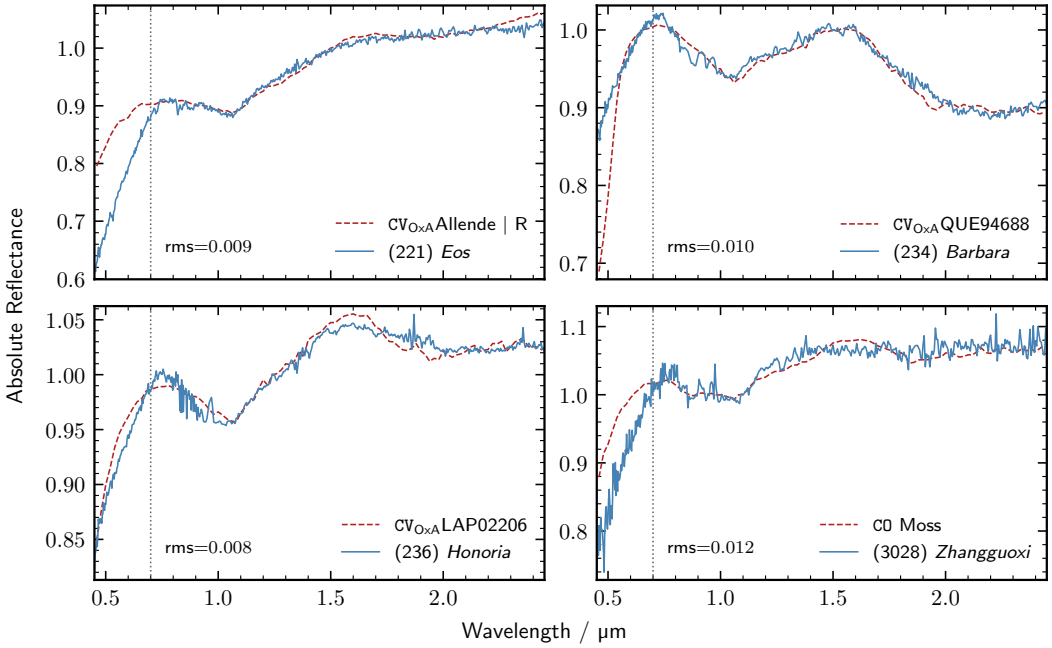

Figure 3.3: Examples of spectral matches between chondrite and asteroid spectra after de-space weathering using the model presented in Brunetto et al. (2006). Image was taken from Mahlke et al. (in prep.)

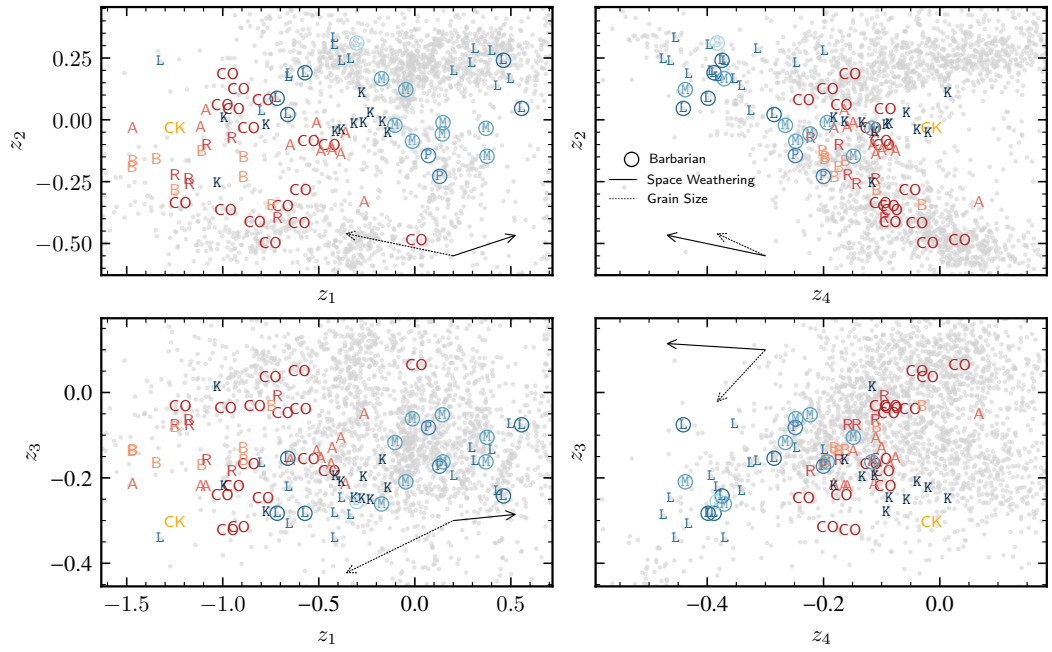

Figure 3.4: Plot of the different dimensions of the lower-dimensional space determined for CVs, COs, CKs as well as L-type, K-type and M-type asteroids. The dotted arrow gives the direction of the effect of decreasing SW on the lower-dimensional space. The solid arrow gives the direction of the effect of decreasing grain size in the lower-dimensional space. Image was taken from Mahlke et al. (in prep.).

Icarus 354 (2021) 114034

Contents lists available at ScienceDirect

Icarus

journal homepage: www.elsevier.com/locate/icarus

Spectral reflectance analysis of type 3 carbonaceous chondrites and search for their asteroidal parent bodies

J. Eschrig *, L. Bonal, P. Beck, T.J. Prestgard

Univ. Grenoble Alpes, IPAG, F-38000 Grenoble, France

ARTICLE INFO

Keywords:
Reflectance spectroscopy
CV chondrites
CO chondrites
CR chondrites
Unequilibrated Ordinary Chondrites (UOC)
Asteroids
Aqueous alteration
Thermal metamorphism

ABSTRACT

Non-differentiated asteroids are among the most primitive objects in our Solar System, having escaped intense heating mechanisms. To help us understand the information contained in reflectance spectra measured on asteroids, we analyzed meteorites in the laboratory. We present an in-depth analysis of a large set of reflectance spectra: 23 CV3, 15 CO3, 4 CR2 and 31 Unequilibrated Ordinary Chondrites (UOCs). Each of the samples has a well characterized thermal history . Variations in the reflectance spectra are observed between and within each chondrite group. UOCs systematically exhibit deeper absorption features, distinguishing them from carbonaceous chondrites. The CR2 samples presented in this study are easily distinguished from type 3 chondrites by exhibiting the 1 μm band at lower wavelengths. CV and CO chondrites exhibit comparable mineralogical compositions and can, therefore, not be distinguished solely based on their spectral features. In the case of CV chondrites, the 1 μm band depth increases with increasing metamorphic grade, while among CO chondrites, the spectra exhibit increasing visual slopes.

By comparing the chondrite spectra with the spectra of various end member asteroids we are able to suggest several possible genetic links to the studied chondrites. The method in this work is supported by observed match between UOC and S-type asteroid spectra. A further link is found between CV/CO chondrites and Eos and L-type asteroids. Finally, CK chondrite spectral features match with Eos and K-type asteroids. Lastly, we underline the potential of the 3 μm band to constrain asteroid–meteorite links.

1. Introduction

While some asteroids are clearly differentiated (e.g., Vesta), several asteroid types appear to have escaped differentiation (e.g., Vernazza et al. (2017)). This makes them primitive objects and as such, they are important for the understanding of the formation and evolution of the Solar System. Strides towards understanding their physical and chemical characteristics have been made in the last decades, leading to the discovery of a great variety of asteroid types (e.g. Bus (1999), Zellner et al. (1985) and later DeMeo et al. (2009)). Recently, Greenwood et al. (2020) estimated the number of parent asteroids needed to represent our meteorite collection on Earth between 95 and 148.

There are several techniques constraining the physical and chemical properties and/or the composition of asteroids. Among them, reflectance spectroscopy is one of the most widely applied methods (Burbine et al., 2002; Reddy et al., 2015). For one, it is a remote characterization method that allows for the analysis of asteroid surfaces from the ground or a spacecraft. As a ground based method it can, therefore, constitutes a low cost technique in comparison to, e.g. space missions that return samples. Most importantly however, the possibility of applying this technique in laboratory on Earth enables a direct comparison with a series of samples. While spectral measurements can reveal a lot of information, the reflectance spectra acquired for asteroids in the 0.45 – 2.45 μm region show only two main absorption features, which can be very faint in some cases (DeMeo et al., 2009). To improve the interpretation of asteroid spectra, it can be useful to do some measurements on well known samples. Several in depth studies of reflectance spectroscopy on meteorites have been led in the past (e.g. Cloutis et al. (2012a,b,c), Gaffey (1976) and Vernazza et al. (2014)).

Based on these previous studies, chondritic meteorites have been found to display three main absorption bands in their spectra at 1 μm, 2 μm and 3 μm. The origin of these features are attributed to anhydrous and hydrous silicates whose exact compositions will vary with the considered chondrite group as well as the secondary processes they experienced on their asteroidal parent bodies. Consequently, the position and depth of the absorption bands are modified.

* Corresponding author.
E-mail address: jolantha.eschrig@univ-grenoble-alpes.fr (J. Eschrig).

https://doi.org/10.1016/j.icarus.2020.114034
Received 13 March 2020; Received in revised form 30 July 2020; Accepted 1 August 2020
Available online 7 August 2020

The chondrite groups considered in this work are carbonaceous chondrites (CV, CO, CR) and Unequilibrated Ordinary Chondrites (UOC). The main conclusions from past works are the following:

- **CV chondrites** (Cloutis et al., 2012c): Based on the 11 CV chondrites measured in this previous work, the position and morphology of the 1 μm absorption band is consistent with the presence of ferrous olivine. The 2 μm region shows signs of being affected by Fe-bearing pyroxene, but can also exhibit contributions due to spinel. The spectral slopes in the 1 μm and 2 μm region become increasingly positive or red sloped with increasing metamorphic grade. While Cloutis et al. (2012c) did expect to see an increase in reflectance, bluer spectral slopes and better defined mafic silicate bands with increasing thermal metamorphism, no correlation between the spectral features and the metamorphic grade could be observed with the considered samples.
- **CO chondrites** (Cloutis et al., 2012b): This study included 16 CO chondrites. The major silicate contributing to the 1 μm and 2 μm absorption features is olivine. The abundance of low-Ca pyroxene is expected to be relatively low with possible contributions due to spinel. The position and band depth of the 1 μm absorption feature are both correlated with the metamorphic grade. The overall reflectance in the 700 nm region increases with higher thermal metamorphism. This peak reflectance appears to correlate with the 1 μm and 2 μm band depths as well as with the overall spectral slope.
- **CR chondrites** (Cloutis et al., 2012a): This study was based in 14 CR chondrites. Generally, CR chondrites exhibit only weak 1 μm and 2 μm absorption features due to the low amount of Fe-rich silicates present in the samples. The 1 μm band is related to the presence of low-Fe olivine, low-Fe pyroxene and phyllosilicates. In case of terrestrial weathering, a contribution at 900 nm due to Fe oxyhydroxides can be present. Low-Fe pyroxene shows a second absorption feature at 2 μm. The spectra show a red overall spectral slope. The 1 μm absorption band depth is correlated with the weathering degree of the samples. With increasing aqueous alteration the amount of phyllosilicates increases, which is reflected in a more pronounced absorption band at 900 nm.
- **UOCs** (Gaffey, 1976; Vernazza et al., 2014): Ordinary chondrites (OC) have been well studied in the past showing reddish slopes, a broad peak reflectance in the visible wavelength range (near 700 nm) which is dependent on the metamorphic grade as well as olivine and pyroxene absorption features in the 1 μm and 2 μm region. Gaffey (1976) found feldspar to be linked to various near-IR absorption bands located at 900 nm and 970 nm, near 1900 nm, as well as an inflection in the spectra near 1300 nm. However, the presence of feldspar explaining these absorption features has since been disproved (e.g. Crown and Pieters (1987)). These observations are greatly based on Equilibrated ordinary chondrites (EOCs). UOCs have recently been studied in comparison to EOCs by Vernazza et al. (2014), which analyzed a set of 53 UOCs. Generally, UOCs exhibit stronger absorption features than carbonaceous chondrites.

The present work presents several novelties: we conduct the analysis of more than 70 chondrites (CV, CO, CR and UOCs) and nearly all chondrites we consider have a well constraint post-accretion history. Their metamorphic grade was previously determined by Bonal et al. (2006, 2007, 2016) and Quirico et al. (2009). The aqueous alteration history of CV chondrites was assessed in Bonal et al. (2020). This allows us to analyze the consequences of secondary processes on the reflectance spectra of meteorites and, thus, of asteroids. We contribute to the analysis of UOC spectra which, until recently (Vernazza et al., 2014) have received much less attention EOCs. However, this will not be the main focus of the present paper. By taking advantage of a new spectro-radio goniometer available at the Institute de Planétologie et d'Astrophysique Grenoble (IPAG) (Potin et al., 2018) we enable measurement under vacuum and at higher temperatures than ambient. This allows us to eliminate terrestrial water contamination. We introduce a set of spectral properties, including a range of absorption band depths and positions as well as spectral slopes, following earlier works by Cloutis et al. (2012c). Our objectives are to (i) deepen our understanding of reflectance spectral features, (ii) understand if some of these features are controlled by secondary processes such as thermal metamorphism, and (iii) establish some genetic link between asteroids and carbonaceous chondrites, that are not firmly identified for type 3 chondrites.

2. Sample lists and experimental procedure

2.1. Sample list

In this paper 4 CR (Eschrig et al., 2019a), 23 CV (Eschrig et al., 2019b), 31 UOCs (Eschrig et al., 2019c) and 15 CO (Eschrig et al., 2019d) were measured. All data are available online in the GhoSST/SSHADE spectral database. With the exception of the four type 2 CR chondrites, all samples considered in this work are type 3 chondrites. CV chondrites can generally be sub-divided into oxidized (CV_{Ox}) and reduced (CV_{Red}) based on their metal abundance as well as their Ni in sulfides and Ni in metal content. According to this classification CV_{Ox} can be further sub-divided into CV_{OxA} and CV_{OxB} with CV_{OxA} exhibiting a higher metal abundance and lower Ni in sulfide content than CV_{OxB}. The samples considered in this work were previously classified by Bonal et al. (2020). 6 of the 23 CV chondrites are classified as CV_{Red}, 9 as CV_{OxA} and 8 as CV_{OxB}. A list of the considered samples as well as their classification is given in Tables 1 and 2. UOCs are sub-divided into three classes based on their total iron abundance. H types exhibit a total average metal abundance of 8.4 vol.% while for L types the value reaches 4.1 vol.% and for LL types it is 2.0 vol.% (Krot et al., 2014). 10 of the 31 UOCs considered in this work are classified as H, 15 as L, and 6 as LL as indicated in Tables 3 and 4. All the meteorites characterized in the present work are remaining samples that had been initially allocated for previous studies (Bonal et al. (2016) for CV, CO and UOCs) by the NASA Meteorite Working Group (Johnson Space Center, Houston, USA). Most of the samples presented in this work have a well constraint thermal history. The petrologic type (PT) previously determined by Bonal et al. (2006, 2007, 2016) and Quirico et al. (2009) through Raman spectroscopy is given for each sample in Tables 1 and 3 as well. However, all plotting was done using the $FWHM_D$ values determined from the Raman spectra, since this value allows for a more precise distinction of the metamorphic grades. For more explanation we refer to Bonal et al. (2016).

Additionally to the chondrites that were measured in the present work, a set of 17 asteroidal end member spectra (DeMeo et al., 2009), Database: http://smass.mit.edu/busdemeoclass.html, 24 Eos family member spectra (Mothé-Diniz et al., 2008) and 9 CK chondrite spectra (RELAB Database (http://www.planetary.brown.edu/relab/)) were included. This was done to improve our understanding of asteroid spectra and investigate possible links between asteroid and chondrite types. The asteroidal end member spectra range from 450 nm to 2450 nm. The 24 Eos family spectra range from 850 nm to 2485 nm. The 9 CK chondrite spectra range from 300 nm to 2600 nm. All literature spectra were treated in the same way as the chondrite spectra measured in this work (see Section 2.2). Since the spectral ranges of the literature spectra are smaller than those of our experimental data, not all spectral features could be compared between the data sets. Indeed, none of the literature spectra include the hydration band in the 3 μm range. Moreover, C, Cg, Cgh, Ch, B, T, X, Xc, Xe, Xk and D-type end member spectra exhibit only a faint or no 2 μm absorption band which is why the band depth and position are not considered. The same is true for CK chondrite spectra, however, their 2 μm absorption band features are still considered in later comparisons while keeping the larger uncertainties in mind.

Table 1
Spectral parameters determined from the reflectance spectra of carbonaceous chondrites (CO, CV and CR). The Integrated Band Depth (IBD_{Hyd}), and position of the hydration band (Hyd. Band Pos.) in the 3 μm range are shown for each sample. Furthermore, the spectral slope in the 1 μm and 2 μm range as well as the Visual slope are listed. For each spectral value, the average and the standard deviation are given. For sample marked by (*) the sapphire window correction was done using the measuring program (see Section 2.2). For sample for which the measurements were done at ambient temperatures the IBD_{Hyd} value is highlighted in gray. The petrologic type (PT) as determined by Bonal et al. (2006, 2007, 2016) are given as well. If no value is given, the determination of the PT was unsuccessful in Bonal et al. (2016).

		IBD_{Hyd} (%)	Hyd. Band Pos. (nm)	1 μm slope (10^{-7} nm^{-1})	2 μm slope (10^{-7} nm^{-1})	Visual slope (10^{-5} nm^{-1})	PT
CV_{OxA} chondrites	ALH 81003	5.9 ± 2.7	2960	-18.3±14.8	-13.1±12.3	9.5±0.3	>3.6
	Allende	6.9 ± 1.8	2940	106.0±7.5	25.4±14.6	6.5±0.4	>3.6
	Axtell	19.9 ± 1.2	3000	123.0±2.5	-68.4±6.7	30.9±0.8	>3.6
	GRA 06101	5.1 ± 1.4	2940	118.0±3.1	10.0±14.3	16.4±1.8	>3.6
	LAP 02206	1.6 ± 1.21	2900	76.1±2.1	1.0±8.0	13.1±0.9	>3.7
	MIL 07002	10.8 ± 1.5	2940	158.0±4.7	9.0±31.9	22.6±0.3	-
	MIL 07671	7.4 ± 1.3	2900	97.1±2.8	-17.8±12.3	19.5±0.6	3.1
	MIL 091010	9.8 ± 1.6	2900	72.1±2.7	-12.2±10.0	17.9±1.1	>3.6
	QUE 94688	19.6 ± 1.6	2920	-5.6±3.0	-99.7±9.4	26.5±1.8	>3.6
	average	9.7 ± 2.1	2933	80.7±19.5	-18.4±13.5	18.1±2.6	
CV_{OxB} chondrites	ALH 85006	13.7 ± 2.9	2960	-29.3±11.2	12.1±16.7	9.5±0.2	3.6
	Grosnaja	10.1 ± 1.8	2960	-68.7±2.0	-31.7±6.1	4.6±0.5	∼3.6
	Kaba	11.8 ± 2.0	2980	-12.9±3.2	31.0±6.9	6.7±0.1	3.1
	LAR 06317	16.3 ± 2.5	2980	1.8±6.8	21.3±9.5	11.1±0.2	3.4-3.6
	MCY 05219	5.0 ± 3.0	2960	-88.6±4.6	-12.2±16.7	4.0±0.2	>3.6
	MET 00761	14.2 ± 3.1	2960	-88.8±7.1	-16.8±26.4	21.6±2.5	3.6
	MET 01074 (*)	1.4 ± 0.6	2800	-40.8±0.8	11.6±2.9	3.2±0.5	3.6
	Mokoia (*)	1.9 ± 2.1	2900	36.0±2.4	21.3±11.3	5.8±0.6	∼3.6
	average	9.3 ± 2.0	2967	-36.4±15.7	4.6±7.8	8.3±2.1	
CV_{Red}	Efremovka	12.5 ± 1.7	2960	-11.7±7.4	-22.2±5.2	20.6±0.6	3.1-3.4
	GRO 95652	13.7 ± 2.3	2960	-19.3±3.2	-9.0±12.4	19.2±0.9	3.6
	MIL 07277	6.3 ± 1.3	2940	-27.8±2.9	-5.6±14.7	17.1±0.7	3.4-3.6
	RBT 04302	12.1 ± 1.7	2920	-39.2±3.5	-8.9±5.8	20.0±1.1	3.1-3.4
	Leoville (*)	8.9 ± 3.7	2880	26.5±7.1	30.3±14.8	9.2±0.4	3.1-3.4
	Vigarano (*)	6.2 ± 3.3	2900	-18.2±12.0	-9.2±20.6	14.2±0.2	3.1-3.4
	average	9.9 ± 1.3	2927	-15.0±9.1	-4.1±7.3	16.7±1.8	
CO chondrites	ALHA 77003	6.3 ± 1.5	2980	18.6 ±3.1	-14.6 ±13.1	25.0 ±0.6	>3.6
	DOM 08006	12.1 ± 2.3	2960	34.1 ±2.5	38.4 ±9.2	10.0 ±0.3	3.0
	MIL 05024	9.2 ± 2.1	2900	-11.9 ±2.8	32.7 ±9.6	10.8 ±0.4	3.1
	MIL 07193	11.0 ± 2.2	2900	-31.1 ±2.3	8.2 ±6.6	11.0 ±0.5	3.1
	ALH 83108 (*)	7.8 ± 0.3	2960	-8.7 ±3.5	-106.0 ±3.1	36.7 ±2.0	-
	EET 92126 (*)	11.2 ± 0.3	2960	-13.5 ±0.9	-102.0 ±2.0	51.1 ±1.2	-
	MET 00737 (*)	11.4 ± 0.3	2920	-10.4 ±1.2	-21.7 ±2.4	41.5 ±1.3	-
	MIL 05104 (*)	12.4 ± 0.4	2900	24.1 ±1.2	65.0 ±2.0	19.5 ±0.8	3.1
	MIL 07709 (*)	13.3 ± 0.3	2940	90.0 ±1.0	-28.0 ±2.1	22.7 ±4.1	3.7
	Moss (*)	5.6 ± 0.4	2880	95.5 ±1.6	11.4 ±3.1	15.3 ±1.8	3.6
	Kainsaz (*)	6.1 ± 0.5	2960	80.2 ±0.9	54.2 ±1.9	16.8 ±0.2	3.6
	LAP 031117 (*)	15.7 ± 1.0	2940	12.3 ±0.7	26.3 ±1.9	10.0 ±0.4	3.05
	QUE 97416 (*)	16.5 ± 0.3	2960	51.9 ±1.2	-62.5 ±3.0	52.4 ±1.8	-
	ALH 85003 (*)	9.8 ± 0.3	2960	20.2 ±1.1	-84.2 ±3.2	37.2 ±2.2	-
	DOM 03238 (*)	9.8 ± 0.8	2960	-8.5 ±1.2	31.0 ±3.3	13.2 ±0.5	3.1
	average	9.7 ± 1.3	2935	22.9 ±10.4	-10.1 ±14.5	24.9 ±3.9	
CR	EET 92042	17.2 ± 1.0	2920	142.0±2.2	78.9±12.3	25.3±0.8	
	GRA 95229	20.9 ± 1.0	2960	127.0±3.0	42.9±9.9	31.8±1.4	
	LAP 04720	17.4 ± 1.5	2940	55.1±2.6	43.6±7.4	24.6±1.5	
	MIL 090657	20.9 ± 1.4	2900	51.4±5.8	2.5±8.3	21.8±1.2	
	average	19.1 ± 1.0	2930	93.9±23.7	42.0±15.6	25.9±2.1	

2.2. Experimental procedure

The reflectance spectroscopy was measured using the SHADOWS instrument (Potin et al., 2018), a spectro-radio goniometer available at IPAG (France). The chondrites were all carefully ground using a mortar and pestle until they resembled a fine powder with sub-millimeter grain sizes. In previous works by Garenne et al. (2016) the volume weighted average grain size of hand ground chondrites was estimated to be between 100 μm and 200 μm. However, no sieving was performed to determine the exact grain size of the powders. The samples we are looking at are dark and we are interested in a heterogeneous powder containing a continuum of grain sizes as would be expected on asteroid surfaces. To ensure the representativity of all chondrite components, approximately 100 mg of sample were ground and 50 mg were used to fill the sample holder. To further ensure the comparability between different chondrites the measurements were done on flat surfaces. Thus, a spatula was set onto the edge of the sample holder and run over the top, smoothing and flattening the surface of the powdered sample.

The spectra were obtained in the 340 nm to 4200 nm region and were measured under vacuum ($P < 1 \times 10^{-4}$ mbar) and at 80 °C. These temperature and pressure conditions ensured the desorption of most terrestrial water contamination, therefore, leaving the hydration feature mostly controlled by chondritic hydration. It needs to be noted here that a few samples, which are highlighted in gray in Tables 1 and 3, were measured under vacuum but at ambient temperature. Each sample was measured with a spectral resolution of 20 nm and a measuring geometry of $i = 0°$, $e = 30°$. This geometry was chosen as a standard for good comparability between measurements of different laboratories. To

Table 2
Spectral parameters determined from the reflectance spectra of carbonaceous chondrites (CO, CV and CR). Listed are the peak reflectance value in the 700 nm range as well as the band depths and positions of the 1 µm and 2 µm bands. For each spectral value, the average and the standard error are given. For sample marked by (*) the sapphire window correction was done using the measuring program (see Section 2.2). Samples which are provided with highlighted 2 µm band depth and position values exhibit very faint spectral features, therefore, making the exact determination of these spectral parameters difficult.

		700 nm peak (%)	1 µm band depth (%)	2 µm band depth (%)	1 µm band pos. (nm)	2 µm band pos. (nm)
CV_{OxA} chondrites	ALH 81003	13.2±0.1	5.3±1.8	5.7±0.9	1080	2040
	Allende	9.8± < 0.1	4.4±0.9	4.3±0.8	1060	1960
	Axtell	10.8± < 0.1	6.9±0.4	7.4±0.5	1060	1960
	GRA 06101	11.1± < 0.1	4.0±0.5	3.3±1.0	1040	2100
	LAP 02206	9.8± < 0.1	5.8±0.5	4.1±0.7	1080	1940
	MIL 07002	14.4± < 0.1	5.9±0.5	4.4±0.9	1080	1960
	MIL 07671	10.5± < 0.1	6.2±0.6	4.3±0.9	1060	1960
	MIL 091010	10.1± < 0.1	5.1±0.6	4.0±0.7	1040	1960
	QUE 94688	10.8± < 0.1	7.2±0.6	6.9±0.7	1060	1960
	average	11.2±0.5	5.6±0.4	4.9±0.5	1062	1982
CV_{OxB} chondrites	ALH 85006	9.4±0.1	3.9±1.4	4.9±1.3	1040	1960
	Grosnaja	8.6± <0.1	3.7±0.5	3.5 ± 0.6	1060	2380
	Kaba	7.3± <0.1	2.6±0.7	2.8±0.8	1100	1980
	LAR 06317	9.3± <0.1	3.8±1.0	4.4±0.7	1060	1960
	MCY 05219	8.7± <0.1	2.9±0.9	3.6±1.2	1060	1960
	MET 00761	11.1± <0.1	2.8±1.0	3.6±1.3	1060	1920
	Mokoia	6.8± <0.1	4.4±0.8	2.6±1.0	1060	1920
	MET 01074	7.6± <0.1	2.3±0.2	2.1±0.4	1060	1920
	average	8.6±0.5	3.3±0.3	3.0±0.5	1062	1946
CV_{Red}	Efremovka	13.1± <0.1	2.3±0.7	2.5±0.4	1040	1960
	GRO 95652	7.1± <0.1	4.3±0.9	4.3 ± 1.0	1020	2380
	MIL 07277	10.2± <0.1	3.3±0.7	3.1±1.1	1040	1960
	RBT 04302	8.1± <0.1	3.0±0.8	3.9±0.8	1040	1860
	Leoville (*)	6.7± <0.1	1.4±3.2	1.2±1.7	1380	1860
	Vigarano (*)	7.5± <0.1	2.6±2.0	2.7±2.5	1380	1900
	average	8.8±1.0	2.8±0.4	2.7±0.4	1150	1908
CO chondrites	ALHA 77003	10.5 ± <0.1	7.3 ±0.6	5.3 ±1.0	1080	1960
	DOM 08006	5.0 ± <0.1	2.8 ±0.4	3.4 ± 1.1	980	2460
	MIL 05024	5.5 ± <0.1	4.6 ±0.9	2.5 ± 1.0	1120	2400
	MIL 07193	5.2 ± <0.1	3.2 ±1.1	2.8 ± 1.2	1000	2300
	ALH 83108 (*)	19.2 ± <0.1	9.9 ±0.2	6.4 ±0.1	1060	1860
	EET 092126 (*)	17.3 ± <0.1	7.5 ±0.1	5.0 ±0.1	1060	1900
	MET 00737 (*)	16.1 ± <0.1	8.7 ±0.1	6.5 ±0.2	1060	1900
	MIL 05104 (*)	9.5 ± <0.1	3.4 ±0.2	3.0 ±0.2	1400	1840
	MIL 07709 (*)	11.6 ± <0.1	5.2 ±0.2	3.1 ±0.2	1060	1940
	Moss (*)	13.2 ± <0.1	4.9 ±0.2	3.4 ±0.2	1060	1840
	Kainsaz (*)	10.1 ± <0.1	2.2 ± <0.1	2.2 ±0.3	940	1840
	LAP 031117 (*)	4.5 ± <0.1	3.4 ±0.3	1.4 ±0.5	1380	1840
	QUE 97416 (*)	15.9 ± <0.1	5.2 ±0.2	4.4 ±0.2	1060	1840
	ALH 85003 (*)	16.8 ± <0.1	6.2 ±0.2	4.8 ±0.2	1080	2100
	DOM 03238 (*)	6.6 ± <0.1	2.4 ±0.3	1.2 ±0.3	1400	1840
	average	11.1 ±1.3	5.1 ±0.6	3.8 ±0.5	1116	1885
CR	EET 92042	9.7± <0.1	2.9±0.1	3.2 ± 0.7	920	2400
	GRA 95229	11.4± <0.1	4.5±0.1	1.9±0.5	920	1820
	LAP 04720	9.9± <0.1	5.0±0.1	4.0 ± 0.6	920	2400
	MIL 090657	8.1± <0.1	5.4±0.2	1.7±0.8	920	1940
	average	9.8±0.7	4.4±0.5	1.8±0.1	920	1880

normalize the spectra to the Lambertian surface, two reference spectra were measured prior to the samples. In the wavelength range between 340 nm and 2100 nm a spectralon™ standard was used. For longer wavelengths between 2100 nm and 4200 nm an infragold™ standard was used.

The environmental cell containing the sample holder was closed by a sapphire window. To correct for the reflection on this window, the sample was first measured without the window, then with the window and finally with the window under vacuum and at 80 °C. By comparing the spectra measured with and without the window a correction factor could be calculated that allowed for the correction of the values measured under vacuum and at 80 °C. During the course of the measurements done in this work the correction of the window reflectance was integrated into the program used for the measurements. This allowed for direct measurements under vacuum and at 80 °C. Although no difference could be observed between manually and non-manually corrected samples, Tables 1 to 4 indicate which method was applied to each sample.

Table 3
Spectral parameters determined from the reflectance spectra of UOCs. The Integrated Band Depth (IBD_{Hyd}), and position of the hydration band (Hyd. Band Pos.) in the 3 μm range are shown for each sample. Furthermore, the spectral slope in the 1 μm and 2 μm range as well as the Visual slope are listed. For each spectral value, the average and the standard deviation are given. For sample marked by (*) the sapphire window correction was done using the measuring program (see Section 2.2). For sample for which the measurements were done at ambient temperatures the IBD_{Hyd} value is highlighted in gray. The petrologic type (PT) as determined by Bonal et al. (2006, 2007, 2016) are given as well. If no value is given, the determination of the PT was unsuccessful in Bonal et al. (2016). The "M" for ALHA 78119 stands for highly structured carbonaceous matter for which no reference sample was given to determine the PT (Bonal et al., 2016).

		IBD_{Hyd} (%)	Hyd. Band Pos (nm)	1 μm slope (10^{-7} nm^{-1})	2 μm slope (10^{-7} nm^{-1})	Visual slope (10^{-5} nm^{-1})	PT
H	BTN 00302	0.5 ± 1.0	2900	58.2 ± 2.3	52.2 ± 3.9	16.6 ± 1.8	3.1–3.4
	EET 83248	17.2 ± 0.9	2900	69.6 ± 1.5	3.9 ± 3.7	30.7 ± 3.6	>3.6
	RBT 04251 (*)	10.4 ± 0.2	2900	129.1 ± 1.1	51.9 ± 1.6	42.6 ± 3.5	3.4
	MCY 05218 (*)	16.3 ± 0.4	2920	129.0 ± 1.0	59.3 ± 1.6	35.2 ± 3.6	3.05–3.1
	WIS 91627 (*)	15.8 ± 0.2	2900	108.6 ± 0.8	−9.9 ± 2.6	36.9 ± 4.1	>3.6
	DOM 08468 (*)	5.5 ± 4.5	2920	44.3 ± 6.5	16.3 ± 38.0	25.5 ± 0.8	3.6
	LAR 04382 (*)	13.4 ± 2.2	2900	122.3 ± 7.8	18.3 ± 24.5	40.5 ± 2.2	3.1–3.4
	MAC 88174 (*)	5.4 ± 2.4	2920	77.9 ± 4.2	74.5 ± 22.1	30.0 ± 0.6	>3.6
	MET 00506 (*)	22.2 ± 0.5	2900	168.6 ± 1.5	96.3 ± 4.6	11.3 ± 2.7	3.1
	WSG 95300 (*)	8.8 ± 2.8	2920	99.6 ± 2.6	53.7 ± 22.9	30.2 ± 1.3	3.4
	Average	11.6 ± 2.1	2908	100.9 ± 12.1	44.5 ± 11.2	29.9 ± 3.2	
L	EET 90066	17.7 ± 1.3	2900	139.9 ± 2.1	25.5 ± 6.2	30.2 ± 3.5	3.1
	EET 90628	10.9 ± 0.9	2920	110.4 ± 3.0	44.9 ± 6.4	38.2 ± 2.5	3.0
	GRO 06054 (*)	12.8 ± 0.9	2900	98.4 ± 2.1	34.0 ± 5.7	35.0 ± 3.0	3.05
	LEW 87248 (*)	4.8 ± 0.3	2900	43.3 ± 0.7	71.3 ± 2.2	29.3 ± 2.4	3.0
	MET 00489 (*)	10.3 ± 0.3	2900	127.6 ± 0.6	32.4 ± 1.2	47.2 ± 2.7	3.05-3.1
	LEW 87284 (*)	4.9 ± 0.2	2900	83.4 ± 0.8	89.6 ± 3.1	39.1 ± 1.3	3.1–3.4
	ALH 83008 (*)	20.7 ± 0.4	2980	89.7 ± 0.8	−0.1 ± 2.3	28.5 ± 3.1	>3.6
	ALH 84086 (*)	7.5 ± 0.2	2960	180.9 ± 2.5	126.9 ± 3.2	44.7 ± 1.9	–
	ALH 84120 (*)	6.7 ± 0.2	3000	83.6 ± 3.3	123.8 ± 3.0	41.7 ± 1.8	–
	DOM 03287 (*)	13.2 ± 2.6	2900	13.7 ± 8.8	13.7 ± 18.4	33.6 ± 1.7	3.6
	EET 87735 (*)	12.7 ± 2.9	2920	92.8 ± 2.3	15.9 ± 6.4	19.8 ± 2.4	3.05-3.1
	LEW 88617 (*)	11.9 ± 2.4	2900	137.5 ± 4.6	49.1 ± 14.9	34.1 ± 2.3	3.6
	LEW 88632 (*)	18.4 ± 1.5	2900	155.4 ± 9.4	10.3 ± 11.0	40.7 ± 3.2	3.4
	MIL 05050 (*)	13.9 ± 1.9	2800	224.4 ± 10.3	81.7 ± 11.0	31.6 ± 1.0	3.1
	MIL 05076 (*)	18.1 ± 2.0	2920	113.1 ± 2.8	−2.3 ± 8.7	25.7 ± 1.8	3.4
	Average	12.3 ± 1.3	2913	112.8 ± 13.5	51.9 ± 11.3	34.6 ± 1.9	
LL	ALHA 76004	10.5 ± 1.0	2900	−8.1 ± 3.0	−4.7 ± 5.2	30.0 ± 1.2	3.1-3.4
	TIL 82408 (*)	14.9 ± 0.3	2920	180.7 ± 0.6	128.7 ± 2.8	34.1 ± 1.6	3.05-3.1
	EET 96188 (*)	12.4 ± 0.3	2900	137.1 ± 0.5	69.1 ± 2.3	44.7 ± 4.0	3.1-3.4
	LAR 06279 (*)	18.4 ± 0.2	2940	218.2 ± 2.9	51.2 ± 2.3	49.2 ± 5.1	3.05-3.1
	ALHA 78119 (*)	12.7 ± 2.4	2940	76.6 ± 4.3	33.8 ± 16.5	33.8 ± 1.8	M
	LAR 06469 (*)	14.3 ± 0.8	2900	−0.3 ± 1.1	39.3 ± 6.7	27.9 ± 1.9	>3.6
	Average	13.9 ± 1.1	2917	100.7 ± 38.4	59.6 ± 18.0	36.6 ± 3.5	

2.3. Analytical procedure

The obtained reflectance spectra are analyzed following previous works by Cloutis et al. (2012c). A set of spectral features including absorption band depths and positions as well as spectral slopes and peak reflectance values are introduced. A summary of all spectral features that are determined from each individual spectrum is shown in Fig. 1.

The 1 μm and 2 μm absorption bands are fit with linear baselines which are then used to determine the depth of the band as calculated by Clark (1999). Furthermore, the positions of the bands are determined at the minimum of reflectance. Besides the two absorption features at 1 μm and 2 μm, an absorption band attributed to hydration (OH and H_2O) can be seen at 3 μm. To characterize it, the Integrated Band Depth (IBD_{Hyd}) is calculated. For this, the organic bands (if present) located in the 3500 nm range are excluded by linearly fitting this region. Subsequently, the IBD_{Hyd} of the hydration band is calculated according to Milliken and Mustard (2005) between 2550 nm and 4000 nm. The peak reflectance value in the visible wavelength range is determined between 500 nm and 760 nm. The visual slope is determined by calculating the steepest slope in the 340 nm to 520 nm range and linearly fitting the points around this area. The overall spectral slope is defined as the inclination of the entire spectrum. Additionally, the spectral slope in the 1 μm and 2 μm range are considered by determining the slope of the 1 μm and 2 μm baselines fits.

It should be noted that some spectra display weak absorption features, leading to the determination of the band positions occasionally being ambiguous. This is the case of CV samples ALH 85006 and GRO 95652, CO samples DOM 08006, MIL 05024, MIL 07193, LAP 031117 and DOM 03238 as well as CR samples EET 92042 and LAP 04720 (Tables 1 and 2 as well as Figs. 2, 3 and 5).

3. Results

The reflectance spectra obtained for the 23 CVs, 15 COs, 4 CRs and 31 UOCs show variable spectral features. Significant spectral variations are visible between chondrite groups as well as within a given chondrite group (see Figs. 2 to 8). To allow for the quantification of these variations, the spectral features introduced in Section 2.3 are determined. The resulting parameters are listed in Tables 1, 2 (for carbonaceous chondrites) and 3, 4 (for UOCs). Furthermore, average spectral parameters are given to ease the investigation of spectral differences between chondrite groups.

The spectra of CVs Leoville and Vigarano as well as the UOCs ALH 78119, DOM 03287, DOM 08468, EET 87735, LAR 04382, LAR 06469, LEW 88617, LEW 88632, MAC 88174, MET 00506, MIL 05050, MIL 05076 and WSG 95300 exhibit a much lower Signal to Noise Ratio (SNR) (Figs. 2 and 4) than the other samples. This results from the aging of the IR detector. To treat these samples, a gaussian smoothing of the spectra was performed before the determination of the spectral features. It needs to be kept in mind, that especially for samples Leoville and Vigarano which exhibit faint absorption features, the determined band depths and positions have a higher uncertainty.

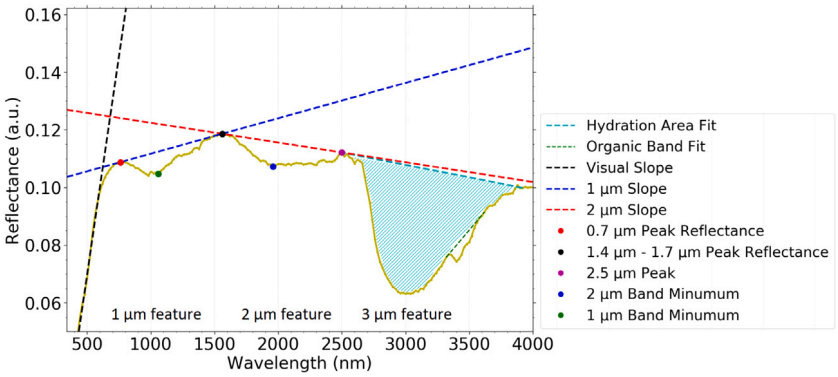

Fig. 1. Reflectance spectrum of the CV chondrite Axtell indicating the different spectral values which are systematically determined for each sample. The different slopes considered are the visual slope in black, the 1 µm region spectral slope in blue and the 2 µm region spectral slope in red. The cyan line indicates the linear fit to the hydration area. The green dotted line shows the linear fit to the organic bands. The peak reflectance in the visible wavelength range is shown as a red dot, the peak reflectance between 1400 nm and 1700 nm is indicated by a black dot and the peak reflectance between 2300 nm and 2600 nm is shown as a purple dot. The 1 µm and 2 µm band minima are shown as green and blue dots, respectively. (For interpretation of the references to color in this figure legend, the reader is referred to the web version of this article.)

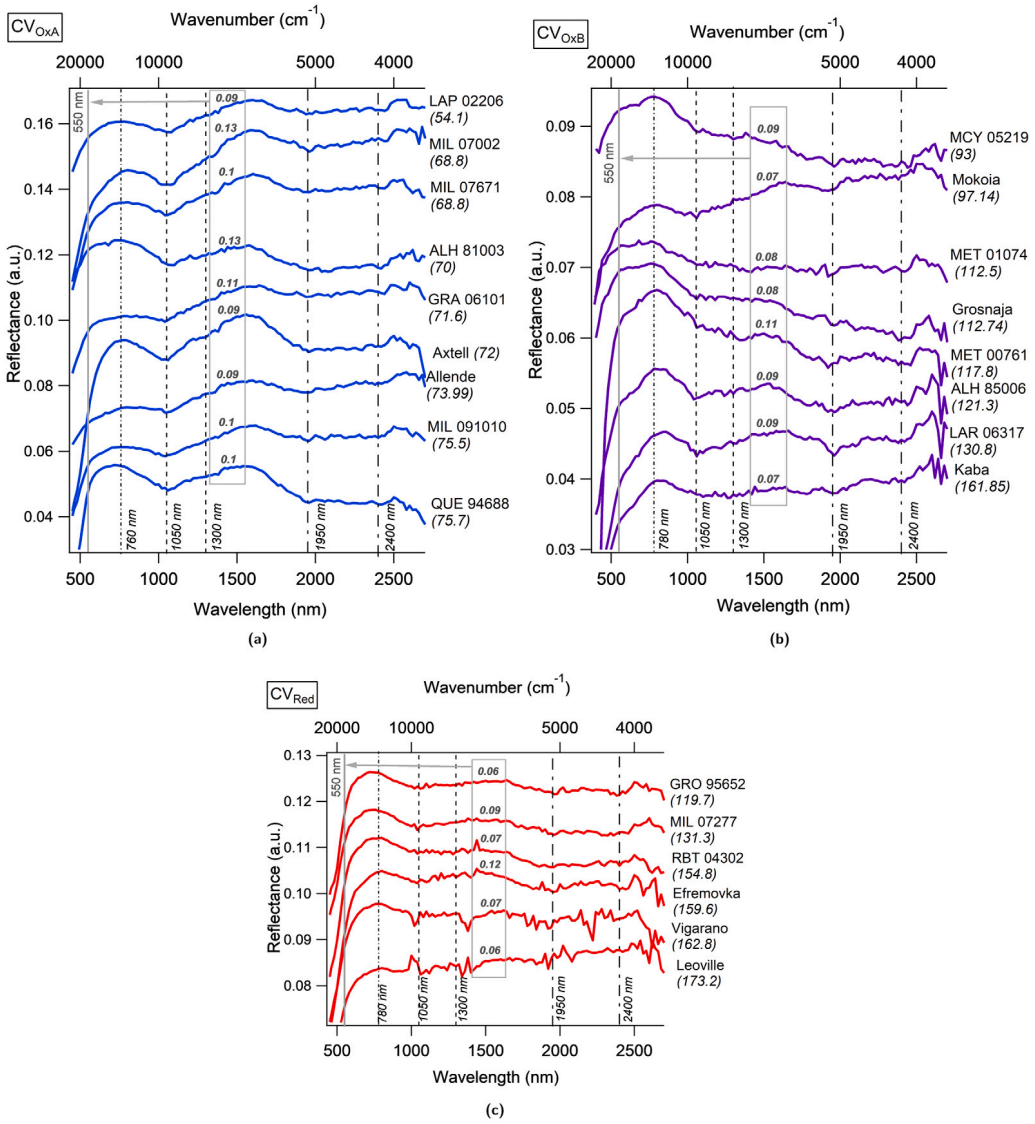

Fig. 2. Reflectance spectra obtained (a) for CV_{OxA} (b) for CV_{OxB} and (c) for CV_{Red}. Spectra are shown between 400 nm and 2600 nm and are plotted with an vertical offset, for better visibility. The reflectance value at 550 nm for each spectrum is given in the gray box. They are sorted by metamorphic grade with metamorphic grades increasing from bottom to top as indicated by the $FWHM_D$ (cm^{-1}) values (Bonal et al., 2016) given in parenthesis behind each sample name. The dotted lines indicate the position of the peak reflectance values in the visible wavelength range. The dashed lines indicate the position of the olivine absorption features in the 1 µm spectral region. The dash-dotted line indicates the spinel or pyroxene absorption features in the 2 µm region.

Table 4
Spectral parameters determined from the reflectance spectra of UOCs. Listed are the peak reflectance value in the 700 nm range as well as the band depths and positions of the 1 μm and 2 μm band. For each spectral value, the average and the standard error are given. For sample marked by (*) the sapphire window correction was done using the measuring program (see Section 2.2).

		700 nm peak (%)	1 μm band depth (%)	2 μm band depth (%)	1 μm band pos. (nm)	2 μm band pos. (nm)
H	BTN 00302	14.1 ± 0.1	11.5 ± 0.1	5.5 ± 0.2	940	1920
	EET 83248	11.7 ± <0.1	11.8 ± 0.1	6.5 ± 0.3	940	1960
	RBT 04251 (*)	16.3 ± <0.1	13.6 ± <0.1	5.7 ± 0.1	940	1840
	MCY 05218 (*)	12.4 ± <0.1	10.2 ± 0.1	4.0 ± 0.1	940	1860
	WIS 91627 (*)	15.6 ± <0.1	15.9 ± <0.1	8.5 ± 0.1	940	1840
	DOM 08468 (*)	11.4 ± <0.1	12.4 ± 0.1	11.8 ± 0.1	960	1920
	LAR 04382 (*)	14.8 ± <0.1	17.1 ± 0.1	15.8 ± 0.1	940	1960
	MAC 88174 (*)	13.9 ± <0.1	12.8 ± 0.1	14.5 ± <0.1	940	1940
	MET 00506 (*)	11.9 ± <0.1	14.0 ± 0.5	13.3 ± <0.1	1000	2400
	WSG 95300 (*)	11.1 ± <0.1	11.5 ± 1.5	12.0 ± <0.1	1000	1940
	Average	13.3 ± 0.6	13.1 ± 0.7	9.8 ± 1.3	954	1958
L	EET 90066	10.3 ± <0.1	11.4 ± 0.4	5.5 ± 0.4	1000	1920
	EET 90628	13.5 ± <0.1	15.1 ± 0.1	7.5 ± 0.2	960	1840
	GRO 06054 (*)	11.7 ± <0.1	12.6 ± 0.4	5.5 ± 0.3	1000	1880
	LEW 87248 (*)	14.2 ± <0.1	11.5 ± <0.1	5.1 ± 0.1	940	1840
	MET 00489 (*)	17.3 ± <0.1	18.8 ± <0.1	8.3 ± 0.1	940	1940
	LEW 87284 (*)	15.5 ± <0.1	12.3 ± <0.1	5.3 ± 0.1	920	1840
	ALH 83008 (*)	12.6 ± <0.1	12.5 ± <0.1	5.0 ± 0.1	940	1860
	ALH 84086 (*)	20.1 ± <0.1	19.5 ± 0.1	10.5 ± 0.1	940	1980
	ALH 84120 (*)	20.3 ± <0.1	14.1 ± 0.1	7.5 ± 0.1	920	1980
	DOM 03287 (*)	12.9 ± <0.1	13.0 ± 0.1	13.1 ± 0.1	940	1940
	EET 87735(*)	9.4 ± <0.1	12.2 ± <0.1	10.1 ± <0.1	940	1940
	LEW 88617 (*)	13.3 ± <0.1	14.6 ± 0.1	14.5 ± <0.1	960	1960
	LEW 88632 (*)	14.2 ± <0.1	15.8 ± 0.3	15.4 ± 0.1	1020	1960
	MIL 05050 (*)	11.3 ± <0.1	9.4 ± 1.5	13.2 ± 0.1	1000	1940
	MIL 05076 (*)	10.7 ± <0.1	11.1 ± 0.1	11.7 ± <0.1	940	1920
	Average	13.8 ± 0.9	13.6 ± 0.7	9.3 ± 0.9	957	1916
LL	ALHA 76004	13.9 ± <0.1	15.5 ± 0.1	8.0 ± 0.2	940	1920
	TIL 82408 (*)	12.5 ± <0.1	12.1 ± <0.1	5.4 ± 0.1	940	1840
	EET 96188 (*)	16.2 ± <0.1	14.9 ± <0.1	6.2 ± 0.0	940	1840
	LAR 06279 (*)	17.7 ± <0.1	15.3 ± 0.1	7.3 ± 0.1	940	1840
	ALHA 78119 (*)	14.5 ± <0.1	16.0 ± 0.1	15.1 ± <0.1	940	1940
	LAR 06469 (*)	13.2 ± <0.1	11.2 ± <0.1	13.2 ± <0.1	940	1960
	Average	14.7 ± 0.8	14.2 ± 0.8	9.3 ± 1.6	940	1893

Five of the CO chondrites measured in this work (MET 00737, ALH 85003, ALH 83108, EET 92126 and QUE 97416) and two of the UOCs (ALH 84120 and ALH 84086) could not be previously characterized by Raman spectroscopy (Bonal et al., 2016). They are plotted in black in Figs. 3 and 4. For the five COs the intense absorption features as well as the trend of the spectral features becoming more pronounced with increasing metamorphic grade (Fig. 3) point towards all five of these samples being highly metamorphosed. This is consistent with one possible hypothesis to explain the lack of successful Raman acquisitions by Bonal et al. (2016).

Since the main focus of this work is type 3 chondrites, only four CR2 chondrites were measured. This does not allow for statistically significant statements, however, the results are included for comparison. In the following sections, each spectral feature is described for the different chondrite groups.

3.1. Overall characterization of the reflectance spectra

3.1.1. 700 nm region peak reflectance

The reflectance spectra measured for CV chondrites show slight variations between samples of different sub-classifications (Fig. 2 and Tables 1 and 2). Indeed, CV_{OxA} samples exhibit the most pronounced absorption features and generally show a higher reflectance than CV_{OxB} and CV_{Red}. On average, the peak reflectance values in the visible wavelength range reach 11.2 ± 0.5% for CV_{OxA}, 8.6 ± 0.5% for CV_{OxB} and 8.8 ± 1.0% for CV_{Red} (Table 2). The positions of these features vary between 720 nm and 760 nm for CV_{OxA} and are less variable for CV_{OxB}, which are located at 780 nm. For CV_{Red} this feature is located at approximately 780 nm and shifts to lower wavelengths with increasing metamorphic grade (dotted lines in Fig. 2). The peak reflectance of GRO 95652, the most metamorphosed CV_{Red}, is located at 720 nm. Interestingly, a second feature is visible at 560 nm (dotted lines in Fig. 2b) for CV_{OxB}. This feature is not visible for CV_{OxA} and CV_{Red}.

The largest spectral variability within a chondrite group is seen for CO chondrites. As shown in Fig. 3, spectral features become more pronounced with increasing metamorphic grade. All samples exhibit a peak reflectance in the visible wavelength range with values ranging from 4.5 ± <0.1% for LAP 031117 to 19.2 ± <0.1% for ALH 83108 (Table 1). On average, the peak reflectance for CO chondrites reaches 11.1 ± 1.3%. This value is comparable to the average peak reflectance value determined for CV_{OxA} (Table 1 and Fig. 3). The position of the peak reflectance in the visible wavelength range is located close to 740 nm. A second, weaker feature closer to 660 nm can be seen for samples LAP 031117, DOM 03238, MIL 05104, Kainsaz, Moss, EET 92126, ALH 83108, ALH 85003 and MET 00737.

All UOCs exhibit reflectance spectra with distinct absorption features generally much more pronounced than for carbonaceous chondrites (Fig. 4). The peak reflectance in the visible wavelength range is located at 740 nm and exhibits average values of 13.3 ± 0.6% for H, 13.8 ± 0.9% for L and 14.7 ± 0.8% for LL. For some samples a shoulder at around 600 nm is seen, especially for samples classified as L-types, such as GRO 06054, EET 90066 and EET 90628 (Fig. 4c).

The four considered CR chondrites show rather featureless spectra with a red overall spectral slope (Fig. 5). The peak reflectance value in the visible wavelength range is located at 760 nm and has an average value of (9.8 ± 0.7)% (Table 1 and Fig. 3).

3.1.2. 1000 nm region absorption feature

For CV chondrites, the 1 μm absorption band depth decreases from CV_{OxA} to CV_{OxB} to CV_{Red}. On average the band depth values reach

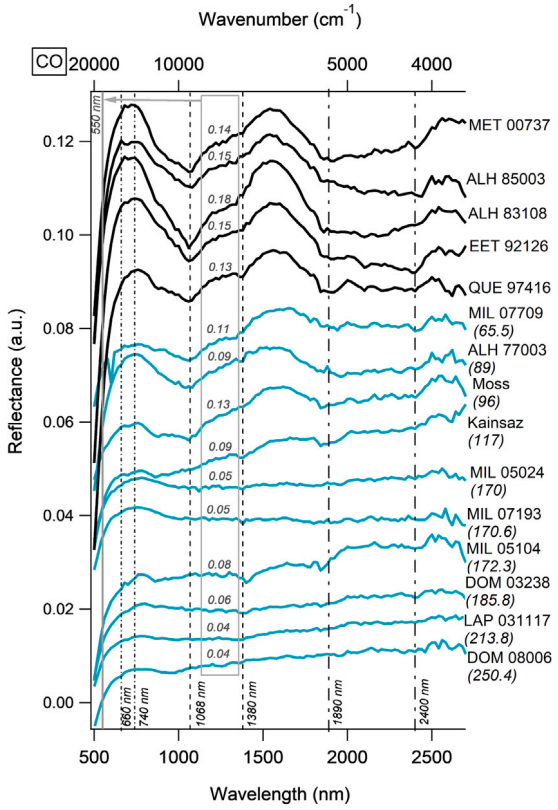

Fig. 3. Reflectance spectra obtained for COs. Spectra are shown between 500 nm and 2700 nm and are plotted with an vertical offset, for better visibility. The reflectance value at 550 nm for each spectrum is given in the gray box. They are sorted by metamorphic grade with metamorphic grades increasing from bottom to top as indicated by the $FWHM_D$ (cm^{-1}) values (Bonal et al., 2016) given in parenthesis behind each sample name. The dotted lines indicate the position of the peak reflectance values in the visible wavelength range. The dashed lines indicate the position of the olivine absorption features in the 1 μm spectral region. The dash-dotted line indicates the spinel or pyroxene absorption features in the 2 μm region. Five of the 15 samples measured were not provided with $FWHM_D$ values by Bonal et al. (2016). They are plotted in black. (For interpretation of the references to color in this figure legend, the reader is referred to the web version of this article.)

5.6 ± 0.4%, 3.3 ± 0.3% and 2.8 ± 0.4%, respectively. The main minimum of the 1 μm band is located at 1050 nm. A slightly less pronounced feature around 1300 nm can be observed for CV_{OxA} but is less visible for CV_{OxB} and CV_{Red} (dashed lines in Fig. 2). The positions of these features are associated with ferrous olivine present in the samples (Cloutis et al., 2012c). The tilt of the spectra in the 1 μm region is red to neutrally sloped for CV_{OxA} (average value of 80.7 ± 19.5 nm^{-1}) while it is neutrally to blue sloped for CV_{OxB} and CV_{Red} (average values of −36.4 ± 15.7 nm^{-1} and −15.0 ± 9.1 nm^{-1}, respectively). There are some exceptions to these overall observations. Indeed, the CV_{OxA} ALH 81003 and QUE 94688 are neutrally to blue sloped. LAR 06317 (CV_{OxB}) is neutrally sloped and Mokoia (CV_{OxB}) is redder slope than the other CV_{OxB}.

For CO chondrites the 1 μm absorption band is pronounced for high metamorphic grades (average absorption band depth of 5.1 ± 0.6%). On the other hand, CO chondrites with low metamorphic grades such as DOM 08006 (3.0) and LAP 031117 (3.05) exhibit virtually no spectral features (Fig. 3). The main minimum is also located at 1050 nm and a second feature at 1300 nm is observed. These features indicate the presence of olivine. The slope of the 1 μm region varies between red, blue and neutrally sloped samples (Table 1, Fig. 3).

For UOCs the 1 μm region has a narrow, deep absorption band. The average 1 μm band depths are 13.3 ± 0.6%, 13.6 ± 0.9% and 14.2 ± 0.8% for H, L and LL, respectively. The 1 μm absorption band is thus more than twice as deep as those observed for carbonaceous chondrites. A slight shift in the average position of the 1 μm feature can be observed between H chondrites (954 nm), L chondrites (957 nm) and LL chondrites (940 nm) (Table 4). A fainter feature around 1300 nm is seen as well. These two features are due to the presence of calcium-rich Fe-bearing pyroxene, which exhibits absorption features around 940 nm, and olivine which has a side band at 1300 nm (Cloutis et al., 2012c). Generally, the 1 μm band area is red sloped with the exception of LL samples ALH 76004 and LAR 06469. These two samples exhibit neutrally to blue 1 μm slopes.

For CR chondrites, the 1 μm region shows a narrow absorption band located at 920 nm. This feature is most likely due to Fe oxy-hydroxides, but can also be associated with low-Fe pyroxene, olivine or Fe-bearing phyllosilicates (Cloutis et al., 2012a). Since the CR chondrites measured in this work experienced strong aqueous alteration it is expected to see hydrated minerals such as oxy-hydroxides as well as phyllosilicates like serpentine, saponite and chlorite. A slight indent at approximately 1050 nm points towards the presence of low-Fe olivine. The average 1 μm band depth of 4.4 ± 0.5% is comparable to that of CO chondrites (Table 2). The 1 μm region is red sloped for all samples (average slope of 93.9 ± 23.7 nm^{-1}).

3.1.3. 2000 nm region absorption feature

For carbonaceous chondrites, the 2 μm region is dominated by contributions of pyroxene and spinel (Cloutis et al., 2012c). At 2400 nm a faint absorption feature observed in previous works by Cloutis et al. (2012c) was attributed to the presence of fassaite.

For the CV chondrites analyzed in this work, the 2 μm absorption band shows a minimum at 1950 nm (dash-dotted lines Fig. 2). Grosnaja (CV_{OxB}) and GRO 95652 (CV_{Red}) exhibit a 2 μm position at much longer wavelengths. This is due to the very shallow 2 μm absorption feature seen for these chondrites which makes the band position determination imprecise (Fig. 2). The average 2 μm band depths are 4.9 ± 0.5%, 3.0 ± 0.5% and 2.7 ± 0.4% for CV_{OxA}, CV_{OxB} and CV_{Red}, respectively (Table 1). Therefore, the 1 μm and 2 μm bands show similar depths for the CV chondrites considered here (see Section 3.1.2). For CV_{OxA} the tilt of the spectra in the 2 μm region is variable: from blue sloped for QUE 94688 (−99.7 ± 9.4 nm^{-1}), to neutrally sloped for LAP 02206 (1.0 ± 8.0 nm^{-1}), and red sloped for Allende (25.4 ± 14.6 nm^{-1}) (Table 1 and Fig. 2a). On average CV_{OxA} are blue sloped (−18.4 ± 13.5 nm^{-1}). The tilt in the 2 μm range of CV_{OxB} and CV_{Red} samples is also variable. On average CV_{OxB} and CV_{Red} are neutrally sloped (4.6 ± 7.8 nm^{-1} and −4.1 ± 7.3 nm^{-1}, respectively). For CO chondrites, the 2 μm region shows a feature at 1850 nm pointing towards the presence of low-Ca pyroxene but spinel could contribute as well (Cloutis et al., 2012b). A feature at 2400 nm is also observed. The 2 μm band is slightly less deep than the 1 μm band showing an average depth of 3.8 ± 0.5%. This band depth is comparable to the other carbonaceous chondrite groups. The spectral slope in the 2 μm range is variable as well, ranging from red to blue sloped samples (Table 1). On average the slope is −10.1 ± 14.5 nm^{-1}

For UOCs, the 2 μm feature generally is much broader and shallower than the 1 μm feature. It is located around 1900 nm (Fig. 4) and shows an average depth of 9.8 ± 1.3%, 9.3 ± 0.9% and 9.3 ± 1.6% for H, L and LL types, respectively (Table 4). A faint feature at 2400 nm is seen. The slope in the 2 μm range is predominantly red sloped for all UOC types. The exceptions are L chondrites ALH 83008 (−0.1 ± 2.3 nm^{-1}) and MIL 05076 (−2.3 ± 8.7 nm^{-1}), LL chondrite ALH 76004 (−4.7 ± 5.2 nm^{-1}), and H chondrites EET 83248 (3.9 ± 3.7 nm^{-1}) and WIS 91627 (−9.9 ± 2.6 nm^{-1}) which are neutral to blue sloped (Table 3 and Fig. 4). On average the slopes are 44.5 ± 11.2 nm^{-1}, 51.9 ± 11.3 nm^{-1} and 59.6 ± 18 nm^{-1}) for H, L and LL types, respectively.

The 2 μm region of CR chondrites is rather broad and shows several smaller absorption features. At 1950 nm a feature due to low-Fe pyroxene is observed in all spectra. An additional feature is seen at approximately 2440 nm (Fig. 5). There are several contributions of phyllosilicates between 2310 nm and 2380 nm such as serpentine, saponite and chlorite, which could possibly explain this absorption band. The 2 μm band is generally less pronounced than the 1 μm band with an average band depth of 1.8 ± 0.1% (Table 2). The spectral tilt in this region is red sloped (average slope of 42.0 ± 15.6 nm^{-1}).

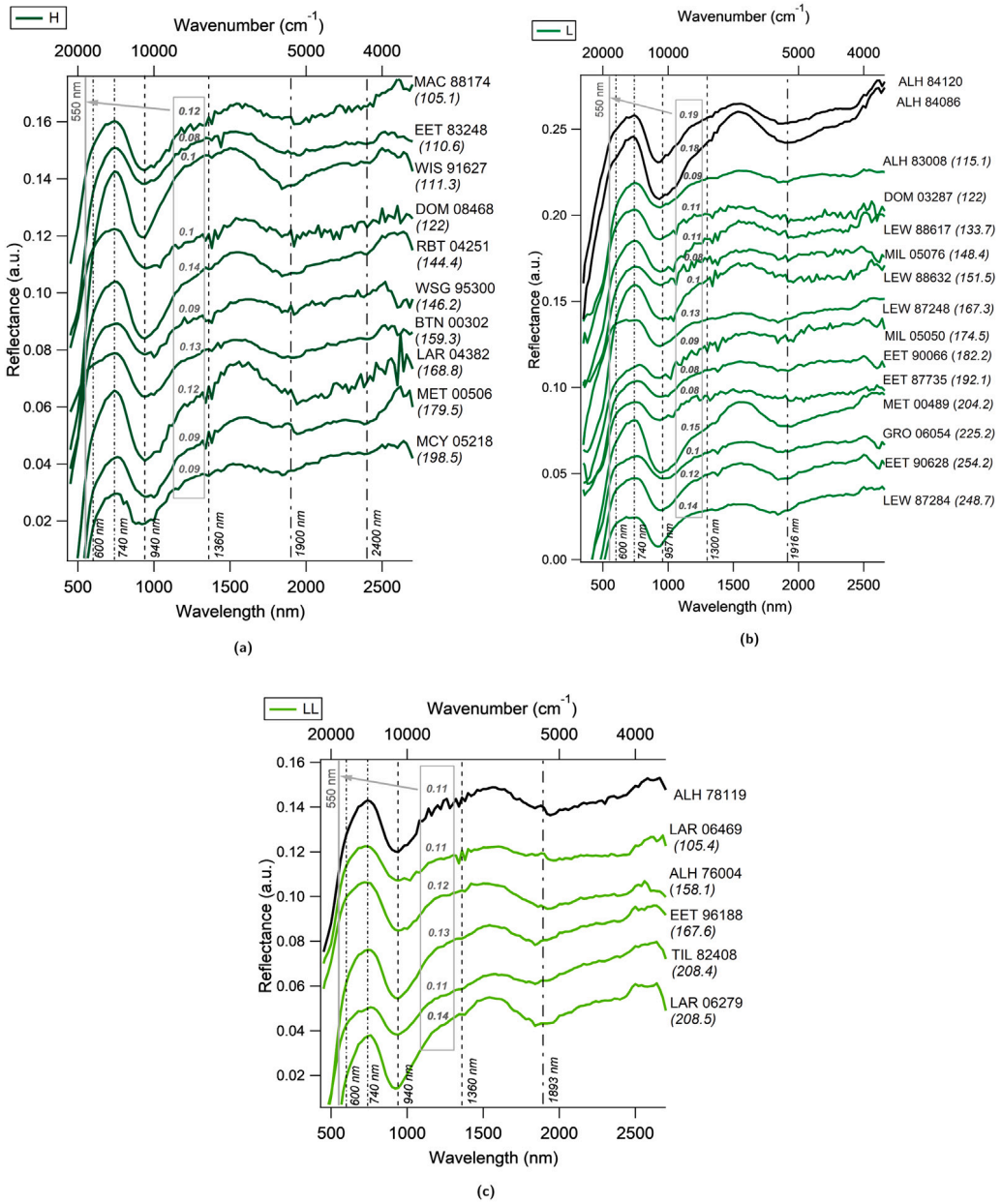

Fig. 4. Reflectance spectra obtained for (a) H (b) L and (c) LL UOCs. Spectra are shown between 350 nm and 2660 nm and are plotted with an vertical offset, for better visibility. The reflectance value at 550 nm for each spectrum is given in the gray box. They are sorted by metamorphic grade with metamorphic grades increasing from bottom to top as indicated by the $FWHM_D$ (cm^{-1}) values (Bonal et al., 2016) given in parenthesis behind each sample name. The dotted lines indicate the position of the peak reflectance values in the visible wavelength range. The dashed lines indicate the position of the olivine absorption features in the 1 μm spectral region. The dash-dotted line indicate pyroxene absorption feature in the 2 μm region. Two of the L type UOC measured were not provided with $FWHM_D$ values by Bonal et al. (2016). They are plotted in black. (For interpretation of the references to color in this figure legend, the reader is referred to the web version of this article.)

3.1.4. Overall spectral slope and visual slope

For CV chondrites, the overall spectral slope is variable between sub-groups. Generally, the overall spectral slopes of CV_{OxA} are red to neutrally sloped. In contrast the overall spectral slope of CV_{OxB} are blue sloped and those of CV_{Red} are neutrally to red sloped. Some exceptions to these trends can be observed. The spectra of ALH 81003 (CV_{OxA}) and QUE 94688 (CV_{OxA}) exhibit a blue slope (Fig. 2). The spectrum of Mokoia is characterized by a strong red overall spectral slope (Fig. 2b). This could be related to terrestrial weathering (Section 4.2.2). While the terrestrial weathering degree of the hand-specimen of ALH 81003 and QUE 94688 is moderate (Grossman (1998) and Grossman (1994), respectively), a whitish/greyish color could be noted during the preparation of our allocated samples. This coloration is usually a sign of terrestrial weathering. The visual slope in the 360 nm to 600 nm region reaches an average value of $(18.1 \pm 2.6) \cdot 10^{-5}$ nm^{-1} for CV_{OxA}, $(8.3 \pm 2.1) \cdot 10^{-5}$ nm^{-1} for CV_{OxB} and $(16.7 \pm 1.8) \cdot 10^{-5}$ nm^{-1} for CV_{Red} (Table 1). The steepness of the visual slope decreases in the order CV_{OxA} to CV_{Red} to CV_{OxB}.

For CO chondrites, the overall spectra are generally neutrally sloped with the exception of the samples Moss, Kainsaz and MIL 05104 which show red slopes (Fig. 3). On average, the visual slope reaches $(24.9 \pm 3.9) \cdot 10^{-5}$ nm^{-1}. This value is comparable to the average visual slope determined for CV_{OxA} chondrites (Table 1).

All UOCs have a red overall spectral slope (Fig. 4). The visual slope reaches average values of $(29.9 \pm 3.2) \cdot 10^{-5}$ nm for H, $(34.6 \pm 1.9) \cdot 10^{-5}$ nm for L and $(36.6 \pm 3.5) \cdot 10^{-5}$ nm for LL (Table 3). Thus, UOCs exhibit much steeper visual slopes than carbonaceous chondrites (Tables 1 vs. 3).

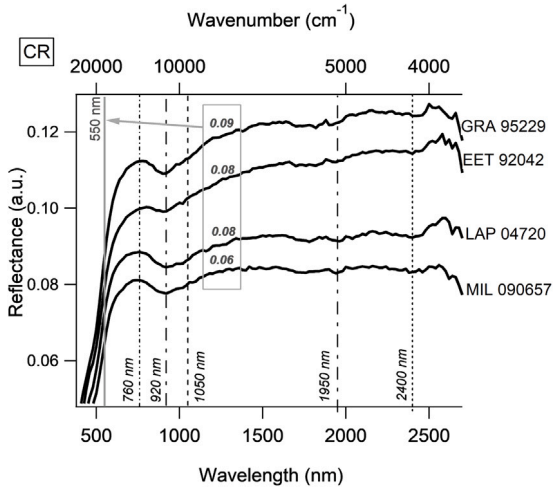

Fig. 5. Reflectance spectra obtained for CRs. Spectra are shown between 360 nm and 2600 nm and are plotted with an vertical offset, for better visibility. The reflectance value at 550 nm for each spectrum is given in the gray box. The dotted lines indicate the position of the peak reflectance values in the visible wavelength range. The dashed lines indicate the position of the olivine absorption features in the 1 μm spectral region. The dash-dotted line indicate pyroxene absorption feature in the 1 μm and 2 μm region.

Lastly, CR chondrites have an red overall spectral slope (Fig. 5). The visual slope of the samples has an average value of $(25.9 \pm 2.1) \cdot 10^{-5}$ nm^{-1} and, thus, is comparable to the average value for carbonaceous chondrites.

3.2. 3 μm region absorption band

Hydration of chondrites takes place on the asteroidal parent body through aqueous alteration and may occur through terrestrial weathering as well. These processes lead to previously non-hydrated minerals becoming hydrated as well as OH and H_2O being stored in the form of interlayer and adsorbed water. In the reflectance spectra this hydration becomes visible as a convolution of three bands in the 3 μm region. At ~2700 nm a band due the vibrational stretching modes of strongly bound OH is observed. Convoluted with this are two bands due to the vibrational stretching modes of adsorbed water at ~2900 nm and of strongly bound (interlayer) H_2O at ~3100 nm (Bishop et al., 1994; Frost et al., 2000). The shape, position and intensity of the 3 μm band is dependent on the extent of hydration as well as the chemical composition of the chondrites (Bishop et al., 1994; Pommerol and Schmitt, 2008).

To characterize the 3 μm band, the position as well as the IBD_{Hyd} are determined (Tables 1, 3). The few samples that were measured at ambient temperature include a contribution due to water adsorption that takes place during the storage of the samples. The IBD_{Hyd} of COs ALH 83108, EET 92126, MET 00737, MIL 05104, MIL 07687, MIL 07709, Moss, Kainsaz, LAP 031117, QUE 97416, ALH 85003 and DOM 03238 (Table 1) and UOCs ALH 83008, ALH 84087 and ALH 84120 are, thus, less comparable to the rest of our sample set.

A pronounced hydration band is visible for most samples (Figs. 6–8). CVs LAP 02206, Mokoia, MET 01074 and the UOC BTN 00302 are the exceptions showing only faint hydration bands. Generally, the shape of the bands are asymmetric with a minimum located between 2900 nm and 3000 nm. Indeed, within the CV sub-groups, the band minimum is located at approximately 2933 nm for CV_{OxA}, while for CV_{OxB} and CV_{Red} it is closer to 2967 nm and 2927 nm, respectively (Table 1 and Fig. 6). For the calculation of the average minimum position of CV_{OxB}, samples MET 01074 and Mokoia were excluded since their shallow hydration band made the determination of the minimum difficult. For CO chondrites, the average hydration band minimum is located at approximately 2935 nm (Table 1 and Fig. 7). For UOCs, it is located at ~2908 nm for H and is shifted to longer wavelength closer to 2913 nm and 2917 nm for L and LL, respectively (Table 3 and Fig. 8). Lastly, for CR chondrites the average minimum position is located closer to 2930 nm (Table 1 and Fig. 9). On average, the IBD_{Hyd} decreases from CV_{Red} to CV_{Ox} (CV_{Red}: 9.9 ± 1.3%, CV_{OxB}: 9.3 ± 2.0%, CV_{OxA}: 9.7 ± 2.1%).

Out of the 15 CO samples that were measured in this work, only 4 were heated to 80 °C. This heating process will eliminate adsorbed water and can, therefore, lead to a change of the IBD_{Hyd} value. In the following we only consider the four heated samples for the analysis of the hydration band area. The average hydration area of COs is 9.7 ± 1.3% (Table 1) making them similarly hydrated to the CVs considered in this work.

The common belief in the literature seems to be that UOCs are little to not hydrated with some exceptions (e.g. Semarkona and Inman) (e.g. Brearley (2003), Grossman et al. (2000) and Quirico et al. (2003)). In contrast, UOCs measured in this work surprisingly all exhibit well distinct hydration bands (Fig. 8). In fact, when comparing the average hydration area of UOCs (11.6 ± 2.1% for H, 12.3 ± 1.3% for L and 13.9 ± 1.1% for LL) with those of the CV and CO chondrites, UOCs exhibit slightly higher IBD_{Hyd} values.

For CR chondrites the 3 μm absorption band is especially pronounced, exhibiting an average IBD_{Hyd} value of 19.1 ± 1.0%. This value exceeds that of all type 3 chondrites considered in this work, consistently with their post accretion history (Krot et al., 2014). Additionally, Fe oxyhydroxides due to terrestrial weathering might contribute to the 3 μm band (Cloutis et al., 2012a).

3.3. Aliphatic bands

Since organics are systematically present in primitive chondrites (Alexander et al., 2017; Scott and Krot, 2014), we expect to see two further absorption features positioned between ~3400 nm and ~3500 nm. However, only CVs Axtell, MIL 091010, GRA 06101, Grosnaja, MET 01074, Mokoia, Efremovka and MIL 07277, COs MIL 05104, Kainsaz, Moss, QUE 97416, EET 92126, ALH 83108, ALH 85003 and MET 00737 and UOCs WIS 91627, RBT 04251, MCY 05218, EET 96188, LAR 06279, ALH 84120, ALH 84086, MET 00489 and LEW 87284 show well pronounced aliphatic bands. All other samples considered in this work exhibit either no or only very faint organic bands. There are some possible explanations for the varying abundances of organics in chondrites. For one, the abundance of organics decreases with increasing metamorphic grade. Furthermore, all organics are contained in the matrix material of the chondrites. Therefore, varying abundances of matrix material will lead to a variation in aliphatic band intensities. Nevertheless, no correlation between the presence of aliphatic bands and the metamorphic grade can be observed for the samples in this work (Figs. 6–9). Furthermore, the abundance of matrix material for some of the CV chondrites considered in this work can be found in Bonal et al. (2020). The aliphatic band intensity does not seem to be correlated to the matrix abundance either. It is, thus, not understood yet why organics are only present in some of the spectra.

4. Discussion

Our objectives are to (i) evaluate spectral variability between chondrite groups, (ii) determine whether post-accretion processes can be assessed based on reflectance spectra and (iii) investigate the link between chondrites and their possible parent asteroid.

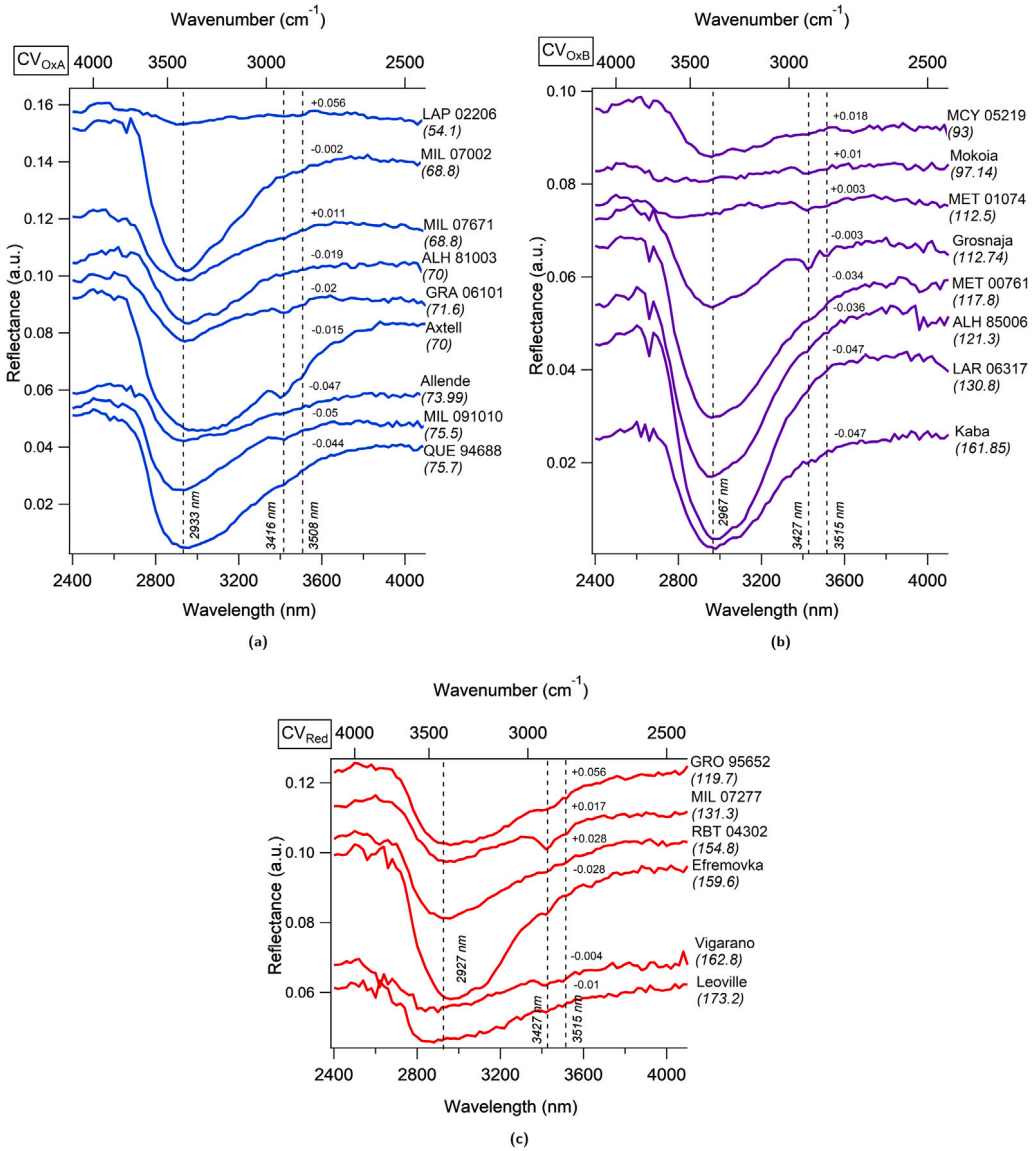

Fig. 6. Reflectance spectra obtained for (a) CV_{OxA} (b) CV_{OxB} and (c) CV_{Red}. Spectra are shown between 2600 nm and 4000 nm and are plotted with an vertical offset, indicated by the $(+/-x)$ values, for better visibility. They are sorted by metamorphic grade with metamorphic grades increasing from bottom to top as indicated by the $FWHM_D$ (cm^{-1}) values (Bonal et al., 2016) given in parenthesis behind each sample name. The dotted lines indicate the position of the 3 µm band minimum as well as the position of aliphatic bands.

4.1. Reflectance spectra as a tool to investigate the hydration of chondrites

As mentioned before, the 3 µm band is related to the stretching and anti-stretching modes of metal-OH as well as bound H_2O and adsorbed water. We, thus, expect the IBD_{Hyd} to reflect the hydration of the observed asteroids. To verify its suitability as a thin tracer for the hydration of asteroids, we consider the IBD_{Hyd} series of CV chondrites, for which the hydration has been independently evaluated through Thermogravimetric Analysis (TGA) (Bonal et al., 2020).

A correlation can be observed ($r^2 = 0.5879$) (Fig. 10) between the IBD_{Hyd} and the total mass loss between 80 °C and 900 °C. Generally, the CV_{OxA} considered in this work are less hydrated than CV_{OxB} and CV_{Red} with the exception of samples Axtell, QUE 94688 and MIL 091010 (Fig. 10). These three samples were previously identified as weathered samples (Bonal et al. (2020) and references within) which could explain their increased hydration. Axtell shows a larger IBD_{Hyd} than the trend would suggest. TGA and reflectance measurements were performed on different days and using different pieces of the same sample. Therefore, this could be an effect of sample heterogeneity.

The TGA measurements are based on the dehydration and dehydroxylation of (oxy)-hydroxides and phyllosilicates but also include contributions due to the decomposition of iron sulfides (Garenne et al., 2016). These iron sulfides cannot be distinguished from the hydrated minerals. The IBD_{Hyd} value determined by reflectance spectroscopy on the other hand only includes contributions due to hydrated minerals. Therefore, we expect this to influence the correlation between the IBD_{Hyd} and the TGA mass loss. We conclude that the IBD_{Hyd} of the 3 µm band is a qualitative tracer of the asteroids hydration.

4.2. Thermal metamorphism effects on reflectance spectra

As discussed in Sections 1 and 2.3 the spectra of carbonaceous chondrites and UOCs exhibit two strong absorption features in the 1 µm and 2 µm region due to the presence of Fe-bearing silicates. The exact mineralogy of these silicates will vary between chondrite groups. Since chondrules are the dominant petrographic component in CVs, COs, CRs and UOCs, the spectra are most likely controlled by their chemistry. Furthermore, the mineralogy of the chondrites can vary within a chondrite group depending on the degree of secondary processes. Thus, by

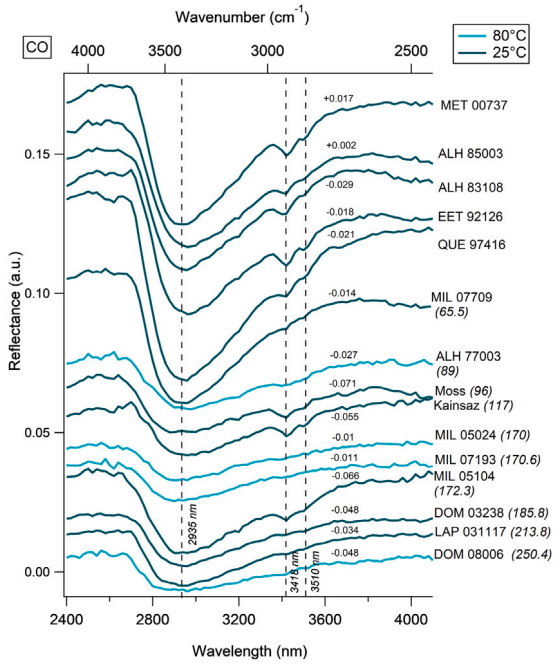

Fig. 7. Reflectance spectra obtained for COs. Spectra are shown between 2600 nm and 4000 nm and are plotted with an vertical offset, indicated by the $(+/-x)$ values, for better visibility. They are sorted by metamorphic grade with metamorphic grades increasing from bottom to top as indicated by the $FWHM_D$ (cm^{-1}) values (Bonal et al., 2016) given in parenthesis behind each sample name. The dotted lines indicate the position of the 3 μm band minimum as well as the position of aliphatic bands. Five of the samples were not provided with metamorphic grade values by Bonal et al. (2016). Samples in dark blue were measured at 80 °C while samples in light blue were measured at ambient temperatures. (For interpretation of the references to color in this figure legend, the reader is referred to the web version of this article.)

comparing these two spectral features with a quantitative parameter reflecting the thermal history of the samples (Bonal et al., 2016) the objective is to find out if and in what way the spectral features reflect the asteroids thermal history.

4.2.1. 1 μm and 2 μm absorption bands

The 1 μm band depth is correlated to the abundance of olivine in chondrites (see references in introduction). Furthermore, the abundance of iron in olivine increases with increasing metamorphic grade (McSween, 1977a). We, therefore, expect the 1 μm band depth to increase with increasing metamorphic grade if the dominant silicate in this region is olivine (Fig. 11). Indeed, this can be observed for CV chondrites (Fig. 11a, $r^2 = 0.711$). Samples QUE 94688 and Axtell are the exceptions showing deeper 1 μm bands than the trend would suggest. This might be related to the presence of oxy-hydroxides formed through terrestrial weathering. For UOCs and COs this trend is not seen (Fig. 11a). The dominant silicate contributing to the 1 μm region of UOCs is pyroxene (Gaffey, 1976). Thus, for UOCs the increase in olivine abundance does not affect the 1 μm band depth as strongly as for carbonaceous chondrites. The absence of the trend within the considered CO chondrites might be explained by their metamorphic grades which are systematically lower than those of the considered CV chondrites (most COs considered here are indeed characterized by larger $FWHM_D$ values than CVs (Fig. 11a)). Moreover, samples with the lowest metamorphic grades (DOM 08006, LAP 031117, DOM 03238, MIL 05104, MIL 07193 and MIL 05024) exhibit practically no absorption features (Fig. 3). Perhaps it is only above a given metamorphic temperature that sufficient chemical modification of olivine (McSween, 1977b) occurs resulting in significant spectral changes. Hence, low metamorphosed CO samples do not follow the trend defined by CV chondrites (Fig. 11a).

The 2 μm band is dominated by contributions of pyroxene and spinel at around 1900 nm (see references in introduction). Since spinel is mainly contained within the Calcium–Aluminum-Rich inclusions (CAIs) (e.g. MacPherson (2003)), we expect a variation of the spinel band depth as well as the spectral slope in the 2 μm area with varying CAI abundances. The volume percent of CAIs contained in the different chondrite groups decreases in the order: CV chondrites (3 vol.%), CO chondrites (1 vol.%), CR chondrites (0.12 vol%), H chondrites (0.01–0.2 vol.%), L chondrites (<0.1 vol.%) and LL chondrites (<0.1 vol.%) (Scott and Krot, 2014). Therefore, we expect that the 2 μm region is dominated by pyroxene for CAI-poor groups such as CR, H, L and LL. For higher CAI abundances (i.e. CV and CO) we expect spinel to play a significant role in the 2 μm band. Moreover, the thermal metamorphism process leads to the chemical equilibration of the chondrite components. The transfer of chemical elements which are present in the matrix material, such as iron, to chondrite components, such as chondrules, results in an increase in band depths. However, no correlation between the 2 μm band depth and the metamorphic grade can be observed for the chondrites measured in the present work (Fig. 11b). The UOCs and COs considered here show low metamorphic grades. Furthermore, pyroxene equilibrates at even higher temperatures than olivine (Scott and Jones, 1990). Perhaps the metamorphic temperature of the chondrites considered in this work was not sufficiently high for the equilibration of pyroxene to take place. Moreover, the high CAI abundance in COs and CVs could lead to a significant spinel band in the 2 μm region overlaying with the pyroxene band. Taken all together, this could explain why there is no correlation observed between the 2 μm band and the metamorphic grade.

4.2.2. Spectral slopes

A negative trend between the 2 μm spectral slope and the metamorphic grade of the chondrites is observed (Fig. 12c). The least metamorphosed UOCs and COs show positive to neutrally sloped spectra in the 2 μm region (slopes between 0 and 1.28×10^{-5} nm^{-1}). The higher metamorphosed CVs, on the other hand, show predominantly negative 2 μm slopes (slopes varying from -0.99×10^{-5} nm^{-1} to 0.31×10^{-5} nm^{-1}). As explained above, we expect the 2 μm spectral slope to become bluer with higher CAI content and thus with increased Fe content in spinel. This can be a further explanation for the differences in spectral slope between chondrite groups. As the abundance of CAIs decreases from CVs to COs to UOCs we expect the 2 μm slope to become bluer from UOCs to COs to CVs.

It was suggested before that the overall spectral slope can be influenced by the terrestrial weathering experienced by the samples (Cloutis et al., 2012c; Salisbury et al., 1974). This could explain why Axtell (CV_{OxA}) and QUE 94688 (CV_{OxA}) are falling off the trend, showing strong blue 2 μm slopes (Fig. 12c). Furthermore, it was suggested that "falls" are redder sloped than "finds" since terrestrial weathering did not affect them as intensely (Cloutis et al., 2012c). The falls Allende, Mokoia, Kainsaz and Moss, indeed, show redder overall spectral slope in comparison to the "finds" (Figs. 2 and 3). However, this is not the case for falls Kaba, Grosnaja and Vigarano which stands in disagreement with the previous suggestions (Cloutis et al., 2012c). The UV absorption at wavelengths shorter than 500 nm, due to iron in silicates and oxidized iron, are reflected in the visual slope. Indeed, steeper visual slopes indicate stronger absorption in the UV range, while more shallow visual slopes point towards more shallow UV absorption bands. COs show a correlation between the visual slope and metamorphic grade of the samples (Fig. 12b, $r^2 = 0.586$). This indicates an increase of iron abundance in silicates and/or oxidized iron abundance with increasing metamorphic grade. On the other hand, for CVs and UOCs no trend can be observed (Fig. 12a).

As mentioned before, 5 of the 15 COs considered in this work (ALH 85003, ALH 83108, EET 92126, MET 00737 and QUE 97416) could previously not be provided with a $FWHM_D$ value (Bonal et al., 2016). Their deep spectral features point towards a strong metamorphic grade.

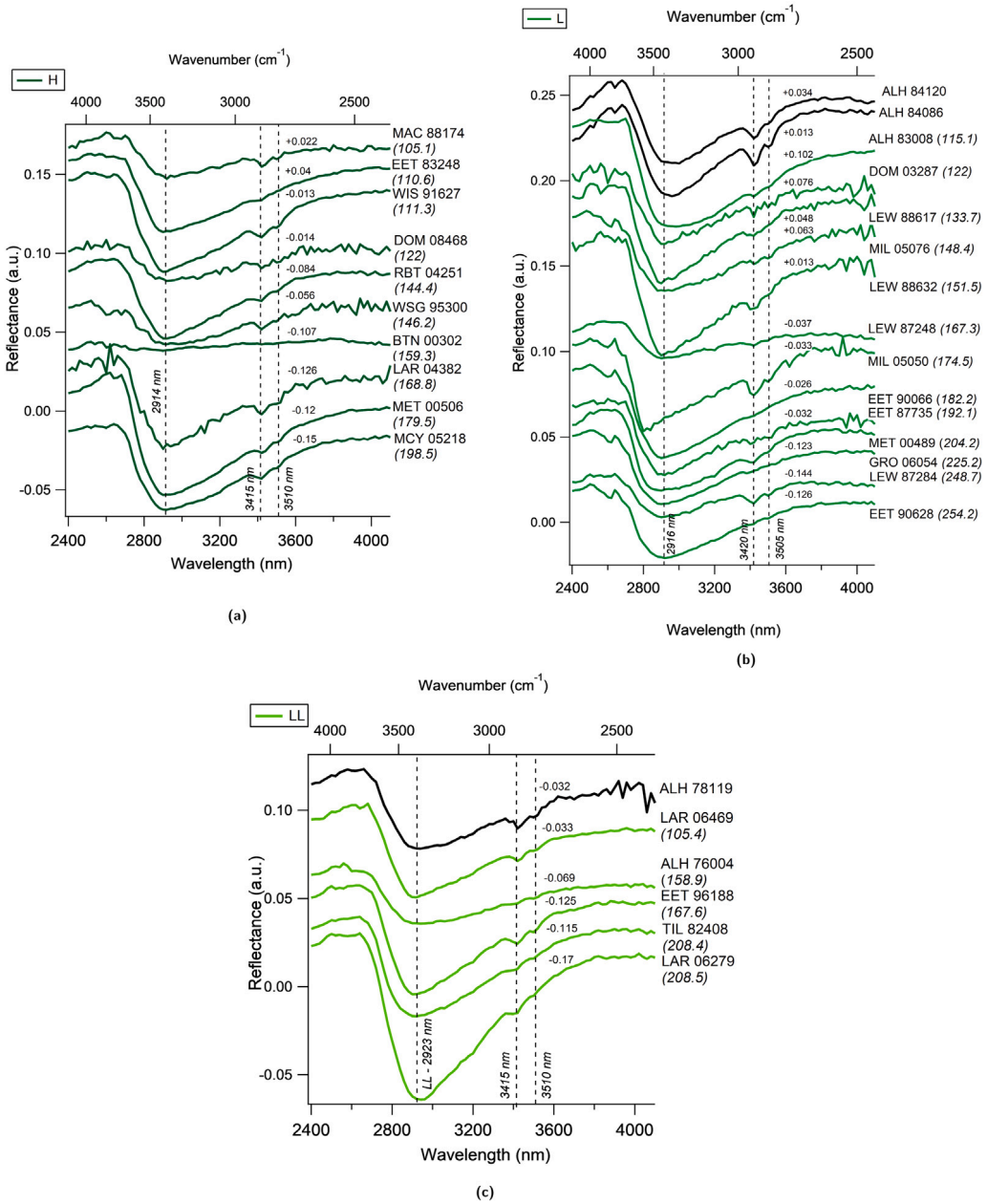

Fig. 8. Reflectance spectra obtained for (a) H (b) L and (c) LL UOCs. Spectra are shown between 2600 nm and 4000 nm and are plotted with an vertical offset, indicated by the $(+/-x)$ values, for better visibility. They are sorted by metamorphic grade with metamorphic grades increasing from bottom to top as indicated by the $FWHM_D$ (cm^{-1}) values (Bonal et al., 2016) given in parenthesis behind each sample name. The dotted lines indicate the position of the 3 μm band minimum as well as the position of aliphatic bands. Samples which were not provided with $FWHM_D$ (cm^{-1}) values by Bonal et al. (2016) are plotted in black. (For interpretation of the references to color in this figure legend, the reader is referred to the web version of this article.)

To support this suggestion, the visual slope is compared with the 1 μm band depth (Fig. 12d). Three main groupings can be observed. UOCs are clearly separated from carbonaceous chondrites by exhibiting deeper 1 μm bands and slightly steeper visual slopes (Fig. 12d). Furthermore, a small group of CO chondrites can be observed which exhibit stronger visual slopes than the other carbonaceous chondrites. These samples are the 5 COs EET 92126, QUE 97416, ALH 85003, MET 00737 and ALH 83108 previously not provided with $FWHM_D$ values. Indeed, the strong iron abundances in silicates and/or oxidized iron abundances point towards high metamorphic grades in these 5 CO chondrites.

4.3. Finding asteroidal parent bodies

Several possible links between carbonaceous chondrites and asteroidal parent bodies have been suggested in the past which are not always coherent with each other. (Bell et al., 1988) suggest K-type asteroids (Eos family) as a possible parent asteroid of CV and CO chondrites. CO, CK, CV and CR chondrites were suggested to be related to K-type asteroids (Vernazza et al., 2015). C-type asteroids were suggested as possible parent bodies for CK chondrites (Gaffey and McCord, 1978) and CR chondrites (Hiroi et al., 1996). This shows, that it is challenging to unambiguously identify the parent body of a meteorite based solely on remote spectroscopic data. Since the return of asteroid samples with the Hayabusa 1 space mission (Nakamura et al., 2011) the link between S-type asteroids and EOCs is confirmed. This information can be used to validate the method we chose for the asteroidal parent body search of carbonaceous chondrites. This will be further discussed in Sections 4.3.3 and 4.3.4.

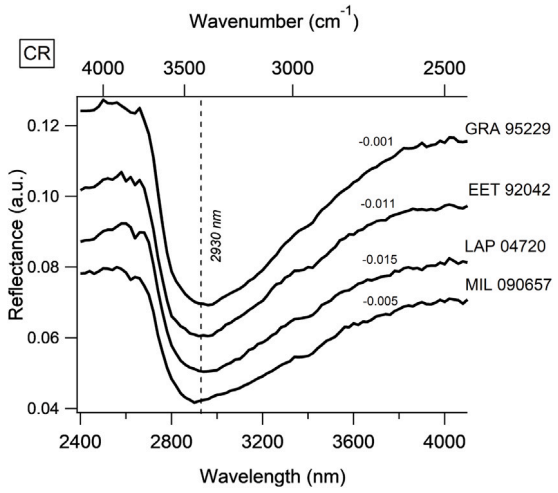

Fig. 9. Reflectance spectra obtained for CRs. Spectra are shown between 2600 nm and 4000 nm and are plotted with an vertical offset, indicated by the $(+/-x)$ values, for better visibility. The dotted line indicates the position of the 3 µm band minimum.

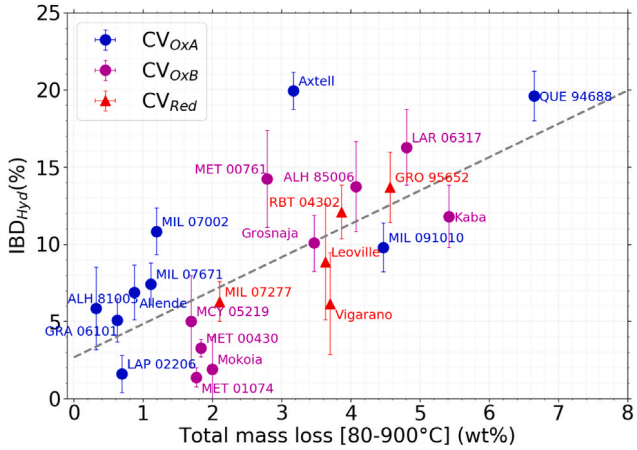

Fig. 10. IBD_{Hyd} over the total mass loss measured by TGA. Reflectance spectra were measured on the bulk material at 80 °C and under vacuum. TGA measurements were done in the 80 °C to 900 °C range.

4.3.1. Chosen spectral parameters for asteroid–chondrite comparison

Spectral slopes and reflectance have been used in the past to compare meteorites and asteroids observations. However, the overall spectral slope is influenced by a lot of external factors such as measuring geometry, grain size or weathering degree. Indeed, Salisbury et al. (1974) showed that when artificially weathering a L6 chondrite, the spectral slope becomes steeper while the 1 µm region remains unchanged. Because they are exposed to the space environment, asteroid surfaces can experience specific processes described as space weathering (SW). For silicate-rich (S-type) asteroids SW leads to the reddening and darkening of the spectra (Marchi et al., 2005). For carbonaceous asteroid (C-Type) large advances have been made in the last few years to understand SW effects (e.g. Brunetto et al. (2015, 2020), Lantz et al. (2013) and Matsuoka et al. (2020)), in particular in the framework of the Hayabusa-2 and Osiris-REx sample-return missions. From ion- or laser-irradiation experiments, spectral reddening was observed for some CV, CO and CM samples (Brunetto et al., 2014; Lazzarin et al., 2006; Moroz et al., 1996). For Tagish Lake, an ungrouped CC, spectral flattening was observed (Vernazza et al., 2013). For Murchison (CM), spectral flattening, darkening and decrease of the 0.7 µm and 3 µm was observed (Matsuoka et al., 2020). In their study, Lantz et al. (2017) showed complex behaviors for carbonaceous chondrites, with dark samples revealing a bluing, and brighter sample showing reddening with increasing irradiation dose. There are still several open questions regarding the effects of SW on the spectra of dark objects. How does it effect other CC-groups (e.g. CK or CR)? Is there a connection between different petrographic types of CV, CO or CR and the amount of SW experienced on their asteroidal parent bodies? What is the dependency of SW signatures on petrographic type of CV, CO or CR? Until these questions can be answered, we restrict the asteroid–meteorite comparison on the 1 µm and 2 µm absorption features, since they seem to be the least affected by SW. Lastly, temperature differences between the measurements done on meteorite and asteroid exist but have a negligible influence on the band positions of the spectra (Dunn et al., 2013), typically below the spectral resolution of the measurement from this study.

As these results show, the 1 µm and 2 µm absorption features appear to be mostly unaffected by processes such as SW, grain size and temperature, making them a promising spectral feature for the identification of parent bodies. Devogèle et al. (2018), for example, suggests a link between L-type asteroids and CAI rich chondrites such as CV and CO chondrites based on a strong spinel absorption feature observed in the asteroid spectra. Similar arguments can be found in Burbine et al. (1992) and Sunshine et al. (2008). Therefore, in this work we base our spectral comparison on the 1 µm and 2 µm absorption features and not on the spectral slopes. The comparisons between asteroid and chondrite features are made in Fig. 13.

4.3.2. Spectral differences between chondrite groups

Our results show that carbonaceous chondrites can generally be distinguished from UOCs by exhibiting much less pronounced spectral features (Figs. 2–4). Between carbonaceous chondrite groups this separation is not as clear. This can make a clear identification of asteroidal parent bodies difficult, since different chondrite groups overlap. This is especially true for CO and CV chondrites. Both groups exhibit similar 1 µm and 2 µm absorption band depths as well as band positions and spectral slopes (Figs. 13a, 13b and 13c). CR chondrites can be clearly separated from CO and CV by showing much lower 1 µm band positions (Fig. 13b). CK chondrites can be distinguished from CO, CV and CR by having deeper 1 µm absorption band depths, similar to those of UOCs. They exhibit less deep 2 µm absorption bands and their band positions are located at longer wavelengths than UOCs (Figs. 13a, 13b and 13c).

4.3.3. S-type asteroids and UOCs

Ordinary chondrites (OCs) are pieces of S-type asteroids as first proposed through reflectance spectroscopy (e.g. Chapman and Salisbury (1973)) and confirmed by the return of the Hayabusa-1 space mission in 2010 (Nakamura et al., 2011). More specifically, the connection was found between EOCs (LL4 to LL6) and S-Type asteroids. In terms of reflectance spectral features, EOCs exhibit stronger absorption features and stronger peak reflectance values in the visible range than UOCs. The 2 µm band positions of UOCs might be shifted slightly towards shorter wavelengths due to lower amounts of Fe in pyroxene.

Our results show, the 1 µm and 2 µm band depth of the S-type asteroid spectrum match those of UOCs (see Fig. 13a). Furthermore, the 1 µm band position is in good agreement with the UOC values (Fig. 13b). As expected, the 2 µm band position of the UOCs is shifted towards lower wavelengths (~1840 nm) in comparison to the S-type asteroid (~1950 nm) (Fig. 13c).

In conclusion, it is possible to identify S-type asteroids as the parent body of UOCs based on the reflectance spectral parameters. This validates our approach.

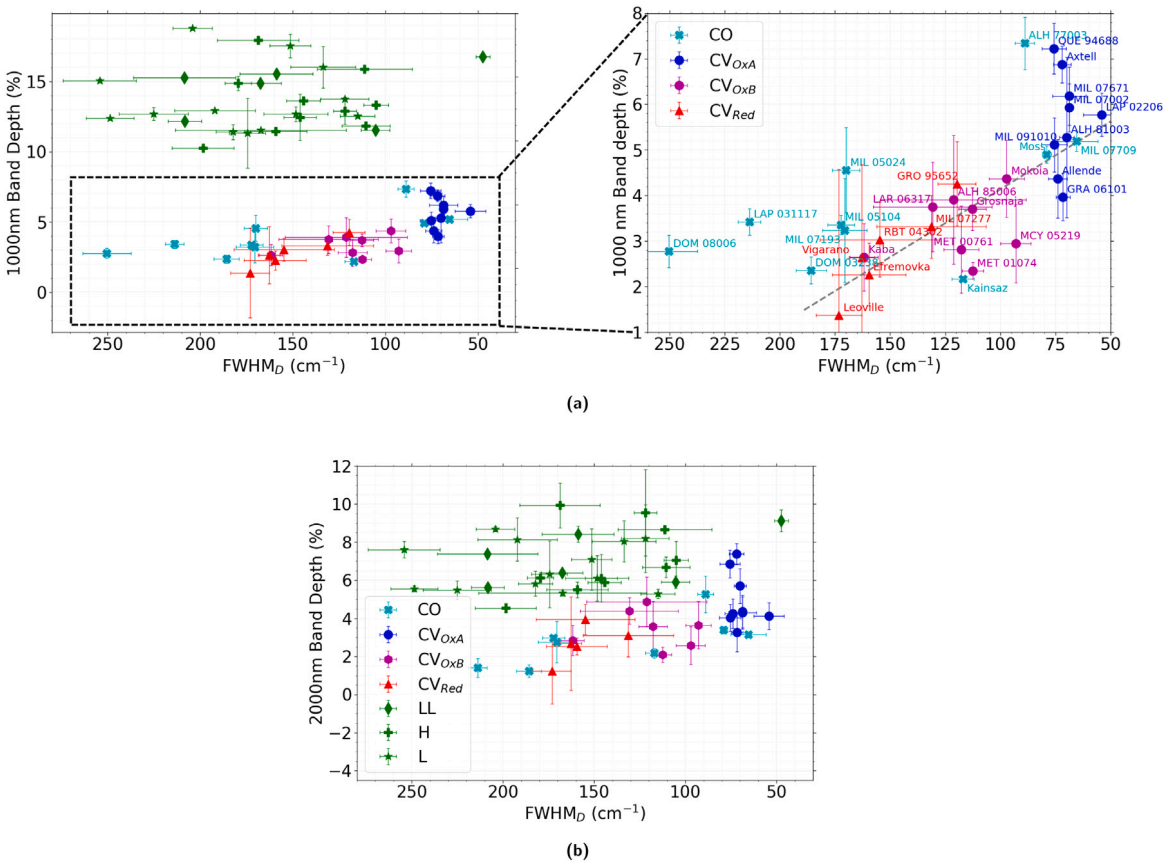

Fig. 11. Comparison between spectral values and the FWHM$_D$ value measured by Raman spectroscopy (Bonal et al., 2016). (a) 1 μm band depth of CVs, COs and UOCs over the FWHM$_D$ value (left) and the same for COs and CVs only (right); (b) 2 μm band depth of CVs, COs and UOCs over the FWHM$_D$ value.

4.3.4. *Carbonaceous chondrite asteroid links*

Taking the difficulties discussed in Sections 4.3.1 and 4.3.2 into account, similarities between asteroid and CC spectra can be analyzed (Figs. 13a, 13b and 13c). Good matches of band depths and positions can be found between L-Type and Cb-Type asteroids and COs and CVs (Fig. 13). The same can be said when comparing Eos spectra with COs and CVs. C, Cg and B-Type asteroids match COs and CVs well in the 1 μm range but do not show any 2 μm feature that could be included in the comparison. As for CVs and COs, CRs show a similar 1 μm and 2 μm band depths as L, Cb and Eos asteroids. The band positions, however, are closer to X, Xe, Xk, Cgh or Ch-Type asteroids (Figs. 13b and 13c). However, none of these asteroid matches show any 2 μm feature that could be included in the comparison. It should also be mentioned here that other criteria such as albedo were not considered in this comparison but can be used to further narrow down possible links between asteroids and meteorites. The albedo of CR chondrites (p_v = 0.15 Piironen et al., 1998) is generally lower than that of high albedo Xe-asteroids (p_v > 0.3 Fornasier et al., 2011) making this affiliation unlikely. A larger set of CR chondrites should be considered as well to increase the statistics of the results. The four CRs analyzed here are finds from Antarctica making the presence of terrestrial weathering products probable. Since CR chondrites are rich in metal and sulfides (Scott and Krot, 2014) these weathering products can have a larger influence on the slope as well as the 1 μm band of the reflectance spectra. For future works it would be interesting to leach these samples, ridding them from the weathering products and repeating the asteroid–meteoroid comparisons. The 1 μm and 2 μm band depths and positions of CK chondrites match those of K-type asteroids (Fig. 13). Due to the faint 2 μm features of the CKs analyzed here, the 2 μm band position values vary over a broad range (Fig. 13c) making matches less clear. Additionally, Eos family asteroids show a similar 1 μm band positions and 2 μm band depths and positions as CKs. The difference in 1 μm band depth might be due to space weathering effects on Eos family asteroids.

We conclude, L-type, Cb-Type and Eos family asteroids match the spectral values of CV and COs in compliance with previous suggestions by Bell et al. (1988) and Devogèle et al. (2018). CR chondrites match the band positions of X, Xe, Xk, Cgh and Ch-type asteroids. Lastly, K-type and/or Eos family asteroids match CK chondrites in compliance with Vernazza et al. (2015).

4.4. 3 μm *band for asteroid–chondrite comparison*

As mentioned before, the 3 μm hydration band is not present in the asteroid spectra used in this work. Shown in Fig. 14 is the 3 μm band depth over the 3 μm band position for the CC measured in this work as well as some CM, CI and Tagish Lake samples from Potin et al. (2020). Additionally, some C-type main belt asteroid (MBA) spectra taken from Usui et al. (2018) are shown. The 3 μm band shows strong spectral variations between and within different CC groups. Furthermore, a good match between the 3 μm band of the C-type asteroids and type 2 CMs as well as possibly Tagish Lake is seen. No match is seen with type 3 CC. To match our type 3 CC spectra we expect asteroid spectra which show a strong 3 μm band at longer wavelengths than those matching CMs. No such asteroid spectra are available yet. We, thus, conclude that the 3 μm band has the potential to be a good tracer for meteorite parent bodies. To further investigate the link between chondrites and their parent asteroids using reflectance spectroscopy we therefore suggest to extend the asteroid spectra, typically acquired in the 450–2450 nm spectral range to the 450–4000 nm spectral range, thus including the 3 μm band.

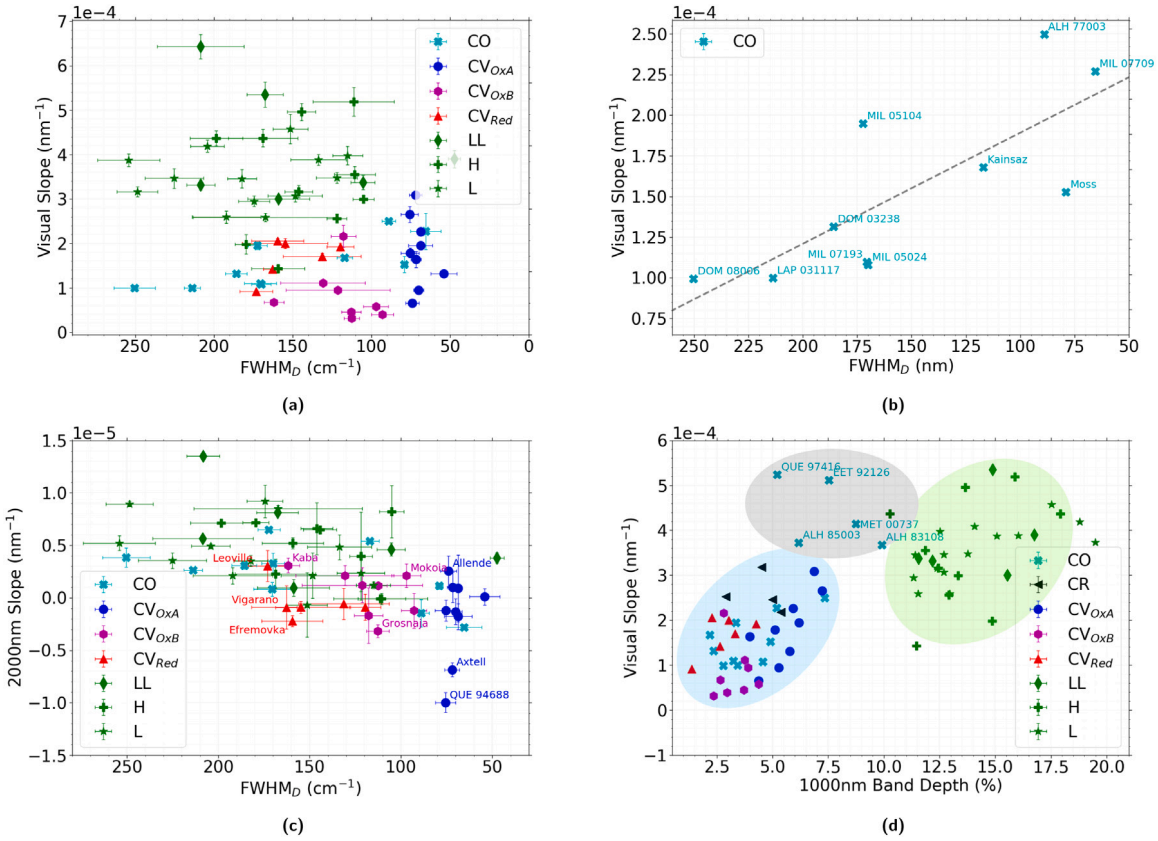

Fig. 12. Comparison between spectral values and the $FWHM_D$ value measured by Raman spectroscopy (Bonal et al., 2016). (a) The visual slope of COs, CVs and UOCs over the $FWHM_D$ value; (b) The visual slope of COs over the $FWHM_D$ value; (c) The 2000 nm slope of COs, CVs and UOCs over the $FWHM_D$ value; (d) The visual slope of all considered chondrites over the 1 μm band depth. (For interpretation of the references to color in this figure legend, the reader is referred to the web version of this article.)

5. Conclusion

To increase our understanding of asteroid reflectance spectral features we acquired reflectance spectra (from 340 nm to 4200 nm) of 23 CV, 15 CO, 4 CR and 31 UOCs. Clear differences in the reflectance spectra of different chondrite groups as well as a large variability between chondrites of the same group were observed. The parameters used for comparing the spectra were the band depth, position and slope in the 1 μm and 2 μm region, the visual slope and peak reflectance in the visible wavelength range and the IBD_{Hyd} as well as location of the 3 μm band. Furthermore, we looked at the overall spectral slope of all the spectra. In comparison to carbonaceous chondrites, UOCs systematically exhibit deeper absorption features which are located at lower wavelengths. Type 2 CR chondrites exhibit absorption features in the 1 μm region at even lower wavelengths than UOCs, thus clearly separating them from type 3 chondrites. On the other hand, none of the considered spectral parameters allow to separate CV and CO chondrites. This is not surprising due to their comparable mineralogical composition (Krot et al., 2014).

Secondly, we investigated the link between these reflectance spectral features and the thermal history of the chondrites. Several spectral features appear to be controlled by the metamorphic grade of the samples. The depth of the 1 μm absorption band becomes deeper with increasing metamorphic grade along the considered series of CV chondrites. This was not observed previously (Cloutis et al., 2012c) which might be related to the significantly greater number of CV chondrites considered in the present work. To be noted, this correlation was not observed for the other chondrite groups. The absence of the trend within the considered CO chondrites might be explained by systematically lower metamorphic grades than those of the considered CV chondrites. Perhaps it is only above a given metamorphic temperature that sufficient chemical modification of olivine (McSween, 1977b) occurs resulting in significant spectral changes. No correlation between the 2 μm absorption feature and the metamorphic grade was observed. For CO chondrites the visual slope becomes steeper with increasing metamorphic grade. This indicated an increase in iron in silicates and/or oxidized iron in the samples with increasing metamorphic grade. The spectral slope in the 2 μm region seems to be negatively correlated to the metamorphic grade for all samples. This indicates a decrease in pyroxene content with increasing peak metamorphic temperature (Cloutis et al., 2012c; Bonal et al., 2016).

Lastly, we investigated the genetic link between asteroids and chondrites based on the reflectance spectral features. The comparison of spectral features of asteroids and chondrites led to a good match between the following types: S-type asteroids have similar 1 μm and 2 μm absorption band depths as UOCs. This is expected (Nakamura et al., 2011), and legitimates our approach. The parent bodies of CK and CV/CO chondrites have previously been suspected to be K-type asteroids, particularly Eos family members (Clark et al., 2009). This genetic affiliation is confirmed by the data we looked at for CK chondrites which exhibit similar 1 μm and 2 μm absorption features as K-type asteroids and similar 1 μm band positions and 2 μm band depths and positions as Eos family members. For CO/CV chondrites the absorption band depths and 1 μm absorption band position match those of the Eos family. However, a match with L-type and Cb-Type asteroids exists as well. This is consistent with previous work (Sunshine et al., 2008; Devogèle et al., 2018) suggesting a link between CAI-rich chondrites and L-type asteroids.

Lastly, we underline the potential of the 3 μm band to constrain asteroid–meteorite links.

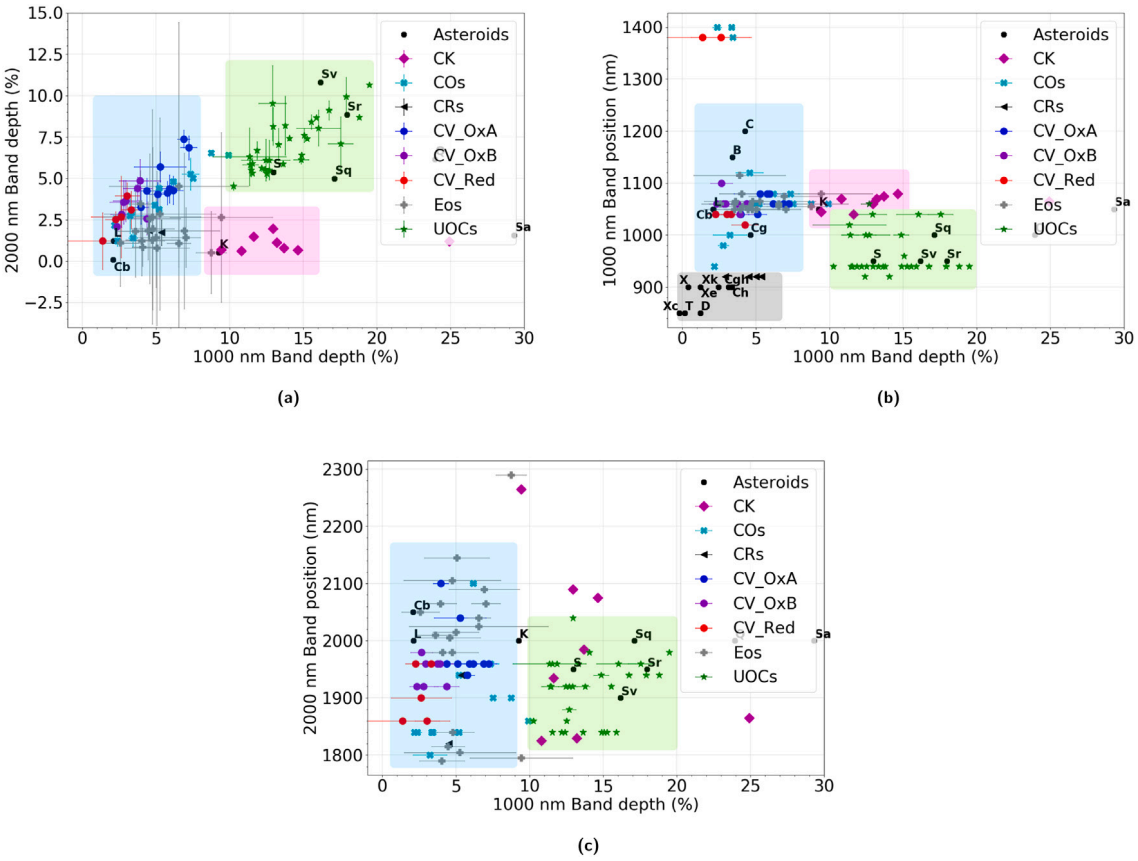

Fig. 13. Comparison between spectral values of asteroids (in black symbols) and chondrites (in colored symbols). (a) Comparison of the 2 μm band depth with the 1 μm band depth of chondrites and asteroids; (b) 1 μm band position over the 1 μm band depth; (c) 2 μm band position over the 1 μm band depth. (For interpretation of the references to color in this figure legend, the reader is referred to the web version of this article.)

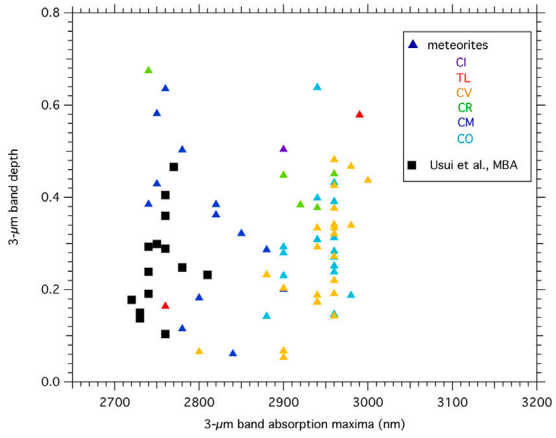

Fig. 14. The 3 μm band depth over the 3 μm band position for carbonaceous chondrites and C-Type main belt asteroids (MBA). All CVs, COs and CRs were taken from this work. The CIs, CMs and Tagish Lake were taken from Potin et al. (2020). Lastly, the C-Type MBA come from Usui et al. (2018).

Acknowledgments

This work has been funded by the Centre National d'Etudes Spatiales (CNES-France) and by the ERC grant SOLARYS ERC-CoG2017-771691

References

Alexander, C., Cody, G., Gregorio, B.D., Nittler, L., Stroud, R., 2017. The nature, origin and modification of insoluble organic matter in chondrites, the major source of Earth's C and N. Geochemistry 77 (2), 227–256. http://dx.doi.org/10.1016/j.chemer.2017.01.007, URL: http://www.sciencedirect.com/science/article/pii/S0009281916301350.

Bell, J.F., Owensby, P.D., Hawke, B.R., Gaffey, M.J., 1988. The 52-color asteroid survey: Final results and interpretation. In: Lunar and Planetary Science Conference, Vol. 19. p. 57.

Bishop, J., Pieters, C., Edwards, J., 1994. Infrared spectroscopic analyses on the nature of water in montmorillonite. Clay Miner 42 (702), URL: http://www.sciencedirect.com/science/article/pii/S0040603199003664, https://doi-org.gaelnomade-1.grenet.fr/10.1346/CCMN.1994.0420606.

Bonal, L., Bourot-Denise, M., Quirico, E., Montagnac, G., Lewin, E., 2007. Organic matter and metamorphic history of CO chondrites. Geochim. Cosmochim. Acta 71 (6), 1605–1623. http://dx.doi.org/10.1016/j.gca.2006.12.014, URL: http://www.sciencedirect.com/science/article/pii/S0016703706022617.

Bonal, L., Gattacceca, J., Garenne, A., Eschrig, J., Rochette, P., Ruggiu, L.K., 2020. Water and heat: New constraints on the evolution of the CV chondrite parent body. Geochim. Cosmochim. Acta 276, 363–383. http://dx.doi.org/10.1016/j.gca.2020.03.009, URL: http://www.sciencedirect.com/science/article/pii/S0016703720301708.

Bonal, L., Quirico, E., Bourot-Denise, M., Montagnac, G., 2006. Determination of the petrologic type of CV3 chondrites by Raman spectroscopy of included organic matter. Geochim. Cosmochim. Acta 70 (7), 1849–1863. http://dx.doi.org/10.1016/j.gca.2005.12.004, URL: http://www.sciencedirect.com/science/article/pii/S0016703705009415.

Bonal, L., Quirico, E., Flandinet, L., Montagnac, G., 2016. Thermal history of type 3 chondrites from the Antarctic meteorite collection determined by Raman spectroscopy of their polyaromatic carbonaceous matter. Geochim. Cosmochim. Acta 189, 312–337. http://dx.doi.org/10.1016/j.gca.2016.06.017.

Brearley, A.J., 2003. Nebular versus parent-body processing. Treatise Geochem. 1, 711. http://dx.doi.org/10.1016/B0-08-043751-6/01068-9.

Brunetto, R., Lantz, C., Ledu, D., Baklouti, D., Barucci, M., Beck, P., Delauche, L., Dionnet, Z., Dumas, P., Duprat, J., Engrand, C., Jamme, F., Oudayer, P., Quirico, E., Sandt, C., Dartois, E., 2014. Ion irradiation of Allende meteorite probed by visible, IR, and Raman spectroscopies. Icarus 237, 278–292. http://dx.doi.org/10.1016/j.icarus.2014.04.047, URL: http://www.sciencedirect.com/science/article/pii/S0019103514002395.

Brunetto, R., Lantz, C., Nakamura, T., Baklouti, D., Pivert-Jolivet, T.L., Kobayashi, S., Borondics, F., 2020. Characterizing irradiated surfaces using IR spectroscopy. Icarus 113722. http://dx.doi.org/10.1016/j.icarus.2020.113722, URL: http://www.sciencedirect.com/science/article/pii/S0019103520301135.

Brunetto, R., Loeffler, M.J., Nesvorný, D., Sasaki, S., Strazzulla, G., 2015. Asteroid surface alteration by space weathering processes. In: Michel, P., DeMeo, F.E., Bottke, W.F. (Eds.), Asteroids IV. pp. 597–616. http://dx.doi.org/10.2458/azu_uapress_9780816532131-ch031.

Burbine, T.H., Gaffey, M.J., Bell, J.F., 1992. S-asteroids 387 aquitania and 980 anacostia: Possible fragments of the breakup of a spinel-bearing parent body with C03/CV3 affinities. Meteoritics 27 (4), 424–434. http://dx.doi.org/10.1111/j.1945-5100.1992.tb00224.x, URL: https://onlinelibrary.wiley.com/doi/abs/10.1111/j.1945-5100.1992.tb00224.x, arXiv:https://onlinelibrary.wiley.com/doi/pdf/10.1111/j.1945-5100.1992.tb00224.x.

Burbine, T.H., McCoy, T.J., Meibom, A., Gladman, B., Keil, K., 2002. Meteoritic parent bodies: Their number and identification. In: Bottke, Jr., W.F., Cellino, A., Paolicchi, P., Binzel, R.P. (Eds.), Asteroids III. pp. 653–667.

Bus, S.J., 1999. Compositional Structure in the Asteroid Belt: Results of a Spectroscopic Survey (Ph.D. thesis). MASSACHUSETTS INSTITUTE OF TECHNOLOGY.

Chapman, C.R., Salisbury, J.W., 1973. Comparisons of meteorite and asteroid spectral reflectivities. Icarus 19 (4), 507–522. http://dx.doi.org/10.1016/0019-1035(73)90078-X, URL: http://www.sciencedirect.com/science/article/pii/001910357390078X.

Clark, R.N., 1999. Spectroscopy of rocks and minerals and principles of spectroscopy. In: Remote Sensing for the Eartb Sciences: Manual of Remote Sensing, Vol. 3.

Clark, B.E., Ockert-Bell, M.E., Cloutis, E.A., Nesvorny, D., Mothé-Diniz, T., Bus, S.J., 2009. Spectroscopy of K-complex asteroids: Parent bodies of carbonaceous meteorites? Icarus 202 (1), 119–133. http://dx.doi.org/10.1016/j.icarus.2009.02.027, URL: http://www.sciencedirect.com/science/article/pii/S0019103509001067.

Cloutis, E., Hudon, P., Hiroi, T., Gaffey, M., 2012a. Spectral reflectance properties of carbonaceous chondrites: 3. CR chondrites. Icarus 217 (1), 389–407. http://dx.doi.org/10.1016/j.icarus.2011.11.004, URL: http://www.sciencedirect.com/science/article/pii/S0019103511004313.

Cloutis, E., Hudon, P., Hiroi, T., Gaffey, M., Mann, P., 2012b. Spectral reflectance properties of carbonaceous chondrites – 5: CO chondrites. Icarus 220 (2), 466–486. http://dx.doi.org/10.1016/j.icarus.2012.05.019, URL: http://www.sciencedirect.com/science/article/pii/S0019103512002011.

Cloutis, E., Hudon, P., Hiroi, T., Gaffey, M., Mann, P., Bell, J., 2012c. Spectral reflectance properties of carbonaceous chondrites: 6. CV chondrites. Icarus 221 (1), 328–358. http://dx.doi.org/10.1016/j.icarus.2012.07.007, URL: http://www.sciencedirect.com/science/article/pii/S0019103512002813.

Crown, D.A., Pieters, C.M., 1987. Spectral properties of plagioclase and pyroxene mixtures and the interpretation of lunar soil spectra. Icarus 72 (3), 492–506. http://dx.doi.org/10.1016/0019-1035(87)90047-9, URL: http://www.sciencedirect.com/science/article/pii/0019103587900479.

DeMeo, F.E., Binzel, R.P., Slivan, S.M., Bus, S.J., 2009. An extension of the Bus asteroid taxonomy into the near-infrared. Icarus 202 (1), 160–180. http://dx.doi.org/10.1016/j.icarus.2009.02.005, URL: http://www.sciencedirect.com/science/article/pii/S0019103509000554.

Devogèle, M., Tanga, P., Cellino, A., Bendjoya, P., Rivet, J.-P., Surdej, J., Vernet, D., Sunshine, J., Bus, S., Abe, L., Bagnulo, S., Borisov, G., Campins, H., Carry, B., Licandro, J., McLean, W., Pinilla-Alonso, N., 2018. New polarimetric and spectroscopic evidence of anomalous enrichment in spinel-bearing calcium-aluminium-rich inclusions among L-type asteroids. Icarus 304, 31–57. http://dx.doi.org/10.1016/j.icarus.2017.12.026, URL: http://www.sciencedirect.com/science/article/pii/S0019103517300271. Asteroids and Space Debris.

Dunn, T.L., Burbine, T.H., Bottke, W.F., Clark, J.P., 2013. Mineralogies and source regions of near-earth asteroids. Icarus 222 (1), 273–282. http://dx.doi.org/10.1016/j.icarus.2012.11.007, URL: http://www.sciencedirect.com/science/article/pii/S0019103512004538.

Eschrig, J., Bonal, L., Beck, P., 2019a. NIR reflectance spectrum ($i = 0°$, $e = 30°$) of bulk CR chondrites under vacuum at $T = 80°$c. http://dx.doi.org/10.26302/SSHADE/EXPERIMENT_LB_20191220_003.

Eschrig, J., Bonal, L., Beck, P., 2019b. NIR reflectance spectrum ($i = 0°$, $e = 30°$) of bulk CV chondrites under vacuum at $T = 80°$c. http://dx.doi.org/10.26302/SSHADE/EXPERIMENT_LB_20191220_001.

Eschrig, J., Bonal, L., Beck, P., 2019c. NIR reflectance spectrum ($i = 0°$, $e = 30°$) of bulk UOC chondrites under vacuum at $T = 80°$c. http://dx.doi.org/10.26302/SSHADE/EXPERIMENT_LB_20191220_004.

Eschrig, J., Bonal, L., Beck, P., Prestgard, T., 2019d. NIR reflectance spectrum ($i = 0°$, $e = 30°$) of bulk CO chondrites under vacuum at $T = 80°$c. http://dx.doi.org/10.26302/SSHADE/EXPERIMENT_LB_20191220_002.

Fornasier, S., Clark, B., Dotto, E., 2011. Spectroscopic survey of X-type asteroids. Icarus 214 (1), 131–146. http://dx.doi.org/10.1016/j.icarus.2011.04.022, URL: http://www.sciencedirect.com/science/article/pii/S0019103511001576.

Frost, R.L., Ruan, H., Kloprogge, J.T., Gates, W., 2000. Dehydration and dehydroxylation of nontronites and ferruginous smectite. Thermochim. Acta 346 (1), 63–72. http://dx.doi.org/10.1016/S0040-6031(99)00366-4, URL: http://www.sciencedirect.com/science/article/pii/S0040603199003664.

Gaffey, M.J., 1976. Spectral reflectance characteristics of the meteorite classes. J. Geophys. Res. (1896-1977) 81 (5), 905–920. http://dx.doi.org/10.1029/JB081i005p00905, URL: https://agupubs.onlinelibrary.wiley.com/doi/abs/10.1029/JB081i005p00905, arXiv:https://agupubs.onlinelibrary.wiley.com/doi/pdf/10.1029/JB081i005p00905.

Gaffey, M.J., McCord, T.B., 1978. Asteroid surface materials: Mineralogical characterizations from reflectance spectra. Space Sci. Rev. 21 (5), 555–628. http://dx.doi.org/10.1007/BF00240908.

Garenne, A., Beck, P., Montes-Hernandez, G., Brissaud, O., Schmitt, B., Quirico, E., Bonal, L., Beck, C., Howard, K., 2016. Bidirectional reflectance spectroscopy of carbonaceous chondrites: Implications for water quantification and primary composition. Icarus 264, 172–183. http://dx.doi.org/10.1016/j.icarus.2015.09.005, URL: http://www.sciencedirect.com/science/article/pii/S001910351500408X.

Greenwood, R.C., Burbine, T.H., Franchi, I.A., 2020. Linking asteroids and meteorites to the primordial planetesimal population. Geochim. Cosmochim. Acta 277, 377–406. http://dx.doi.org/10.1016/j.gca.2020.02.004, URL: http://www.sciencedirect.com/science/article/pii/S0016703720301058.

Grossman, J.N., 1994. Meteoritical bulletin, No. 76. Meteoritics 29 (1), 100. http://dx.doi.org/10.1111/j.1945-5100.1994.tb00661.x.

Grossman, J.N., 1998. The meteoritical bulletin, No. 82, 1998 july. Meteorit. Planet. Sci. Suppl. 33, 221–239.

Grossman, J.N., Alexander, C.M.O., Wang, J., Brearley, A.J., 2000. Bleached chondrules: Evidence for widespread aqueous processes on the parent asteroids of ordinary chondrites. Meteorit. Planet. Sci. 35 (3), 467–486. http://dx.doi.org/10.1111/j.1945-5100.2000.tb01429.x, URL: https://onlinelibrary.wiley.com/doi/abs/10.1111/j.1945-5100.2000.tb01429.x, arXiv:https://onlinelibrary.wiley.com/doi/pdf/10.1111/j.1945-5100.2000.tb01429.x.

Hiroi, T., Zolensky, M.E., Pieters, C.M., Lipschutz, M.E., 1996. Thermal metamorphism of the c, g, b, and f asteroids seen from the 0.7 /textmu m, 3 /textmu m, and UV absorption strengths in comparison with carbonaceous chondrites. Meteorit. Planet. Sci. 31 (3), 321–327. http://dx.doi.org/10.1111/j.1945-5100.1996.tb02068.x, URL: https://onlinelibrary.wiley.com/doi/abs/10.1111/j.1945-5100.1996.tb02068.x, arXiv:https://onlinelibrary.wiley.com/doi/pdf/10.1111/j.1945-5100.1996.tb02068.x.

Krot, A.N., Keil, K., Scott, E.R.D., Goodrich, C.A., Weisberg, M.K., 2014. Classification of meteorites and their genetic relationships. In: Davis, A.M. (Ed.), Meteorites and Cosmochemical Processes. pp. 1–63.

Lantz, C., Brunetto, R., Barucci, M., Fornasier, S., Baklouti, D., Bourçois, J., Godard, M., 2017. Ion irradiation of carbonaceous chondrites: A new view of space weathering on primitive asteroids. Icarus 285, 43–57. http://dx.doi.org/10.1016/j.icarus.2016.12.019, URL: http://www.sciencedirect.com/science/article/pii/S0019103516300252.

Lantz, C., Clark, B.E., Barucci, M.A., Lauretta, D., 2013. Evidence for the effects of space weathering spectral signatures on low albedo asteroids. Astron. Astrophys. 554, A138. http://dx.doi.org/10.1051/0004-6361/201321593.

Lazzarin, M., Marchi, S., Moroz, L., Brunetto, R., Magrin, S., Paolicchi, P., Strazzulla, G., 2006. Space weathering in the main asteroid belt: The big picture. Astrophys. J. Lett. 647, http://dx.doi.org/10.1086/507448.

MacPherson, G.J., 2003. Calcium-aluminum-rich inclusions in chondritic meteorites. Treatise Geochem. 1, 711. http://dx.doi.org/10.1016/B0-08-043751-6/01065-3.

Marchi, S., Brunetto, R., Magrin, S., Lazzarin, M., Gandolfi, D., 2005. Space weathering of near-earth and main belt silicate-rich asteroids: observations and ion irradiation experiments. Astron. Astrophys. 443 (3), 769–775. http://dx.doi.org/10.1051/0004-6361:20053525.

Matsuoka, M., Nakamura, T., Hiroi, T., Okumura, S., Sasaki, S., 2020. Space weathering simulation with low-energy laser irradiation of murchison CM chondrite for reproducing micrometeoroid bombardments on C-type asteroids. Astrophys. J. 890 (2), L23. http://dx.doi.org/10.3847/2041-8213/ab72a4.

McSween, H.Y., 1977a. Carbonaceous chondrites of the Ornans type: A metamorphic sequence. Geochim. Cosmochim. Acta 41 (4), 477–491. http://dx.doi.org/10.1016/0016-7037(77)90286-1, URL: http://www.sciencedirect.com/science/article/pii/0016703777902861.

McSween, H.Y., 1977b. Petrographic variations among carbonaceous chondrites of the Vigarano type. Geochim. Cosmochim. Acta 41 (12), 1777–1790. http://dx.doi.org/10.1016/0016-7037(77)90210-1, URL: http://www.sciencedirect.com/science/article/pii/0016703777902101.

Milliken, R.E., Mustard, J.F., 2005. Quantifying absolute water content of minerals using near-infrared reflectance spectroscopy. J. Geophys. Res.: Planets 110 (E12), http://dx.doi.org/10.1029/2005JE002534, URL: https://agupubs.onlinelibrary.wiley.com/doi/abs/10.1029/2005JE002534, arXiv:https://agupubs.onlinelibrary.wiley.com/doi/pdf/10.1029/2005JE002534.

Moroz, L., Fisenko, A., Semjonova, L., Pieters, C., Korotaeva, N., 1996. Optical effects of regolith processes on s-asteroids as simulated by laser shots on ordinary chondrite and other mafic materials. Icarus 122 (2), 366–382. http://dx.doi.org/10.1006/icar.1996.0130, URL: http://www.sciencedirect.com/science/article/pii/S001910359690130X.

Mothé-Diniz, T., Carvano, J., Bus, S., Duffard, R., Burbine, T., 2008. Mineralogical analysis of the Eos family from near-infrared spectra. Icarus 195 (1), 277–294. http://dx.doi.org/10.1016/j.icarus.2007.12.005, URL: http://www.sciencedirect.com/science/article/pii/S0019103507006069.

Nakamura, T., Noguchi, T., Tanaka, M., Zolensky, M.E., Kimura, M., Tsuchiyama, A., Nakato, A., Ogami, T., Ishida, H., Uesugi, M., Yada, T., Shirai, K., Fujimura, A., Okazaki, R., Sandford, S.A., Ishibashi, Y., Abe, M., Okada, T., Ueno, M., Mukai, T., Yoshikawa, M., Kawaguchi, J., 2011. Itokawa dust particles: A direct link between s-type asteroids and ordinary chondrites. Science 333 (6046), 1113–1116. http://dx.doi.org/10.1126/science.1207758, URL: http://science.sciencemag.org/content/333/6046/1113, arXiv:http://science.sciencemag.org/content/333/6046/1113.full.pdf.

Piironen, J., Muinonen, K., Nousiainen, T., Sasse, C., Roth, S., Peltoniemi, J., 1998. Albedo measurements on meteorite particlesfn1fn1Presented at ACM96, Versailles, 8–12.7.1996. Also university of pisa, department of mathematics, Pisa, Italy. Planet. Space Sci. 46 (8), 937–943. http://dx.doi.org/10.1016/S0032-0633(98)00035-X, URL: http://www.sciencedirect.com/science/article/pii/S003206339800035X.

Pommerol, A., Schmitt, B., 2008. Strength of the H2O near-infrared absorption bands in hydrated minerals: Effects of particle size and correlation with albedo. J. Geophys. Res.: Planets 113 (E10), http://dx.doi.org/10.1029/2007JE003069, URL: https://agupubs.onlinelibrary.wiley.com/doi/abs/10.1029/2007JE003069, arXiv:https://agupubs.onlinelibrary.wiley.com/doi/pdf/10.1029/2007JE003069.

Potin, S., Beck, P., Usui, F., Bonal, L., Vernazza, P., Schmitt, B., 2020. Style and intensity of hydration among C-complex asteroids: A comparison to desiccated carbonaceous chondrites. Icarus 348, 113826. http://dx.doi.org/10.1016/j.icarus.2020.113826, URL: http://www.sciencedirect.com/science/article/pii/S0019103520302086.

Potin, S., Brissaud, O., Beck, P., Schmitt, B., Magnard, Y., Correia, J.-J., Rabou, P., Jocou, L., 2018. SHADOWS: a spectro-gonio radiometer for bidirectional reflectance studies of dark meteorites and terrestrial analogs: design, calibrations, and performances on challenging surfaces. Appl. Opt. 57 (28), 8279–8296. http://dx.doi.org/10.1364/AO.57.008279, URL: http://ao.osa.org/abstract.cfm?URI=ao-57-28-8279.

Quirico, E., Montagnac, G., Rouzaud, J.-N., Bonal, L., Bourot-Denise, M., Duber, S., Reynard, B., 2009. Precursor and metamorphic condition effects on Raman spectra of poorly ordered carbonaceous matter in chondrites and coals. Earth Planet. Sci. Lett. 287 (1), 185–193. http://dx.doi.org/10.1016/j.epsl.2009.07.041, URL: http://www.sciencedirect.com/science/article/pii/S0012821X09004646.

Quirico, E., Raynal, P.-I., Bourot-Denise, M., 2003. Metamorphic grade of organic matter in six unequilibrated ordinary chondrites. Meteorit. Planet. Sci. 38 (5), 795–811. http://dx.doi.org/10.1111/j.1945-5100.2003.tb00043.x, URL: https://onlinelibrary.wiley.com/doi/abs/10.1111/j.1945-5100.2003.tb00043.x, arXiv:https://onlinelibrary.wiley.com/doi/pdf/10.1111/j.1945-5100.2003.tb00043.x.

Reddy, V., Dunn, T.L., Thomas, C.A., Moskovitz, N.A., Burbine, T.H., 2015. Mineralogy and surface composition of asteroids. In: Michel, P., DeMeo, F.E., Bottke, W.F. (Eds.), Asteroids IV. University of Arizona Press, Tucson, http://dx.doi.org/10.2458/azu_uapress_9780816532131-ch003.

Salisbury, W., Hunt, J., Graham, 1974. Meteorite spectra and weathering. J. Geophys. Res. 79, 4439–4441. http://dx.doi.org/10.1029/JB079i029p04439.

Scott, E.R.D., Jones, R.H., 1990. Disentangling nebular and asteroidal features of c03 carbonaceous chondrite meteorites. Geochim. Cosmochim. Acta 54 (9), 2485–2502. http://dx.doi.org/10.1016/0016-7037(90)90235-D, URL: http://www.sciencedirect.com/science/article/pii/001670379090235D.

Scott, E.R.D., Krot, A.N., 2014. Chondrites and their components. In: Davis, A.M. (Ed.), Meteorites and Cosmochemical Processes. pp. 65–137.

Sunshine, J.M., Connolly, H.C., McCoy, T.J., Bus, S.J., La Croix, L.M., 2008. Ancient asteroids enriched in refractory inclusions. Science 320 (5875), 514–517. http://dx.doi.org/10.1126/science.1154340, URL: http://science.sciencemag.org/content/320/5875/514, arXiv:http://science.sciencemag.org/content/320/5875/514.full.pdf.

Usui, F., Hasegawa, S., Ootsubo, T., Onaka, T., 2018. AKARI/IRC near-infrared asteroid spectroscopic survey: AcuA-spec. Publ. Astron. Soc. Japan 71 (1), http://dx.doi.org/10.1093/pasj/psy125, arXiv:https://academic.oup.com/pasj/article-pdf/71/1/1/27641283/psy125.pdf. 1.

Vernazza, P., Castillo-Rogez, J., Beck, P., Emery, J., Brunetto, R., Delbo, M., Marsset, M., Marchis, F., Groussin, O., Zanda, B., Lamy, P., Jorda, L., Mousis, O., Delsanti, A., Djouadi, Z., Dionnet, Z., Borondics, F., Carry, B., 2017. Different origins or different evolutions? Decoding the spectral diversity among c-type asteroids. Astron. J. 153 (2), 72. http://dx.doi.org/10.3847/1538-3881/153/2/72.

Vernazza, P., Fulvio, D., Brunetto, R., Emery, J., Dukes, C., Cipriani, F., Witasse, O., Schaible, M., Zanda, B., Strazzulla, G., Baragiola, R., 2013. Paucity of tagish lake-like parent bodies in the asteroid belt and among jupiter trojans. Icarus 225 (1), 517–525. http://dx.doi.org/10.1016/j.icarus.2013.04.019, URL: http://www.sciencedirect.com/science/article/pii/S001910351300184X.

Vernazza, P., Marsset, M., Beck, P., Binzel, R.P., Birlan, M., Brunetto, R., Demeo, F.E., Djouadi, Z., Dumas, C., Merouane, S., Mousis, O., Zanda, B., 2015. Interplanetary dust particles as samples of ICY asteroids. Astrophys. J. 806 (2), 204. http://dx.doi.org/10.1088/0004-637x/806/2/204.

Vernazza, P., Zanda, B., Binzel, R.P., Hiroi, T., DeMeo, F.E., Birlan, M., Hewins, R., Ricci, L., Barge, P., Lockhart, M., 2014. Multiple and fast: The accretion of ordinary chondrite parent bodies. Astrophys. J. 791 (2), 120. http://dx.doi.org/10.1088/0004-637x/791/2/120.

Zellner, B., Tholen, D., Tedesco, E., 1985. The eight-color asteroid survey: Results for 589 minor planets. Icarus 61 (3), 355–416. http://dx.doi.org/10.1016/0019-1035(85)90133-2, URL: http://www.sciencedirect.com/science/article/pii/0019103585901332.

4 Investigating S-type asteroid surfaces through reflectance spectra of ordinary chondrites

As shown in Chapter 3, the search for asteroidal parent bodies of chondrites based on reflectance spectroscopy is a difficult endeavor. Nonetheless, S-type asteroids have previously been proposed as parent bodies of OCs based on reflectance spectroscopy (e.g. Binzel et al. (2004), Chapman and Salisbury (1973) and Moroz et al. (1996a)). The link was finally confirmed by the NEAR Shoemaker space mission (Trombka et al., 2000) which visited the S-type asteroid Eros and the return of the Hayabusa space mission (Nakamura et al., 2011) which collected samples from the S-type asteroid Itokawa. Laboratory measurement could confirm that the retrieved samples are, indeed, metamorphosed (PT 4-6) LL material.

Within the OC group, a wide range of metamorphic grades and variations in mineralogy can be observed. As the largest group of meteorites in our current collection (about 80 % of finds and falls (Meteoritical Bulletin Database, 2022)) they are subdivided into two groups based on petrology (UOCs and EOCs, with 94 % of OCs being EOCs and only 6 % UOCs (Meteoritical Bulletin Database, 2022)) and further into three groups based on bulk iron contents and oxidation state (H, L and LL) (see Section 2.1.1). This suggests that variations in mineralogy and petrology, such as UOCs-like and EOCs-like material, should also be present among S-type asteroids. Indeed, spectral variations can be observed in a large set of 466 S-type asteroid reflectance spectra available to us (Mahlke et al., 2022) but is it possible to relate spectral variations in asteroids to specific properties of OCs?

In the present chapter, spectral differences between UOCs and EOCs (independently of their chemical group) as well as H, L and LL (independently of their PT) were analyzed. Through comparisons with S-type asteroid spectra insights into whether it is possible to identify EOC-like and UOC-like S-type asteroid surfaces could be drawn. This will allow to further constrain the already established link between OCs and S-type asteroids. The radial structure of S-type asteroids is still an open question. One suggested model is that of the onion shell model, which suggests that S-type asteroid have metamorphosed (EOC-like) cores and primitive (UOC-like) surfaces (Figure 4.1). In the case of such a structure, we expect the surfaces of large asteroids to be UOC-like (assuming that they are not rubble piles and have not had their surfaces removed by impacts). Depending on the duration of accretion, the thickness of the UOC-like crust varies (e.g. Ghosh et al. (2003)). In the case of fast accretion ($T < 0.3$ Myr, (Vernazza

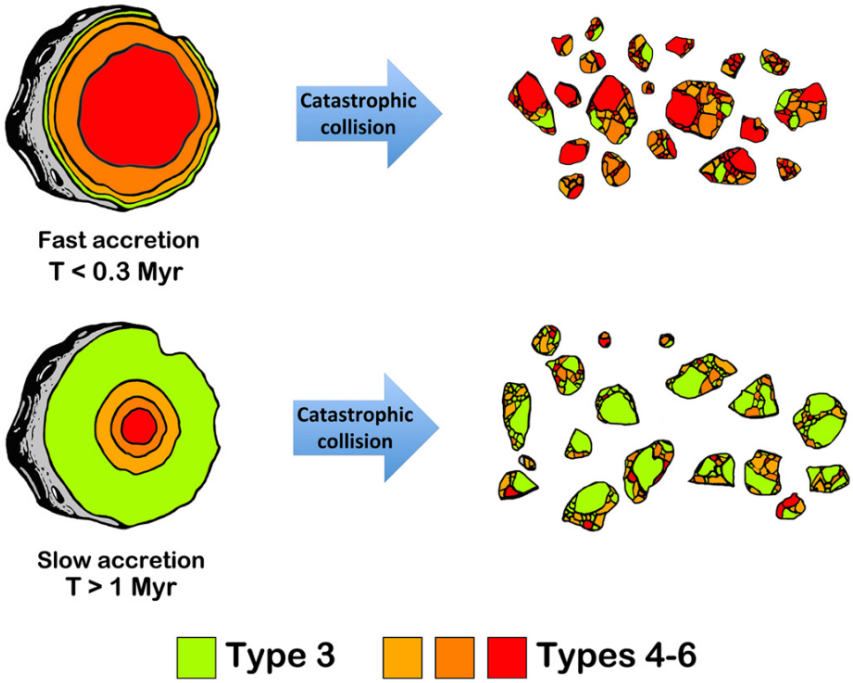

Figure 4.1: Schematic view of the onion shell model. The radial structure of the S-type asteroid is devided into a metamorphosed interior (EOC material) and a primitive exterior (UOC material). Depending on the accretion time we expect the UOC-like crust of the asteroid to be thicker or thinner. Image was taken from Vernazza et al. (2014).

et al., 2014)) smaller asteroids (D < 20 km), which result from collisions should have predominantly EOC-like surfaces while for slow accretion they should be UOC-like (Figure 4.1, Vernazza et al. (2014))).

I obtained a large set of 41 UOC and 39 EOC reflectance spectra while using consistent measuring conditions. The PT of each UOC has been previously been assessed (Bonal et al., 2016). For EOCs the metamorphic grades are taken from the Meteoritical Bulletin Database (2022). The classification into H, L and LL subgroups of the UOCs was checked by MS measurements and petrography including the determination of the modal abundance of metal through point counting and chondrule size measurements on thin/thick sections (see Section 2.2.5 for details). It revealed that 74 % of all Antarctic UOCs are misclassified in the Meteoritical Bulletin Database (2022).

Subsequently, various spectral features were determined for each chondrite as explained in Section 2.3.1 to identify any possible spectral differences between UOCs and EOCs as well as between H, L and LL. This analysis revealed that the spectral features of UOCs and EOCs form a continuum more than a clear cut dichotomy. The Ol/(Ol + Px) ratio of EOCs slightly exceeds that of UOCs with some also showing comparable ratios. Some EOCs show absorption features and peak reflectance values that are stronger than for UOCs, while some are comparable. Since decreasing grain size leads to higher reflectance and more shallow band depths (Mustard and Hays (1997) and Sultana et al. (2021)) reflectance spectra of a total of 6 EOCs and one UOC were measured after varying grinding times. After each grinding the approximate grain size

was determined under a microscope. As expected, the UOC, which contains a higher percentage of fine grained, porous matrix could be ground more easily than the EOCs. The results showed that the difference in absorption band depths and peak reflectance values between some EOCs and UOCs can be explained by grain size. Comparing H, L and LL revealed that LL of PT $\geq$ 5 are distinguishable from H and L based on a shallower 2 µm band depth and a 1 µm band position at longer wavelengths. For PT $\geq$ 4 the average Ol/(Ol + Px) ratio decreases slightly from LL and L to H.

A total of 466 S-type asteroid spectra (Mahlke et al., 2022) were processed. The effect of SW was taken into account as explained in Section 2.3.1 by analytically de-space weathering the asteroid spectra following Brunetto et al. (2006). This allows for the comparison between chondrite and asteroid spectra. Additionally, the effects of SW and grain size on the different spectral features of S-type asteroids were studied by principal component analysis (PCA).

The comparison with OC 1 µm and 2 µm spectral features revealed that most S-type asteroid spectra cluster in between UOCs and EOCs. The average Ol/(Ol + Px) ratio of S-type asteroids matched that of EOCs slightly better than UOCs. However, PCA showed that the goodness of a match between chondrites and asteroids is strongly dependent on the SW model used. De-space weathering the asteroid spectra led to spectral bluing and an increase in 1 µm and 2 µm absorption features. Depending on how much the S-type asteroid got space weathered, the reflectance spectra will shift from having spectral features comparable to UOCs, to comparable to EOCs, to not matching at all.

Lastly, an anti-correlation between the 1 µm band depth of S-type asteroids and their diameter was found. As the grain size experiments during this work have shown, we expect the band contrast to decrease with decreasing grain size. This result therefore points towards larger asteroid bodies having finer-grained regoliths, while smaller bodies have coarser grained regoliths. This results, together with the better match of the Ol/(Ol + Px) ratio of S-type asteroids to EOCs is in line with, but does not definitively prove, an onion shell model structure for S-type asteroids.

The fact that no clear spectral differences could be found between UOCs and EOCs based on the 1 µm and 2 µm bands alone, underlines the potential of using the 3 µm hydration band as a further constraint. With EOCs having higher PTs, they are expected to be dryer than UOCs and therefore be distinguishable from UOCs by showing little to no 3 µm band. For UOCs on the other hand, 3 µm bands have clearly been observed (see Chapter 5 for in-depth investigation of the 3 µm band of UOCs). Extending the spectral range measured on S-type asteroids to the 3 µm region could help to further constrain the asteroid-meteorite link.

The following paper has been published in Icarus 2022, 381, 115012

Icarus 381 (2022) 115012

Contents lists available at ScienceDirect

Icarus

journal homepage: www.elsevier.com/locate/icarus

Investigating S-type asteroid surfaces through reflectance spectra of ordinary chondrites

J. Eschrig [a,*], L. Bonal [a], M. Mahlke [b], B. Carry [b], P. Beck [a], J. Gattacceca [c]

[a] Institut de Planétologie et d'Astrophysique de Grenoble, Université Grenoble Alpes, CNRS CNES, 38000 Grenoble, France
[b] Université Côte d'Azur, Observatoire de la Côte d'Azur, CNRS, Laboratoire Lagrange, France
[c] CNRS, Aix Marseille Univ, IRD, Coll France, CEREGE, Aix-en-Provence, France

ARTICLE INFO

Keywords:
Meteorites
Asteroids
Surfaces
Spectroscopy
Mineralogy

ABSTRACT

The search for asteroidal parent bodies of chondrites through various techniques is an ongoing endeavor. A link between ordinary chondrites (OCs) and S-type asteroids has previously been established by the sample return of the Hayabusa space mission. OCs are the class with the most abundant samples in our meteorite collection. We present an in-depth study of the reflectance spectra of 39 equilibrated and 41 unequilibrated ordinary chondrites (EOCs and UOCs). We demonstrate that consistent measuring conditions are vital for the direct comparison of spectral features between chondrites, otherwise hampering any conclusions. We include a comparison with a total of 466 S-type asteroid reflectance spectra from various databases. We analyze (i) if a difference between EOCs and UOCs as well as between H, L and LL can be seen, (ii) if it is possible to identify unequilibrated and equilibrated S-type asteroid surfaces and (iii) if we can further constrain the match between OCs and S-type asteroids all based on reflectance spectra.

As a first step, we checked the classification of the 31 Antarctic UOCs analyzed in the present work, using petrography and magnetic measurements, and evidenced that 74% of them were misclassified. Reflectance spectra were compared between EOCs and UOCs as well as between H, L and LL chondrites using a set of spectral features including band depths and positions, peak reflectance values, spectral slopes and the Ol/(Ol + Px) ratio. UOCs and EOCs reflectance spectra show no clear-cut dichotomy, but a continuum with some EOCs showing stronger absorption bands and peak reflectance values, while others are comparable to UOCs. Moreover, we show by the example of 6 EOCs that their band depths decrease with decreasing grain size. Based on reflectance spectra alone, it is thus highly challenging to objectively identify an unequilibrated from an equilibrated S-type surface. There is no clear distinction of the chemical groups: only LL EOCs of petrographic type >4 can be distinguished from H and L through less deep 2000 nm band depths and 1000 nm band positions at longer wavelengths. No dichotomy of S-type asteroids can be seen based on the Ol/(Ol + Px) ratio. Their average Ol/(Ol + Px) ratio matches EOCs better than UOCs. A principal component analysis (PCA) was performed illustrating that both the unknown degree of space weathering and the unknown regolith grain size on asteroid surfaces hinder the distinction between equilibrated and unequilibrated surfaces. Lastly, an anti-correlation between the diameter of the asteroids and their 1000 nm band depth is found indicating that larger sized S-type asteroids show finer grained surfaces.

1. Introduction

The investigation of asteroids is an important and extremely useful tool for uncovering the formation and evolution history of the Solar System. As many asteroid types have escaped differentiation they are primitive objects (Vernazza et al., 2017). Studying them through laboratory measurements of chondrites, which are readily available on Earth, and remotely through reflectance spectroscopy are common practices. Within these studies, the search for asteroidal parent bodies of chondrites through various techniques is an ongoing endeavor.

Ordinary chondrites (OCs) are the class with the most abundant samples in our meteorite collection ("Meteoritical Bulletin Database,", 2021). As such, they have been studied widely, giving us a good understanding of their chemical and petrographic properties. They are sub-

* Corresponding author.
E-mail address: jolantha.eschrig@univ-grenoble-alpes.fr (J. Eschrig).

https://doi.org/10.1016/j.icarus.2022.115012
Received 17 January 2022; Received in revised form 11 March 2022; Accepted 28 March 2022
Available online 3 April 2022

divided into equilibrated and unequilibrated ordinary chondrites (EOCs and UOCs, respectively) based on their thermal metamorphic grade. As a measure for the metamorphic grade, chondrites are assigned petrologic types (PT) with UOCs representing PT 3.0–3.9 and EOCs PT 4–7. Moreover, to reflect their mineralogical variability, OCs are further subdivided into H, L and LL based on their total average iron and iron in metal abundance in decreasing order (Krot et al., 2014). The oxidation state increases from H to L to LL.

A link between S-type asteroids and ordinary chondrites has previously been proposed through reflectance spectroscopy (e.g. Binzel et al. (2004); Chapman and Salisbury (1973); Moroz et al. (1996)). This has been confirmed by the Hayabusa space mission that sampled the S-type asteroid Itokawa that is comparable to LL4, LL5 and LL6 type ordinary chondrites (Nakamura et al., 2011).

Besides sample return missions, reflectance spectroscopy is a powerful tool for comparing asteroids with meteorites and looking for links between them (e.g. Sears et al., 2021). Both OCs and S-type asteroids can show variable reflectance spectra. Close to 500 S-type asteroid reflectance spectra are available in the 500–2400 nm wavelength range from various databases (Mahlke et al., in preparation). Equally, 64 and 60 reflectance spectra have previously been obtained for UOCs and EOCs, respectively and made available in the "Reflectance Experiment LABoratory" database ("RELAB,", 2021). However, differences in measuring conditions between OC spectra in the RELAB database impair the comparability between samples.

The goal of the present work is to further investigate the link between S-type asteroids and OCs by comparing a large set of S-type asteroid spectra (466) with a large set of OC spectra (80) which have been acquired under consistent measuring conditions. We analyzed the mineralogical variability of the OCs taking into account their post-accretion history (Bonal et al., 2016). With OCs being mineralogically and petrographically diverse, our objective is to investigate whether differences can be seen as well through the tools used for the observation of asteroids. For this a set of spectral features (including band depths and positions as well as spectral slopes) has been determined for each spectrum following previous works (Cloutis et al., 1986; Eschrig et al., 2021). A principal component analysis (PCA) has been performed to investigate the effect of space weathering and regolith grain size on different constituents of the S-type spectra. If a spectral difference between EOCs and UOCs can be found, it raises the question whether a spectral difference between equilibrated and unequilibrated S-type asteroid surfaces can be seen.

2. Samples and methods

2.1. Sample list and experimental procedures

This work includes reflectance spectra of 41 UOCs (Eschrig et al., 2019) and of 39 EOCs (Eschrig et al., 2020) (Figs. 1 and 2). Ten out of the 41 UOCs are falls while the remaining 31 are Antarctic finds. For EOCs, 16 are falls and 23 are finds. Samples were provided from different Institutes and Museums as indicated in Tables 1 and 2. Additionally, Tables 1 and 2 show the petrologic type (PT), which was previously determined through Raman spectroscopy on polyaromatic carbonaceous matter (Bonal et al., 2016) for UOCs and the one given in the Meteoritical Bulletin ("Meteoritical Bulletin Database,", 2021) for EOCs. To allow for the comparison between meteorites and asteroids, a total of 466 S-type asteroid reflectance spectra (of 323 unique S-type asteroids) were taken from a compilation of reflectance spectra by Mahlke et al., in preparation. The asteroid data in that work was compiled from online resources such as the Small Main-Belt Asteroid Spectroscopic Survey[1] as well as data published in the literature and provided by personal correspondence with the observers. The compilation of asteroid reflectance spectra will be made publicly available upon publication of the Mahlke et al. work. The subset of S-type asteroid spectra used in this work was selected based on the taxonomic classifications of the asteroids found in the literature via the Virtual Observatory Solar System Open Database Network[2] service. We note that the spectral appearance of some asteroids is closer to the olivine-rich A-types than the S-type given in the literature. Some asteroids have more than one spectrum observed. 71 out of these 466 S-type spectra belong to asteroids which have previously been assigned to asteroid dynamical families.

The assessed classification into H, L and LL of each of the UOCs was verified by petrography and magnetic measurements (Table 1). The magnetic susceptibility (MS) was measured at CEREGE (France) on bulk UOCs using an Agico MFK1 instrument operating with a field of 200 A/m and a frequency of 976 Hz. Thin sections and/or thick polished sections (depending on availability) were obtained for each UOC. For petrographic observations, we used a Leica DM2500P petrographic optical microscope at CEREGE. This allowed for the determination of the modal abundance of the different chondrite components (metal, matrix, magnetite, sulfides (troilite) and chondrules/chondrule fragments) through point counting. The degree of terrestrial weathering of each UOC was determined by assessing the amount of metal and troilite weathering products (iron oxides and oxyhydroxides) using the scale defined by Wlotzka (1993). The shock stage of each UOC was determined by looking at thin section in transmitted light and using the shock indicators from Bennett III and McSween (1996); Scott et al. (1992) and Stöffler et al. (1991). Mosaic pictures in reflected and/or transmitted light of the sections were used to determine the average chondrule size. Chondrules were manually outlined in the images using a graphics editor. The average chondrule apparent diameter was then determined for each sample. For EOCs, we use the classification given in the Meteoritical Bulletin, since their classification is more straightforward and unquestionable than that of UOCs.

Reflectance spectra were acquired using the SHADOWS instrument (Potin et al., 2018), a spectro-radio goniometer available at IPAG (Grenoble, France). Measurements were done on powdered chondrites. For this, chondrites were manually crushed into a fine powder and transferred to a sample holder located in an environmental cell. Subsequently, reflectance spectra were measured on the flat, smoothed surface of the powders, under vacuum ($P < 10^{-4}$ mbar) and at 80 °C temperature. Evacuating and heating the samples reduces the terrestrial water contamination, leaving the hydration feature of the spectra predominantly due to chondritic hydration. Spectra were acquired between 340 and 4200 nm at a 20 nm spectral resolution. The measuring geometry of $i = 0°$ and $e = 30°$ was chosen according to previous works (Eschrig et al., 2021). The reflectance spectra were normalized to the Lambertian surface using a Spectralon™ standard between 340 and 2100 nm and an Infragold™ standard between 2100 and 4200 nm. All spectra were photometrically corrected for reflection effects induced by the sapphire window used to close the environmental cell (Potin et al., 2020).

To evaluate the effect that grain size has on the shape of EOC reflectance spectra, a small series of test was performed in which 6 EOC (Kernouvé (H6), Ste. Marguerite (H4), NWA 12961 (L7), Monte das Forte (L5), Moshampa (LL5) and Los Vientos 423 (H6)) and one UOC (RBT 04251 (LL 3.4)) were first ground by hand (as all UOCs and EOCs presented in this work) and then ground at 30 Hz using a laboratory ball mill for 5 min and lastly for 10 min. Sample Kernouvé was additionally ground in the ball mill for 20 min at 30 Hz. At each stage, the grain size was estimated by looking at the powder under an optical binocular and measuring the largest grains visible at 5–10 different spots. A reflectance spectrum was measured for each powder using the measuring conditions described previously.

[1] https://smass.mit.edu

[2] https://ssp.imcce.fr/webservices/ssodnet/

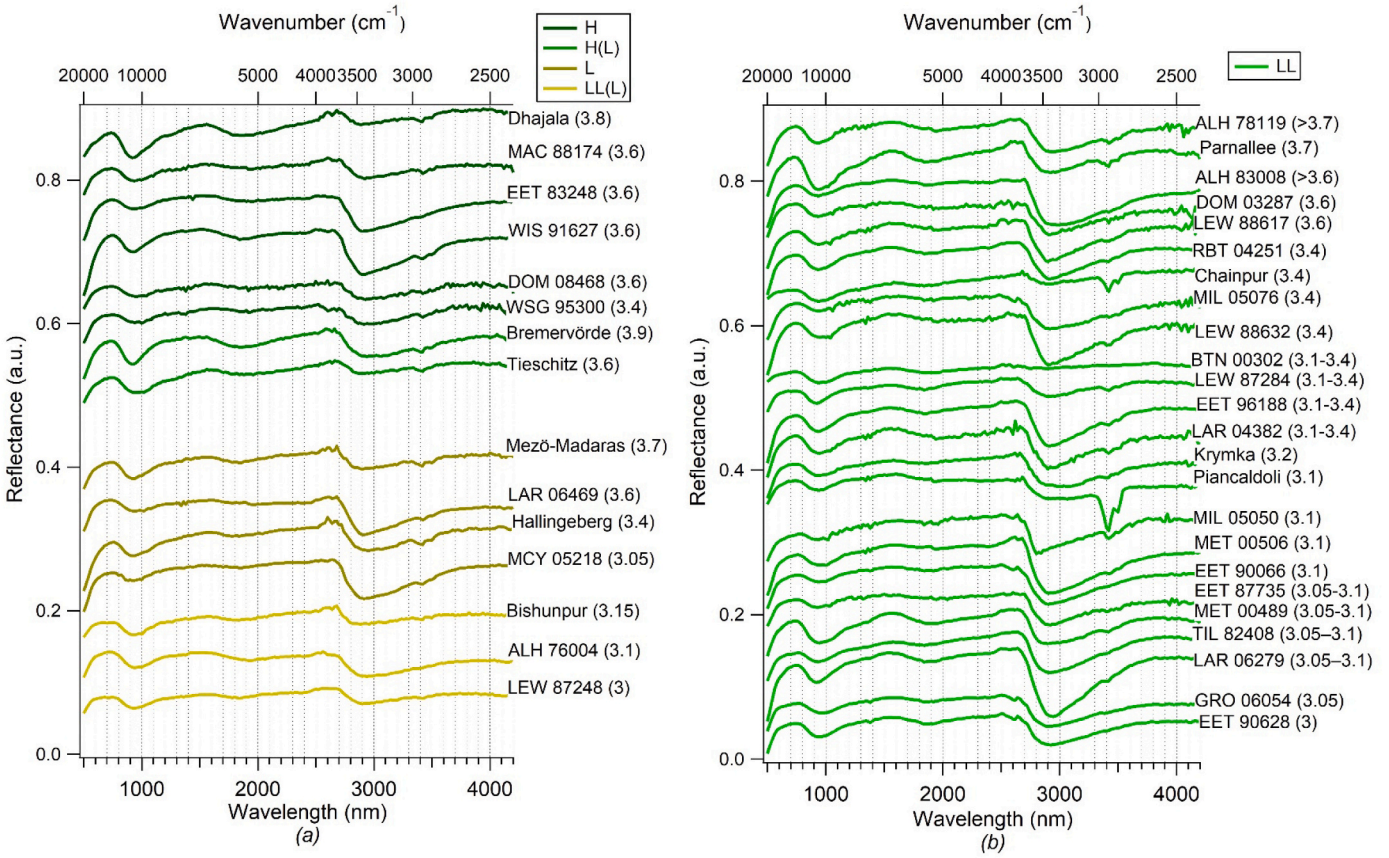

Fig. 1. Reflectance spectra of the 41 UOCs measured in the present work in the 500–4200 nm wavelength range. The spectra are shifted along the y-axis for better visibility and sorted by metamorphic grade within each class (H, H(L), L, LL(L) and LL) with increasing metamorphic grade from bottom to top as indicated by the Petrographic type (PT) values (Bonal et al., 2016) given in parenthesis behind each sample name. The classification used in this graph is the same as determined in the present work (see Table 1).

2.2. Analytical procedure

For the classification of the UOCs, the results of MS, chondrule apparent diameter and modal abundances were considered. For the MS measurements, the reference values of $\log(\chi) = 5.24 \pm 0.08$ ($n = 10$) for H3, $\log(\chi) = 4.79 \pm 0.11$ ($n = 11$) for L3 and $\log(\chi) = 4.41 \pm 0.16$ ($n = 14$) for LL3 were used, with χ in 10^{-9} m^3kg^{-1} (Table 1) (unpublished updated version of Rochette et al., 2003). Since increasing terrestrial weathering results in a decrease of the magnetic susceptibility of ordinary chondrites, the magnetic classification for finds must take their weathering grade into account (Rochette et al., 2012).

The metal modal abundance determined by point counting was compared to the average abundances in H: 7.80 ± 0.62 vol% ($n = 25$), L: 3.54 ± 0.34 vol% ($n = 53$) and LL: 1.16 ± 0.59 vol% (n = 14) as computed by Gattacceca et al. (2014) and using meteorite densities from Consolmagno et al. (2008). For the average chondrule apparent diameter (Table 1) the reference values of H: 450 μm, L: 500 μm and LL: 690 μm (Metzler, 2018) were used.

A set of spectral features has been determined to ease the comparison process of reflectance spectra. The reflectance spectra of OCs are characterized by three main bands at 1000, 2000 and 3000 nm. They are due to olivine showing a strong absorption feature around 1000 nm and pyroxene having an absorption feature both around 900 nm and 2000 nm (e.g. Gaffey, 1976). The exact position of the 2000 nm band depends of the relative abundance of low- to high-Ca pyroxene (namely, ortho- and clinopyroxene). Mixtures dominated by low-Ca pyroxene show 2000 nm bands located around 1900 nm while for those dominated by high-Ca pyroxene it is located around 2100 nm (Cloutis and Gaffey, 1991; Singer, 1981). In general, the abundance of pyroxene in ordinary chondrites is dominated by orthopyroxene (e.g. Dunn et al. (2010a)). For hydrated samples, a hydration band is present at 3-μm, whose shape and position depends on the type of hydration (phyllosilicates, oxyhydroxide, molecular water). The determination of the spectral features is done as described in Eschrig et al. (2021). The spectral features include the depth and position of the 1000 and 2000 nm bands which were determined by fitting the bands with a polynomial fit around the absorption minima. Then a linear baseline fit was done to the band areas and the band depth was calculated following Clark (1999). The maxima to either side of the 1000 and 2000 nm band were chosen as boundaries for the linear baseline fit. The peak reflectance at around 700 nm was determined. The visual slope at wavelengths lower than 700 nm was determined by calculating the steepest slope in the 340 nm to 520 nm range and linearly fitting the points around this area. We assess the relative abundance of the end-members olivine (Ol) and pyroxene (Px) in the samples, as previously done e.g. by Vernazza et al. (2014). For this the Ol/(Ol + Px) ratio is determined according to Dunn et al. (2010b) by calculating the Band Area Ratio (BAR) of the 1 and 2 μm band (Band 2 Area over Band 1 area) and then using the following equation:

$$\frac{\mathrm{Ol}}{(\mathrm{Ol}+\mathrm{Px})} = -0.424 \times \mathrm{BAR} + 0.728$$

All spectral values are reported in Tables 3 and 4.

Space Weathering (SW) is a process that affects the asteroid surface through bombardment with micro-meteorites, and irradiation by solar wind and cosmic ions (Brunetto et al., 2006). The effect of SW on the reflectance spectra of silicon-rich S-type asteroids is described as reddening and darkening of the spectra (Marchi et al., 2005) while not significantly changing the position or relative intensities of the mafic

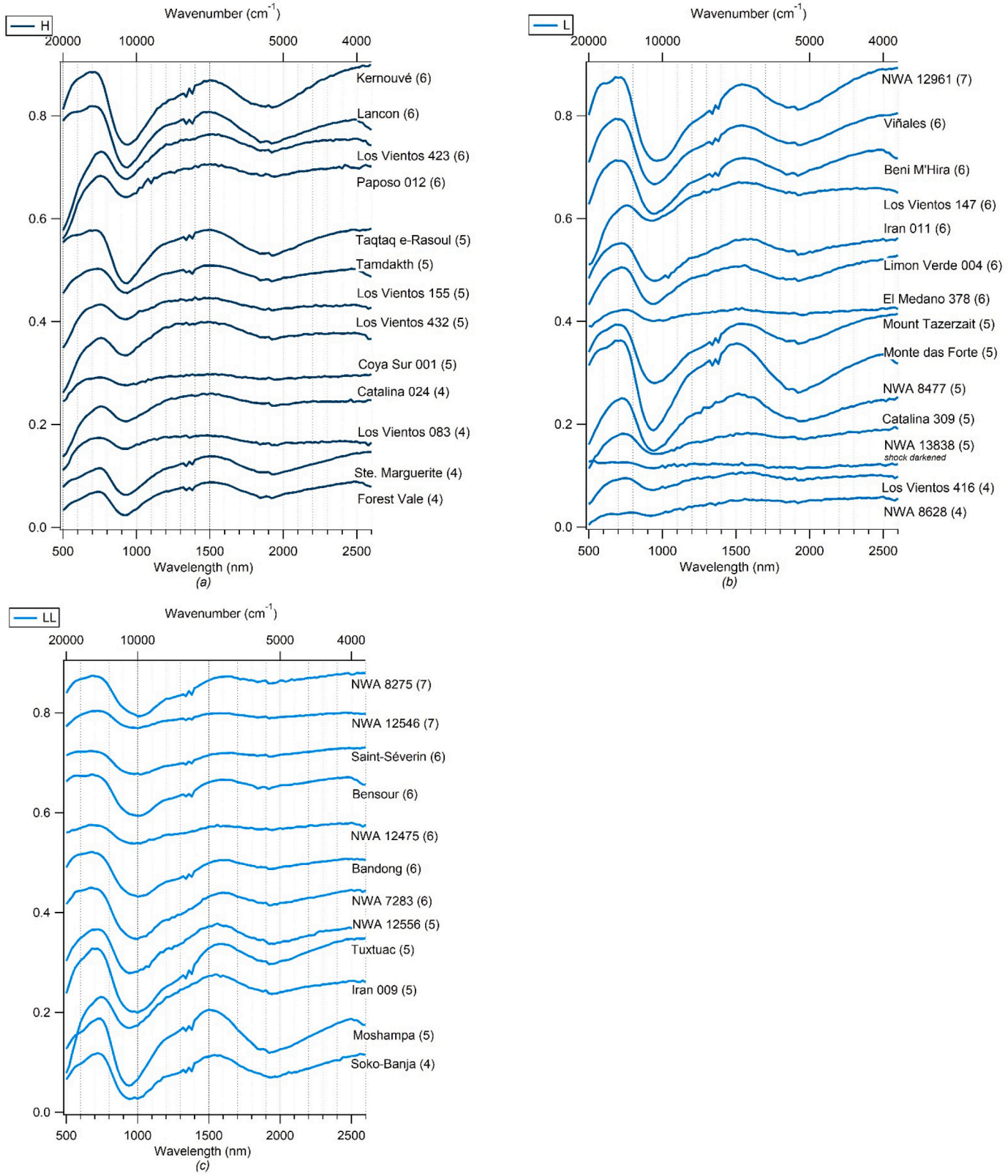

Fig. 2. Reflectance spectra of the 38 EOCs measured in the present work in the 500–2600 nm wavelength range. The spectra are shifted along the y-axis for better visibility and sorted by metamorphic grade within each class (H, H(L), L, LL(L) and LL). The metamorphic grade increases from bottom to top as indicated by the Petrographic type (PT) values (Bonal et al., 2016) given in parenthesis behind each sample name. The classification used in this graph is the same as determined in the present work (see Table 1).

Table 1
List of all UOCs measured in the present work. Shown are the results from point counting (metal + iron oxide abundance in vol%) thin section measurements (average apparent chondrule diameter ± standard deviation (s.d.) in μm) and magnetic susceptibility (MS) measurements (log(x) with x in 10^{-9} m^3/kg) as well as the weathering grade for each sample. The classification that were attributed based on these results as well as the classification given in the Meteoritical Bulletin are listed. Lastly, the petrographic type (PT) as determined by Bonal et al., 2016 (for Piancaldoli Marrocchi et al., 2020) and the providers of the bulk samples measured in this work are mentioned. Samples marked with a (*) are falls, the others are finds. The superscription "sv" stands for "shock veins" and marks samples for which shock veins and melt pockets were observed.

sample	Metal + Iron oxides (vol%)	Average apparent diam. ± s.d. (μm)	MS log (x)	Weathering	Shock stage	Classification (MetBul)	Final classification	PT (Bonal et al., 2016)	Provider bulk samples
ALH 76004	3.1	580 ± 274 (n = 54)	4.52	W0	S3/S2+	LL	L(LL)	3.1–3.4	NASA
ALH 78119	1.9	546 ± 316 (n = 39)	4.43	W1	S1	LL	LL(L)	3.5	NASA
ALH 83008	8.8	–	4.35	W0	S3	L	LL	>3.6	NASA
ALH 84086	4.8	779 ± 464 (n = 26)	4.43	W0	S3	L	LL	3.8	NASA
ALH 84120	5.5	596 ± 371 (n = 51)	4.64	W0	S1	L	L	3.8	NASA
Bishunpur*	3.6	–	4.67	W0	S2	LL	L/LL	3.2	ASU
Bremervörde*	5.8	–	4.98	W0	S2	H(L)	H/L	3.9	ASU
BTN 00302sv	2.1	670 ± 316 (n = 64)	4.58	W0	S4/S5	H	LL	3.1–3.4	NASA
Chainpur*	1.8	–	4.46	W1	S1	LL	LL	3.4	ASU
Dhajala*	10.9	–	5.12	W0	S1	H	H	3.8	ASU
DOM 03287	2.8	791 ± 270 (n = 25)	4.48	W1	S3	L	LL	3.6	NASA
DOM 08468	7.8	473 ± 200 (n = 86)	4.47	W3	S1	H	H	3.6	NASA
EET 83248	7.7	385 ± 308 (n = 40)	4.87	W2	S1	H	H	>3.6	NASA
EET 87735	6.9	587 ± 284 (n = 19)	4.00	W1	S1	L	LL	3.05–3.1	NASA
EET 90066	–	–	3.83	W1	S2	LL	LL	3.1	NASA
EET 90628	–	–	4.27	W1	S3-	LL	LL	3.0	NASA
EET 96188	–	–	4.31	W0	S3	L/LL	LL	3.1–3.4	NASA
GRO 06054	3.3	639 ± 451 (n = 42)	4.36	W1	S2	L	LL	3.1	NASA
Hallingeberg*	3.3	–	4.78	W0	S1/S2	L	L	3.4	ASU
Kymka*	1.2	–	4.03	W1	S3	LL	LL	3.2	MNHN, Paris
LAR 04382	1.6	692 ± 324 (n = 72)	4.23	W0	S3	H	LL	3.1–3.4	NASA
LAR 06279sv	1.1	886 ± 506 (n = 29)	4.00	W1	S4/S5	LL	LL	3.05–3.1	NASA
LAR 06469	10.8	456 ± 239 (n = 75)	4.20	W2	S2/S3	LL	L	>3.6	NASA
LEW 87248	3.6	486 ± 211 (n = 23)	4.50	W0	S3	L	L(LL)	3.0	NASA
LEW 87284	–	684 ± 364 (n = 42)	4.44	W0	S3+	L	LL	3.1–3.4	NASA
LEW 88617	1.1	536 ± 312 (n = 24)	3.86	W1	S3	L	LL	3.6	NASA
LEW 88632	1.6	788 ± 449 (n = 26)	4.13	W1	S2	L	LL	3.4	NASA
MAC 88174	7.8	337 ± 170 (n = 177)	5.10	W1	S3	H	H	>3.6	NASA
MCY 05218	6.2	614 ± 272 (n = 79)	4.55	W2	S3	H	L	3.05–3.1	NASA
MET 00489	–	–	3.92	W1	S2/3	L	LL	3.05–3.1	NASA
MET 00506	6.6	581 ± 244 (n = 75)	4.07	W1	S2+/S3	H	LL	3.1	NASA
Mezö-Madaras*	3.7	590 ± 331 (n = 91)	–	W0	S4	L	L	3.7	NHM, Vienna
MIL 05050	3.8	563 ± 266 (n = 40)	4.21	W1	S3	L	LL	3.1	NASA
MIL 05076	5.3	808 ± 466 (n = 53)	3.92	W1	S3	L	LL	3.4	NASA
Parnallee*	1.7	–	4.49	W0	S3	LL	LL	3.7	NHM, Vienna
Piancaldoli*	2.7	901 ± 445(n = 352)	–	W0	S2/S3	LL	LL	3.1	CRPG, Nancy
RBT 04251	3.9	746 ± 332 (n = 16)	4.34	W1	S3	H	LL	3.4	NASA
Tieschitz*	3.7	446 ± 289 (n = 23)	–	W0	S1/S2	H/L	H/L	3.6	NHM, Vienna
TIL 82408	–	–	4.03	W1	S3	LL	LL	3.05–3.1	NASA
WIS 91627	9.6	329 ± 269 (n = 72)	5.23	W0	S2	H	H	>3.6	NASA
WSG 95300	11.2	426 ± 247 (n = 41)	4.89	W1	S1	H	H	3.4	NASA

silicate bands (Brunetto et al., 2006). It affects only the most upper layer of the asteroid surface (Pieters and Noble, 2016). As the chondrite travels through the Earth's atmosphere, any surface signature of SW is removed. To overcome this difference between asteroids and chondrites, two approaches can be used: i) "de-space weathering" the asteroid spectra analytically or ii) artificially "space weathering" the meteorite spectra. Approach ii) has the disadvantage that the amount of artificial SW that needs to be added to each spectrum is unknown. For approach i) on the other hand, irradiation experiments have shown that L6 chondrites that were space-weathered in the laboratory experienced strong modification of their spectral slope but negligible changes of their 1000 nm and 2000 nm bands (Brunetto et al., 2006; Salisbury and Hunt, 1974). Brunetto et al. (2006) shows that the ratio between the space weathered (sw) and non-space weathered (non-sw) spectrum can be fitted with an exponential function

$$\frac{sw\ spectrum}{non-sw\ spectrum} = K \bullet e^{\frac{C_S}{\lambda}}$$

with K being a scaling factor, C_S being the strength of the SW and λ the wavelength. Under the assumptions that SW mainly influences the slope of the spectra (Brunetto et al., 2006; Salisbury and Hunt, 1974) and that the overall slope has no contributions other than SW, the asteroid spectra are thus "de-space weathered" by fitting the spectra with an exponential function and dividing the SW spectrum by this fit. After this correction, the same spectral features as mentioned above were determined for the asteroid spectra.

We further perform a Principal Component Analysis (PCA) of the OC and asteroid spectra (Fig. 8). PCA is a dimensionality reduction technique which projects the input data into a lower-dimensional space along a set of orthogonal vectors that maximize the variability of the projected data points. PCA is particularly suited for exploration and

Table 2
List of all EOCs measured in the present work. Listed are the classification and petrologic type (PT) as given in the Meteoritical Bulletin. Lastly, the providers of the bulk EOCs are mentioned. Samples marked with a (*) are falls, the others are finds. The superscription "sv" stands for "shock veins" and marks samples for which shock veins and melt pockets were observed. The superscription "sd" stands for "shock darkened".

Sample	Classification	Providers
Bandong*	LL6	MNHN, Paris
Beni M'hira*	L6	CEREGE, Aix-en-Provence
Bensour*	LL6	CEREGE, Aix-en-Provence
Catalina 024	H4	CEREGE, Aix-en-Provence
Catalina 309	L5	CEREGE, Aix-en-Provence
Coya Sur 001	H6	CEREGE, Aix-en-Provence
El Medano 378	L6	CEREGE, Aix-en-Provence
Forest Vale*	H4	MNHN, Paris
Iran 009^{sv}	LL5	CEREGE, Aix-en-Provence
Iran 011	L6	CEREGE, Aix-en-Provence
Kernouve*	H6	MNHN, Paris
Lançon*	H6	MNHN, Paris
Limon Verde 004	L6	CEREGE, Aix-en-Provence
Los Vientos 083	H4	CEREGE, Aix-en-Provence
Los Vientos 147	L6	CEREGE, Aix-en-Provence
Los Vientos 155	H5	CEREGE, Aix-en-Provence
Los Vientos 416	L4	CEREGE, Aix-en-Provence
Los Vientos 423	H6	CEREGE, Aix-en-Provence
Los Vientos 432	H5	CEREGE, Aix-en-Provence
Monte Das Forte*	L5	MNHN, Paris
Moshampa*^{sv}	LL5	CEREGE, Aix-en-Provence
Mount Tazerzait*	L5	MNHN, Paris
NWA 12475	LL6	CEREGE, Aix-en-Provence
NWA 12546	LL7	CEREGE, Aix-en-Provence
NWA 12556	LL5	CEREGE, Aix-en-Provence
NWA 12961	L7	CEREGE, Aix-en-Provence
NWA 13838^{sd}	L5	CEREGE, Aix-en-Provence
NWA 7283	LL6	CEREGE, Aix-en-Provence
NWA 8628	L4	CEREGE, Aix-en-Provence
NWA 8275^{sv}	LL7	CEREGE, Aix-en-Provence
NWA 8477	L5	CEREGE, Aix-en-Provence
Paposo 012	H6	CEREGE, Aix-en-Provence
Saint-Séverin*	LL6	MNHN, Paris
Soko-Banja*	LL4	MNHN, Paris
Ste. Marguerite*	H4	MNHN, Paris
Tamdakht*	H5	CEREGE, Aix-en-Provence
Taqtaq-e Rasoul*	H5	CEREGE, Aix-en-Provence
Tuxtuac*	LL5	MNHN, Paris
Viñales*^{sv}	L6	CEREGE, Aix-en-Provence

visualization of high-dimensional datasets such as reflectance spectra. In essence, PCA finds the components responsible for the largest variance in the data and allows to visualize them separately. These components are referred to as principal components (PCs) (Hotelling, 1933; Pearson, 1901) and are mathematically given by the eigenvectors of the covariance matrix of the input data. Since the wavelength-resolution of the OC spectra is higher than for the S-type spectra, we compute the PCs based on the latter and project the meteorite spectra into the resulting lower-dimensional space. Computing the PCs based on the OC spectra would lead to PCs that may contain high-frequency signals which the lower-resolution asteroid spectra cannot resolve. After determining the PCs, the principal score of each sample can be calculated. It is given by the vector product of the spectrum and the corresponding PC. PCA was computed on the demeaned spectra, hence the score of zero in all components indicates the position of the mean S-type spectrum. Spectra which are, e.g., redder than the average have a positive principal score. PCA requires a complete data matrix as input. Therefore, we could only compute it based on 339 of the 466 S-type spectra. The remaining ones had to be dropped due to unobserved or later-removed reflectance values at the edges of the wavelength range. We further excluded 7 spectra which are likely misclassified A-types and presented as outliers in the PCA results. As PCA is based on the covariance structure of the data, it is strongly susceptible to outliers.

2.3. Importance of consistent measuring conditions

The majority (53) of the UOC spectra that are already available in the RELAB database were measured under consistent measuring conditions by Vernazza et al. (2014). In their work the powdered samples were first sieved ensuring particle sizes between 0 and 45 μm. Then the measurements were performed presumably at ambient temperature and pressure (information not systematically mentioned on the RELAB database).

The samples measured in the present work have not been sieved to avoid introducing a bias in chondrite components. Metal is less easily ground than matrix material resulting in a possible depletion of metal in sifted chondrite powders. Therefore, the grain size, being sub-millimetric in our work as determined during microscope inspection, exceeds that of the samples in Vernazza et al. (2014). Furthermore, our dataset was systematically measured under vacuum and at 80 °C to mimic the highly desiccating environment present at the surface of asteroids.

When comparing the UOC spectra that appear in both datasets (Fig. 3) it clearly appears that the spectra measured by Vernazza et al. (2014) show consistently smaller band depths (Fig. 3a) and higher peak reflectance values (Fig. 3b). This is consistent with the fact that reflectance increases and band depths become shallower with decreasing grain size (as shown for instance by Mustard and Hays, 1997 and Sultana et al., 2021 for pure olivine and pyroxene).

For EOCs, the measuring conditions of the reflectance spectra in the RELAB database vary largely, ranging from bulk powder to bulk piece measurements as well as presenting varying measuring temperatures, atmospheres and geometries ("RELAB", 2021). When comparing the spectra of EOCs that are both in the RELAB database and in the dataset presented in the present work there is no clear trend. Indeed, the 1000 nm and 2000 nm band depths of the RELAB data range from less deep to comparable to deeper than those of the dataset in the present work (Fig. 3a). The overall reflectance at 700 nm of the RELAB spectra can range from lower to comparable to higher than those of our dataset as well (Fig. 3b). This corroborates the fact that the grain sizes of the EOC spectra in the RELAB database are either smaller than or comparable to our data set. The difficulty of comparison of EOC spectra from the RELAB database to the present dataset is therefore strongly increased. We conclude that consistent measuring conditions are vital when directly comparing spectral features between chondrites, otherwise hampering any conclusions. In the present work, we thus decided not to include RELAB spectra of OCs.

3. Results

3.1. Classification of UOCs

The classification of UOCs is not as straightforward as the classification of EOCs. Indeed, the absence of equilibration of olivine and pyroxene in UOCs results in the electron probe microanalyses, which are classically used to separate equilibrated H, L, and LL chondrites, not being readily useable to separate H3, L3, and LL3 chondrites. This especially applies to the most primitive UOCs. The most accurate way of classifying UOCs is, therefore, through petrographic indicators, such as metal abundance (determined by microscopy, or through the measurement of magnetic susceptibility), and chondrule size. For the classification of UOCs from ANSMET (the Antarctic Search for Meteorites program that provided the Antarctic UOCs in the present work), these indicators were either not in common use or no information was given on the procedure of classification at all. We, therefore, checked the classification of all Antarctic UOCs used in the present study.

The results of the magnetic susceptibility and chondrule apparent diameter measurements used to verify the classification of UOCs are listed in Table 1. The abundance of metal and iron oxides (used as a proxy of the initial abundance of metal, neglecting a possible minor

Table 3
List of the spectral features determined for each of the UOCs considered in the present work. Given are the visual slope at wavelengths lower than 700 nm, the 700 nm peak reflectance, the 1000 nm and 2000 nm band depth and positions as well as the Ol/(Ol + Px) ratio. All spectral features where determined as explained in Section 2.2 following Eschrig et al. (2021).

Sample	Visual slope (10^{-5} nm^{-1})	700 nm Peak refl. (%)	1000 nm Band Depth (%)	2000 nm Band Depth (%)	1000 nm Band Pos. (nm)	2000 nm Band Pos. (nm)	Ol/(Ol + Px) (%)
ALH 76004	30.01 ± 0.88	13.89 ± 0.01	15.64 ± 0.15	7.46 ± 0.04	960	1937	38.2
ALH 78119	38.99 ± 1.9	14.53 ± 0.02	16.54 ± 0.49	7.87 ± 0.06	950	1996	31.9
ALH 83008	39.5 ± 1.85	12.62 ± 0	12.31 ± 0.12	4.34 ± 0.07	959	1889	48.4
ALH 84086	36.39 ± 0.81	20.07 ± 0.02	19.6 ± 0.86	10.36 ± 0.09	964	2005	30.4
ALH 84120	32.72 ± 0.91	20.37 ± 0.03	14.01 ± 0.76	6.77 ± 0.02	942	1956	30.0
Bishunpur	20.38 ± 0.39	13.03 ± 0.01	14.5 ± 0.29	4.88 ± 0.05	950	1890	48.0
Bremervörde	38.16 ± 1.59	16.9 ± 0	19.07 ± 0.37	9.57 ± 0.01	928	1901	18.8
BTN 00302	14.35 ± 0.69	14.13 ± 0.01	11.56 ± 0.28	4.78 ± 0.1	962	1918	44.0
Chainpur	13.97 ± 2.12	13.02 ± 0.01	13.63 ± 0.08	4.81 ± 0.04	961	1892	47.9
Dhajala	23.16 ± 0.6	18.52 ± 0.01	19.63 ± 0.73	8.19 ± 0.07	937	1933	40.9
DOM 03287	35.81 ± 1.36	12.97 ± 0	13.06 ± 0.2	5.46 ± 0.08	945	1965	37.8
DOM 08468	26.08 ± 0.85	11.41 ± 0	12.8 ± 0.37	4.75 ± 0.15	969	1973	51.7
EET 83248	35.79 ± 1.96	11.74 ± 0	11.87 ± 0.13	6.01 ± 0.08	960	1945	30.4
EET 87735	25.93 ± 1.38	9.43 ± 0	12.72 ± 0.18	5.28 ± 0.09	960	1949	37.2
EET 90066	33.08 ± 2.57	10.34 ± 0	11.15 ± 0.08	4.84 ± 0.12	965	1901	38.2
EET 90628	38.74 ± 1.41	13.45 ± 0.01	15.01 ± 0.15	7.09 ± 0.33	964	1893	40.1
EET 96188	53.52 ± 2.8	16.24 ± 0	14.72 ± 0.25	5.59 ± 0.16	952	1875	42.4
GRO 06054	34.61 ± 1.47	11.74 ± 0.01	12.61 ± 0.04	4.96 ± 0.08	988	1916	46.5
Hallingeberg	56.47 ± 3.44	18.49 ± 0.01	11.59 ± 0.56	4.25 ± 0.07	953	1914	39.0
Kymka	38.54 ± 1.37	13.57 ± 0	12.35 ± 0.14	3.47 ± 0.09	961	1869	54.1
LAR 04382	43.08 ± 1.5	14.84 ± 0.01	17.86 ± 0.59	8.29 ± 0.09	970	1997	39.9
LAR 06279	64.35 ± 2.75	17.65 ± 0.02	15.07 ± 0.7	6.92 ± 0.11	938	1896	36.3
LAR 06469	33.76 ± 1.6	13.19 ± 0	11.66 ± 0.09	5.3 ± 0.03	964	2098	31.7
LEW 87248	26.12 ± 0.87	14.21 ± 0	11.4 ± 0.15	4.66 ± 0.05	950	1867	39.6
LEW 87284	31.72 ± 1.01	15.48 ± 0	12.34 ± 0.32	4.45 ± 0.1	927	1841	51.3
LEW 88617	38.85 ± 1.24	13.39 ± 0	14.34 ± 0.21	4.73 ± 0.06	962	1969	54.3
LEW 88632	48.24 ± 2.79	14.22 ± 0.02	16.01 ± 0.47	5.13 ± 0.19	980	2008	49.8
MAC 88174	31.66 ± 0.69	13.96 ± 0.02	13.33 ± 0.29	5.34 ± 0.07	962	1976	41.3
MCY 05218	41.34 ± 1.34	12.37 ± 0	10.53 ± 0.27	3.58 ± 0.08	948	1861	47.1
MET 00489	43.28 ± 1.26	17.34 ± 0	19.01 ± 0.27	8.46 ± 0.16	968	1946	42.0
MET 00506	38.31 ± 2.05	11.93 ± 0	14.23 ± 0.1	4.98 ± 0.08	980	2019	39.3
Mezö-Madaras	34.68 ± 0.67	17.22 ± 0.01	13.89 ± 0.43	4.65 ± 0.1	940	1858	53.2
MIL 05050	32.34 ± 1.3	11.37 ± 0	9.02 ± 0.6	3.93 ± 0.65	952	1889	48.0
MIL 05076	30.69 ± 1.34	10.74 ± 0	11.81 ± 1.97	3.83 ± 0.2	940	1913	52.3
Parnallee	59.1 ± 7.25	22.56 ± 0.02	20.71 ± 3.01	7.33 ± 0.23	958	1929	47.8
Piancaldoli	26.14 ± 0.37	15.84 ± 0	9.43 ± 0.06	3.65 ± 0.13	949	1944	41.9
RBT 04251	49.63 ± 1.95	16.29 ± 0	13.65 ± 0.21	5.57 ± 0.05	958	1907	38.3
Tieschitz	29.92 ± 2.59	16.29 ± 0	14.55 ± 0.12	5.44 ± 0.04	979	1981	46.2
TIL 82408	33.91 ± 1.18	12.52 ± 0	12.01 ± 0.08	5.19 ± 0.03	955	1894	36.4
WIS 91627	51.92 ± 3.25	15.61 ± 0	15.54 ± 0.6	7.7 ± 0.08	937	1887	28.2
WSG 95300	31.74 ± 1.08	11.17 ± 0.01	11.48 ± 0.15	3.76 ± 0.06	977	1951	53.2

contribution from the weathering of troilite), as well as the terrestrial weathering degree determined for each UOC is given in Table 1 as well. Some UOCs were classified solely based on a few of the methods mentioned above as shown in Table 1.

The abundance of metal and iron oxides, as determined by point counting, ranges from 1.2 vol% for Krymka (LL3.2) to 12 vol% for EET 83248 (H > 3.6). The average apparent chondrule diameter ranges from 285 μm for MAC 88174 (H > 3.6) to 901 μm for Piancaldoli (LL3.1, Marrocchi et al., 2020). log(χ) ranges from 3.83 for EET 90066 (LL3.1) to 5.23 for WIS 91627 (H > 3.6). Lastly, the weathering grade of the UOCs range from W0 for un-weathered samples to W3 for the most weathered sample DOM 08468 (H3.6). Any differences to the initial classifications of H, L and LL (given in the "Meteoritical Bulletin Database," (2021)) were altered accordingly. As a result, 14 Antarctic UOCs (ALH 83008, ALH 84086, DOM 03287, EET 87735, EET 90066, EET 90628, GRO 06054, LEW 87248, LEW 87284, LEW 88617, LEW 88632, MET 00489, MIL 05050, MIL 05076) initially classified as L were found to be LL or LL(L), 5 Antarctic UOCs (BTN 00302, LAR 04382, MCY 05218, MET 00506, RBT 04251) initially classified as H were found to be LL or L, 3 Antarctic UOCs (ALH 76004, LAR 06469, ALH 83010) initially classified as LL found to be LL(L) or L and 1 Antarctic UOC (EET 96188) initially classified as L(LL) found to be LL, adding up to a total of 23 miss-classified Antarctic UOCs among the 31 considered. This is equivalent to a miss-classification rate of 74% for Antactic UOCs. Additionally, the fall Bishunpur, which was initially classified as LL, was found to be L/LL.

3.2. EOC and UOC spectra

In Figs. 1 and 2 the reflectance spectra of all UOCs and EOCs measured in the present work are shown. For better visibility the spectra were offset along the y-axis and sorted by PT with increasing PT from bottom to top. UOC spectra are plotted in the 500–4200 nm wavelength range while EOCs are plotted in the 500–2600 nm wavelength range. It immediately becomes apparent that on average EOCs (Fig. 2) exhibit stronger absorption bands than UOCs (Fig. 1). UOCs show the so called 1000 nm absorption band at wavelengths shorter than 1000 nm. The 2000 nm absorption band is weak. EOCs have very pronounced 1000 nm absorption bands which are located below 1000 nm for H and shift towards longer wavelengths from H to L to LL (Fig. 2). The exception is NWA 13838 (L5) which has been shock darkened ("Meteoritical Bulletin Database,", 2021) and will therefore not be considered in the following discussion. The 2000 nm band of EOCs is broad with varying intensity. The shape and location of the 1000 nm and 2000 nm bands match the presence of olivine and low-Ca pyroxene. As discussed in Section 2.2, spectra dominated by orthopyroxene show 2000 nm band positions around 1900 nm, which is the case for all OCs considered in the present

Table 4
List of the spectral features determined for each of the EOCs considered in the present work. Given are the visual slope at wavelengths lower than 700 nm, the 700 nm peak reflectance, the 1000 nm and 2000 nm band depth and positions as well as the Ol/(Ol + Px) ratio. All spectral features where determined as explained in Section 2.2 following Eschrig et al. (2021).

Sample	Visual slope (10^{-5} nm^{-1})	700 nm Peak refl. (%)	1000 nm Band Depth (%)	2000 nm Band Depth (%)	1000 nm Band Pos. (nm)	2000 nm Band Pos. (nm)	Ol/(Ol + Px) (%)
Bandong	47.09 ± 1.27	25.38 ± 0.01	33.43 ± 0.13	6.92 ± 0.39	1000	1946	64.6
Beni M'hira	72.72 ± 2.14	31.32 ± 0.04	33.48 ± 3.13	11.18 ± 1.42	952	1923	56.3
Bensour	29.63 ± 2.48	25.14 ± 0.01	32.04 ± 0.59	7.01 ± 0.46	994	1943	63.7
Catalina 024	54.29 ± 4.27	18.06 ± 0.01	18.43 ± 0.89	7.49 ± 0.33	943	1905	38.7
Catalina 309	37.28 ± 4.35	19.18 ± 0.02	20.88 ± 0.24	6.38 ± 0.16	970	1956	55.7
Coya Sur 001	27.62 ± 2.65	16.85 ± 0.02	9.44 ± 0.33	5.18 ± 0.04	942	1957	10.9
El Medano 378	18.44 ± 2.57	15.99 ± 0.02	13.93 ± 0.18	5.39 ± 0.05	965	1949	45.6
Forest Vale	26.36 ± 0.61	21.27 ± 0	22.89 ± 2.53	12.61 ± 1.68	931	1908	31.0
Iran 009	93.19 ± 7.57	25.33 ± 0.02	27.91 ± 0.62	10.42 ± 0.29	968	1949	47.2
Iran 011	45.8 ± 4.19	27.88 ± 0.02	26.92 ± 0.31	9.19 ± 0.72	954	1942	54.8
Kernouve	71.82 ± 1.5	29.61 ± 0.01	46.95 ± 3.35	20.8 ± 0.44	945	1923	45.6
Lançon	32.89 ± 1.52	37.62 ± 0.04	30.8 ± 8.46	14.86 ± 4.06	938	1910	42.6
Limon Verde 004	55.26 ± 4.04	22.21 ± 0.03	32.06 ± 1.69	14.54 ± 0.15	951	1929	40.8
Los Vientos 083	40.34 ± 4.91	16.36 ± 0.03	13.46 ± 0.04	6.38 ± 0.32	924	1872	35.0
Los Vientos 147	62.3 ± 3.19	20.46 ± 0.02	18.31 ± 0.58	6.16 ± 0.46	959	1912	52.6
Los Vientos 155	50.19 ± 4.22	18.43 ± 0.02	16.35 ± 0.08	7.69 ± 0.29	929	1896	34.4
Los Vientos 416	29.7 ± 2.84	17.4 ± 0.02	14.27 ± 0.72	6.16 ± 0.26	960	1927	47.5
Los Vientos 423	77.14 ± 5.82	23.9 ± 0.02	24.18 ± 2.27	9.61 ± 0.4	945	1898	45.0
Los Vientos 432	56.35 ± 2.88	20.37 ± 0.02	19.33 ± 1.5	9.05 ± 0.51	937	1917	31.6
Monte Das Forte	58.56 ± 2.62	45.12 ± 0.01	38.34 ± 8.01	18.87 ± 1.06	947	1930	42.8
Moshampa	49.06 ± 1.66	34.39 ± 0.01	39.88 ± 3.58	21.24 ± 0.93	957	1943	39.1
Mount Tazerzait	50.11 ± 1.27	30.58 ± 0.01	37.67 ± 1.76	13.11 ± 0.23	963	1943	54.3
NWA 12475	7.59 ± 1.16	9.38 ± 0.04	38.6 ± 0.23	8.51 ± 0.13	988	1955	63.1
NWA 12546	27.18 ± 0.52	16.05 ± 0	20.42 ± 0.14	5.68 ± 0.08	988	1949	59.6
NWA 12556	47.68 ± 8.26	32.44 ± 0.03	28.05 ± 3.01	11.23 ± 2	971	1961	49.2
NWA 12961	80.77 ± 2.17	35.53 ± 0.01	45.48 ± 1.68	16.3 ± 0.53	977	1936	54.5
NWA 13838	−0.01 ± 1.11	10.18 ± 0.04	9.24 ± 0.46	6.32 ± 0.02	939	1964	6.7
NWA 7283	26.46 ± 4.75	27.39 ± 0.04	36.31 ± 0.21	8.96 ± 0.2	995	1966	61.7
NWA 8628	11.56 ± 5.97	11.95 ± 0.02	7.91 ± 0.46	3.52 ± 0.19	947	1912	36.3
NWA 8275	43.74 ± 1.99	26.72 ± 0.01	29.92 ± 0.44	5.11 ± 0.42	1012	1968	64.9
NWA 8477	52.66 ± 3.31	33.54 ± 0.02	30.75 ± 3.14	13.68 ± 0.41	953	1949	43.6
Paposo 012	68.72 ± 4.24	21.93 ± 0.02	20.5 ± 0.91	8.33 ± 0.33	945	1911	38.7
Saint-Séverin	10.21 ± 0.61	17.57 ± 0	25.92 ± 0.35	5.03 ± 0.3	994	1954	65.3
Soko-Banja	40.43 ± 1.84	29.73 ± 0.01	31.02 ± 3.26	14.75 ± 0.75	972	1964	45.1
Ste. Marguerite	27.73 ± 0.65	21.77 ± 0	25.56 ± 1.58	15.27 ± 0.35	941	1946	20.8
Tamdakht	40.44 ± 0.83	24.53 ± 0	19.16 ± 2.85	10.12 ± 1	944	1919	39.6
Taqtaq-e Rasoul	24.56 ± 1.19	32.15 ± 0	31.63 ± 5.85	15.1 ± 0.72	939	1916	38.2
Tuxtuac	78.11 ± 1.01	33.82 ± 0.21	38.52 ± 0.68	11.7 ± 0.35	1001	1961	59.0
Viñales	69.55 ± 2.09	29.76 ± 0.04	42.16 ± 1.96	14.83 ± 0.33	957	1942	53.5

work (Figs. 1 and 2, Tables 3 and 4). The exception is LAR 06469 (L > 3.6) for which the position is close to 2100 nm. We, thus, conclude that the pyroxene abundance of all but possibly one of the OCs considered in the present work is dominated by orthopyroxene.

19 of the EOCs show an increase of reflectance at wavelengths shorter than 500 nm. This is an experimental artifact related to the measuring instrument. Because of the steep decrease in the light source intensity below 500 nm, the reflectance system becomes sensitive to background signal below this wavelength, in particular for dark samples. This introduces a strong signal at low wavelengths.

The shock values of UOCs range from S1 to S3 with the exception of BTN 00302 (LL 3.1–3.4) and LAR 06279 (LL 3.05–3.1) which have shock stages of S4/S5 (Table 1). Shock darkened samples are identified through the existence of melt pockets and veins of metal and sulfides in olivine and pyroxene fractures. The shock pressures estimated to be needed for this process corresponds to shock stages between S5 and S6 (Kohout et al., 2020). Some small melt pockets and shock veins were visible in the thin sections of samples BTN 00302 and LAR 06279. Out of these two samples, only BTN 00302 seems to show a rather flat, featureless spectrum (Fig. 1) as is common for shock darkened chondrites.

As mentioned above, EOC NWA 13838 (L5) is shock darkened as stated in the "Meteoritical Bulletin Database" (2021) which is confirmed by the absence of spectral features in Fig. 2. Furthermore, the presence of shock veins and melt pockets is mentioned for EOCs Iran 009 (LL5), Moshampa (LL5), NWA 8275 (LL7) and Viñales (L6) ("Meteoritical Bulletin Database," 2021). None of these samples show noticeable difference in band depths in comparison to the other EOCs considered in the present work (Fig. 2).

Therefore, with the exception of BTN 00302 (LL 3.1–3.4) and NWA 13838 (L5), we conclude that none of the OCs considered in the present work experienced shock darkening. This does not mean that shock did not impact their spectra at all, but no obvious consequence of shock can be observed.

3.2.1. *Reflectance spectral features*

In Tables 3 and 4, the reflectance spectral features determined from the spectra as explained in Section 2.2 are given for UOCs and EOCs, respectively. Listed are the visual slope at wavelength lower than 700 nm, the 700 nm peak reflectance value, the 1000 nm and 2000 nm band depths and band positions and the Ol/(Ol + Px) ratio. The visual slopes range from 1.4E-4 nm^{-1} (Chainpur (LL3.4)) to 6.44E-4 nm^{-1} (LAR 06279 (LL 3.05)) for UOCs and from 7.59E-5 nm^{-1} (NWA 12475 (LL6)) to 9.32E-4 nm^{-1} (Iran 009 (LL5)) for EOCs. The 700 nm peak reflectance ranges from 9.4% (EET 87735 (LL3.05)) to 22.5% (Parnallee (LL3.6)) for UOCs and from 9.4% (NWA 12475 (LL6)) to 45.1% (Monte Das Forte (L5)) for EOCs. The 1000 nm band is located between 920 nm and 1020 nm for UOCs and EOCs. The depth of the 1000 nm band ranges from

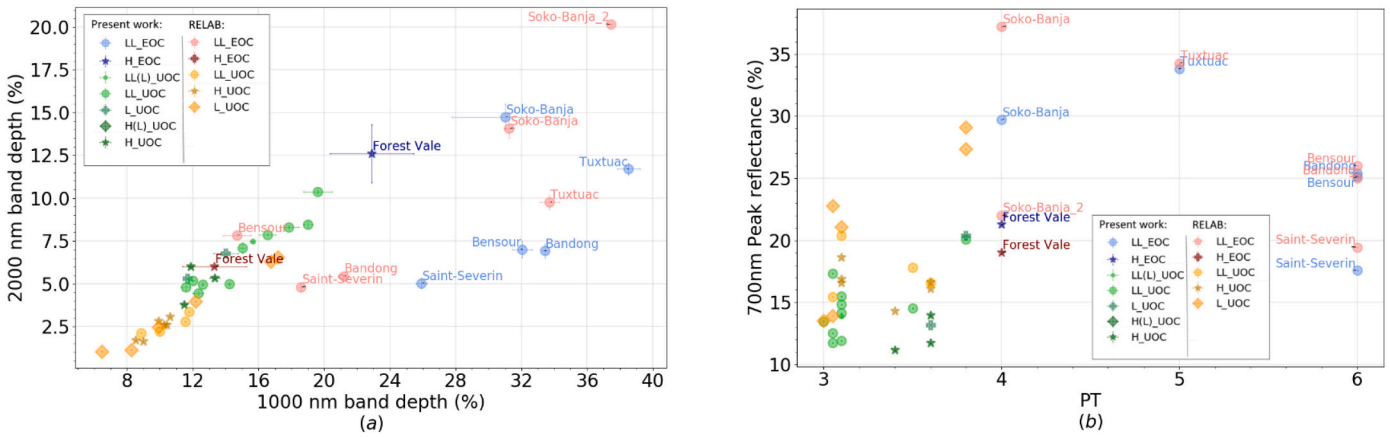

Fig. 3. Comparison of the spectral features of the UOCs and EOCs measured in the present work with those already present in the RELAB database. (a) 2000 nm band depth (%) over the 1000 nm band depth (%) (b) 700 nm peak reflectance (%) over the PT.

9.0% (MIL 05050 (LL3.1)) to 20.7% (Parnallee (LL3.6)) for UOCs and from 7.91% (NWA 8268 (L4)) to 46.95% (Kernouvé (H6)) for EOCs. The 2000 nm band is located between 1840 nm and 2020 nm for UOCs and between 1870 nm and 1970 nm for EOCs. The exception is UOC LAR 06469 (L > 3.6) which shows a 2000 nm band position at 2098 nm. The 2000 nm band depths range from 3.5% (Krymka (LL3.2)) to 10.4% (ALH 84086 (LL3.8)) for UOCs and from 3.52% (NWA 8628 (L4)) to 21.24% (Moshampa (LL5)) for EOCs. Lastly, the Ol/(Ol + Px) ratio ranges from 18.8% (Bremervörde (H(L)3.9)) to 54.3% (LEW 88617 (LL3.6)) for UOCs and from 10.8% (Coya Sur 001 (H5)) to 65.3% (Saint-Séverin (LL6)) for EOCs.

3.2.2. *Grain size effects on reflectance spectral features*

The approximate grain size of the powders of EOCs Kernouvé (H6), Ste. Marguerite (H4), NWA 12961 (L7), Monte das Forte (L5), Moshampa (LL5) and Los Vientos 423 (H6) and UOC RBT 04251 (LL3.4) for different grinding times are listed in Table 5. For EOCs, the grain size of the powders decreases from being hand ground to being ground for 5 min in the ball mill to being ground for 10 min (20 min) in the ball mill. After hand-grinding, the powders are coarse grained when examining them under an optical binocular. After 5 min in the ball mill, the powder becomes significantly finer. Overall, it consists of a fine grayish/whitish powder (~a few μm grain size) mixed with several dark grains that can have much larger sizes (see Table 5). In some cases, the fine-grained powder initially sticks together forming a fine grained "sand cake"-like structure but can be broke apart easily using a needle. After 10 min in the ball mill, the powders become darker to the naked eye. They show a similar texture to the powder ground for 5 min but less large dark grains can be seen mixed with the fine-grained grayish/whitish powder. The maximum size of the largest grains decreases even more (see Table 5). The same can be said after grinding Kernouvé for 20 min. For the UOC RBT 04251 (LL 3.4), on the other hand, the grain size after hand grinding is already small enough, that it is comparable to the grain size of EOCs after 5–10 min of grinding in the ball mill (Table 5). After 5 min of grinding the UOC in the ball mill the grain size decreases and becomes <150 μm. Fig. 4a shows the reflectance spectra of the OCs at different grain sizes. The spectral features determined from the spectra are listed in Table 5. As can be seen, spectral features immediately become much smaller after 5 min of grinding in the ball mill. Especially for UOC RBT 04251 the spectrum practically becomes featureless. Therefore, the UOC

Table 5
List of the spectral features determined for EOCs at different grain sizes. Listed are samples measured after being hand ground (hg), after being ground for 5 min in a ball mill, after being ground for 10 min in a ball mill and after being ground for 20 min in a ball mill. Given are the visual slope at wavelengths lower than 700 nm (for spectra where it could be determined), the 700 nm peak reflectance, the 1000 nm and 2000 nm band depth and positions as well as the Ol/(Ol + Px) ratio. All spectral features where determined as explained in Section 2.2 following Eschrig et al. (2021).

sample	approx. size of biggest grains (μm)	Visual slope (10^{-5} nm^{-1})	700 nm Peak refl. (%)	1000 nm Band Depth (%)	2000 nm Band Depth (%)	1000 nm Band Pos. (nm)	2000 nm Band Pos. (nm)	Ol/(Ol + Px) (%)
Kernouve hg	<1000	66.51 ± 2.94	29.61 ± 0.01	46.99 ± 3.6	20.84 ± 0.44	949	1924	45.4
Kernouve 10 min	<500	–	22.29 ± 0.01	8.57 ± 0.9	3.71 ± 0.53	932	1894	46.3
Kernouve 20 min	<150	–	12.23 ± 0.01	4.03 ± 0.04	2.38 ± 0.01	944	1962	21.4
Monte Das Forte hg	<1000	65.14 ± 5.61	45.12 ± 0.01	38.55 ± 0.03	19.89 ± 0.11	956	1934	42.8
Monte Das Forte 5 min	<500	10.73 ± 1.38	37.2 ± 0.01	16.85 ± 21.81	9.13 ± 2.26	930	1946	22.7
Monte Das Forte 10 min	<200	–	25.93 ± 0.01	9.73 ± 0.53	4.77 ± 0.29	929	1933	24.7
Moshampa hg	<800	49.06 ± 1.66	34.39 ± 0.01	39.88 ± 3.58	21.24 ± 0.93	957	1943	39.1
Moshampa 5 min	<500	39.68 ± 5.26	21.49 ± 0.01	15.71 ± 0.54	9.29 ± 0.22	926	1982	−4.2
Moshampa 10 min	<400	–	14.79 ± 0.01	6.84 ± 0.42	3.54 ± 0.2	928	1947	20.4
NWA 12961 hg	<2000	80.77 ± 2.17	35.53 ± 0.01	45.48 ± 1.68	16.3 ± 0.53	977	1936	54.5
NWA 12961 5 min	<1500	8.01 ± 1.35	26.6 ± 0.03	11.13 ± 3.73	3.01 ± 0.48	946	1917	54.6
NWA 12961 10 min	<350	–	15.17 ± 0.01	6.16 ± 0.04	1.99 ± 0.28	933	1919	51.9
Ste Marguerite hg	<1040	27.73 ± 0.65	21.77 ± 0	25.56 ± 1.58	15.27 ± 0.35	941	1946	20.8
Ste Marguerite 5 min	<700	3.02 ± 0.51	19.2 ± 0.01	9.02 ± 3.02	3.56 ± 0.17	931	1931	37.0
Ste Marguerite 10 min	<500	–	13.55 ± 0.01	4.67 ± 0.03	3.28 ± 0.04	914	1889	−27.2
Los Vientos 423 hg	<1000	77.14 ± 5.82	23.9 ± 0.02	24.18 ± 2.27	9.61 ± 0.4	945	1898	45.0
Los Vientos 423 5 min	<500	62.85 ± 3.32	22.25 ± 0.01	10.2 ± 0.89	4.51 ± 0.06	931	1973	12.8
Los Vientos 423 10 min	<400	39.17 ± 3.35	15.4 ± 0.01	5.48 ± 0.15	3.54 ± 0.04	948	2059	4.1
RBT 04251 hg	<400	49.63 ± 1.95	16.29 ± 0	13.65 ± 0.21	5.57 ± 0.05	958	1907	38.3
RBT 04251 5 min	<150	15.91 ± 2.12	14.08 ± 0.01	3.72 ± 0.05	1.43 ± 0.06	929	2081	37.6

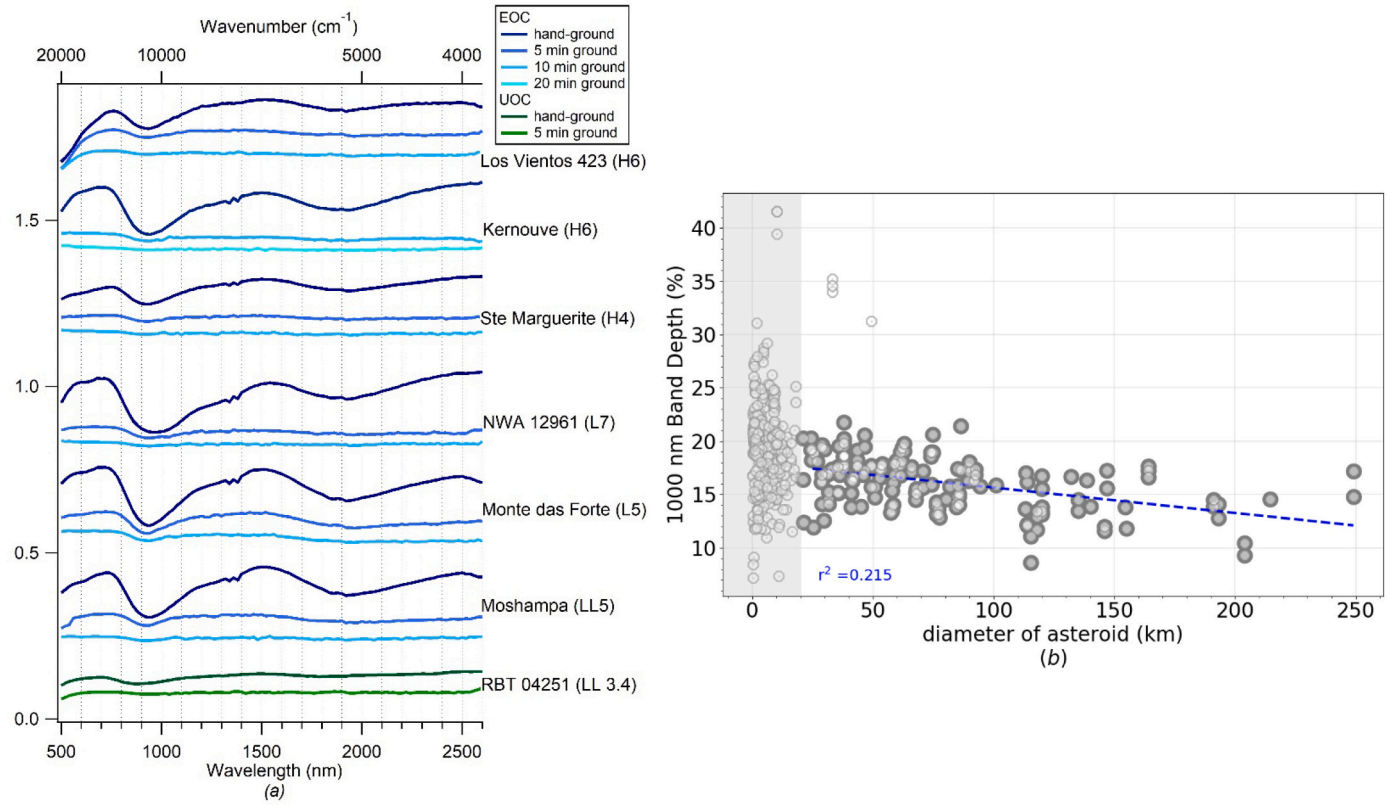

Fig. 4. (a) Reflectance spectra of EOCs Kernouvé, Ste. Marguerite, NWA 12961, Monte das Forte, Moshampa and Los Vientos 423 as well as UOC RBT 04251 at different grain sizes. For each sample a spectrum is shown after being hand ground and ground for 5 min, 10 min and 20 min in a ball mill. The spectra are shifted along the y-axis for better visibility and samples were sorted by increasing metamorphic grade from bottom to top. (b) the 1000 nm band depth of the S-type asteroids over their diameter. Only asteroids highlighted in dark gray were used for the fit.

is not ground for longer periods of time. For EOCs, basically no features are left in the spectra after 10 min or even 20 min (Kernouvé) in the ball mill (Fig. 4a). The 1000 nm band depths decrease by 91.41% of their original depth for Kernouvé (H6) after 20 min of grinding and by 86.46% of their original depth for NWA 12961 (L7) after 10 min. For the 2000 nm band depths similar decreases can be observed. The 1000 nm band positions tend to shift to shorter wavelengths with decreasing grain size while the 2000 nm band position seems to decrease in some cases and remain comparable in other cases (Table 5). It needs to be mentioned here that the determination of the band position becomes less accurate as the band depths decrease since the signal to noise ratio (SNR) becomes more important in comparison to the spectral features. Interestingly, the 700 nm peak reflectance decreases with grain size as well, dropping to more than half of the original value for most samples after 10 min of grinding. The visual slope becomes less steep with decreasing grain size (Table 5). Due to the SNR and the increase of reflectance at wavelengths shorter than 500 nm due to an experimental artifact (see Section 3.2) the visual slope could not be determined for samples ground longer than 5 min.

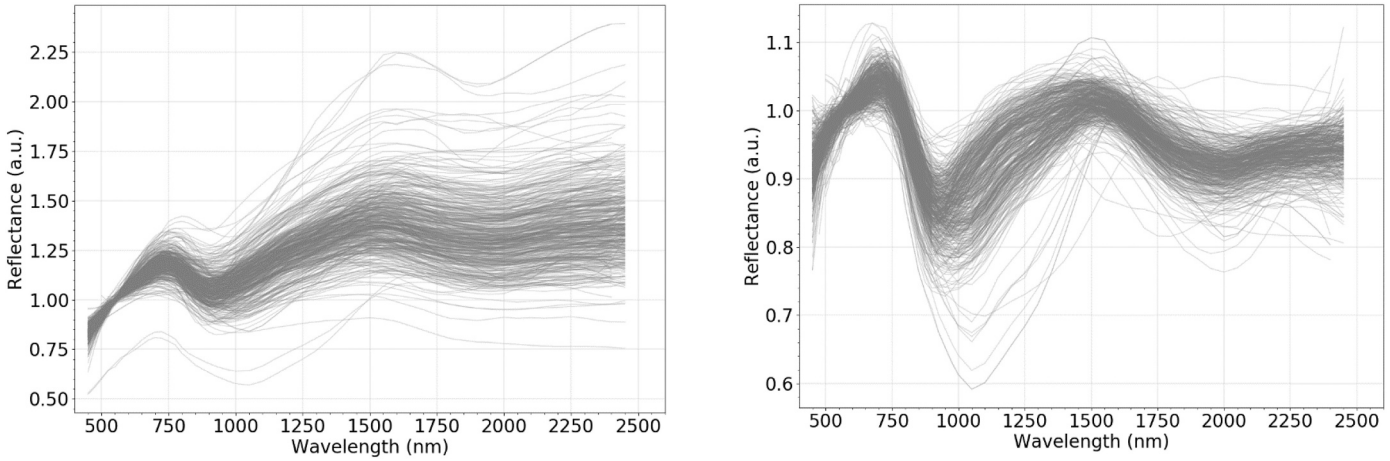

Fig. 5. (a) Reflectance spectra of the 466 raw S-type asteroid spectra considered in the present work. (b) Reflectance spectra of the 466 de-space weathered S-type asteroid spectra considered in the present work.

3.2.3. S-type Asteroid reflectance spectral features

The reflectance spectra of the 466 S-type asteroids which were included in the present work as a comparison to OCs are shown in Fig. 5. Shown are both the raw and de-space weathered S-type asteroid spectra. As expected (Brunetto et al., 2006), de-space weathering the spectra mainly modifies the spectral slope. Looking at the de-space weathered S-type spectra, a low spectral variability can be seen (Fig. 5b). The visual slope ranges from 1.11E-4 nm^{-1} to 2.35E-3 nm^{-1} and the 700 nm peak relative reflectance from 99.4% to 112.9%. The 1000 nm and 2000 nm band depths vary from 7.21% to 41.57% and 1.08% to 20.51%, respectively. The 1000 nm and 2000 nm band positions are located between 870 nm to 1070 nm and between 1630 nm to 2220 nm, respectively. Lastly, the Ol/(Ol + Px) ratio ranges from 0.46% to 70.72%. All spectral values related to S-type asteroids are available online at the CDS.[3]

4. Discussion

4.1. Comparing EOC and UOC reflectance spectra

EOCs are thermally metamorphosed UOCs. With increasing metamorphic grade, the chondrites progressively approach chemical equilibrium, transferring elements such as iron from the matrix to chondrule silicates (e.g., Krot et al. (2014)). There is, indeed, a decrease of the total abundance of metal (mostly present in the matrix) as well as a loss of small grained metal particles in the matrix. This modification of the iron valence state (from Fe^0 to Fe^{2+} and Fe^{3+}) influences the position and depth of the 1000 nm and 2000 nm absorption bands. The mafic silicate bands become deeper and shift to shorter wavelengths with increasing metamorphic grade. The equilibration process starts at lower temperatures for olivine than for pyroxene (Scott and Jones, 1990) because of a higher diffusivity of Fe—Mg in olivine. Thus, it is expected to see an increase of band depth and a small shift to shorter wavelengths (less than 50 nm) for the 1000 nm olivine band even with less metamorphosed OCs.

As expected, the 1000 nm and 2000 nm bands of the EOCs are deeper than those of UOCs with band depths increasing with increasing petrologic type (PT) (see Fig. 6 a and b, *p*-values of 2.48E-10 and 3.09E10–6, respectively). There are some exceptions (12 EOCs out of 39) to this trend especially for the 2000 nm band. Specifically, samples Coya Sur 001 (H5), Catalina 024 (H4), Catalina 309 (L5), El Medano 378 (L6), Los Vientos 083 (H4), Los Vientos 147 (L6), Los Vientos 155 (H5), Los Vientos 416 (L4), Los Vientos 432 (H5), NWA 8628 (L4), Paposo 012 (H6) and Tamdakht (H5) show very similar 1000 nm and 2000 nm band depths to UOCs. Samples Tuxtuac (LL5), Bensour (LL6), Bandong (LL6), Saint-Severin (LL6), NWA 7283 (LL6), NWA 12475 (LL6), NWA 8275 (LL7) and NWA 12546 (LL7) show stronger 1000 nm band depths but 2000 nm band depths similar to UOCs. As expected, the increase in band depth is seen more clearly for the 1000 nm band than for the 2000 nm band in EOCs. Overall, the band positions are comparable between UOCs and EOCs (Fig. 6c and d, p-values of 0.433 and 0.0319, respectively). The 1000 nm band position of a few LL EOCs exceeds those of the UOCs. In the 2000 nm region, EOCs collectively show band positions between 1900 nm and 1970 nm. The 2000 nm band positions of UOCs ranges from 1840 nm to 2020 nm making their band positions comparable or lower than those of EOCs. The outlier, LAR 06469 (L > 3.6) at 2098 nm shows a secondary band around 2400 nm shifting the 2000 nm band position to longer wavelengths. The peak reflectance at around 700 nm is on average higher for EOCs than for UOCs (Fig. 6e, p-values of 1.26E-9). Lastly, the visual slope at wavelengths lower than 700 nm of EOCs is comparable to slightly steeper than for UOCs (Fig. 6f, p-values of 3.5E-3).

[3] Data is only available at CDS via anonymous ftp to cdsarc.u-strasbg.fr (130.79.128.5) or via https://cdsarc.unistra.fr/viz-bin/cat/J/other/Icar

The comparison of EOC and UOC reflectance spectra, therefore, shows that while there is some spectral variability, there seems to be more of a continuum of spectral signatures. EOCs can show deeper 1000 nm and 2000 nm band depths and higher peak reflectance values but several EOC spectra are also comparable to UOC spectra. In addition, the band positions are comparable between UOCs and EOCs. Overall, the maximum 2D KS p-value of these sample pairs was 0.433, indicating a statistical difference in the underlying distributions.

4.2. Comparing H, L and LL reflectance spectra

The reflectance spectra of OCs are dominated by contributions of the iron-bearing mineral phases olivine (Ol) and pyroxene (Px) (Vernazza et al., 2014 and ref. therein) in the 1000 nm and 2000 nm region. The Ol/(Ol + Px) ratio is thus particularly relevant for spectral comparisons between OCs. In particular Vernazza et al. (2014) found that the Ol/(Ol + low-Ca Px) ratio of H decreases significantly in comparison to those of L and LL with increasing metamorphic grade. This observation allowed them to distinct H from L and LL and to advocate for the existence of two S-type asteroid groups: H-like and LL-like (see more in Section 4.3). In the following section we explore the spectral differences we could observe between H, L and LL.

Among EOCs, LL are spectrally distinct from H and L. Indeed, when considering the 1000 nm and 2000 nm band depths, EOC LLs Tuxtuac (LL5), Bensour (LL6), Bandong (LL6), Saint-Severin (LL6), NWA 7283 (LL6), NWA 12475 (LL6), NWA 8275 (LL7) and NWA 12546 (LL7) plot separately (Fig. 7a). Additionally, EOC LL show 1000 nm band positions around 980–1020 nm while for H and L the position is shifted to shorter wavelengths around 920–980 nm (Fig. 6c). The exceptions to this rule are the LL Iran 009 (LL5), Moshampa (LL5), NWA 12556 (LL5) and Soko Banja (LL4), having a 1000 nm band positions around 960–970 nm, making them comparable to H and L. While H and L of PT > 5 show signs of deepening of both the 1000 nm and 2000 nm band as well as shifting of the 1000 nm band to shorter wavelengths due to the equilibration process, LL seem to be less affected by this process and only show a deepening of the 1000 nm band in comparison to UOCs. Since LL type have a lower total metal abundance than H and L (Scott and Krot, 2003), they are less effected by the decrease of the total iron in metal along the metamorphic sequence and hence show a smaller shift of the 1000 nm band to shorter wavelengths and less deep 2000 nm band depths in comparison to H and L type EOCs. For UOCs no clear spectral separation between H, L and LL can be seen.

In Fig. 7b, the Ol/(Ol + Px) ratios of the EOCs and UOCs are plotted over their PT. The majority of OCs between PT3–4 have Ol/(Ol + Px) ratios between 0.3 and 0.6. A few UOCs show lower ratios <0.3. In contrast to the work by Vernazza et al. (2014) no systematic difference in the Ol/(Ol + Px) ratio between H and L, LL is observed. For PT 5–7 an increase in ratios can be seen up to 0.7. It seems that within each PT group ≥4, H show lower ratios than L and LL with the exception of Moshampa (LL5), Limon Verde 004 (L6) and El Médano 378 (L6) which show low Ol/(Ol + Px) ratios within their group despite being L and LL, not H. For UOCs no distinction of H, L and LL based on the Ol/(Ol + Px) ratio is possible.

The different conclusions in the present work and in Vernazza et al. (2014) can be explained by the use of different classifications and PT values. The classification into H, L and LL of the UOCs in the present work has been reassessed through magnetic susceptibility and petrography: more than half (24/41) of the UOCs were reclassified in the present work (see Table 1 and Section 3.1). Out of the 16 UOCs which were considered both in the present work and by Vernazza et al., (2014), 10 have been reclassified. Moreover, the PT values of the UOCs in this work were taken from Bonal et al. (2016) based on the structural order of the polyaromatic carbonaceous matter assessed by Raman spectroscopy. They showed in their study that the PT initially assigned for the sample declaration in the Meteoritical Bulletin are not necessarily correct as most of the time they only reflect preliminary descriptions of

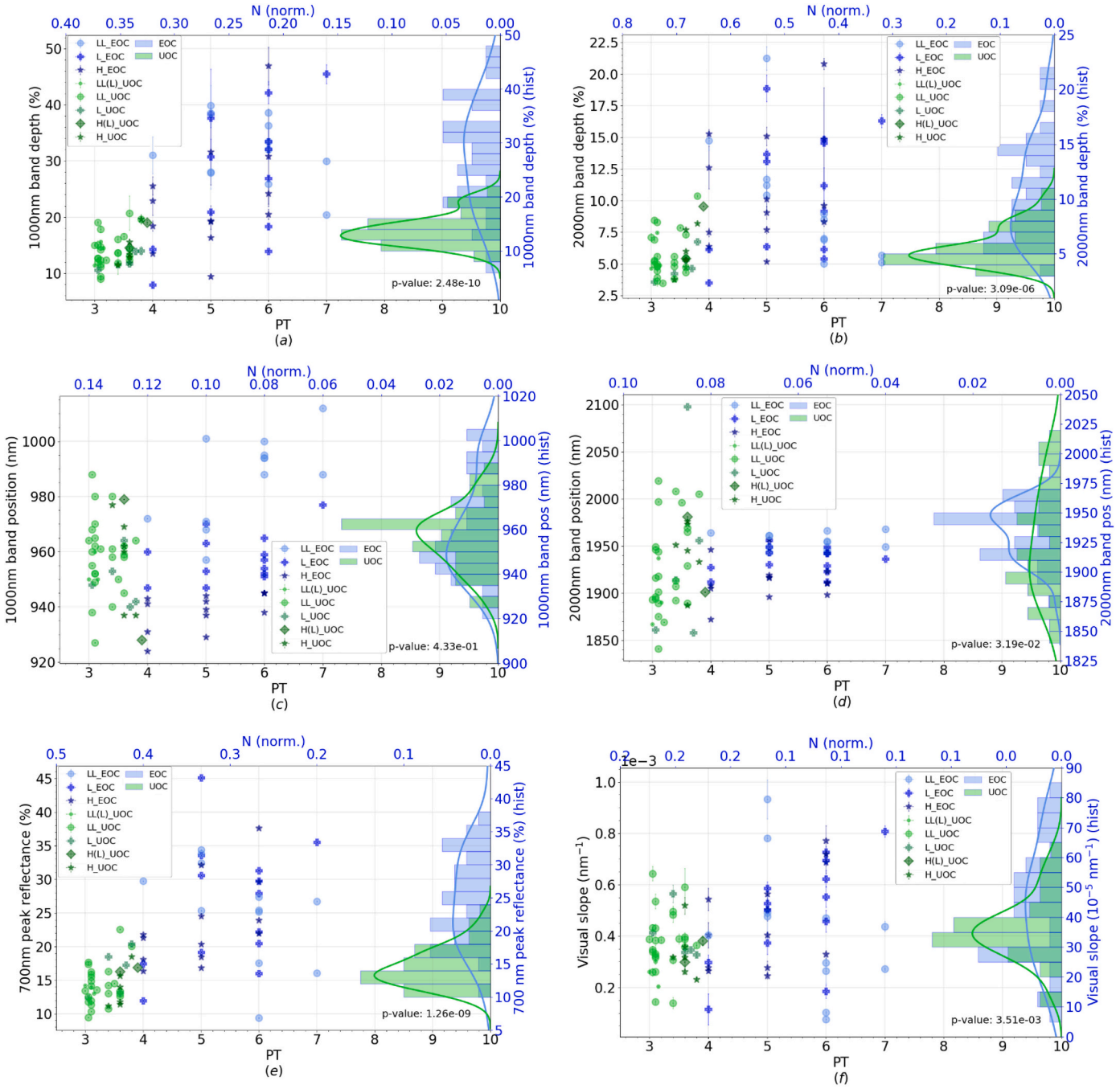

Fig. 6. Comparison of the spectral features determined for UOCs and EOCs with their petrologic type (PT). Shown are: (a): The 1000 nm band depth over the PT, (b): The 2000 nm band depth over the PT, (c): 1000 nm band position over the PT, (d): 2000 nm band position over the PT, (e): 700 nm peak reflectance over the PT and (f): Visual slope over the PT. For each plot the y-axis is depicted as a histogram on a second y-axis to illustrate the separation between UOCs and EOCs. Each histogram is plotted with its gaussian kernel density estimate (kde). A 2D Kolmogorov Smirnof Test (2D KS-test) was performed for each spectral feature and the *p*-value is given as a measure of the distance between the two histograms in each plot.

samples. Lastly, with the reclassification of 24 out of the 41 UOCs we only have 8H, 4 L but 29 LL or LL(L) UOCs in the present work. This disproportionate representation of the different classes among UOCs increases the difficulty of finding systematic differences between them.

In conclusion, LL of PT $\geq$ 5 can be distinguished from H and L based on their 2000 nm band depth and 1000 nm band position which is shallower and shifted to longer wavelengths for LL in comparison to H and L. This is in agreement with previous works which found that LL can be recognized based on their Ol/(Ol + Px) ratio (Dunn et al., 2010b). The Ol/(Ol + Px) ratios of EOCs can slightly exceed those of UOCs for PT > 4. However, the majority of the spectral indicators used here are comparable between EOCs and UOCs. This is in contrast to the observations made by Vernazza et al. (2014) according to which the ratio becomes lower with increasing metamorphic grade for H. A slight separation between H, L and LL is visible within each PT groups $\geq$4 of EOCs for our data, with ratios decreasing from LL and L to H.

4.3. *Ordinary chondrites versus S-type asteroids*

The link between S-type Asteroids and EOCs has previously been confirmed by the sample return of the Hayabusa-1 space mission (Nakamura et al., 2011). In their work on UOCs, Vernazza et al. (2014)

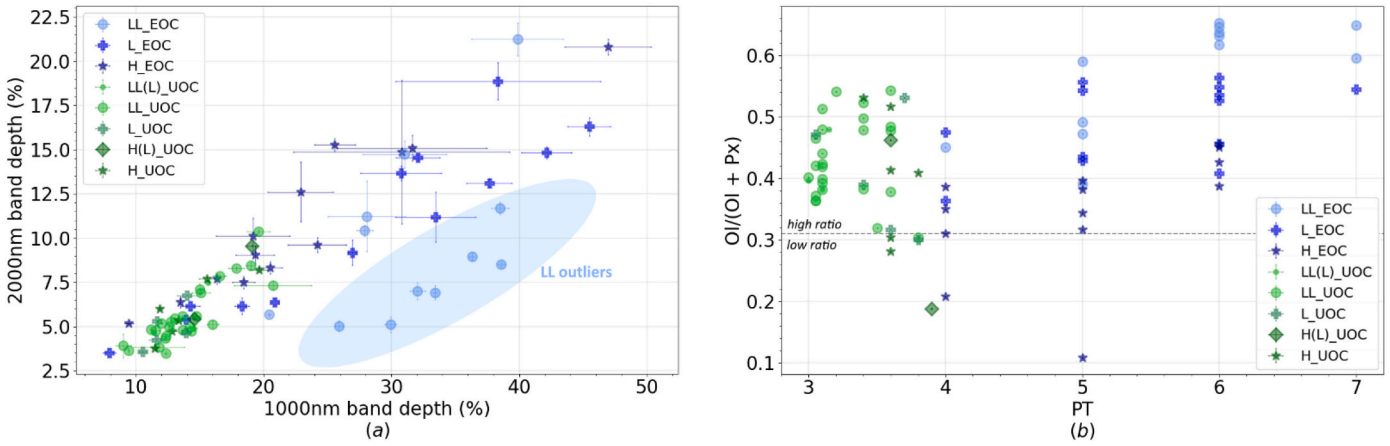

Fig. 7. (a) 2000 nm band depth over the 1000 nm band depth of UOCs and EOCs. (b) Ol/(Ol + Px) ratio over the PT for EOCs and UOCs.

found that S-type asteroids can be sub-divided into two distinct compositional groups: H-like and LL-like S-type asteroids. This conclusion was based on the observation of a clear separation of the Ol/(Ol + Px) ratio of H versus L and LL UOCs and a bimodality in the Ol/(Ol + Px) ratios of a large set (83) of S-type asteroid spectra.

In the present work we have found that while EOCs can have distinct spectral features from UOCs there seems to be more of a continuum, with the exception of the 2000 nm band position which is comparable between all UOCs and EOCs (Section 4.1). In this section we explore if the observations of Vernazza et al. (2014) can be reproduced with our larger dataset. Will the dichotomy between H and L, LL UOCs be visible for EOCs as well? Lastly, can a difference between equilibrated and unequilibrated S-type asteroid surfaces be seen?

4.3.1. PCA and space weathering

For the comparison of meteorite to asteroid reflectance spectra, space weathering plays an important role. As explained in Section 2.2, space weathering was here removed from the S-type asteroid spectra before determining the spectral values. However, the unknown degree of space weathering on the asteroids surfaces yields a systematic uncertainty on the spectral parameters which cannot be quantified without detailed knowledge of the asteroids surface properties. In the following,

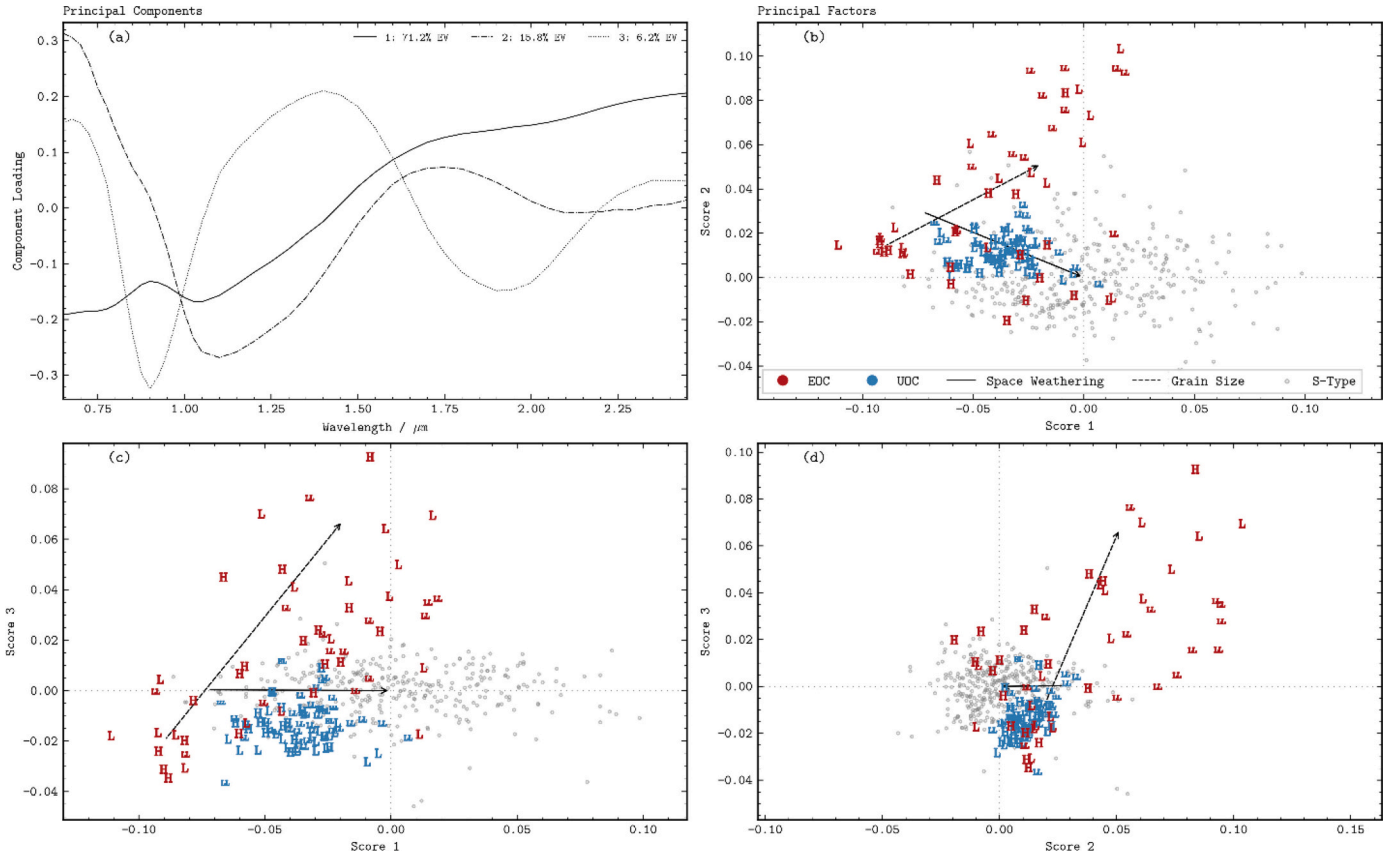

Fig. 8. Principal Components Analysis of the S-type and OC spectra. (a) The first three principal components computed from the S-type spectra. The labels give the percentage of explained variance (EV) for each component. (b), (c) and (d) show the principal scores of the S-type spectra (gray circles), EOCs (red) and UOCs (blue). The symbols give the mineralogic group of each spectrum. The solid black and dashed black arrows give the directions of increased space weathering and grain size respectively, as outlined in the text. (For interpretation of the references to colour in this figure legend, the reader is referred to the web version of this article.)

the influence of space weathering is thus analyzed as a gradual change of the asteroid spectral properties via PCA.

The first three PCs of the raw S-type asteroid spectra are shown in Fig. 8a. The percentages assigned to each component in the legend state the explained variance (EV) of the component. The EV quantifies the ratio of variance retained in the projection of the data along the PC to the total variance in the data. As can be seen, the PC1 contributes to about 78% of the whole information in the asteroid spectra, while PC2 and PC3 contribute 11.9% and 5.3%, respectively.

PC1 resembles the overall slope of the asteroid spectra with a 1000 nm olivine band. Comparing the PC1 to the raw asteroid spectra in Fig. 5, it becomes apparent that the main variability within S-type spectra is given by their slope. PC2 and PC3 in Fig. 8a resemble the absorption features of olivine and orthopyroxene, respectively. Disregarding the slope, the main difference between the 466 S-type spectra is given by their surface mineralogy, which is to be expected.

Fig. 8b, c and d show the principal scores of the S-type spectra in comparison to the H, L and LL EOC and UOC spectra. Fig. 8b shows the principal scores 1 versus 2. As the PCs have been computed from the raw S-type spectra, the asteroids are centered around the score 0. Most OCs have a negative score 1 as they are less red than the average raw S-type. The positive score 2 of most OC indicates an increase in the olivine-like absorption signature around 1000 nm in comparison to S-type spectra. When comparing the principal scores 2 and 3 in Fig. 8d the difference in the mineralogical signatures are highlighted: EOCs show much stronger principal score 2 and 3 than UOCs and S-type spectra, indicating a stronger olivine- and orthopyroxene-like signature in EOCs. Furthermore, LL EOCs have considerably stronger principal score 2 (olivine-like) setting them apart from L and H. This is in accordance with the observation based on spectral parameters (Section 4.2).

To quantify the influence of space weathering on the reflectance spectra, we computed the principal scores of the mean S-type spectrum after de-weathering it. The line between the de-weathered mean spectrum and the raw mean (by definition at score 0) is shown as solid black arrow in the principal score plots of Fig. 8. We interpret this as the direction in which S-type spectra are shifted with increasing degree of space weathering within each plot. What can be seen, is that de-space weathering the S-type asteroid spectra results in (i) spectral blueing (principal score 1 shifting to negative values) (ii) an increase of olivine-like absorption features (principal score 2 shifting to positive values) and (iii) an increase in orthopyroxene-like features (principal score 3 shifting to positive values). It also shows that a better match between S-type asteroids and OCs can be achieved, depending on how strongly the S-type spectra are de-space weathered or in other words: the more the S-type asteroid gets space weathered, the more it will shift from having spectral features comparable to UOCs, to comparable to EOCs, to not matching at all.

In conclusion, it is important to note that a match between S-type and OC spectra is very dependent on the treatment of the SW in the S-type asteroid spectra. SW mostly influences the slope of S-type spectra. Since such a big variability in slopes is seen for S-type spectra in Fig. 5a, in the following parts we will compare OCs with de-space weathered S-type spectra in order to be less sensitive to slope and avoid formulating a hypothesis based on the extent of SW experienced by the asteroid surfaces.

4.3.2. Comparison of OCs with de-space weathered S-type asteroids

In Fig. 9a the 1000 nm and 2000 nm band depths of the UOC and EOC spectra are compared with those of the de-space weathered S-type asteroid spectra. As can be seen, the majority of the S-type asteroid spectra cluster closer to UOCs and EOCs with faint spectral features. This is consistent with previous works (Eschrig et al., 2021) where the end member S-type spectra taken from DeMeo et al. (2009) match UOCs. In Fig. 9b the 700 nm peak reflectance (for spectra normalized to 550 nm) over the 1000 nm band depth of the S-type asteroids is compared to those of UOCs and EOCs. It shows that the majority of UOCs and EOCs show stronger 700 nm peak reflectance values than S-type asteroids.

In Fig. 10 a histogram of the Ol/(Ol + Px) ratios of the de-space weathered S-type asteroids considered in the present work is shown. A large peak centered around 50–60% can be seen. No bimodality is visible as was previously observed by Vernazza et al. (2014). The analytical method for determining the Ol/(Ol + Px) ratio used in the present work differs from Vernazza et al. (2014). Here, we used the Band Area Ratio (BAR) to calculate the ratio as indicated in Dunn et al. (2010b). The advantages of this method are that it is simple yet sufficient for the present work. It does not require any assumptions about e.g. grain size since it can be determined directly from the spectra. In contrast, Vernazza et al. (2014) applied a more sophisticated Radiative transfer model to determine the Ol/(Ol + low-Ca Px) ratio. Hypothesis such as the grain size distribution are thus necessary. Furthermore, Vernazza et al. (2014) excluded objects of collisional families in their histogram.

Fig. 10 also includes the Ol/(Ol + Px) ratios of all 41 UOCs and 39 EOCs. Two things can be seen: i) UOCs show ratios slightly to the left of the center of the peak of S-type asteroid ratios and ii) EOCs, whose ratios are slightly higher than those of UOCs, fall right in the center of the S-type asteroid ratio peak. This indicates that the average Ol/(Ol + Px) ratio of S-type asteroids match those of EOCs better than those of UOCs.

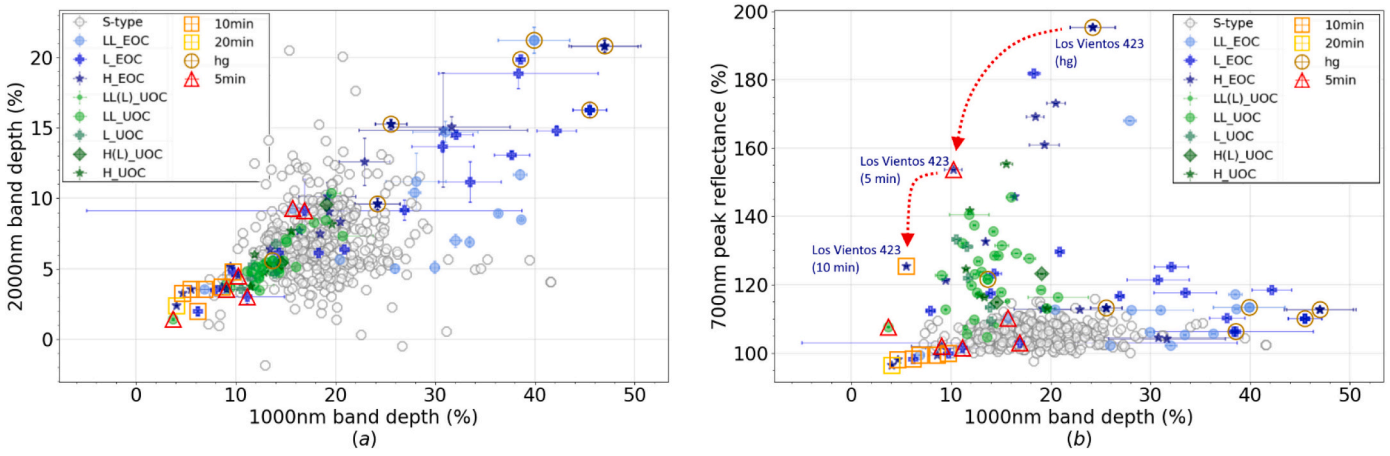

Fig. 9. Comparison of the de-space weathered S-type asteroids with EOCs and UOCs. (a) 2000 nm band depth over the 1000 nm band depth. (b) 700 nm peak relative reflectance (of spectra normalized to 550 nm) over the 1000 nm band depth. Samples that were measured at different grainsizes are outlined as follows: hand-ground (hg) by brown circles, 5 min ground in a ball mill by red triangles, 10 min ground in a ball mill by orange squares and 20 min ground in a ball mill by yellow squares. (For interpretation of the references to colour in this figure legend, the reader is referred to the web version of this article.)

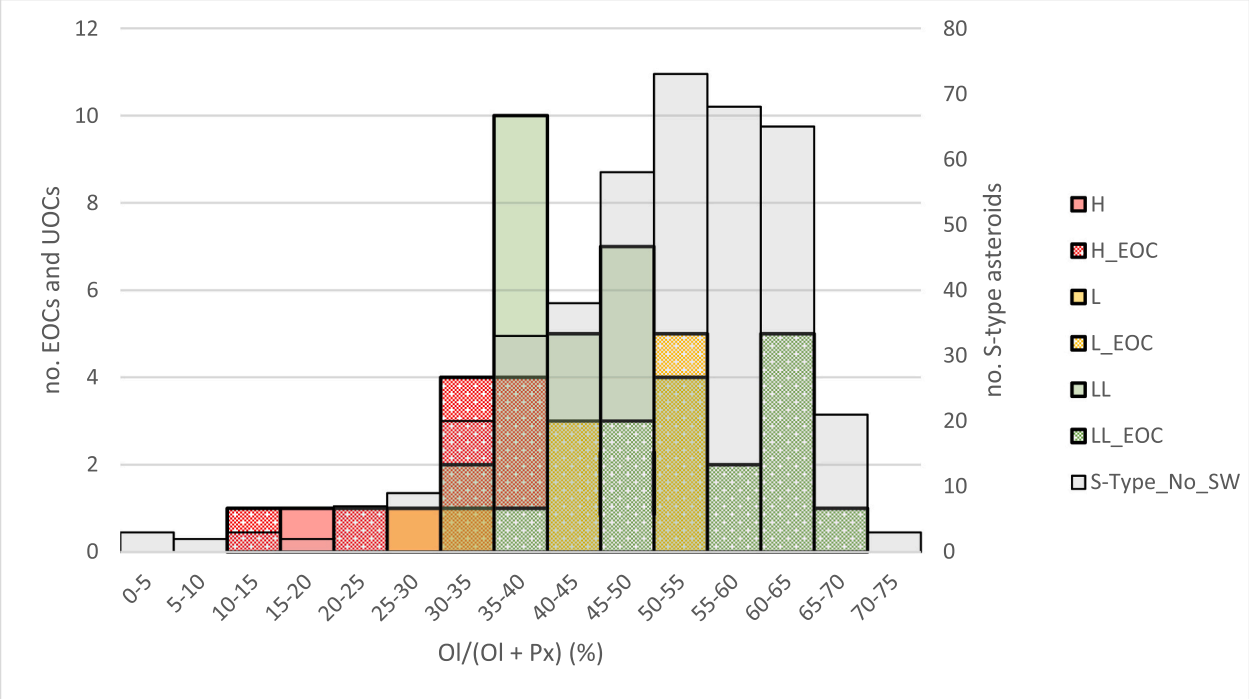

Fig. 10. Histogram of the Ol/(Ol + Px) ratio of S-type asteroids (on the right axis) as well as UOCs and ECOs (on the left axis). UOCs are plotted in solid colors, EOCs in pattern fill. S-type asteroids are plotted in solid gray colour. Since the number of S-type spectra greatly exceeds those of EOCs and UOCs the histograms are plotted on two axes.

4.3.3. *Grain size effects*

Interestingly, no S-type matches can be found for the EOCs with strong absorption features based on the 1000 nm and the 2000 nm band depths (Fig. 9a). This is consistent with the observations based on PCA (Fig. 8, Section 4.3.1): no match for these EOCs can be found with either the raw or de-space weathered S-type spectra. A possible explanation for this could be a difference in grain size between the powders measured in the laboratory and the actual regolith on the S-type asteroid surfaces. UOCs usually contain more fine-grained and porous matrix material than EOCs and are thus more easily ground into fine powders by hand as shown by the example of RBT 04251 (LL 3.4) (Table 5 and Section 3.2.2).

In Fig. 9, the spectral features of 6 EOCs and 1 UOC measured at different grain sizes (see Section 3.2.2) were added into the plots comparing the 2000 nm and 1000 nm band depths (Fig. 9a). They were also added to the 700 nm peak reflectance over the 1000 nm band depth plot in Fig. 9b. As can be seen, decreasing the grain size of the powders moves the 1000 nm and 2000 nm band depths from out of the reach of any S-type asteroid (top right corner) to being comparable to UOC band depths. After 20 min of grinding, the 1000 nm and 2000 nm band depths decrease to even lower values than for UOCs (Fig. 9a). The 700 nm peak reflectance decreases with decreasing grain size as indicated by the example of Los Vientos 423 (H6) in Fig. 9b. After 10 min of grinding in the ball mill, the 700 nm peak reflectance of Los Vientos 423 goes from significantly higher than UOC and S-type spectra, to comparable to UOCs.

We further add an indicator of the effect of increasing grain size to the principal score plots in Fig. 8. For this the mean of the scores determined from fine grained powders that were ground for 5 min, 10 min and 20 min was taken. The dashed arrows in Fig. 8 connects the mean score of the fine-grained EOC spectra to the mean score of the EOCs before additional grinding. We expect the OC spectra to shift in this direction with increasing grain size. It is apparent, in all three score plots, that decreasing the grain size of the EOCs moves them closer to the asteroid distribution. These results highlight the already well-known importance of grain size for the study of asteroid surfaces as well as for the comparison of asteroid and meteorite spectra (e.g., Krämer Ruggiu et al., 2021).

When plotting the diameter of the asteroids considered in the present work as a function of the 1000 nm band depth (Fig. 4b) there seems to be a loose anti-correlation ($r^2 = 0.215$), for asteroids of $d > 20$ km. This means that larger asteroids tend to show finer grained surfaces, consistent with Delbo et al. (2015) (and references therein). Therefore, the analysis of grain size effects on spectral features done in the present work appears to be a meaningful explanation of the differences in the observed distributions between asteroids and OCs, and between UOCs and EOCs.

4.4. *Consequences for S-type asteroids*

We have shown so far that i) the spectral differences between UOCs and EOCs are not a clear-cut dichotomy. EOCs can show stronger band depths and higher peak reflectance values than UOCs but depending on their grain size they can also be comparable to UOC spectra (Figs. 6 and 9); ii) the average Ol/(Ol + Px) ratios of S-type asteroids match those of EOCs better than those of UOCs (Fig. 10) and iii) an anti-correlation between the 1000 nm band depth of S-type asteroids and their diameter could be seen (Fig. 4b). These results allow us to make some hypothesis of the structure of S-type asteroids.

4.4.1. *Indications on the S-type asteroid structure*

Based on the identification of metamorphic sequence among OCs, the common view of S-type asteroid structure is an onion shell model. In the case of an onion shell model, the surface and outer crust of the undisturbed S-type asteroid is expected to be UOC-like, while the main bulk of the material in the center of the asteroid is EOC-like (McSween et al., 2002). In this scenario, the S-type asteroids start off as large, intact bodies and then become brecciated into smaller pieces through impact processes. The result is a few objects which retain the pristine UOC-like surface and a larger number of bodies which show EOC-like surfaces

exposed by the brecciation of their previously parent bodies (e.g. McSween Jr. and Patchen, 1989).

In the present work we find that the average Ol/(Ol + Px) ratio of S-type asteroids matches those of EOCs better than those of UOCs (Fig. 10). While it does not definitely prove it, this result is aligned with the presence of a few large asteroids with UOC-like surfaces and many small asteroids with EOC-like surfaces as we would expect for an onion shell model. This hypothesis would also be in line with UOCs being strongly under-represented in our meteorite collection with only about 5.4% of all OC being UOCs and the remaining being EOCs (based on falls in the "Meteoritical Bulletin Database," (2021)).

5. Conclusion

With OCs being mineralogically and petrographically diverse, our objective was to understand whether or not such a diversity is visible among asteroid surfaces based on reflectance spectroscopy. In the present work we conducted an in-depth study of a large number of UOCs using varying measuring techniques to make sure of their classification. It appears that 74% (23 of the 31) of the Antarctic UOCs were misclassified. The most common misclassification is LL3 chondrites being classified as L3 chondrites. We attribute this high number of misclassifications to the lack of robust classification data used in the "Meteoritical Bulletin Database," (2021).

Reflectance spectra of 80 OCs (39 EOCs and 41 UOCs) were measured under consistent measuring conditions. The spectral features of UOCs and EOCs were compared and found to not be a clean-cut dichotomy but rather a continuum. Among EOCs, LL of PT $\geq$ 5 can be distinguished from H and L based on their 2000 nm band depth and 1000 nm band position which is shallower and shifted to longer wavelengths for LL in comparison to H and L. Comparing the Ol/(Ol + Px) ratios of EOCs and UOCs showed that EOCs can slightly exceed those of UOCs for PT > 4. However, many of the ratios are comparable between EOCs and UOCs. A slight single separation between H, L and LL is visible within each PT groups $\geq$4, with ratios decreasing from LL and L to H.

We studied the influence of grain size on the reflectance spectra of 6 EOCs and 1 UOC and showed that decreasing the grain size of the powders leads to a significant decrease in 1000 nm and 2000 nm band depth. It also leads to a decrease in the 700 nm peak reflectance and a shift of the 1000 nm band position to shorter wavelengths, possibly due to the comminution of opaque components into fine grains. Overall, it leads to EOC spectra becoming more comparable to UOC spectra. UOCs are ground into fine powders easier by hand than EOCs since they contain a larger quantity of porous matrix material.

Surfaces of S-type asteroids are subject to space weathering which induces a change in slope in their reflectance spectra. Considering this as well as the influence grain size has on reflectance spectra, the comparison between S-type asteroid spectra and OC spectra is difficult.

A large set (466) of de-space weathered S-type asteroid reflectance spectra was analyzed in the same way as the OCs. The comparison with the OC spectra showed that the 1000 nm and 2000 nm band depths of S-type asteroids cluster between EOC and UOCs. The exact match is strongly dependent on the amount of SW removed from the S-type asteroid spectra as illustrated by PCA. We also found that the 1000 nm band depth of S-type asteroids is anti-correlated with their diameter. Since we expect a reduced band contrast with smaller grain size (see Section 4.3.3) this advocates for large bodies having a fine-grained regolith, while smaller bodies have a coarser grained regolith.

All these results are in line with, but do not definitely prove an onion shell model for S-type asteroids. The surface and outer crust of the undisturbed S-type asteroids are expected to be UOC-like, while the main bulk of the material in the center of the asteroid is EOC-like. The majority of the bulk OC material would stem from young dynamical families, where EOC-like bodies are the major contributors to the meteorite production. This could explain the strong under-representation of UOCs among OCs and is supported by the good match between S-type asteroid and EOC Ol/(Ol + Px) ratios.

There are still several open questions surrounding OCs. In the overall representation of H to L to LL in our OC collection only 11.1% of OCs are LL type (in comparison to 47.6% being L and 41.2% being H) (percentages based on number of falls in the "Meteoritical Bulletin Database," (2021)). Misclassification can be a partial but not sole explanation. As discussed in Vernazza et al. (2014) possible other reasons for LL-type samples to be less common may be related to the location and age of the source region as well as the size and type of the body. Furthermore, a pronounced hydration band could be observed for most UOCs in this work (Fig. 1), indicating the presence of hydrated minerals. It would, therefore, be interesting to obtain more S-type asteroid spectra in the 2500–4200 nm range (e.g. during the SPHEREx space mission (Ivezić et al., 2022)), which would allow for the 3-μm band to be used as a further constrain on the S-type-OC match.

Declaration of Competing Interest

None.

Acknowledgements

This work has been funded by the Centre National d'Etudes Spatiales (CNES-France) and by the ERC grant SOLARYS ERC-CoG2017-771691.

US Antarctic meteorite samples are recovered by the Antarctic Search for Meteorites (ANSMET) program which has been funded by NSF and NASA, and characterized and curated by the Department of Mineral Sciences of the Smithsonian Institution and Astromaterials Acquisition and Curation Office at NASA Johnson Space Center. We thank the Natural History Museum, Vienna, Department of Mineralogy and Petrography for providing us with a thick section of Mezö-Madaras (Inv-Nr. NHMV-N2140) and bulk samples of Mezö-Madaras (NHMV_ID_#3993_B2), Parnallee (NHMV_ID_#6207_B2) and Tieschitz (NHMV_ID_#7152_A).

We also thank the Museum D'Histoire Naturelle National (MNHN), the Arizona State University (ASU), the Centre de Recherches Pétrographiques et Geochimiques (CRPG) at Nancy and lastly the Centre Européen de Recherche et D'Enseignement des Géosciences de l'Environnement (CEREGE), Aix-En-Provence for providing us with the remaining EOC and UOC samples.

References

Bennett III, M.E., McSween, H.Y., 1996. Shock features in iron-nickel metal and troilite of L-group ordinary chondrites. Meteorit. Planet. Sci. 31, 255–264. https://doi.org/10.1111/j.1945-5100.1996.tb02021.x.

Binzel, R.P., Rivkin, A.S., Stuart, J.S., Harris, A.W., Bus, S.J., Burbine, T.H., 2004. Observed spectral properties of near-Earth objects: results for population distribution, source regions, and space weathering processes. Icarus 170, 259–294. https://doi.org/10.1016/j.icarus.2004.04.004.

Bonal, L., Quirico, E., Flandinet, L., Montagnac, G., 2016. Thermal history of type 3 chondrites from the Antarctic meteorite collection determined by Raman spectroscopy of their polyaromatic carbonaceous matter. Geochim. Cosmochim. Acta 189, 312–337. https://doi.org/10.1016/j.gca.2016.06.017.

Brunetto, R., Vernazza, P., Marchi, S., Birlan, M., Fulchignoni, M., Orofino, V., Strazzulla, G., 2006. Modeling asteroid surfaces from observations and irradiation experiments: the case of 832 Karin. Icarus 184, 327–337. https://doi.org/10.1016/j.icarus.2006.05.019.

Chapman, C.R., Salisbury, J.W., 1973. Comparisons of meteorite and asteroid spectral reflectivities. Icarus 19, 507–522. https://doi.org/10.1016/0019-1035(73)90078-X.

Clark, R.N., 1999. Spectroscopy of Rocks and Minerals and Principles of Spectroscopy, pp. 3–58.

Cloutis, E.A., Gaffey, M.J., 1991. Pyroxene spectroscopy revisited: spectral-compositional correlations and relationship to geothermometry. J. Geophys. Res. Planets 96, 22809–22826. https://doi.org/10.1029/91JE02512.

Cloutis, E.A., Gaffey, M.J., Jackowski, T.L., Reed, K.L., 1986. Calibrations of phase abundance, composition, and particle size distribution for olivine-orthopyroxene mixtures from reflectance spectra. J. Geophys. Res. Solid Earth 91, 11641–11653. https://doi.org/10.1029/JB091iB11p11641.

Consolmagno, G.J., Britt, D.T., Macke, R.J., 2008. The significance of meteorite density and porosity. Geochemistry 68, 1–29. https://doi.org/10.1016/j.chemer.2008.01.003.

Delbo, M., Mueller, M., Emery, J.P., Rozitis, B., Capria, M.T., 2015. Asteroid thermophysical modeling. In: Asteroids IV. University of Arizona Press, Tucson, Arizona, pp. 107–128.
DeMeo, F.E., Binzel, R.P., Slivan, S.M., Bus, S.J., 2009. An extension of the Bus asteroid taxonomy into the near-infrared. Icarus 202, 160–180. https://doi.org/10.1016/j.icarus.2009.02.005.
Dunn, T.L., Cressey, G., McSWEEN Jr., H.Y., McCOY, T.J., 2010a. Analysis of ordinary chondrites using powder X-ray diffraction: 1. Modal mineral abundances. Meteorit. Planet. Sci. 45, 123–134. https://doi.org/10.1111/j.1945-5100.2009.01011.x.
Dunn, T.L., McCoy, T.J., Sunshine, J.M., McSween, H.Y., 2010b. A coordinated spectral, mineralogical, and compositional study of ordinary chondrites. Icarus 208, 789–797. https://doi.org/10.1016/j.icarus.2010.02.016.
Eschrig, J., Bonal, L., Beck, P., 2019. NIR Reflectance Spectrum (I=0°, e=30°) of Bulk UOC Chondrites under Vacuum at T = 80°C. DatasetSpectral Data, SSHADEGhoSST OSUG Data Cent. https://doi.org/10.26302/SSHADE/EXPERIMENT_LB_20191220_004.
Eschrig, J., Bonal, L., Beck, P., 2020. NIR Reflectance Spectrum (I=0°, e=30°) of Bulk EOC Chondrites under Vacuum at T = 80°C. DatasetSpectral Data, SSHADEGhoSST OSUG Data Cent. https://doi.org/10.26302/SSHADE/EXPERIMENT_LB_20220119_001.
Eschrig, J., Bonal, L., Beck, P., Prestgard, T.J., 2021. Spectral reflectance analysis of type 3 carbonaceous chondrites and search for their asteroidal parent bodies. Icarus 354, 114034. https://doi.org/10.1016/j.icarus.2020.114034.
Gaffey, M.J., 1976. Spectral reflectance characteristics of the meteorite classes. J. Geophys. Res. 1896-1977 (81), 905–920. https://doi.org/10.1029/JB081i005p00905.
Gattacceca, J., Suavet, C., Rochette, P., Weiss, B.P., Winklhofer, M., Uehara, M., Friedrich, J.M., 2014. Metal phases in ordinary chondrites: magnetic hysteresis properties and implications for thermal history. Meteorit. Planet. Sci. 49, 652–676. https://doi.org/10.1111/maps.12268.
Hotelling, H., 1933. Analysis of a complex of statistical variables into principal components. J. Educ. Psychol. 24, 417–441. https://doi.org/10.1037/h0071325.
Ivezić, Ž., Ivezić, V., Moeyens, J., Lisse, C.M., Bus, S.J., Jones, L., Crill, B.P., Doré, O., Emery, J.P., 2022. Simulated SPHEREx spectra of asteroids and their implications for asteroid size and reflectance estimation. Icarus 371, 114696. https://doi.org/10.1016/j.icarus.2021.114696.
Kohout, T., Penttilä, A., Mann, P., Cloutis, E., Čuda, J., Filip, J., Malina, O., Reddy, V., Grokhovsky, V.I., Yakovlev, G.A., Halodova, P., Haloda, J., 2020. Distinguishing between shock-darkening and space-weathering trends in ordinary chondrite reflectance spectra. Planet. Sci. J. 1, 37. https://doi.org/10.3847/PSJ/aba7c2.
Krämer Ruggiu, L., Beck, P., Gattacceca, J., Eschrig, J., 2021. Visible-infrared spectroscopy of ungrouped and rare meteorites brings further constraints on meteorite-asteroid connections. Icarus 362, 114393. https://doi.org/10.1016/j.icarus.2021.114393.
Krot, A.N., Keil, K., Scott, E.R.D., Goodrich, C.A., Weisberg, M.K., 2014. Classification of meteorites and their genetic relationships. In: Meteorites and Cosmochemical Processes.
Marchi, S., Brunetto, R., Magrin, S., Lazzarin, M., Gandolfi, D., 2005. Space weathering of near-earth and main belt silicate-rich asteroids: observations and ion irradiation experiments. Astron. Astrophys. 443, 769–775. https://doi.org/10.1051/0004-6361:20053525.
Marrocchi, Y., Bonal, L., Gattacceca, J., Piani, L., Beck, P., Greenwood, R., Eschrig, J., Basque, A., Nuccio, P.M., Martin, F.F., 2020. The Piancaldoli meteorite: a forgotten primitive LL3.10 ordinary chondrite. Meteorit. Planet. Sci. 55 https://doi.org/10.1111/maps.13552.
McSween Jr., H.Y., Patchen, A.D., 1989. Pyroxene thermobarometry in LL-group chondrites and implications for parent body metamorphism. Meteoritics 24, 219–226. https://doi.org/10.1111/j.1945-5100.1989.tb00696.x.
McSween, H.Y., Ghosh, A., Grimm, R.E., Wilson, L., Young, E.D., 2002. Thermal evolution models of asteroids. In: Asteroids, III, p. 559.
Meteoritical Bulletin Database [WWW Document], 2021. URL. https://www.lpi.usra.edu/meteor/metbull.php?sea=O (accessed 12.3.21).
Metzler, K., 2018. From 2D to 3D chondrule size data: some empirical ground truths. Meteorit. Planet. Sci. 53, 1489–1499. https://doi.org/10.1111/maps.13091.
Moroz, L.V., Fisenko, A.V., Semjonova, L.F., Pieters, C.M., Korotaeva, N.N., 1996. Optical effects of regolith processes on S-asteroids as simulated by laser shots on ordinary chondrite and other mafic materials. Icarus 122, 366–382. https://doi.org/10.1006/icar.1996.0130.
Mustard, J.F., Hays, J.E., 1997. Effects of hyperfine particles on reflectance spectra from 0.3 to 25 μm. Icarus 125, 145–163. https://doi.org/10.1006/icar.1996.5583.
Nakamura, T., Noguchi, T., Tanaka, M., Zolensky, M.E., Kimura, M., Tsuchiyama, A., Nakato, A., Ogami, T., Ishida, H., Uesugi, M., Yada, T., Shirai, K., Fujimura, A., Okazaki, R., Sandford, S.A., Ishibashi, Y., Abe, M., Okada, T., Ueno, M., Mukai, T., Yoshikawa, M., Kawaguchi, J., 2011. Itokawa dust particles: a direct link between S-type asteroids and ordinary chondrites. Science 333, 1113–1116. https://doi.org/10.1126/science.1207758.
Pearson, K., 1901. LIII. On lines and planes of closest fit to systems of points in space. Lond. Edinb. Dublin Philos. Mag. J. Sci. 2, 559–572. https://doi.org/10.1080/14786440109462720.
Pieters, C.M., Noble, S.K., 2016. Space weathering on airless bodies. J. Geophys. Res. Planets 121, 1865–1884. https://doi.org/10.1002/2016JE005128.
Potin, S., Brissaud, O., Beck, P., Schmitt, B., Magnard, Y., Correia, J.-J., Rabou, P., Jocou, L., 2018. SHADOWS: a spectro-gonio radiometer for bidirectional reflectance studies of dark meteorites and terrestrial analogs: design, calibrations, and performances on challenging surfaces. Appl. Opt. 57, 8279–8296. https://doi.org/10.1364/AO.57.008279.
Potin, S., Beck, P., Usui, F., Bonal, L., Vernazza, P., Schmitt, B., 2020. Style and intensity of hydration among C-complex asteroids: a comparison to desiccated carbonaceous chondrites. Icarus 348, 113826. https://doi.org/10.1016/j.icarus.2020.113826.
RELAB [WWW Document], 2021. Reflectance Exp. Lab. RELAB. URL https://pds-geosciences.wustl.edu/speclib/urn-nasa-pds-relab/data_reflectance/ (accessed 12.3.21).
Rochette, P., Sagnotti, L., Bourot-Denise, M., Consolmagno, G., Folco, L., Gattacceca, J., Osete, M.L., Pesonen, L., 2003. Magnetic classification of stony meteorites: 1. Ordinary chondrites. Meteorit. Planet. Sci. 38, 251–268. https://doi.org/10.1111/j.1945-5100.2003.tb00263.x.
Rochette, P., Gattacceca, J., Lewandowski, M., 2012. Magnetic classification of meteorites and application to the Sołtmany fall. Meteor. 2.
Salisbury, J.W., Hunt, G.R., 1974. Meteorite spectra and weathering. J. Geophys. Res. 1896-1977 (79), 4439–4441. https://doi.org/10.1029/JB079i029p04439.
Scott, E.R.D., Jones, R.H., 1990. Disentangling nebular and asteroidal features of c03 carbonaceous chondrite meteorites. Geochim. Cosmochim. Acta 54, 2485–2502. https://doi.org/10.1016/0016-7037(90)90235-D.
Scott, E.R.D., Krot, A.N., 2003. Chondrites and their components. Treat. Geochem. 1, 711. https://doi.org/10.1016/B0-08-043751-6/01145-2.
Scott, E.R.D., Keil, K., Stöffler, D., 1992. Shock metamorphism of carbonaceous chondrites. Geochim. Cosmochim. Acta 56, 4281–4293. https://doi.org/10.1016/0016-7037(92)90268-N.
Sears, D., Ostrowski, D., Smith, H., Sissay, A., Trivedi, M., 2021. A new method for determining the petrologic type of unequilibrated ordinary chondrites that can be applied to asteroids. Icarus 363, 114442. https://doi.org/10.1016/j.icarus.2021.114442.
Singer, R.B., 1981. Near-infrared spectral reflectance of mineral mixtures: systematic combinations of pyroxenes, olivine, and iron oxides. J. Geophys. Res. Solid Earth 86, 7967–7982. https://doi.org/10.1029/JB086iB09p07967.
Stöffler, D., Keil, K., Edward, R.D.S., 1991. Shock metamorphism of ordinary chondrites. Geochim. Cosmochim. Acta 55, 3845–3867. https://doi.org/10.1016/0016-7037(91)90078-J.
Sultana, R., Poch, O., Beck, P., Schmitt, B., Quirico, E., 2021. Visible and near-infrared reflectance of hyperfine and hyperporous particulate surfaces. Icarus 357, 114141. https://doi.org/10.1016/j.icarus.2020.114141.
Vernazza, P., Zanda, B., Binzel, R.P., Hiroi, T., DeMeo, F.E., Birlan, M., Hewins, R., Ricci, L., Barge, P., Lockhart, M., 2014. Multiple and fast: the accretion of ordinary chondrite parent bodies. Astrophys. J. 791, 120. https://doi.org/10.1088/0004-637X/791/2/120.
Vernazza, P., Castillo-Rogez, J., Beck, P., Emery, J., Brunetto, R., Delbo, M., Marsset, M., Marchis, F., Groussin, O., Zanda, B., Lamy, P., Jorda, L., Mousis, O., Delsanti, A., Djouadi, Z., Dionnet, Z., Borondics, F., Carry, B., 2017. Different origins or different evolutions? Decoding the spectral diversity among C-type asteroids. Astron. J. 153, 72. https://doi.org/10.3847/1538-3881/153/2/72.
Wlotzka, F., 1993. A weathering scale for the ordinary chondrites. Meteoritics 28, 460. https://ui.adsabs.harvard.edu/abs/1993Metic..28Q.460W.

5 The hydration history of unequilibrated ordinary chondrites

5.1 Background and main findings

During the final chapter of my dissertation, I focused on the detailed analysis of the post-accretion history of UOCs. As explained in Section 1.2.4 and shown in Figure 1.8, comparing stable-isotopic anomalies of different Solar System small bodies shows two distinct groups indicating two distinct formation reservoirs. The first group, called the NC group includes, among others, the OCs as well as inner Solar System bodies like Earth and Mars. The second group called the C group includes the CCs. Terrestrial planets and inner Solar System asteroids are depleted in volatiles, including water, in comparison to outer Solar System bodies such as the giant planets, comets and outer Solar System asteroids (Morbidelli et al., 2015). This puts the OCs in the formation region of dry, inner Solar System bodies which presumably formed inward of the snow-line. The exact location of the snowline at the time of chondrite formation is not well constrained yet. The in-depth analysis of the post-accretion history of chondrites can contribute important information to better constrain this location.

Indeed, hydrated minerals have been previously observed in a few, most primitive UOCs such as Semarkona (LL3.00) and Bishunpur (LL3.15) (e.g. Hutchison et al. (1987), Krot et al. (1997), Alexander et al. (1989), Alexander et al. (2010), Alexander et al. (2012), Alexander (2019), Grossman et al. (2000), Grossman et al. (2002), GROSSMAN and BREARLEY (2005),Brearley (2006), Dobrică et al. (2019), P. et al. (2015) and Sutton et al. (2017)). As explained in Section 1.2.4 the current hydration of a chondrite is controlled by a combination of terrestrial and extraterrestrial hydration episodes as well as heating processes. For this reason, I performed an in-depth analysis of the aqueous alteration and shock history of a large set of 41 UOCs. The thermal history of the UOCs was previously constrained by Raman spectroscopy (Bonal et al., 2016). Petrographic measurements were used to assess the shock stage and terrestrial weathering grade of each UOC. To assess the hydration of the UOCs, I performed TGA on 31 of the UOCs and FTIR spectroscopy on 14 of them (see Sections 2.2.3 and 2.2.4).

These measurements revealed, that in contrast to common belief, UOCs are hydrated. Therefore, their asteroidal parent bodies must have not been dry. Indeed, I showed that once normalized to the matrix abundance the hydration of UOCs is comparable to that previously observed for CVs (Bonal et al., 2020). A correlation

between the hydration and the metamorphic grade was observed when comparing the IBD of the 3 µm band of the FTIR spectra to the $FWHM_D$ values. This correlation was also observed for the matrix normalized mass loss determined by TGA, when only considering UOCs with matrix abundances $\geq$ 19 %. This correlation extends the one previously observed for CVs. These results indicated that the inner Solar System was not dry and that the location of the snowline must have been inward the UOC formation region at the time of accretion. This conclusion is in line with previous works by Alexander et al. (2018).

A manuscript on this topic was submitted to Geochimica et Cosmochimica Acta (GCA) and is inserted at the end of this chapter after the description of some perspectives.

5.2 Prospects

TGA and FTIR spectroscopy were chosen as complementary measuring techniques to determine the hydration history of UOCs. However, both of them have their limitations. Because FTIR spectroscopy on matrix fragments is very sensitive to the vibrational modes of hydrated minerals (Section 2.3.2) it is suited for the detection of small amounts of hydration without the need of matrix normalization. However, since the thickness and the measuring area of the pressed matrix fragments were not constrained and the measurements were done in transmitted light, quantification of the hydrated phases from the FTIR spectra is not easy. In future work it would thus be important to constrain both the measuring area and thickness of the pressed fragments, to allow for a better comparison between chondrites and quantification of water abundances.

TGA has previously proven to be a suitable technique for detecting hydration in CVs (Bonal et al., 2020). Since the measurements are done on bulk samples, normalization to the matrix abundance is necessary to ensure comparability of chondrites. This also means that other thermal reactions such as oxidation or reduction of non-matrix material can contribute to the total mass loss. For chondrites with low matrix abundances (such as UOCs) this means that the higher relative abundance of non-hydrated minerals possibly contributing to the mass loss might mask some of the hydration signal. Furthermore, the matrix normalization introduces a higher error than for chondrites with lower matrix abundances. For this reason, only UOCs with matrix abundances higher than 19 % were considered in the submitted paper. To overcome these constraints, matrix enriched TGA measurements are envisaged. I have made first attempts to try and prepare matrix enriched samples. They are summarized in the following Section.

5.2.1 Matrix enriched TGA measurements

TGA could successfully detect hydration in CVs which show an average matrix abundance of 40 %. This corresponds to 14 mg of matrix material in a 35 mg bulk sample. Therefore, if it is not possible to collect enough fragments for pure matrix

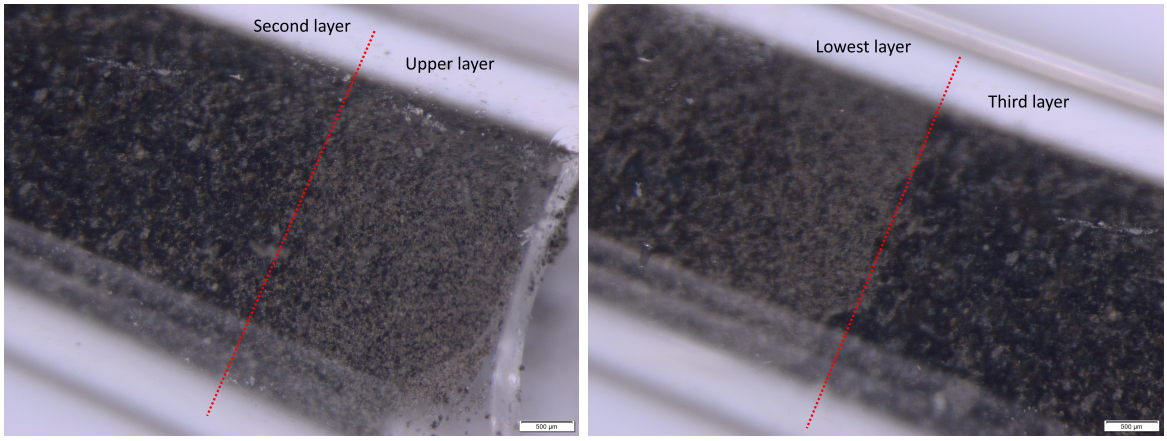

(a) Upper two layers of the powder. **(b)** Lower two layers of the powder.

Figure 5.1: Images of the vial containing the powder of CR GRO 95577 after centrifugation. Shown are the four layers.

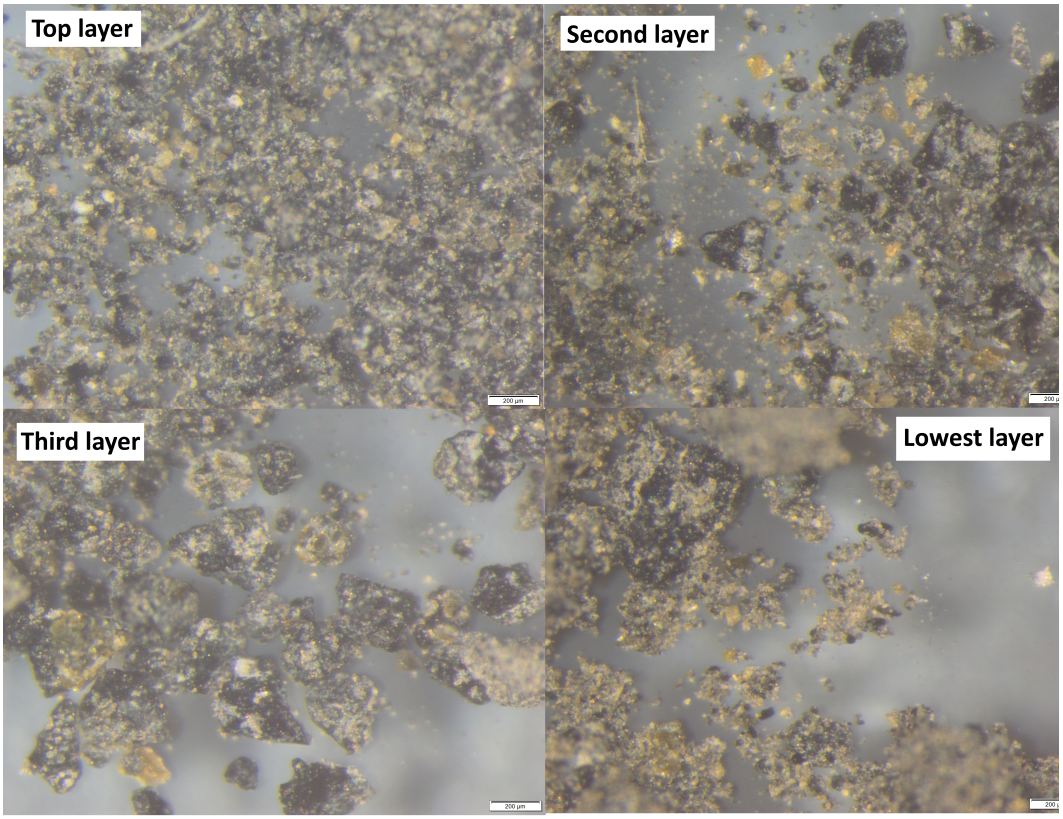

Figure 5.2: Microscopic view of the four layers achieved by centrifugation of the powdered CR GRO 95577 at x5 magnification.

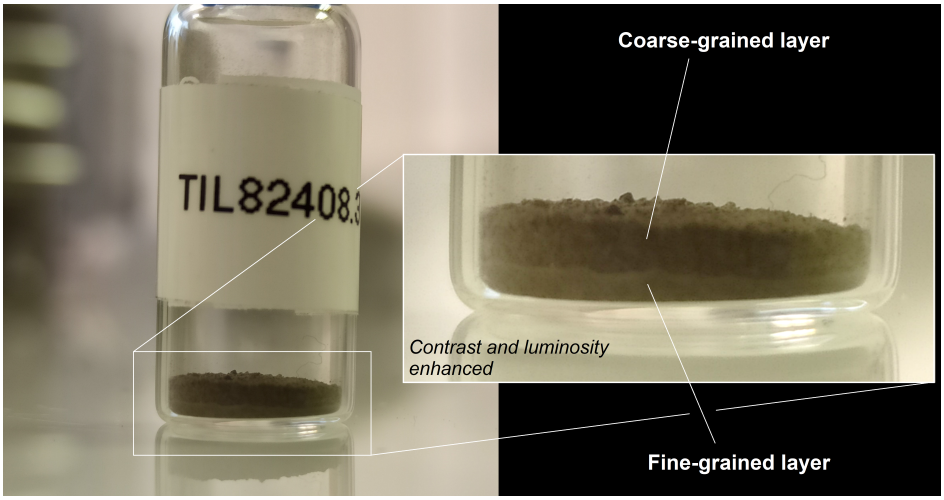

Figure 5.3: Two layers visible after shaking a glass vial with bulk powder of UOC TIL 82408. The top layer is darker and contains coarser grains, the bottom layer is lighter and fine grained.

measurements, a matrix-enriched UOC sample (40 % matrix) might produce better measurements.

For TIL 82408 (UOC) which shows a high overall matrix abundance (22.84 %) this means that the bulk sample should be enriched with about 7 mg of matrix material. I have made first attempts to hand pick 7 mg worth of matrix fragments under a microscope (as described in Section 2.2.3). However, after 3 months of picking only 2 mg could be collected. Due to the time intensity of this picking process several other matrix separation methods have been investigated.

Firstly, I considered the freeze-thaw method. This method is widely used for extracting whole chondrules from chondrites by inserting a chondrite in a freezing liquid (water) and periodically heating it to high enough temperatures to liquefy the water ice and then freezing it to low temperatures (e.g. Charles (2011) and Grossmann (2010)). However, since we are interested in the hydration of the UOCs, inserting them into water is not an option. It would thus be necessary to find a solvent that is i) safe to use with the UOCs to preserve their initial hydration, ii) that freezes at temperatures that can be reached with liquid nitrogen and iii) that has a sufficient expansion coefficient when frozen to weaken the rock. So far, the search for such a solvent is ongoing. A test of adding liquid nitrogen directly onto a terrestrial rock was done by me to induce an extreme drop in temperature and then use a slight impact from a hammer to disintegrate it. This test did not work.

In any case, once the chondrite components have been dis-aggregated by some method the matrix material still needs to be picked out from the remaining chondrite material either by hand, using a sieve or a centrifuge. For sieving, the assumption is made that the smallest grains ($< 40\,\mu m$) are matrix material. However, the possibly large loss of material in the sieve makes this method unattractive.

I explored the separation of matrix material through centrifugation of powdered chondrites. This method allows to separate grains based on size, shape and density depending on the time and speed of centrifugation. Therefore, it should be possible to separate matrix material that is expected to be i) finer grained than chondrule

fragments which are not as easily ground by hand and ii) have a lower density. To test this method, I firstly mixed 55.95 mg of the CR powder of GRO 95577 with 1 mL of Toluene Methanol and shaken well. Then two 250 µL glass vials were filled with the mixture and put into the centrifuge at 14000 RPM for 20 min. Subsequently, the liquid in the vials was carefully removed using a paper towel and the samples were left to dry overnight inside the vials. Indeed, with this method it was possible to identify four layers in one of the vials (see Figure 5.1). However, the two main issues of this method are i) that the usage of a solvent might alter the initial hydration of the sample and ii) that it is difficult to identify which of the layers is indeed matrix material since the densities of the different chondrite components can overlap and they are not easily identified by eye (see Figure 5.2).

In conclusion, the separation of matrix material in a chondrite group that has very low matrix abundances is a challenge to say the least. Therefore, the most promising method is to first grind the chondrites into a powder by hand and then roughly pre-sort them by size since we expect larger grains to be mostly chondrule fragments. To simply sort the grains in a powder by size it is sufficient to add the powder into a glass vial and then shake the powder for some minutes using a laboratory shaker until there is a layer of coarser and a layer of finer grains (e.g. Figure 5.3). After using a spatula to carefully remove the coarser grained layer that is most probably not fine grained, porous matrix material, the remaining work will have to be done by hand picking. Given the extent of this task, this exceeds the scope of my PhD. Lastly, to improve the method of dipping the rock directly into liquid nitrogen instead of using a freezing liquid (a dry freeze-thaw method so to speak), an instrument was developed at IPAG which will allow for large numbers of freeze cycles. First test of this dry freeze-thaw method will be started in the near future.

The Hydration History of Unequilibrated Ordinary Chondrites

J. Eschrig[1a], L. Bonal[1], J. Gattacceca[2], P. Beck[1]

[1]Institut de Planétologie et d'Astrophysique de Grenoble, Université Grenoble Alpes, CNRS CNES, 38000 Grenoble (France)

[2]CNRS, Aix Marseille Univ, IRD, INRAE, CEREGE, Aix-en-Provence, France

To be submitted to Geochimica et Cosmochimica Acta

[a] Corresponding author: jolantha.eschrig@univ-grenoble-alpes.fr (J. Eschrig)

Abstract

While evidence for hydration was previously observed in a few, selected unequilibrated ordinary chondrites (UOCs), they are generally considered to be dry. Their stable-isotope anomalies similar to those of terrestrial planets and distinct from carbonaceous chondrites indicate a formation region in the inner Solar System. The exact location of the snowline with regard to this formation reservoir at the time of accretion is not known. We perform an in-depth study of 31 Antarctic and 10 non-Antarctic UOCs using petrography, FTIR spectroscopy of matrix fragments, and Thermogravimetric analysis (TGA) of bulk samples to assess i) whether UOCs are hydrated, and ii) whether their hydration is controlled by their peak metamorphic temperature. In the end, constraints on the location of the snowline at the time of their accretion can be given. We show that UOCs are not dry. FTIR spectra show the presence of hydration bands reflecting extraterrestrial alteration. Based on TGA, we show that UOCs hydration, once normalized to the matrix abundance, is comparable to that of CVs with equivalent metamorphic grade. We show that the hydration of UOCs is controlled by their peak metamorphic temperature and that the correlation observed extends the one previously observed for CV chondrites. Thus, we conclude that the inner Solar System was not dry and that the snowline at the time of accretion must have been located inward of the UOC formation region.

1. Introduction

Stable isotopes anomalies of different Solar System small bodies reflect two distinct groups: non-carbonaceous (NC) and carbonaceous (C) (Warren, 2011). These groups are interpreted as two distinct formation reservoirs believed to have been separated by proto-Jupiter (Kruijer et al., (2017); Morbidelli et al., (2016); Walsh et al., (2011)). Furthermore, it has been observed that the terrestrial planets and asteroids in the inner Solar System are depleted in water (and more generally volatile elements) compared to the giant planet satellites, comets, and outer Solar System asteroids (e.g. Morbidelli et al., (2016)). This

depletion of water may be related to the location of the snowline with reference to their formation reservoirs. So far this location is not definitely known (e.g. Morbidelli et al., (2016)).

The characterization of the post-accretion history experienced by chondrites on their parent asteroid, such as aqueous alteration, thermal, and shock metamorphism, allows for further constraints on this amount of water present at the time of accretion and then the location of the snowline. For most chondrite groups aqueous alteration is believed to be a secondary parent body process rather than a nebular process (Brearley, 2003) and, thus, can only take place outward of the snowline. Aqueous alteration leads to the production of various secondary products such as clays, carbonates, sulfates, iron oxides, sulfides, halides, and oxyhydroxides and can also change the stable isotope composition of the chondrites and their components (Brearley, 2006). The final hydration state of a chondrite, however, is determined not only by the experienced extraterrestrial aqueous alteration but rather by the interplay of several terrestrial and extraterrestrial hydration episodes combined with heating processes. Depending on the initial mineralogy, water-to-rock ratio, peak metamorphic temperature, and shock degree, the final hydration of a chondrite can vary. Terrestrial weathering plays a role too. When assessing the overall hydration of a chondrite in the laboratory, all of these processes need to be fully considered.

Aqueous alteration has been observed in most carbonaceous chondrite groups including CIs, CMs, CRs, COs, and CVs (e.g. Brearley, (2006); Scott and Krot, (2003)). This has led to the belief that carbonaceous chondrites must have formed in the outer Solar System, where the conditions allow for accretion of ice in the asteroids. In contrast, the lack of observation of large extents of hydration in non-carbonaceous objects, including the terrestrial planets, ordinary and enstatite chondrites, and non-chondritic meteorites (such as Ureilites, HEDs, Angrites, Pallasites and Mesosiderites) may be taken as an argument for a formation and alteration region closer to the Sun. However, hydrated minerals have previously been identified in some unequilibrated ordinary chondrites (UOCs) (Brearley, 2006), which are the most primitive chondrites within the ordinary chondrite group. Indeed, transmission electron

microscopy (TEM) of Semarkona (LL3.0) and Bishunpur (LL3.15) revealed traces of aqueous alteration through the presence of phyllosilicates in chondrule rims and matrix (Alexander et al., 1989). Synchrotron-based scanning transmission X-ray microscopy (STXM) allowed for the identification of oxidized iron in microchondrules and matrix material of Semarkona (LL3.0) further pointing towards its hydration (Dobrică et al., 2019). The presence of oxidized iron species produced by the interaction with water on UOC parent bodies was suggested based on the elemental and isotopic composition of insoluble organic matter (IOMs) of Antarctic UOCs QUE 97008 (L3.05), MET 00452 (L(LL)3.05-3.1) and WSG 95300 (H3.4) (Alexander et al., 2010). Scanning electron microscopy (SEM) and TEM were also used to identify amphiboles in voids and veins of Tieschitz (H(L)3.6) matrix indicating aqueous alteration (Dobrică and Brearley, 2014). The isotopic composition of secondary minerals such as fayalite and magnetite in ordinary chondrites Semarkona (LL3.0), EET 90161 (L3.05), MET 00452 (L(LL) 3.05), MET 96503 (L3.1) and Ngawi (LL3.6) are consistent with early aqueous alteration on their asteroidal parent body (Doyle et al., 2015).

While many studies were about identifying secondary minerals via various analytical techniques, most of them focused on a limited selection of the most primitive UOCs (such as Semarkona). In the present work, we present a large-scale survey of 31 Antarctic and 10 non-Antarctic UOCs ranging from petrologic types (PTs) 3.0 to 3.9. The thermal history of these UOCs has previously been characterized by Raman spectroscopy (Bonal et al., 2016). We determine the weathering grade and shock stage of each UOC through petrographic observations and assess the level of hydration by Thermogravimetric analysis (TGA) of bulk samples and Fourier transform infrared (FTIR) spectroscopy of matrix fragments. By doing so, we investigate i) if and to what extent UOCs are hydrated and ii) if the extent of hydration is controlled by the thermal metamorphism as it has been observed in CV chondrites (Bonal et al., 2020). These results are then discussed in terms of snowline location around the UOC formation region, at the time of accretion.

2. Samples and Methods

2.1. Sample list and experimental procedure

We consider a total of 41 UOCs (Table 1), 31 of which are Antarctic finds and 10 non-Antarctic falls. For each sample, a range of measurements was performed to constrain the secondary processes experienced by the meteorite.

Firstly, an in-depth petrographic study was performed on 39 of the 41 selected UOCs. For this, thin sections were obtained for all but two (GRO 95504 and QUE 97008) UOCs from various sources (Table 1). As previously shown (Eschrig et al., 2022) the classification (H, L vs LL) of non-Antarctic UOCs given in the Meteoritical Bulletin Database, (2022) is erroneous in many cases (74 % misclassified samples in a series of 31 Antarctic UOCs). Therefore, the classifications used in the present work are those determined by magnetic susceptibility of bulk samples and chondrule size measurements on thin sections described in Eschrig et al., (2022) and not those reported in the Meteoritical Bulletin Database, (2022). The considered classification for the studied UOCs is listed in Table 1.

Using a Leica DM2500P petrographic optical microscope at CEREGE the modal abundance of the different petrographic components (metal, matrix, sulfides (troilite), magnetite/weathering products, and chondrules/chondrule fragments) was determined by point counting on thin sections, with 500 points per sample. The upper and lower bounds on the modal abundance values are calculated by determining the two-sided confidence bounds following Howarth (1998) and then subtracting them from the total phase abundance values. The obtained modal abundances, as well as their upper and lower bounds, are listed in Table 1.

Shock stage and weathering grade were determined by petrographic observations of the thin sections using the Leica DM2500P petrographic optical microscope at CEREGE as well. The degree of terrestrial weathering of each UOC was determined using the scale defined by Wlotzka (1993). It ranges

Table 1: List of UOCs studies in the present work. Given are their metamorphic grade (FWHMD), classification, petrologic type (PT), modal abundances of the different chondrite components including chondrules and chondrule fragments, matrix, metal, magnetite and weathering products and sulfide (troilite) (± lower error ± upper error), shock stage, weathering degree and providers of the bulk samples and sections.

	class. and TM			point counting results (%) (± lower error ± upper error)					Shock and Weathering			Providers	
sample	**FWHM$_D$ (cm-1) (Bonal et al. 2016)**	**Type (Eschrig et al. 2022)**	**PT**	**chondr./ chondr. fragments (%)**	**matrix (%)**	**metal (%)**	**magnetite + weath. products (%)**	**sulfide (troilite) (%)**	**shock stage**	**percent weathering products**	**weathering grade**	**thin/thick sections**	**bulk samples**
ALH 76004	158.9 ± 19.7	L(LL)	3.1–3.4	81.38 ± 3.72 ± 3.34	11.54 ± 2.68 ± 3.15	-	0.2 ± 0.2 ± 0.92	6.88 ± 2.07 ± 2.6	S3/S2+	<1%	W0	NASA	NASA
ALH 78119	47.4 ± 3.7	LL(L)	-	79.43 ± 3.71 ± 3.38	12.38 ± 2.69 ± 3.13	1.9 ± 0.99 ± 1.57	0	6.29 ± 1.92 ± 2.43	S1	10-15%	W1	NASA	NASA
ALH 83008	115.1 ± 9.4	LL	>3.6	71.59 ± 4.03 ± 3.79	12.52 ± 2.68 ± 3.11	2.8 ± 1.23 ± 1.78	5.98 ± 1.85 ± 2.36	7.1 ± 2.03 ± 2.52	S3	10-15%	W1	NASA	NASA
ALH 84086	-	LL	3.8	87.9 ± 3.06 ± 2.64	4.47 ± 1.59 ± 2.11	4.47 ± 1.59 ± 2.11	0.37 ± 0.33 ± 0.97	2.79 ± 1.22 ± 1.77	S3	<1%	W0	NASA	NASA
ALH 84120	-	L	3.8	86.17 ± 3.32 ± 2.89	2.96 ± 1.3 ± 1.88	4.55 ± 1.64 ± 2.2	0.99 ± 0.67 ± 1.3	5.34 ± 1.79 ± 2.33	S1	<1%	W0	NASA	NASA
Bishunpur	174.1 ± 12.9	L/LL	3.15	72.18 ± 4.02 ± 3.77	18.42 ± 3.21 ± 3.56	3.57 ± 1.41 ± 1.95	0.19 ± 0.18 ± 0.85	5.64 ± 1.8 ± 2.31	S2	0%	W0	MNHN	ASU
Bremervörde	50 ± 0	H/L	3.9	83.13 ± 3.56 ± 3.17	6.35 ± 1.97 ± 2.5	5.16 ± 1.76 ± 2.31	0.6 ± 0.47 ± 1.13	4.76 ± 1.69 ± 2.24	S2	1%	W0	MNHN	ASU
BTN 00302	159.3 ± 16.8	LL	3.1–3.4	76.67 ± 3.87 ± 3.56	17.4 ± 3.15 ± 3.53	2.1 ± 1.05 ± 1.63	0	3.82 ± 1.47 ± 2.02	S4/S5	1%	W0	NASA	NASA
Chainpur	147.8 ± 7.2	LL	3.4	80.64 ± 3.74 ± 3.37	12.77 ± 2.8 ± 3.24	1.6 ± 0.9 ± 1.53	0.2 ± 0.19 ± 0.91	4.79 ± 1.7 ± 2.25	S1	2-3%	W1	MNHN	ASU
Dhajala	-	H	3.8	79.65 ± 3.74 ± 3.39	5.62 ± 1.82 ± 2.35	10.85 ± 2.55 ± 3.01	0	3.88 ± 1.49 ± 2.05	S1	0%	W0	MNHN	ASU
DOM 03287	122 ± 13	LL	3.6	65.36 ± 4.21 ± 4.03	26.22 ± 3.68 ± 3.95	1.12 ± 0.71 ± 1.31	1.69 ± 0.91 ± 1.49	5.62 ± 1.8 ± 2.31	S3	8-10%	W1	NASA	NASA
DOM 08468	122 ± 6.2	H	3.6	66.17 ± 4.16 ± 3.98	22 ± 3.42 ± 3.73	4.44 ± 1.57 ± 2.09	3.33 ± 1.34 ± 1.88	4.07 ± 1.5 ± 2.03	S1	30%	W2	NASA	NASA
EET 83248	110.6 ± 13	H	>3.6	79.8 ± 4.27 ± 3.82	7.2 ± 2.34 ± 2.99	3.5 ± 1.57 ± 2.3	4.2 ± 1.75 ± 2.46	5.2 ± 1.97 ± 2.66	S1	3%	W2	NASA	NASA
EET 87735	192.1 ± 21.8	LL	3.05–3.1	63.56 ± 4.42 ± 4.25	22.87 ± 3.63 ± 3.96	0.61 ± 0.48 ± 1.16	6.28 ± 1.97 ± 2.51	6.68 ± 2.04 ± 2.57	S1	2-5%	W1	NASA	NASA
EET 90066	182.2 ± 9.3	LL	3.1	73.97 ± 4.03 ± 3.75	20.16 ± 3.4 ± 3.74	-	0.39 ± 0.34 ± 1.02	5.48 ± 1.81 ± 2.34	S2	5%	W1	NASA	NASA
EET 90628	254.2 ± 19.7	LL	3	66.67 ± 4.28 ± 4.08	23.33 ± 3.61 ± 3.92	-	3.14 ± 1.33 ± 1.91	6.86 ± 2.04 ± 2.55	S3-	1-2%	W1	NASA	NASA
EET 96188	167.6 ± 11.4	LL	3.1-3.4	76.32 ± 3.93 ± 3.62	18.2 ± 3.25 ± 3.62	-	0	5.48 ± 1.81 ± 2.34	S3	1%	W0	NASA	NASA
GRO 06054	225.2 ± 18.6	LL	3.05	77.03 ± 3.87 ± 3.56	16.02 ± 3.05 ± 3.45	0 ± 0 ± 1.35	3.28 ± 1.36 ± 1.92	3.67 ± 1.45 ± 2	S2	5-10%	W1	NASA	NASA
GRO 95504	149.1 ± 7.3	L	3.4	-	-	-	-	-	-	-	-	-	NASA
Hallingeberg	115.33 ± 0	L	3.4	79.77 ± 3.74 ± 3.39	12.84 ± 2.77 ± 3.2	3.31 ± 1.37 ± 1.94	0	4.09 ± 1.54 ± 2.09	S1/S2	0%	W0	MNHN	ASU
Krymka	173 ± 9.8	LL	3.2	77.28 ± 3.87 ± 3.55	17.28 ± 3.17 ± 3.55	1.17 ± 0.74 ± 1.35	0	4.27 ± 1.58 ± 2.12	S3	2%	W1	MNHN	MNHN
LAR 04382	168.8 ± 22	LL	3.1–3.4	72.87 ± 4.1 ± 3.83	20 ± 3.4 ± 3.76	1.58 ± 0.9 ± 1.51	0	5.54 ± 1.83 ± 2.37	S3	5%	W1	NASA	NASA
LAR 06469	105.4 ± 7.7	L	>3.6	72.88 ± 4.04 ± 3.78	12.5 ± 2.72 ± 3.15	1.92 ± 1 ± 1.59	8.85 ± 2.3 ± 2.78	3.85 ± 1.48 ± 2.03	S2/S3	40-50%	W2	NASA	NASA
LEW 87248	248.7 ± 12.9	L(LL)	3	81.54 ± 3.71 ± 3.33	10.75 ± 2.59 ± 3.07	-	1.01 ± 0.68 ± 1.34	6.69 ± 2.04 ± 2.58	S3	<1%	W0	NASA	NASA
LEW 87284	167.3 ± 46	LL	3.1–3.4	82.59 ± 3.64 ± 3.24	9.92 ± 2.49 ± 2.98	-	1.62 ± 0.92 ± 1.55	5.87 ± 1.9 ± 2.45	S3+	1%	W0	NASA	NASA
LEW 88617	133.7 ± 17.6	LL	3.6	81.67 ± 3.49 ± 3.14	13.79 ± 2.77 ± 3.16	1.09 ± 0.69 ± 1.27	0	3.45 ± 1.36 ± 1.88	S1/S2	5-10%	W1	NASA	NASA
LEW 88632	151.5 ± 11.1	LL	3.4	71.51 ± 4.14 ± 3.88	17.68 ± 3.22 ± 3.6	0.2 ± 0.19 ± 0.89	1.38 ± 0.82 ± 1.44	9.23 ± 2.37 ± 2.86	S2	10%	W1	NASA	NASA
MAC 88174	105.1 ± 6.7	H	>3.6	81.49 ± 3.7 ± 3.32	6.04 ± 1.93 ± 2.47	6.84 ± 2.06 ± 2.59	1.01 ± 0.68 ± 1.33	4.63 ± 1.67 ± 2.24	S3	10%	W1	NASA	NASA
MCY 05218	198.5 ± 16.7	L	3.05-3.1	71.58 ± 4.25 ± 3.99	14.73 ± 3.04 ± 3.48	2.49 ± 1.2 ± 1.82	3.73 ± 1.51 ± 2.1	7.47 ± 2.18 ± 2.72	S3	>20%	W2	NASA	NASA
MET 00489	204.2 ± 10.7	LL	3.05–3.1	86.68 ± 3.23 ± 2.81	8.69 ± 2.28 ± 2.76	-	0.39 ± 0.34 ± 1	4.25 ± 1.57 ± 2.11	S2/3	10-15%	W1	NASA	NASA
MET 00506	179.5 ± 7.1	LL	3.1	67.36 ± 4.17 ± 3.98	19.62 ± 3.3 ± 3.64	0.75 ± 0.55 ± 1.17	5.85 ± 1.84 ± 2.35	6.42 ± 1.93 ± 2.43	S2+/S3	15%	W1	NASA	NASA
Mezö-Madaras	70 ± 0	L	3.7	88.11 ± 2.94 ± 2.54	5.24 ± 1.68 ± 2.16	3.15 ± 1.27 ± 1.78	0.17 ± 0.17 ± 0.8	3.32 ± 1.31 ± 1.82	S4	0%	W0	NHM	NHM
MIL 05050	174.5 ± 9.8	LL	3.1	66.35 ± 4.22 ± 4.03	22.62 ± 3.51 ± 3.82	1.71 ± 0.93 ± 1.51	2.09 ± 1.04 ± 1.62	7.22 ± 2.06 ± 2.56	S3	15%	W1	NASA	NASA
MIL 05076	148.4 ± 17.2	LL	3.4	75.39 ± 3.99 ± 3.69	13.78 ± 2.88 ± 3.31	0.39 ± 0.35 ± 1.02	4.92 ± 1.71 ± 2.26	5.51 ± 1.82 ± 2.36	S3	10-15%	W1	NASA	NASA
Parnallee	74.7 ± 5.3	LL	3.7	77.14 ± 3.83 ± 3.53	14.86 ± 2.93 ± 3.33	1.52 ± 0.86 ± 1.46	0.19 ± 0.19 ± 0.87	6.29 ± 1.92 ± 2.43	S3	1%	W0	MNHN	NHM
Piancaldoli	173.4 ± 20.2	LL	3.1	72.23 ± 4.09 ± 3.83	19.03 ± 3.3 ± 3.66	2.33 ± 1.12 ± 1.7	0.39 ± 0.34 ± 1.01	6.02 ± 1.89 ± 2.42	S2/S3	1%	W0	CRPG	CRPG
QUE 97008	222.4 ± 13.4	L	3.05	-	-	-	-	-	-	-	-	-	NASA
RBT 04251	144.4 ± 9	LL	3.4	74.61 ± 4.02 ± 3.73	16.34 ± 3.11 ± 3.51	2.36 ± 1.14 ± 1.73	1.57 ± 0.89 ± 1.5	5.12 ± 1.75 ± 2.29	S3	3%	W1	NASA	NASA
Tieschitz	125.9 ± 4.5	H(L)	3.6	78.57 ± 3.9 ± 3.55	13.27 ± 2.88 ± 3.33	3.67 ± 1.48 ± 2.07	0	4.49 ± 1.66 ± 2.23	S1/S2	0%	W0	MNHN	NHM
TIL 82408	208.4 ± 9	LL	3.05–3.1	72.02 ± 4.22 ± 3.95	22.84 ± 3.66 ± 3.99	-	2.26 ± 1.13 ± 1.75	2.88 ± 1.3 ± 1.91	S3	11%	W1	NASA	NASA
WSG 95300	146.2 ± 8.8	H	3.4	73.4 ± 4.1 ± 3.82	14.8 ± 3 ± 3.42	6.2 ± 1.95 ± 2.49	0	5.6 ± 1.85 ± 2.39	S1	1-2%	W1	NASA	NASA

from W0 to W6 and is based on the percentage of oxidized metal, sulfides, and, for strongly weathered samples, silicates. Each section was looked at under reflected light and the percentage of weathering products (iron oxides and oxy-hydroxides) was estimated (Table 1). For the samples set considered in the present work the weathering grades range from W0 – W2 only. The shock stage was determined using the shock indicators of Bennett and McSween, (1996), Scott et al., (1992) and Stöffler et al., (1991). For this, 10-20 olivine grains were examined in transmitted light for irregular fractures, the extent of undulatory extinction, planar fractures, and mosaicism. The thin sections were also examined for the presence of polycrystalline or twinned troilite under reflected light. The shock stages determined for the studied UOCs are listed in Table 1 and vary from S1 to S4/S5.

TGA of 35 bulk powdered UOCs were performed using a Mettler-Toledo TGA-DSC3+ instrument at the Institut des Sciences de la Terre (ISTerre), France. The gas evolved from the TGA-DSC instrument was analyzed using an IS50 FTIR instrument from Thermo Scientific. The gas was transferred from the outlet of the TGA-DSC instrument to the FTIR instrument using a heated transfer line (300 °C). A FTIR spectrum of the evolved gas was measured every 23s. To ensure the representativity of all chondrite components, about 50 mg of bulk meteorites were carefully ground using a mortar and pestle until they resembled fine powder. Subsequently, 35 mg of the powder was selected for the TGA measurements. The powders were transferred to 70 µl aluminum crucibles and measured at temperatures from 25 °C to 1075 °C under a N_2 atmosphere flushed at 50 mL/min. To account for any mass loss related to the aluminum crucible, a measurement with an empty crucible was performed. For a question of time, this was not done before each measurement. Instead, a total of 3 empty crucibles were measured and their average TGA curve was used to correct the TGA curves of the UOCs. UOCs, for which an individual empty crucible could be measured, were corrected by their corresponding crucible and are marked in Table 2. Figure A1 of the Appendix shows the TGA curves of all UOCs measured in the present work. For two samples (ALH 76004 (L(LL)3.1-3.4) and BTN 00302 (LL3.1-3.4)) the TGA curve initially increased with increasing temperature

Table 2: TGA results for the UOCs measured in the present work. Given are the matrix normalized mass losses between 0 - 150 °C, 150 – 550 °C and 550 – 1000 °C as well as the total mass loss between 150 – 1000 °C both, matrix normalized and non-normalized. Lastly, the matrix normalized mass loss between 200 – 900 °C is given to be able to compare with the hydration of CVs (Bonal et al. 2020). UOCs for which an individual empty crucible was measured and used for the correction of the TGA curve are marked with (*).

	mass loss (wt.%) Mat. Norm. (± lower error ± upper error)			**Total mass loss (wt.%)**	**Total mass loss (wt.%) Mat. Norm. (± lower error ± upper error)**
sample	**0-150 °C**	**150-550 °C**	**550 - 1000 °C**	**150 - 1000 °C**	**150 - 1000 °C**
ALH 76004	1.27 ± 0.74 ± 0.69	3.45 ± 1.09 ± 0.95	0.75 ± 0.87 ± 0.84	0.55 ± 0.1	4.77 ± 1.41 ± 1.21
ALH 78119	2.43 ± 0.81 ± 0.72	8.77 ± 2.27 ± 1.96	5.59 ± 1.5 ± 1.3	1.93 ± 0.03	15.57 ± 3.96 ± 3.42
ALH 83008	4.77 ± 1.28 ± 1.12	17.6 ± 4.39 ± 3.8	10.21 ± 2.58 ± 2.23	4.14 ± 0.01	33.02 ± 8.21 ± 7.09
ALH 84086	1.77 ± 1.62 ± 1.41	6.64 ± 3.34 ± 2.56	2.09 ± 1.65 ± 1.4	0.35 ± 0.18	7.78 ± 3.85 ± 2.94
ALH 84120	4.42 ± 3.27 ± 2.4	12.03 ± 7.79 ± 5.43	4.04 ± 3.07 ± 2.28	0.44 ± 0.14	14.85 ± 9.55 ± 6.63
BTN 00302	0.1 ± 3.58 ± 3.58	0.54 ± 0.74 ± 0.73	0 ± 626.96 ± 626.96	0.1 ± 0.62	0.55 ± 0.73 ± 0.72
Bishunpur	1.24 ± 0.51 ± 0.49	3.33 ± 0.74 ± 0.68	1.5 ± 0.51 ± 0.48	0.96 ± 0.06	5.23 ± 1.07 ± 0.97
Bremervörde	1.71 ± 1.21 ± 1.07	6.35 ± 2.64 ± 2.11	2.13 ± 1.27 ± 1.09	0.55 ± 0.11	8.71 ± 3.53 ± 2.8
Chainpur	0.93 ± 0.74 ± 0.71	6.61 ± 1.75 ± 1.52	1.88 ± 0.73 ± 0.66	1.18 ± 0.05	9.23 ± 2.39 ± 2.07
DOM 03287	1.87 ± 0.4 ± 0.38	5.56 ± 0.88 ± 0.82	1.96 ± 0.41 ± 0.39	2.07 ± 0.03	7.89 ± 1.22 ± 1.14
DOM 08468	1.61 ± 0.44 ± 0.41	5.44 ± 0.97 ± 0.89	2.53 ± 0.53 ± 0.5	1.87 ± 0.03	8.49 ± 1.47 ± 1.35
Dhajala	0.4 ± 2.76 ± 2.72	-	-	-	-
EET 87735	3.42 ± 0.68 ± 0.63	10.52 ± 1.85 ± 1.7	5.74 ± 1.04 ± 0.96	3.85 ± 0.02	16.83 ± 2.93 ± 2.69
EET 90066 (70mg)	4.35 ± 0.84 ± 0.77	8.79 ± 1.65 ± 1.5	5.22 ± 1 ± 0.91	2.92 ± 0.01	14.47 ± 2.7 ± 2.45
EET 90628*	2.16 ± 0.48 ± 0.45	4.22 ± 0.77 ± 0.71	2.69 ± 0.54 ± 0.51	1.75 ± 0.03	7.48 ± 1.29 ± 1.19
EET 90628 (70mg)	2.36 ± 0.45 ± 0.42	4.67 ± 0.81 ± 0.75	3.11 ± 0.56 ± 0.52	1.97 ± 0.02	8.45 ± 1.43 ± 1.32
GRO 06054*	4.36 ± 1.02 ± 0.91	6.94 ± 1.55 ± 1.38	5.07 ± 1.16 ± 1.04	2.13 ± 0.03	13.28 ± 2.88 ± 2.56
Hallingeberg	1.4 ± 0.68 ± 0.64	5.9 ± 1.55 ± 1.35	2.12 ± 0.75 ± 0.68	1.06 ± 0.06	8.23 ± 2.11 ± 1.83
Krymka	2.74 ± 0.69 ± 0.63	7.63 ± 1.61 ± 1.44	2.74 ± 0.69 ± 0.63	1.85 ± 0.03	10.72 ± 2.23 ± 2
LAR 04382	2.1 ± 0.53 ± 0.49	6 ± 1.18 ± 1.07	2.55 ± 0.59 ± 0.55	1.8 ± 0.03	9.01 ± 1.72 ± 1.56
LAR 06469	4.34 ± 1.2 ± 1.05	13.87 ± 3.53 ± 3.05	6.32 ± 1.67 ± 1.45	3.09 ± 0.02	24.73 ± 6.26 ± 5.4
LEW 87284*	1.53 ± 0.84 ± 0.77	8.66 ± 2.67 ± 2.24	9.05 ± 2.78 ± 2.34	2.07 ± 0.03	20.9 ± 6.31 ± 5.28
LEW 88617	3.16 ± 0.86 ± 0.77	9.79 ± 2.29 ± 2.01	2.09 ± 0.68 ± 0.62	1.65 ± 0.04	11.97 ± 2.78 ± 2.44
LEW 88632	3.23 ± 0.76 ± 0.69	10.74 ± 2.22 ± 1.98	4.19 ± 0.93 ± 0.84	2.7 ± 0.02	15.29 ± 3.13 ± 2.8
MAC 88174	3.55 ± 1.71 ± 1.4	11.66 ± 4.85 ± 3.8	8.86 ± 3.73 ± 2.93	1.44 ± 0.04	23.8 ± 9.77 ± 7.64
MET 00489*	4.21 ± 1.5 ± 1.26	9.34 ± 3.04 ± 2.52	1.91 ± 0.95 ± 0.84	1 ± 0.06	11.53 ± 3.73 ± 3.08
MET 00506	4.13 ± 0.84 ± 0.76	11.57 ± 2.17 ± 1.97	3.82 ± 0.79 ± 0.72	3.15 ± 0.02	16.05 ± 3 ± 2.72
MIL 05050	3.72 ± 0.7 ± 0.64	8.17 ± 1.41 ± 1.3	4.5 ± 0.82 ± 0.75	3.13 ± 0.02	13.82 ± 2.35 ± 2.16
MIL 05076	5.14 ± 1.32 ± 1.16	14.42 ± 3.49 ± 3.04	6.24 ± 1.57 ± 1.37	2.89 ± 0.02	20.98 ± 5.06 ± 4.4
Mezö-Madaras	2.22 ± 1.42 ± 1.22	7.41 ± 3.2 ± 2.52	2.2 ± 1.42 ± 1.22	0.59 ± 0.1	11.28 ± 4.74 ± 3.71
Parnallee	0.89 ± 0.66 ± 0.63	2.88 ± 0.79 ± 0.71	-	-	-
Parnallee (70mg)	0.98 ± 0.42 ± 0.39	2.79 ± 0.7 ± 0.62	-	-	-
Piancaldoli	1.02 ± 0.49 ± 0.47	6.76 ± 1.34 ± 1.22	3.52 ± 0.76 ± 0.7	2.13 ± 0.03	11.19 ± 2.18 ± 1.97
RBT 04251*	2.38 ± 0.66 ± 0.6	4.84 ± 1.11 ± 1	1.39 ± 0.56 ± 0.52	1.05 ± 0.06	6.4 ± 1.43 ± 1.27
TIL 82408*	2.39 ± 0.53 ± 0.49	5.3 ± 0.98 ± 0.9	2.44 ± 0.53 ± 0.5	2.07 ± 0.03	9.06 ± 1.61 ± 1.48
Tieschitz	0.75 ± 0.8 ± 0.77	2.84 ± 0.87 ± 0.78	0.67 ± 0.85 ± 0.82	0.53 ± 0.11	4.03 ± 1.12 ± 0.99
WSG 95300	3.01 ± 0.82 ± 0.74	8.92 ± 2.11 ± 1.85	5.24 ± 1.29 ± 1.14	2.11 ± 0.03	14.26 ± 3.32 ± 2.91

131 reflecting a mass gain instead of a mass loss. Since both of these UOCs show a very low mass loss, the
132 oxidization of metal with increasing temperature had a significant impact on the mass loss curve.
133 Therefore, these two samples were re-measured after a significant amount of metal was extracted from
134 the powders using a magnet. The TGA curves of the resulting metal depleted samples are shown in Figures
135 A1 (a) and (h) and the mass losses determined from these curves are listed in Table 2.

136 The mass losses measured in the present work are small (from 0.09 wt.% to 4.13 wt.%). Thus, the
137 sensitivity of the FTIR spectrometer did not suffice for the detection of typical byproducts of de-
138 hydroxylation (e.g. H_2O, CO_2, CO, CH) from the amount of gas evolved from 35 mg of powder at a given
139 time. Attempts to increase the amount of gas at each given time were performed on three UOCs (EET
140 90066 (LL3.1), EET 90628 (LL3.9), and Parnallee (LL3.7)) by measuring 70 mg of powder using a 150 µl
141 aluminum crucibles under the same measuring conditions (Figure A2 of the Appendix, Table 2).

142 Due to time constraints, FTIR spectroscopic measurements of matrix fragments was performed
143 on only 14 of the 41 UOCs using a BRUKER Vertex 70 FTIR spectrometer equipped with a HYPERION 3000
144 IR microscope at the Institut de Planétologie et d'Astrophysique de Grenoble (IPAG, France). UOCs with
145 low metamorphic grades were intentionally chosen since the sample preparation is easier for these
146 samples. The UOCs were first carefully manually crushed into a fine powder using a mortar and pestle.
147 Then, 15-20 matrix fragments ranging from 30-50 micron in size were manually selected under a binocular
148 microscope and transferred to a diamond window. Matrix fragments were identified under the
149 microscope based on their dark color, having a porous and fluffy texture, and then manually picked using
150 a needle. The diamond windows were transferred into a press, which could lead to the loss of some of the
151 picked fragments. The remaining fragments were subsequently pressed in between two diamond
152 windows allowing for measurements in transmitted light in the 4000-600 cm^{-1} range. The diamond
153 windows were separated and one or both windows were inserted into an environmental cell depending
154 on which side the pressed grains would stick to after pressing. The environmental cell allowed for

155 measurements at P < 10^{-4} mbar and temperatures up to 300 °C. Two spectra were then acquired per
156 fragment under vacuum, one at T = 100 °C and one at T = 300 °C. Heating the UOCs minimizes the amount
157 of adsorbed terrestrial water and, thus, helps in the identification of the asteroidal water and -OH mineral
158 carriers. It should be noted here, that the selection of matrix fragments becomes significantly more
159 difficult the lower the abundance of matrix and the higher the metamorphic grade of a given chondrite
160 are. Therefore, the number of usable fragments for the data treatment of the final average spectrum of
161 each UOC (Section 2.2) was between 3 and 8 fragments out of the 15-20 initially picked (Table 3).

162 The thermal history of all UOCs considered in the present work was previously characterized
163 based on Raman spectroscopy of polyaromatic carbonaceous matter (Bonal et al., 2016). The spectral
164 parameter $FWHM_D$ (Full width at half maximum of the D-band), as well as the corresponding PTs, are
165 listed in Table 1 as an estimate for the metamorphic grade. The exceptions to this are ALH 84086 (LL3.8),
166 ALH 84120 (L3.8), and Dhajala (H3.8). Since these UOCs are highly metamorphosed, the Raman
167 measurements were unsuccessful. Therefore, the PTs attributed to them in the Meteoritical Bulletin
168 Database, (2022) are given in Table 1.

169 **2.2. Analytical procedures**

170 **2.2.1. TGA**

171 The measured TGA curves were first corrected for contributions of mass loss due to the aluminum
172 crucible. For this, the mass loss of the empty crucible was subtracted from the mass loss of the UOCs. To
173 be able to interpret the empty crucible corrected mass loss curve, the first derivative (DTG curve) is taken.
174 This way, temperature ranges with strong mass loss can be easily identified by the minima in the DTG
175 curve. By comparing the DTG curves of a given sample with those of mineral standards, the origin of the
176 mass loss can be identified based on the position of the minima. A common pattern of DTG curve minima
177 can then be identified for a given sample set, to define temperature regions of mass loss due to certain

Table 3: Results of the fit done to the 3-micron band of the IR spectra measured on matrix grains of UOCs at 100 °C and 300 °C. Listed are the position, depth, FWHM and integrated band depth (IBD) of the three fitting bands (at 2.8-micron, 3.2-micron and 2.9-micron) and of the complete fit to the 3-micron band. If no values are given, it means that the corresponding band was not needed for the fitting of the 3-micron band. The number of spectra measured on individual matrix grains and used for the average spectra of each UOC is given as well.

		Phyllosilicate band (~2.8 micron)				**Interlayer water and Oxy-hydroxides (~3.1 micron)**				**Adsorbed water (~2.9 micron)**				**Complete 3-micron band**				
	sample	position (nm)	depth (%)	FWHM (nm)	IBD (%)	position (nm)	depth (%)	FWHM (nm)	IBD (%)	position (nm)	depth (%)	FWHM (nm)	IBD (%)	position (nm)	depth (%)	FWHM (nm)	IBD (%)	no. spectra
100 °C	**ALH 76004**	-	-	-	-	2992	3.02 ± 1.22	283	0.5 ± 0.04	2838	3.84 ± 0.88	198	0.52 ± 0.01	2870	5.37 ± 1.18	328	1.03 ± 0.001	3
	BTN 00302	-	-	-	-	3094	6.86 ± 7.5	175	0.66 ± 1.08	2922	6.2 ± 0.43	278	1.09 ± 0.01	3076	9.82 ± 2.61	334	1.77 ± 1.07	3
	EET 83248	-	-	-	-	3026	5.11 ± 2.87	264	0.77 ± 0.09	2876	12.98 ± 1.54	212	1.83 ± 0.02	2892	15.28 ± 11.64	288	2.62 ± 0.005	8
	EET 90066	2784	16.4 ± 19.54	136	1.68 ± 0.15	3045	23.3 ± 23.34	250	3.27 ± 3.32	2879	31.95 ± 45.62	189	3.9 ± 0.44	2889	46.7 ± 25.05	344	8.91 ± 3.449	8
	EET 90628	2742	16.38 ± 20.64	130	1.71 ± 0.14	2975	16.79 ± 6.23	300	2.96 ± 0.14	2826	21.16 ± 19.3	182	2.73 ± 0.17	2829	39.28 ± 20.41	332	7.45 ± 0.266	8
	EET 96188	2797	3.33 ± 11.99	113	0.28 ± 0.08	3001	8.96 ± 4.63	298	1.54 ± 0.86	2871	5.53 ± 8.34	150	0.55 ± 0.07	2891	12.65 ± 4.5	335	2.4 ± 0.895	5
	GRO 06054	2731	30.4 ± 12.58	93	2.39 ± 0.07	2973	32.46 ± 9.23	303	5.78 ± 0.18	2823	46.06 ± 11.48	201	6.47 ± 0.11	2828	76.21 ± 63.32	331	14.74 ± 0.222	7
	GRO 95504	2790	20.28 ± 23.54	134	2.02 ± 0.18	3020	32.39 ± 17.35	279	5.18 ± 2.82	2879	35.33 ± 24.76	185	4.29 ± 0.23	2894	61.77 ± 15.43	334	11.6 ± 2.921	6
	LEW 87248	2809	2.61 ± 0.46	185	0.35 ± 0	3113	2.43 ± 4.54	174	0.23 ± 0.64	2946	5.05 ± 7.96	289	0.87 ± 1.22	2938	6.56 ± 4.15	400	1.47 ± 1.392	8
	LEW 87284	2800	21.7 ± 15.31	188	2.93 ± 0.14	3058	11.8 ± 18.04	229	1.51 ± 0.21	2895	13.25 ± 90.34	194	1.59 ± 6	2840	30.55 ± 14.49	344	6.07 ± 6.007	3
	MCY 05218	2788	26.02 ± 34.21	143	2.77 ± 0.27	3054	23.32 ± 26.16	267	3.5 ± 3.61	2887	31.75 ± 54.71	192	3.96 ± 0.52	2884	52.12 ± 31.44	355	10.34 ± 3.882	7
	QUE 97008	2802	87.05 ± 46.79	154	9.58 ± 0.4	3079	86.68 ± 86.95	212	10.11 ± 7.73	2913	80.41 ± 179.44	190	9.52 ± 1.98	2897	131.79 ± 86.81	403	29.44 ± 8.201	6
	RBT 04251	2799	6.18 ± 9.94	136	0.62 ± 0.08	3047	10.76 ± 8.5	261	1.57 ± 1.07	2887	13.95 ± 16.56	191	1.71 ± 0.16	2899	20.89 ± 8.72	338	3.95 ± 1.133	5
	TIL 82408	-	-	-	-	3078	30.39 ± 18.6	203	3.41 ± 2.5	2886	26.65 ± 4.76	217	3.69 ± 0.06	3054	36.28 ± 14.28	364	7.16 ± 5.268	8
300 °C	**ALH 76004**	-	-	-	-	2931	3.12 ± 2.48	306	0.57 ± 0.47	2815	1.63 ± 0.39	149	0.18 ± 0	2873	3.98 ± 1.25	310	0.75 ± 0.145	3
	BTN 00302	-	-	-	-	-	-	-	-	-	-	-	-	-	-	-	-	3
	EET 83248	-	-	-	-	2994	6.46 ± 2.1	290	1.09 ± 0.04	2845	6.43 ± 1.95	214	0.93 ± 0.02	2895	10.23 ± 7.22	342	2.04 ± 0.001	8
	EET 90066	2760	13.53 ± 23.92	144	1.52 ± 0.18	2999	13.84 ± 8.71	277	2.24 ± 0.12	2851	19.33 ± 27.41	190	2.52 ± 0.25	2856	33.1 ± 13.97	332	6.31 ± 0.333	7
	EET 90628	2738	13.61 ± 10.33	135	1.49 ± 0.07	2967	6.2 ± 17.83	308	1.13 ± 3.24	2823	11.25 ± 11.4	187	1.51 ± 0.1	2812	23.04 ± 7.58	292	4.15 ± 3.286	8
	EET 96188	2811	3.09 ± 0.47	172	0.39 ± 0	3102	1.24 ± 0.36	123	0.09 ± 0	2918	6.45 ± 3.56	275	1.08 ± 0.76	2887	8.32 ± 3.63	321	1.56 ± 0.759	5
	GRO 06054	2739	35.68 ± 24.46	127	3.7 ± 0.17	2991	15.97 ± 7.12	277	2.59 ± 0.11	2828	25.43 ± 23.22	188	3.37 ± 0.21	2812	52.02 ± 54.72	316	9.71 ± 0.289	7
	GRO 95504	2791	21.4 ± 119.83	144	2.24 ± 0.98	2987	22.17 ± 18.1	287	3.72 ± 0.23	2879	17.76 ± 87.85	180	2.12 ± 0.78	2875	43.26 ± 10.02	319	8.14 ± 1.274	6
	LEW 87248	2818	2.91 ± 0.27	194	0.41 ± 0	2950	1.99 ± 2.48	304	0.36 ± 0.53	0	0 ± 0	0	0 ± 0	2835	4.18 ± 2	668	0.77 ± 0.185	8
	LEW 87284	2803	15.61 ± 1.65	213	2.37 ± 0.02	2989	5.22 ± 10.46	289	0.88 ± 2.05	0	0 ± 0	0	0 ± 0	2812	17.4 ± 8.95	311	3.28 ± 2.878	3
	MCY 05218	2778	17.91 ± 40.68	145	1.94 ± 0.33	3047	15.35 ± 28.98	261	2.27 ± 3.46	2875	22.38 ± 65.48	198	2.88 ± 0.64	2862	35.74 ± 19.25	351	7.15 ± 3.688	7
	QUE 97008	2808	84.73 ± 8.66	191	11.52 ± 0.08	3003	33.65 ± 37.21	295	5.75 ± 7.5	0	0 ± 0	0	0 ± 0	2815	95.33 ± 65.98	310	17.4 ± 38.527	6
	RBT 04251	2782	3.33 ± 9.15	133	0.33 ± 0.07	3015	7.56 ± 5.25	316	1.38 ± 0.97	2871	7.61 ± 7.47	186	0.95 ± 0.07	2889	13.71 ± 5.1	345	2.69 ± 1.032	5
	TIL 82408	-	-	-	-	2955	8.48 ± 1.87	308	1.56 ± 0.03	2832	10.93 ± 1.64	207	1.61 ± 0.02	2857	16.79 ± 8.49	313	3.19 ± 0.001	8

hydrated or hydroxylated minerals. This being said, identifying a pattern is not always easy in particular for UOCs. In previous works (Bonal et al., (2020); Garenne et al., (2014); King et al., (2015)), four regions were defined for carbonaceous chondrites: a mass loss dominated by adsorbed water between 25 °C and 200 °C, a release of oxy-hydroxides between 200 °C and ~400 °C, a release of -OH groups (e.g. phyllosilicates) between 400 °C and 770/850 °C and lastly a contribution of CO_2 due to calcium carbonates between 770 °C and 900 °C. In the case of UOCs, the DTG curves are less homogeneous than those of carbonaceous chondrites. The definition of mass loss regions consistent with the whole dataset is thus more difficult. Figure 1 plots the DTG curves obtained for all 31 UOCs. When considering the shape of all 31 DTG curves, three regions can be identified: 1. between 0 °C and 150 °C mostly controlled by adsorbed water contamination, 2. between 150 °C and 550 °C mostly controlled by oxy-hydroxides (such as goethite and/or ferrihydrite of potentially terrestrial and extraterrestrial origin) and 3. between 550 °C and 1000 °C mostly controlled by phyllosilicates and carbonates. The accuracy of the TGA scale is 10 µg. Using a Gaussian error estimation, the total error on the mass loss σ_m is

$$\sigma_m = \sqrt{\sigma_{m0}^2 + \sigma_{mf}^2} = \sqrt{(10\ \mu g)^2 + (10\ \mu g)^2} = 14\ \mu g$$

with σ_{m0} and σ_{mf} the errors on the mass loss at the start and at the end of the mass loss range. This corresponds to an error of 0.8 % for a mass loss fraction of 5 %. The fine-grained, porous matrix material is the petrographic component most sensitive to secondary processes. Since aqueous alteration in UOCs is limited and no altered chondrules could previously be observed (Brearley, 2003), we assume that the majority of the hydration is in the matrix. For this reason, the mass losses are normalized to the abundance of matrix determined by point counting.

The gas evolved from the TGA instrument was measured using FTIR spectroscopy. A spectrum was measured every 23s. Subsequently, a chemigram was retrieved for different wavelength ranges. For this, the integrated intensity in the 4200-3000 cm^{-1} range for H_2O, the 3000-2800 cm^{-1} range for CH, the 2450-

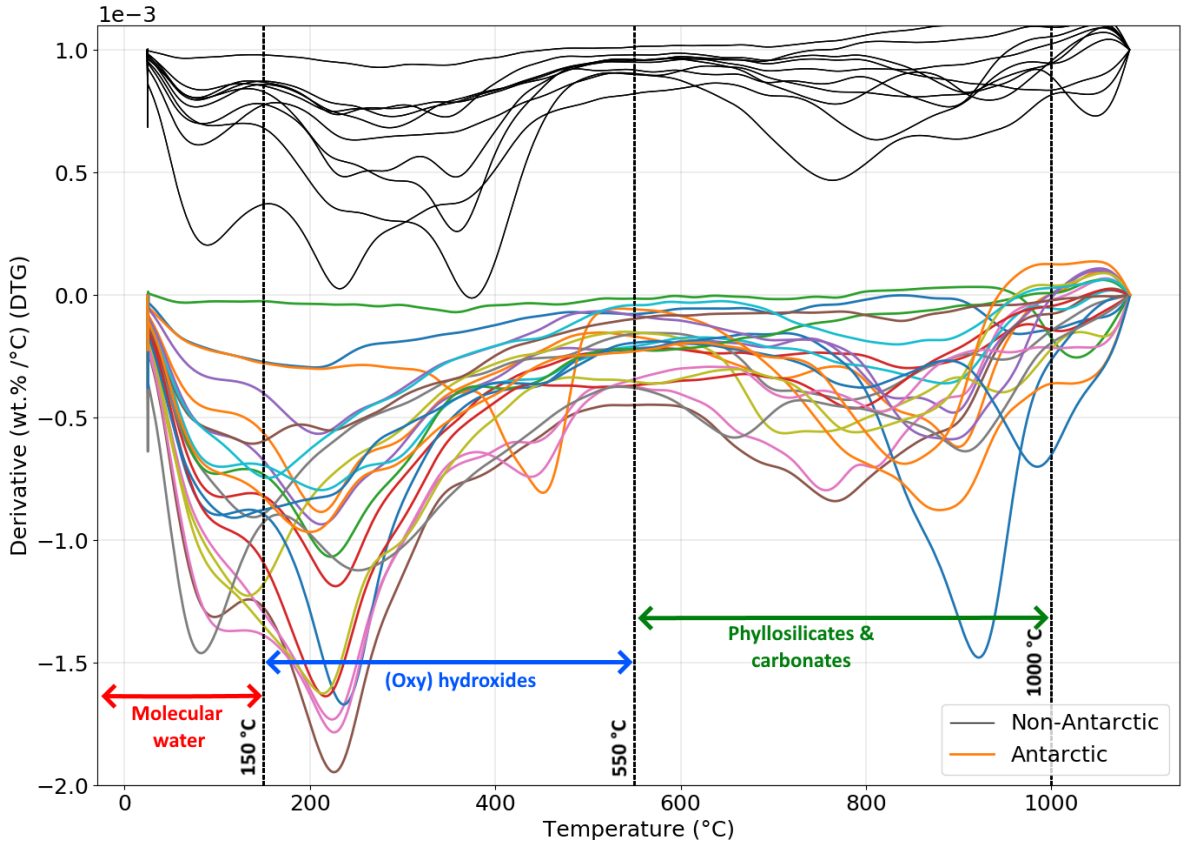

Figure 1: DTG curves of all 31 UOCs measured by TGA in the present work. Shown are the DTG curves of Antarctic UOCs in colors and those of non-Antarctic UOCs in black. An offset was applied to the non-Antarctic DTG curves. The vertical dotted lines indicate the three temperature ranges identified from the shape of the curves: 0 – 150 °C (mass loss due to molecular water), 150 – 550 °C (mass loss due to (oxy)-hydroxides) and 550 – 1000 °C (mass loss due to phyllosilicates and carbonates).

201 2240 cm^{-1} range for CO_2, and the 2240-2040 cm^{-1} range for CO were plotted as a function of the
202 temperature (Figure A3 and A5 of the appendix).

203 **2.2.2. IR spectroscopy**

204 Because organic compounds are expected to be dominantly present in the matrix, only spectra
205 displaying aliphatic bands around 2855 cm^{-1} and 2955 cm^{-1} are considered related to matrix fragments.
206 Then, the baseline is removed by fitting a spline function to each of the matrix fragment spectra.
207 Subsequently, the spectra are normalized to the band around 840 cm^{-1} and the average of the UOC spectra
208 measured for different matrix fragments is taken. This specific band was chosen for the normalization
209 since the maximum of the Si-O stretching region might have been saturated for some spectra (see Section
210 3.3.). We note here that this normalization leads to band depth values higher than 100 % in Table 3. This
211 results in one average spectrum per sample. FTIR spectroscopy allows for the study of hydrated and
212 hydroxylated minerals through the 3 µm absorption band. This band corresponds to a superposition of
213 the stretching modes of hydroxyl groups in hydrated minerals (at 2.8 µm), the symmetric and asymmetric
214 stretching modes of weakly bound adsorbed H_2O molecules (at 2.9 µm), and the stretching modes of
215 strongly bound H_2O molecules to interlayer cations and oxy-hydroxides (such as goethite) (at 3.1 µm) (e.g.
216 Frost et al., (2000); Potin et al., (2020)). The shape and size of the 3 µm band depend on the amount of
217 water and -OH mineral carriers. An exponentially modified Gaussian (EMG) profile is used to model the 3
218 µm band following Potin et al., (2020). Since the IR spectra are noisy between 2500 and 2670 nm a
219 gaussian smoothing was applied to all UOCs in this region. If the entire spectrum looked noisy, the rest of
220 the spectrum was smoothed as well. A least-square fit was then performed by selecting either one, two,
221 or three EMGs based on the overall shape of the 3 µm band as well as the goodness of the fit by eye.
222 Figure A5 of the Appendix shows the fitted 3 µm bands of all 14 UOCs considered in the present work at
223 100 °C and 300 °C. The band positions, depths, FWHM, and integrated band depth (IBD) of the total 3 µm
224 band and the individual fitting bands were determined for each UOC (Table 3).

3. Results

3.1. Petrographic observations

The matrix abundance determined in the present work ranges from 3 % for ALH 84120 (L3.8) to 26.21 % for DOM 03287 (LL3.6). The average abundance of 14.5 ± 5.9 % for all the studied UOCs is in agreement with the average of 10-15 % given in the literature for UOCs (e.g. Krot et al., (2014); Weisberg et al., (2006))). Looking at the individual groups, the average matrix abundance is 10.8 ± 6.2 % (n = 7) for H and H(L), 9.7 ± 5.2 % (n = 8) for L, 13.3 ± 3.4 % (n = 4) for LL(L), and 17.0 ± 5.2 % (n = 23) for LL. The matrix abundance of LL UOCs, thus slightly exceeds those of H, L, and LL(L).

Terrestrial weathering products are identified in 24 of the 39 Antarctic and non-Antarctic UOCs with weathering degrees ranging from W1 to W2. The percentages of oxidized metal and sulfides determined for each UOC are listed in Table 1. ALH 76004 (LL(L)3.1-3.4), ALH 84086 (LL3.8), ALH 84120 (L 3.8), Bishunpur (LL(L)3.15), Bremervörde (H(L)3.9), BTN 00302 (LL3.1), EET 96188 (LL3.1-3.4), Hallingeberg (L3.4), LEW 87248 (LL(L)3.0), LEW 87284 (LL3.1), Mezö-Madaras (L3.7), Parnallee (LL 3.6), Piancaldoli (LL3.1) and Tieschitz (H(L)3.6) show less than 1 % of oxidized metal and/or sulfides and are defined as W0. Samples classified as W1 range from 2% of weathering products for Krymka (LL3.2) to 15 % for MET 00506 (LL3.1). Three UOCs were found to be W2, with LAR 06469 (L3.6) showing 40-50 % weathered metal and sulfides, DOM 08468 (H3.6) showing 30 % and MCY 05218 (L3.05-3.1) showing >20 %. Figure 2 shows some examples of corroded metal grains as well as oxidized metal and sulfides in Krymka (W1), MIL 05076 (W1), DOM 08468 (W2), and LAR 06469 (W2). Iron oxy-hydroxide veins due to terrestrial weathering are clearly visible in these four UOCs as well.

The shock stages of the UOCs considered in the present work range from S1 to S4/S5 (Table 1). The least shocked samples are ALH 78119 (LL3.5), ALH 84120 (L3.8), Chainpur (LL3.4), DOM 08468 (H3.6), EET 83248 (H>3.6), EET 87735 (LL3.05-3.1) and WSG 95300 (H3.4) which are classified as S1 as well as

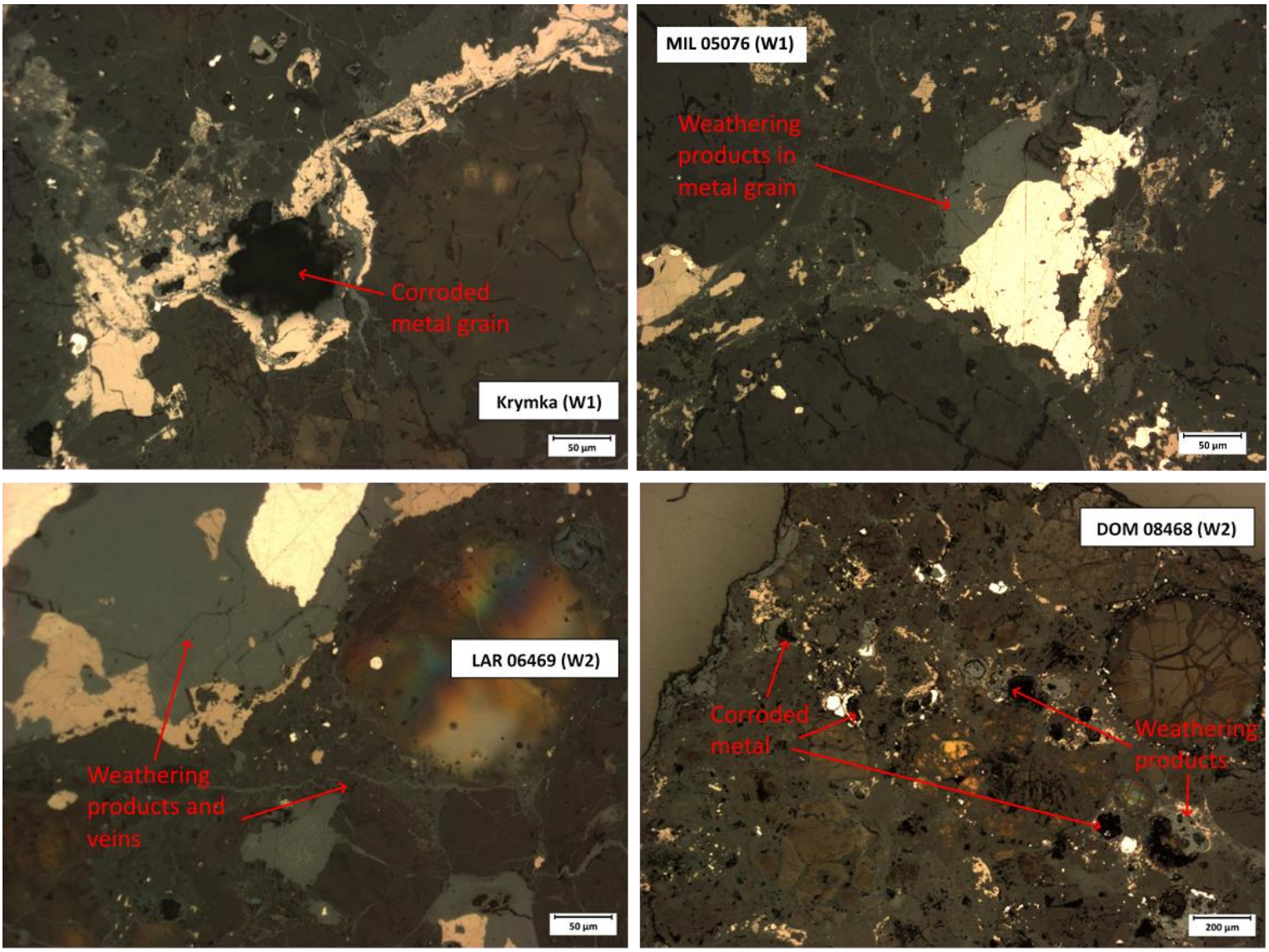

Figure 2: Examples of weathering products shown for different UOCs of varying weathering grades considered in the present work. Shown are: an image of a corroded metal grain and weathering veins in Krymka (W1); Weathering products and veins in MIL 05076 (W1); Weathered metal and weathering veins in LAR 06469 (W2); corroded metal grains and weathering veins in DOM 08468 (W2)

Hallingeberg (L3.4), Tieschitz (H(L)3.6) and LEW 88617 (LL3.6) which are classified between S1/S2. The most shocked samples are Mezö-Madaras (L3.7) classified as S4 and BTN 00302 (LL3.1-3.4) classified as S4/S5. Both of these samples show signs of mosaicism in olivine grains and BTN 00302 additionally shows PDFs (Figure 3).

3.2. TGA results

A mass loss is observed for all UOCs in the present work. The mass loss curves as well as the corresponding DTG curves are shown for each UOC in Figures A1 and A2 of the Appendix. Table 2 summarizes the matrix normalized mass loss for each UOC in the 0 - 150 °C, 150 - 550 °C and 550 – 1000 °C temperature regions defined in Section 2.2 as well as the raw and matrix normalized total mass loss between 150 – 1000 °C. For UOCs Parnallee (LL3.7) and Dhajala (H3.8) the mass loss curves started increasing instead of decreasing for temperatures higher than 500 °C and 750 °C, respectively (Figures A1 (j) and (ac) in the Appendix). Both of these samples are highly metamorphosed and, therefore, show a very low total mass loss which is approaching the limitations of the TGA instrument. Therefore, no mass loss values are given for these UOCs above the corresponding temperatures (Table 2).

Looking at the raw total mass loss between 150 - 1000 °C the lowest mass loss value is 0.35 wt.% for ALH 84086 (LL>3.6) and the highest is 4.14 wt.% for ALH 83008 (L>3.6) (Table 2). Within the groups, H and H(L) show an average total mass loss of 1.3 wt.%, for L it is 1.29 wt.%, for LL(L) it is 1.14 wt.% and for LL it is 2.14 wt.%. The slight increase of mass loss from H, H(L), L and LL(L) to LL could be due to 63 % of all UOCs considered in the present work being classified as LL (Table 1) and/or LL being more matrix enriched (see Section 3.1).

The matrix normalized total mass loss between 150 - 1000 °C ranges from 0.55 wt.% for BTN 00302 (LL3.1-3.4) to 33.02 wt.% for ALH 83008 (LL>3.6). The average matrix normalized total mass losses of the different groups are 11.86 wt.% for H and H(L), 14.77 wt.% for L, 8.52 wt.% for LL(L) and 12.64 wt.%

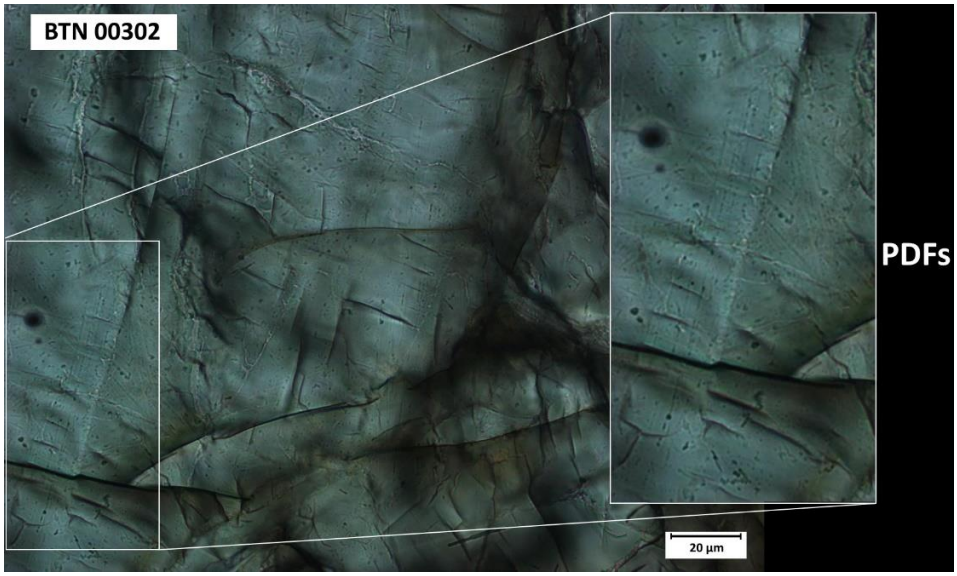

Figure 3: Example of planar deformation features (PDFs) in an olivine grain of BTN 00302 (S4/S5).

for LL. With average matrix abundances of 10.8 % for H, 9.7 % for L, 13.3 % for LL(L) and 17 % for LL (see Section 3.1) this means that while L show the lowest abundance of matrix, their hydration is the highest once normalized, followed by LL, then H and H(L). Based on the three LL(L)/L(LL) samples considered with TGA in the present work, LL(L) seems to be the least hydrated UOC subgroup.

Comparing the hydration determined by TGA between Antarctic and non-Antarctic UOCs shows that on average, Antarctic UOCs show a higher matrix normalized mass loss between 150 – 1000 °C (between 0 - 35 wt.%, average (13.57 ± 6.92) wt.%) while for non-Antarctic UOCs it is lower (between 0 - 15 wt.%, average (8.58 ± 2.7) wt.%). This is due to the higher percentage of weathering products present in Antarctic UOCs (Table 1).

Looking at the chemigrams of H_2O, CH, CO_2 and CO retrieved from the IR spectra measured on the evolved gas coming from the TGA instrument, mostly noise can be seen. No H_2O or CO_2 was detected for any of the UOCs measured in the present work, which is surprising given that we expect at least the presence of terrestrial water contamination. CH could only be detected in two UOCs, namely Chainpur (LL3.4) and Piancaldoli (LL3.1) (Figure A3 of the appendix). Only CO can be clearly seen for most samples in the 500 – 1075 °C temperature range (Figure A4 (a) and (b) of the appendix). The mass losses measured in this work are low in comparison to type 3 carbonaceous chondrites such as CV chondrites (Bonal et al., 2020). With a mass sensitivity of a tenth of micrograms (see Section 2.2), the TGA instrument is being operated at its limits for the UOCs with the lowest mass losses. Thus, we conclude that the sensitivity of the IR spectrometer is not high enough to detect the low concentrations of H_2O, CH and CO_2 released into the instrument at a given time. Only the abundance of CO seems to be high enough to be detected. Additionally, the use of highly hygroscopic KBr windows for the gas chamber might have masked the signal.

To test if the sensitivity limits of the IR spectrometer can be overtaken, the measurements done on 70 mg bulk powder (EET 90628 (LL3) and Parnallee (LL3.7)) (Figure A2 of the Appendix) can be considered. With a raw total mass loss of (1.97 ± 0.02) wt.% at 70 mg versus (1.75 ± 0.03) wt.% at 35 mg for EET 90628 (LL3), this increase of bulk material barely changes the mass loss giving us confidence in the representativity of the 35 mg sample measurements. After matrix normalization, the total mass loss values are (7.48 ± 1.29 ± 1.19) wt.% for 35 mg of sample and (8.45 ± 1.43 ± 1.32) wt.% for 70 mg of sample. Both samples (35 mg and 70 mg) of Parnallee show an increase in mass with increasing temperature (Figure A2 (c) of the Appendix) and can therefore not be used. For the IR spectra of the evolved gas, the chemigrams are still quite noisy at 70 mg of bulk samples but a signal of CO_2 becomes visible between ~700 - 1075 °C as well as CO (Figure A4 (c) and (d) of the appendix). H_2O and CH are still not detected. Therefore, the sensitivity of the IR spectrometer is not sufficient to detect hydration in the gas evolved from 70 mg of bulk sample either.

3.3. FTIR spectroscopy results

The average IR spectra of matrix fragments measured for 14 UOCs are shown in the 4000 – 2500 cm^{-1} range (Figure 4) and the 1400 – 750 cm^{-1} range (Figure 5). The standard deviation (SD) is shown as a shaded area around the spectrum. Although varying in shape and size, all 14 UOCs show a 3 µm band (Figure 4). This is in agreement with reflectance spectroscopy measurements previously done (Eschrig et al., 2022), which also showed the presence of a 3-µm band for UOCs. As discussed in Section 2.2 this 3-µm band reflects the presence of hydrated and hydroxylated minerals. The 3-µm band is visible both for measurements done at 100 °C and at 300 °C (Figures 4 and A5 in Appendix). For ALH 76004 (L(LL)3.1-3.4), BTN 00302 (LL3.1-3.4) and LEW 87248 (LL(L)3.0) the 3 µm band is much smaller than for the other UOCs.

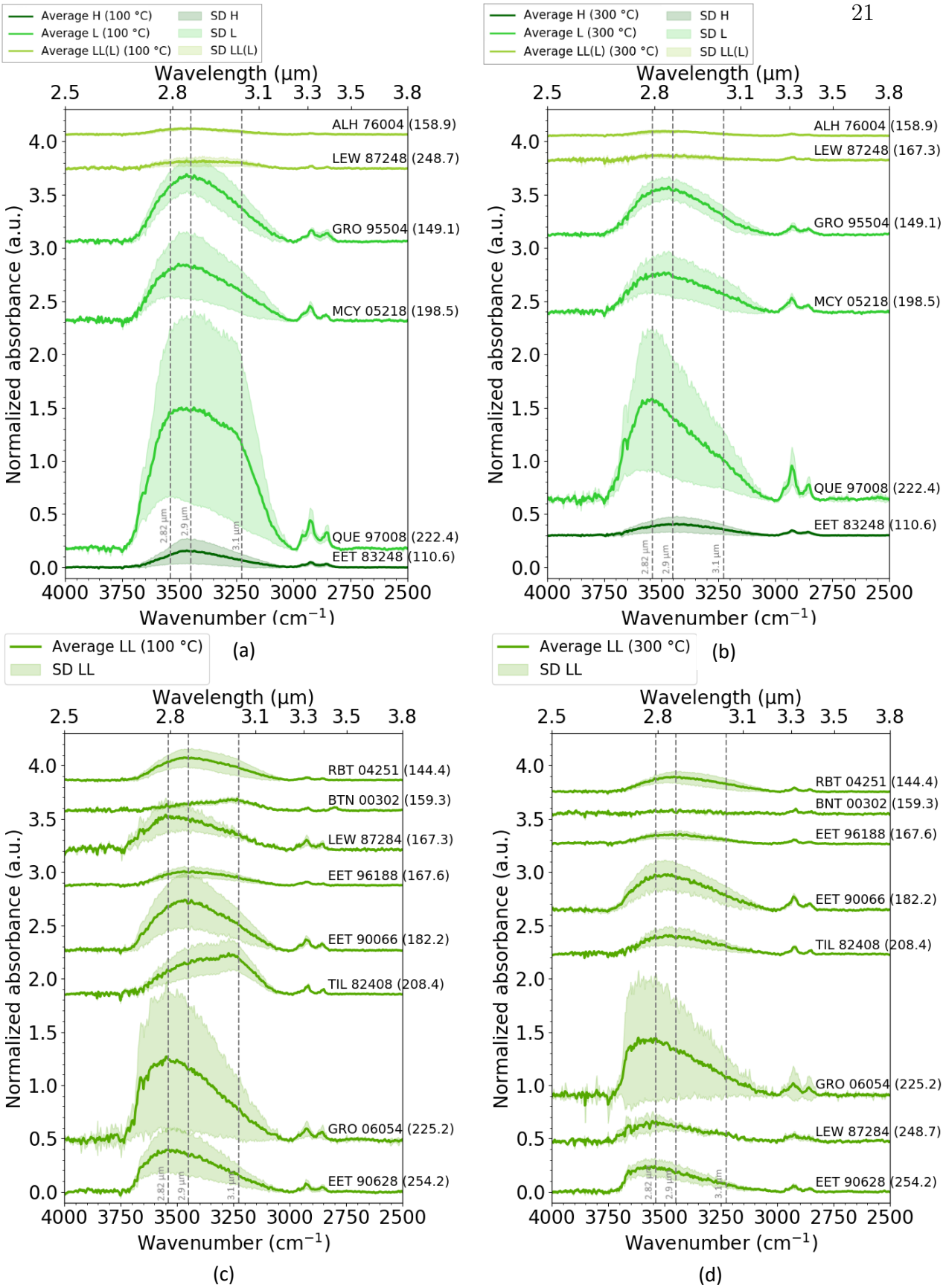

Figure 4: IR spectra of UOCs in the 4000 – 2500 cm^{-1} region for (a) H, L and LL(L) at 100 °C, (b) H, L and LL(L) at 300 °C, (c) LL at 100 °C and (d) LL at 300 °C. Shown is the 3-micron region. Spectra are plotted with an offset for better visibility. They are sorted by type and metamorphic grade with increasing metamorphic grade from bottom to top. Each spectrum is plotted with its error band indicated by the green shaded area.

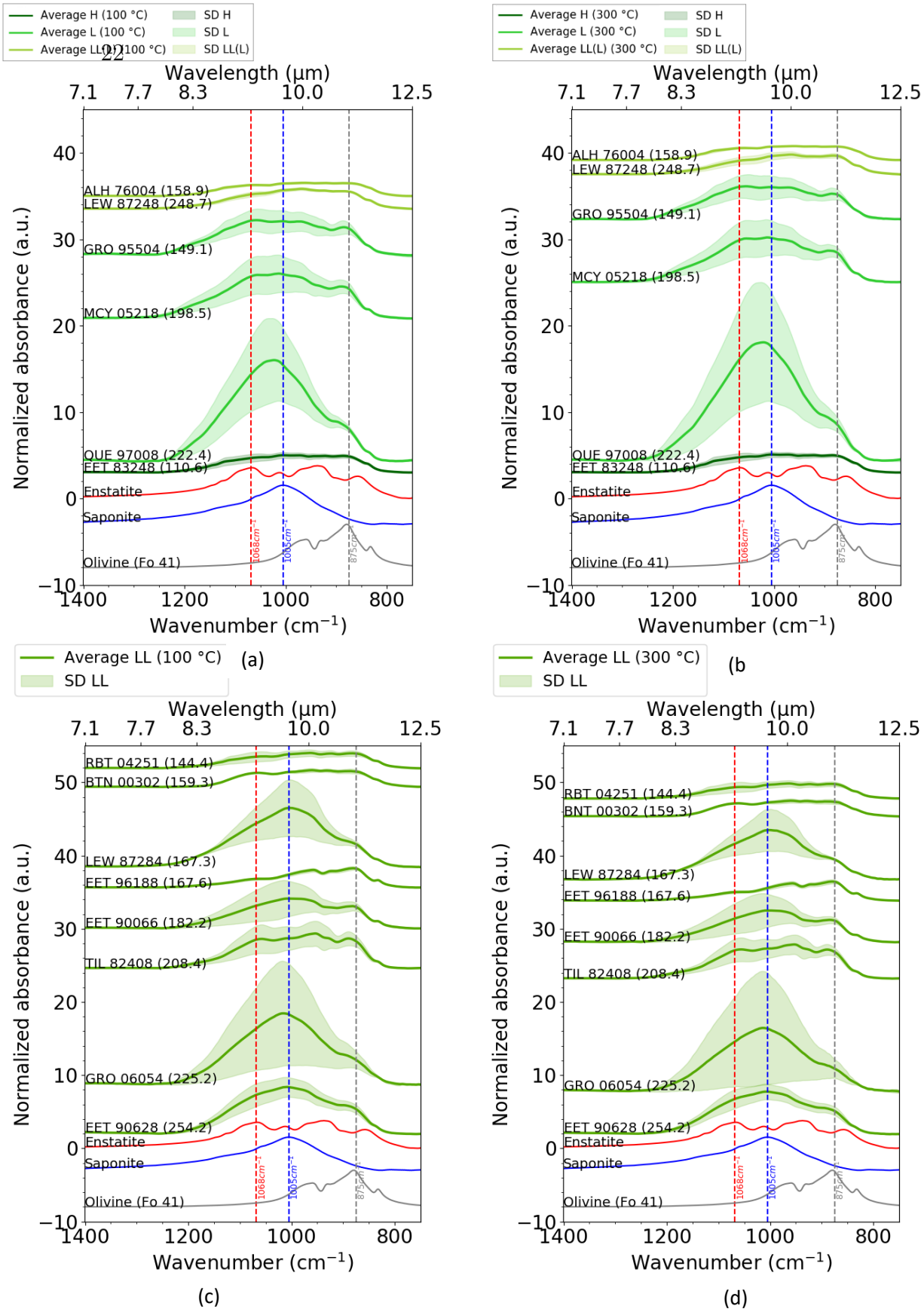

Figure 5: IR spectra of UOCs in the 1400 - 750 cm^{-1} region for (a) H, L and LL(L) at 100 °C, (b) H, L and LL(L) at 300 °C (c) for LL at 100 °C and (d) for LL at 300 °C. Shown is the 10-micron SiO region. Spectra are plotted with an offset for better visibility. They are sorted by type and metamorphic grade with increasing metamorphic grade from bottom to top. Each spectrum is plotted with its error band indicated by the green shaded area. The spectra of Enstatite, Saponite and Olivine (Fo 41) are plotted as comparison.

315 To further interpret the 3 µm band, Figure A5 of the Appendix shows the 3 µm band fits, as
316 described in Section 2.2 for all considered UOCs. At 100 °C, 4 of the 14 UOCs (ALH 76004 (L(LL)3.1-3.4),
317 BTN 00302 (LL3.1-3.4), EET 83248 (H>3.6) and TIL 82408 (LL3.05-3.1)) are best fit using a 2.9 µm adsorbed
318 water and a 3.1 µm interlayer water and oxy-hydroxide band (Figures A5 (a), (c), (e) and (aa) of the
319 Appendix). For the remaining 10 UOCs (EET 90066 (LL3.1), EET 90628 (LL3.0), EET 96188 (LL3.1-3.4), GRO
320 06054 (LL3.05), GRO 95504 (L3.4), LEW 87248 (L(LL)3.0), LEW 87284 (LL3.1-3.4), MCY 05218 (L3.05-3.1),
321 QUE 97008 (L3.05), RBT 04251 (LL3.4)) the best fit is achieved when also including an -OH in hydrated
322 minerals band at 2.8 µm (Figure A5).

323 After heating the samples from 100 °C to 300 °C the shape and size of the 3-µm bands change
324 (Figures 4 and Table 3). In general, it becomes smaller and the band maximum is shifted to shorter
325 wavelengths with increasing temperature. For UOCs ALH 76004 (L(LL)3.1-3.4), EET 83248 (H>3.6) and TIL
326 82408 (LL3.05-3.1) the 3-µm band is still best fitted using a 2.9 µm adsorbed water and a 3.1 µm interlayer
327 water and oxy-hydroxide band (Figures A5 (b), (f) and (ab) of the Appendix). For BTN 00302 (LL3.1-3.4)
328 close to no more 3 µm band is left after heating to 300 °C (Figure A5 (d)) preventing a fit. Out of the 10
329 remaining UOCs, 7 (EET 90066 (LL3.1), EET 90628 (LL3.0), EET 96188 (LL3.1-3.4), GRO 06054 (LL3.05), GRO
330 95504 (L3.4), MCY 05218 (L3.05-3.1) and RBT 04251 (LL3.4)) are best fitted using all three fitting bands
331 while for the other 3 (LEW 87248 (L(LL)3.0), LEW 87284 (LL3.1-3.4) and QUE 97008 (L3.05)) the fit at 300
332 °C is best using only a 2.8 µm and a 3.1 micron fitting band (Figure A5 of the Appendix). With a release of
333 oxy-hydroxides between 150-550 °C and of phyllosilicates between 550 - 1000 °C (based on TGA curves,
334 see Section 2.2) it is expected that the 2.9 µm adsorbed water and the 3.1 µm interlayer water fitting
335 bands decrease in size when heating from 100 °C to 300 °C while the 2.8 µm -OH in hydrated minerals
336 fitting band remains similar in size.

337 Table 3 summarizes the spectral values determined for the band fits as well as the total 3 µm band
338 of each UOC. The total hydration, reflected by the IBD of the entire 3 µm band ranges from 1.03 % for ALH

339 76004 (LL(L)3.1-3.4) to 29.44 % for QUE 97008 (L 3.05) (Table 3) at 100 °C. After heating to 300 °C the IBD
340 values drop to 0.75 % for ALH 76004 (LL(L)3.1-3.4) to 17.4 % for QUE 97008 (L3.05) (Table 3). In general,
341 this drop in total hydration is predominantly due to the decrease in size or the complete disappearance
342 of the 2.9 µm adsorbed water and the 3.1 µm interlayer water and oxy-hydroxide bands (Table 3 and
343 Figure A5). For EET 83248 (H>3.6) and LEW 87248 (L(LL)3.0) a slight increase in the IBD of the 2.9 µm
344 adsorbed water band can be seen from 0.77 % at 100 °C to 1.09 % at 300 °C and from 0.22 % at 100 °C to
345 0.36 % at 300 °C, respectively. Similarly, EET 96188 (LL3.1-3.4) shows an increase of the 3.1 µm interlayer
346 water and oxy-hydroxide band from 0.55 % at 100 °C to 1.08 % at 300 °C. We note that an increase in IBD
347 of these bands with increasing temperature can be possible within the accuracy of the fitting process.
348 Therefore, for the UOCs that exhibit a phyllosilicate band, the IBD of the 2.8 µm band is similar before and
349 after heating as expected.

350 The loss of hydration with increasing temperature is also reflected in the band depth of the 3 µm
351 band which ranges from 5.37 % for ALH 76004 (L(LL)3.1-3.4) to 131.79 % for QUE 97008 (L3.05) at 100 °C
352 and from 3.98 % for ALH 76004 (L(LL)3.1-3.4) to 95.33 % for QUE 97008 (L3.05) at 300 °C. Again, this
353 overall decrease of band depth is mainly due to a decrease in band depth or disappearance of the 2.9 µm
354 adsorbed water and 3.1 µm interlayer water and oxy-hydroxide bands (Table 3). For UOCs with a 2.8 µm
355 band related to phyllosilicates, the band depth, while slightly variable, remains comparable after heating
356 (Table 3).

357 The FWHM of the total 3 µm band ranges from 288 nm for EET 83248 (H>3.6) to 403 nm for QUE
358 97008 (L3.05) at 100 °C and from 284 nm for EET 90628 (LL3.0) and ALH 76004 (L(LL)3.1-3.4) to 712 nm
359 for BTN 00302 (LL3.1-3.4) at 300 °C. Overall, the 3 µm band becomes slightly narrower or remains
360 comparable when heating from 100 °C to 300 °C. The exceptions are EET 83248 (H>3.6) and LEW 87248
361 (L(LL)3.0) with FWHM values changing from 288 nm at 100 °C to 310 nm at 300 °C and from 400 nm at 100
362 °C to 667 nm at 300 °C, respectively. The 3 µm bands of these two UOCs are some of the smallest within

363 the present work at 300 °C, making the fit more difficult. Furthermore, LEW 87248 (L(LL)3.0) shows a very
364 noisy spectrum that needed to be smoothed before fitting.

365 The position of the total 3 µm band ranges from 2828 nm for GRO 06054 (LL3.05) to 3076 nm for
366 BTN 00302 (LL3.1-3.4) at 100 °C. At 300 °C the overall band positions range from 2812 nm for EET 90628
367 (LL3.0), GRO 06054 (LL3.05) and LEW 87284 (LL3.1-3.4) to 2895 nm for EET 83248 (H>3.6). Overall, the 3
368 µm band position at 300 °C shifts to shorter wavenumbers (Table 3) or remains comparable to that at 100
369 °C. This shift is expected with the decrease and/or loss of bands contributing to longer wavenumbers upon
370 heating.

371 The SiO_4 (Si-O) stretching region of the IR spectra at 10 µm is shown in Figure 5 and indicates the
372 presence of anhydrous (and hydrous) silicates. The shape of this band varies between UOCs. Since
373 measurements are done in transmitted light, spectra of thicker grains may be saturated in this region. This
374 might be the case for EET 83248 and ALH 76004. For UOCs QUE 97008 (L3.05), LEW 87284 (LL3.1-3.4), EET
375 90066 (LL3.1), GRO 06054 (LL3.05) and EET 90628 (LL3.0) one wide peak around 1000 nm with a side band
376 around 875 nm is visible (Figure 5). This spectral shape is comparable to a mixture of phyllosilicates such
377 as saponite and olivine (Fo 41). For the other samples, the 10 µm region shows several bands which are
378 consistent with being dominated by olivine (Fo 41) and enstatite. Therefore, the abundance of
379 phyllosilicates is sufficient to be visible in the 10 µm region for at least 5 of the 14 UOCs (QUE 97008
380 (L3.05), LEW 87284 (LL3.1-3.4), EET 90066 (LL3.1), GRO 06054 (LL3.05) and EET 90628 (LL3.0)).

381 ## 4. Discussion

382 As the results show, signatures of hydration were detected in all 41 of the UOC considered in the present
383 work, by TGA measurements of bulk samples and/or by IR spectra of matrix grains. The exact nature of
384 the hydration is discussed in the following sections.

4.1. Selected measuring techniques and their limitations

To identify the hydrated minerals of UOCs, TGA and FTIR spectroscopy were chosen as complementary measuring techniques. Figure 6 (a) and (b) show a good correlation between the IBD of the 3 µm band at 100 °C and the total mass loss between 150-1000 °C as well as the IBD of the 3 µm band at 300 °C and the mass loss between 550-1000 °C. The exception is LEW 87284 for which the hydration determined by TGA greatly exceeds the hydration reflected in its 3 µm band. A possible explanation could be that the hydration is heterogeneous in this UOC and the piece of bulk sample used for the TGA measurement included more water than the matrix fragments used for FTIR spectroscopy.

FTIR spectroscopy is very sensitive to the vibrational modes of hydrated minerals and is, thus, suited for detecting small signatures of hydration, as is the case for the samples in the present work. Since the measurements are performed on matrix fragments and not on the bulk sample, the efficiency of this technique to detecting hydration is independent of the total matrix abundance of the UOCs. On the other hand, FTIR spectroscopy is not easily quantitative. Since the matrix fragments are measured in transmitted light, the intensity of each spectrum is dependent on the thickness of the pressed fragments, as well as the measured area. For the FTIR spectra presented in the present work (Figures 4 and 5), the thickness is unknown and the analytical area was not systematically measured.

However, to get an idea of the thickness variability, it was measured using Atomic Force Microscopy-based Infrared Spectroscopy (AFM-IR) at IPAG (France) for 2-6 fragments at 2-4 different regions on the matrix fragment for EET 90066, EET 90628, MET 00489 and GRO 06054. The results are shown in Table 4. As can be seen, not only does the thickness vary between matrix fragments of the same sample (e.g. 0.56 µm – 0.87 µm for EET 90066) but there is also variability of thickness within different regions of the same fragment (e.g. 0.82 µm (region 2) to 2.25 µm (region 4) of Fragment 5 of GRO 06054). This variability hampers the direct comparison of spectral intensities. This needs to be kept in mind for

the comparability of the quantitative hydration values presented in Table 3. However, it is definitely possible to qualitatively assess the hydration of the UOCs.

TGA has been proven suitable for the characterization of the hydration in CV chondrites. The measured mass loss was normalized to the matrix abundance of each sample as explained in Section 2.2. However, the matrix abundances of UOCs are much lower than for CVs, therefore, increasing the error in the mass losses normalized to the matrix abundance determined for UOCs. Besides the loss of hydration, other thermal reactions (e.g. the oxidation and reduction of organic matter and magnetite (Földvári, 2011)), can also lead to a mass change during TGA measurements. The lower the abundance of matrix in a given UOC, the lower the relative abundance of hydrated minerals to non-hydrated minerals also contributing to the mass loss. The lowest matrix abundance values in UOCs are 2.96 % for ALH 86120 and 4.47 % for ALH 84086 (Table 1), while for the CVs studied in Bonal et al., (2020) they are around 20 % (19.4 % for Efremovka, and 27.6 % for Leoville). The lower limit of matrix abundance in CVs is the upper limit in the UOC studied in the present work (23.3 % for EET 90628 and 26.2 % for DOM 03287 (Table 1)). Added to the low matrix abundance is the difficulty of interpreting the TGA mass loss curves of UOCs which show a much higher variability between samples than CVs (see Section 2.2). Moreover, with the combination of shock, thermal metamorphism and terrestrial weathering products, the exact determination of the extent of asteroidal aqueous alteration becomes very complex in UOCs. For example, the effect of shock on the total hydration can vary with the metamorphic grade of the sample. In order for it to lead to dehydration, the shock temperature needs to exceed the peak metamorphic temperature, which might be more easily achieved for less metamorphosed chondrites.

To minimize some of the above-mentioned effects, we decided to only consider TGA measurements obtained on UOCs with sufficient matrix abundance. The cutoff value as to what is considered “sufficient matrix abundance” was chosen to be 19 % of matrix (in alignment with the lower limit of matrix abundance in CVs). This includes UOCs DOM 03287 (26.2 %), DOM 08468 (22 %), EET 87735

(22.9 %), EET 90066 (20.2 %), EET 90628 (23.3 %), LAR 04382 (20 %), MET 00506 (19.6 %), MIL 05050 (22.6 %), Piancaldoli (19 %) and TIL 82408 (22.8 %) (Table 1). To include UOCs with lower matrix abundance a study of manually matrix enriched samples would be necessary, which is beyond the scope of the present paper.

4.2. Hydration among UOCs

Figures 7 (a) and (b) show the comparison of the IBD of the 3.1 µm interlayer water and oxy-hydroxide fitting band determined from the IR spectra of matrix grains with the percentage of weathering products observed in the thin sections of UOCs (Section 3.1). For UOCs where a range of percentages of weathering products is given in Table 1, the average of the two bounds of the interval are used for plotting in Figure 7 (a) and (b). As can be seen, these two proxies of terrestrial weathering correlate well with each other. Two UOCs (TIL 82408 and MCY 05218) are outside of the trend showing stronger values for the weathering determined from petrographic observations than from their 3 µm band. This might possibly be due to a heterogeneous distribution of weathering products in these UOCs. The samples used for FTIR spectroscopy might have been less weathered than the thin sections.

The correlation between these two methods speaks for the power of the used fitting process which makes it possible to unravel the convolution of the three contributions to the 3 µm band to a certain degree. It also proves that only parts of the 3 µm band hydration are due to terrestrial weathering products. TGA and IR spectroscopy did indeed reveal hydration of extraterrestrial origin in the UOCs of the present work.

As mentioned in Section 4.1, TGA is best suited for detecting hydration in chondrites with sufficient matrix abundances. Thus, Figure 8 shows the total mass loss between 150 – 1000 °C determined by TGA for UOCs with > 19 % matrix abundance. For comparison, Figure 8 also includes the mass loss

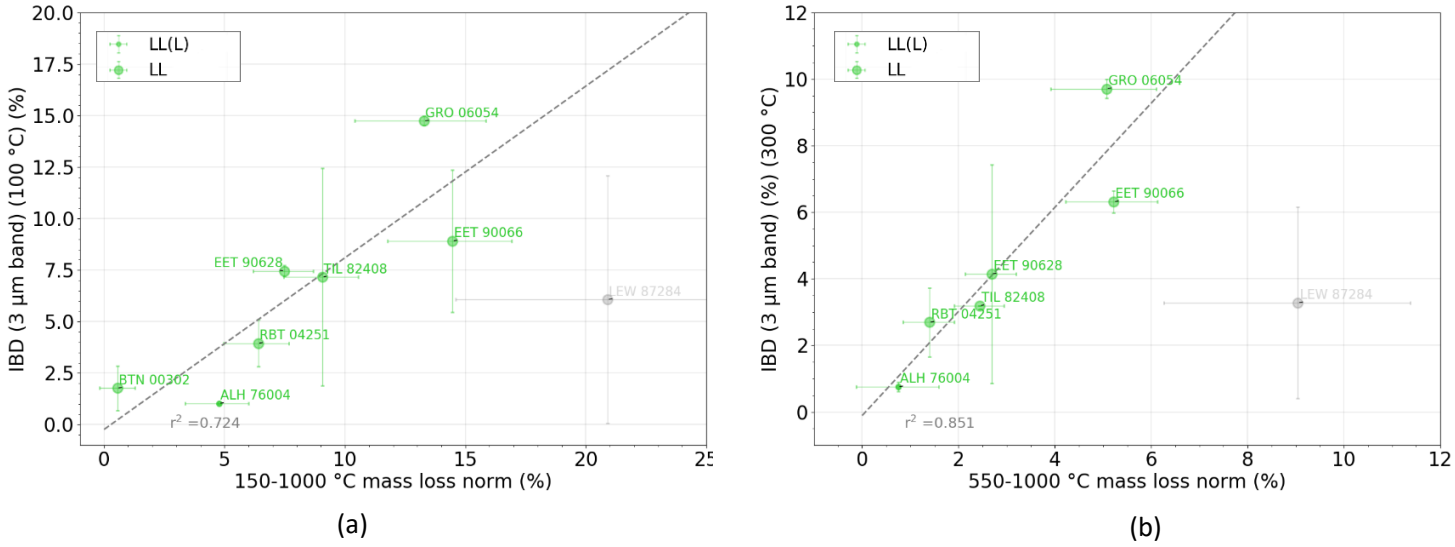

Figure 6: Comparison of FTIR spectroscopy results with TGA data. (a) shows the IBD of the complete 3-micron band measured by IR spectroscopy at 100 °C as a function of the 150 – 1000 °C matrix normalized mass loss determined by TGA (b) shows the IBD of the complete 3-micron band measured by IR spectroscopy at 300 °C as a function of the 550 – 1000 °C matrix normalized mass loss determined by TGA. Outliers are marked in grey.

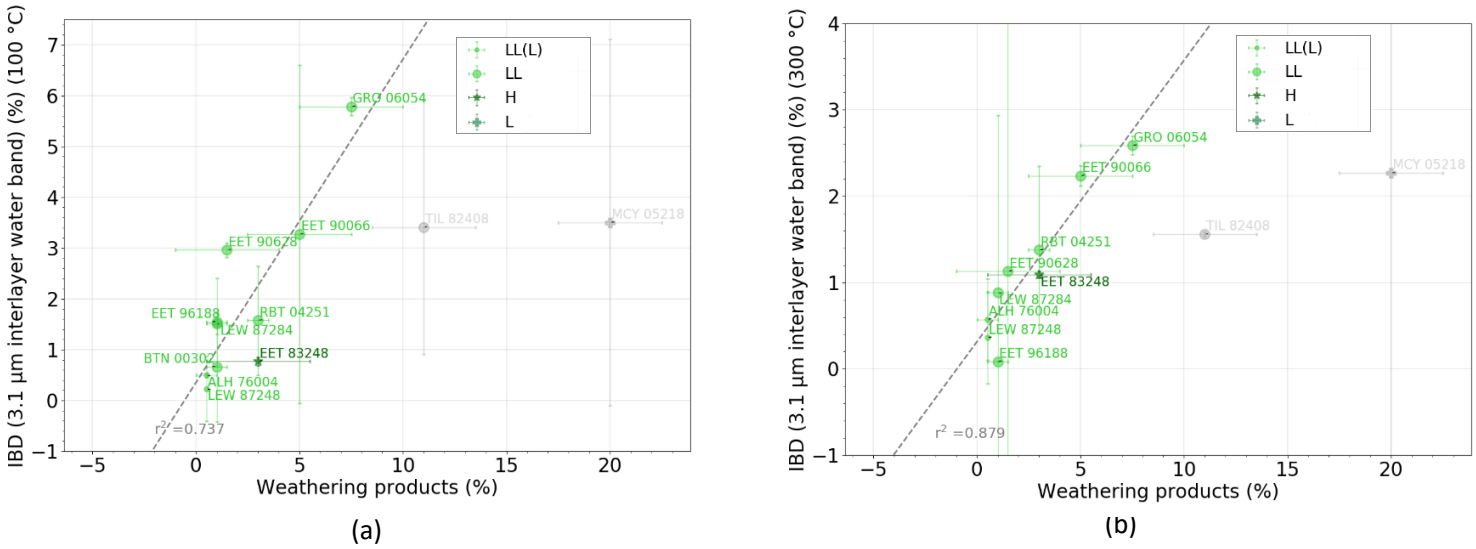

Figure 7: Comparison of FTIR spectroscopy results with Petrographic results (a) shows the comparison of the IBD of the 3.1-micron interlayer water and oxy-hydroxide fitting band measured at 100 °C as a function of the weathering measure determined during petrographic measurements (b) shows the comparison of the IBD of the 3.1-micron interlayer water fitting band measured at 300 °C as a function of the weathering measure determined during petrographic measurements. Outliers are marked in grey.

Table 4: Results of the thickness measurements done on pressed matrix grains of four UOCs using Atomic Force Microscopy-based Infrared Spectroscopy (AFM-IR). Listed are the thickness of different grains in 2-4 regions of the same grain, as well as the average thickness of each grain. Lastly, the average thickness of grains for the overall sample is given.

sample	**Fragment**	**region 1** (µm)	**region 2** (µm)	**region 3** (µm)	**region 4** (µm)	**average** (µm)
EET 90066 (LL)	Fr1	0.54	0.52	0.52	0.65	0.56
	Fr6	0.81	0.79	-	-	0.80
	Fr8	0.71	0.80	0.86	-	0.79
	Fr9	0.15	0.86	0.66	0.83	0.63
	Fr10	0.57	0.63	0.56	-	0.59
	Fr13	0.89	0.84	-	-	0.87
average sample thickness						**0.70**
EET 90628 (LL)	Fr1	1.03	0.66	1.04	-	0.91
	Fr3	1.05	1.00	-	-	1.02
average sample thickness						**0.97**
MET 00489 (LL)	Fr5	1.76	1.20	2.02	-	1.66
	Fr6	1.77	1.72	-	-	1.74
average sample thickness						**1.70**
GRO 06054 (LL)	Fr 5	0.96	0.82	2.25	2.90	1.73
	Fr 6	0.64	0.78	0.88	-	0.77
	Fr 7	0.83	0.69	0.56	-	0.69
average sample thickness						**1.06**

455 values of CVs in the same temperature range (Bonal et al., 2020). As can be seen UOCs are characterized
456 by a similar or even higher hydration to that of CVs once normalized to the matrix abundance. Indeed, the
457 mass loss normalized to the matrix abundance determined by TGA in between 150-1000 °C ranges from
458 7.5 wt.% to 16.8 wt.% (average: 11.42 ± 3.55 wt.%) for UOCs with > 19 % matrix abundance, in comparison
459 to 0.43 wt.% to 9.38 wt.% (average: 4.74 ± 2.81 wt.%) for CVs (Bonal et al., 2020).

460 This comparable hydration is also reflected in the 3 µm band of the IR spectra of matrix fragments.
461 The IBD of the 3 µm band of UOCs are comparable to those of CVs when looking at a similar thermal
462 metamorphic range and exceed those of CVs both at 100 °C and 300 °C for lower metamorphic grades
463 (Figures 9 (a) and (b)). This indicates that the matrix material of UOCs contains similar amounts of hydrated
464 minerals to that of CVs at similar metamorphic grades. Because matrix material is more abundant in CVs
465 (on average 41.8 %, (Bonal et al., 2020)) than UOCs (on average 14.9 %) looking at bulk material without
466 normalizing to the matrix abundance will make CVs appear more hydrated than UOCs.

467 In conclusion, we show that UOCs are significantly hydrated. Specifically, traces of extraterrestrial
468 hydration could be detected for DOM 03287, DOM 08468, EET 87735, EET 90066, EET 90628, LAR 04382,
469 MET 00506, MIL 05050, Piancaldoli and TIL 82408 based on TGA and for EET 90066, EET 90628, EET 96188,
470 GRO 06054, GRO 95504, LEW 87248, LEW 87284, MCY 05218, QUE 97008 and RBT 04251 based on IR
471 spectroscopy.

472 **4.3. Hydration vs thermal metamorphism**

473 The comparison of the matrix normalized mass loss (> 19 % matrix) between 150 – 1000 °C to the
474 metamorphic grade ($FWHM_D$ value) of UOCs in Figure 8 shows a negative correlation indicating decreasing
475 hydration with increasing metamorphic grade (r^2 = 0.701). Two outliers can be seen: EET 90628 and TIL
476 82408. As discussed in Section 3.1, almost all UOCs considered in this work show a certain degree of
477 terrestrial weathering and shock impacts. Since the total hydration is a combination of terrestrial and

asteroidal hydration as well as dehydration due to shock and thermal metamorphism, the consequences of terrestrial weathering and shock needs to be considered when looking for a trend.

EET 90628 (LL3.0) shows a weathering grade of W0 and a shock stage of S3. Being the most primitive UOC considered in the present work (PT 3.0), dehydration due to shock impact might be more significant than for UOCs with higher metamorphic grades (see Section 4.1). It is, thus, possible that EET 90628 has been dehydrated due to shock effects. TIL 82408 (LL3.05-3.1) shows a higher degree of terrestrial weathering (W1) than EET 90628 and a shock value of S3. Similarly to EET 90628, it is possible that TIL 82408 might have been slightly shock dehydrated. Due to the larger amount of terrestrial weathering products detected in TIL 82498 (Table 1) in comparison to the other UOCs in the present work, it is also possible that the majority of the hydration seen in this sample is due to terrestrial water contamination and not parent body aqueous alteration. This is supported by the fact that the 3 µm band measured by IR spectroscopy of TIL 82498 is best fit with only a 2.8 µm adsorbed water band and a 3.1 µm interlayer water and oxy-hydroxide band (Section 3.3).

To see if this TGA result is supported by the IR spectroscopy on matrix fragments, Figures 9 (a) and (b) show the comparison of the IBD of the complete 3 µm band at 100 °C and 300 °C, respectively, over the $FWHM_D$ values. A negative correlation of decreasing hydration with increasing metamorphic grade is also visible based on the 3 µm band both at 100 °C and 300 °C, although slightly less significant than for TGA ($r^2 = 0.571$ and $r^2 = 0.574$, respectively). As discussed in Section 3.3, the best fit of the 3 µm bands of UOCs TIL 82408, BTN 00302, ALH 76004 and EET 83248 only included a 2.9 µm adsorbed water and a 3.1 µm interlayer water and oxy-hydroxide band. Since it is expected that the majority of the hydration contributing to these two bands is due to terrestrial water contamination, these four samples are excluded from the fit in Figures 9 (a) and (b). Additionally, EET 90628 was excluded from the fit (see explanation above).

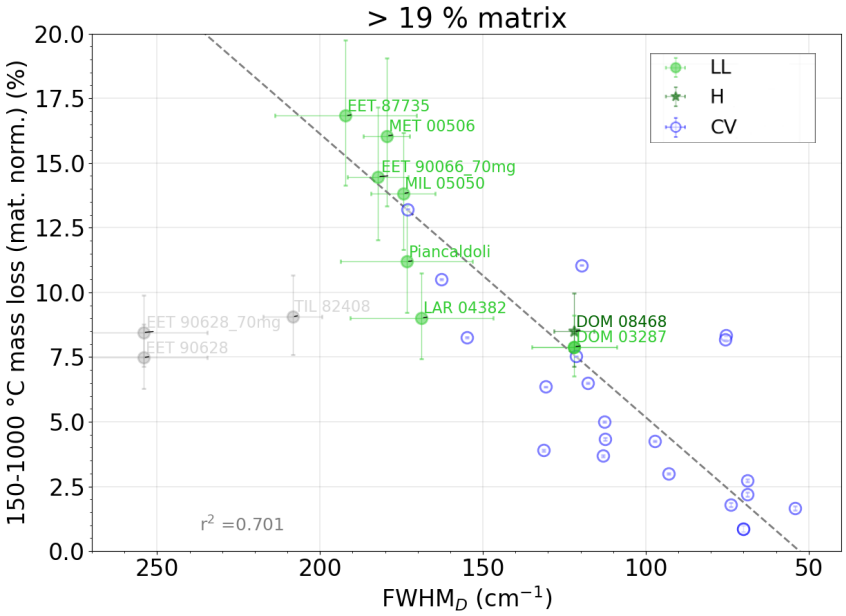

Figure 8: Comparison of the results of TGA with the metamorphic grade of UOC (with matrix abundance higher than 19 %) and CVs. Shown is the 150 - 1000 °C matrix normalized mass loss of UOCs and CVs as a function of the FWHM$_D$. The fit was done to UOC data only. Outliers are marked in grey.

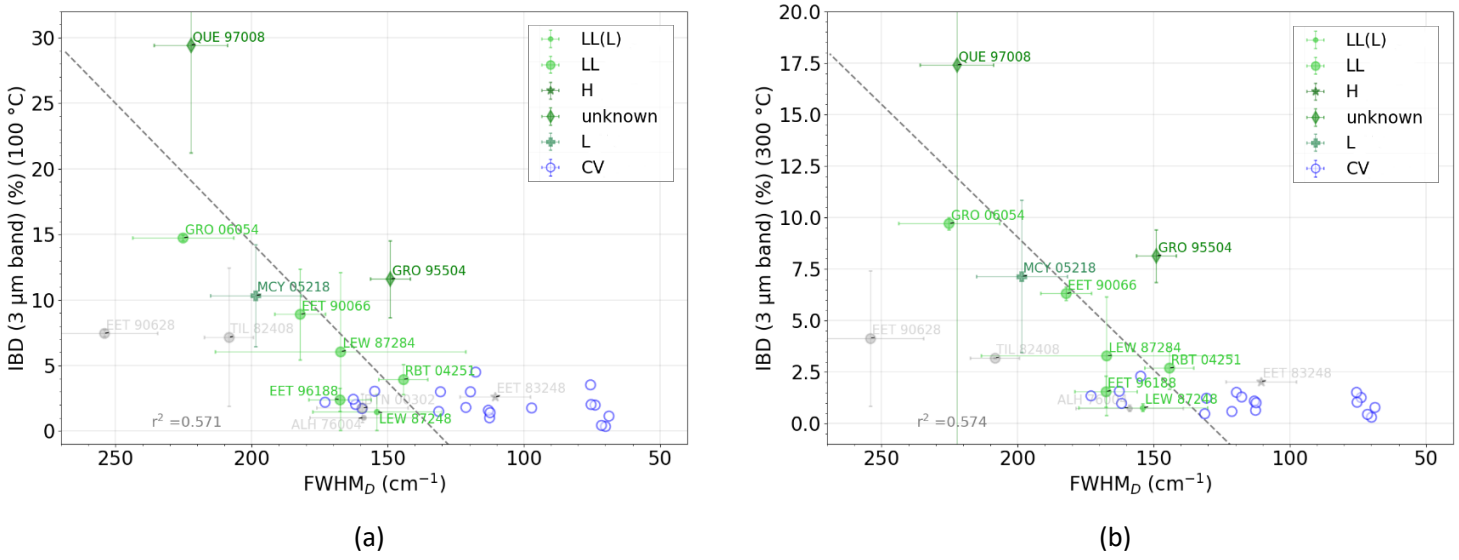

Figure 9: Comparison of the FTIR spectroscopy results with the metamorphic grade. (a) shows the comparison of the IBD of the complete 3-micron band measured at 100 °C as a function of the FWHM$_D$ for UOCs and CVs. (b) shows the comparison of the IBD of the complete 3-micron band measured at 300 °C as a function of the FWHM$_D$ for UOCs and CVs. The fits were done to UOC data only. Outliers are marked in grey.

In conclusion, the hydration of UOCs as currently measured is controlled by their peak metamorphic temperature (as reflected by the $FWHM_D$ value). This is shown both by TGA when focusing on the UOCs with the highest abundance of matrix (> 19%) and by IR spectroscopy of matrix fragments and when excluding the most weathered and/or shocked UOCs.

4.4. Implications the position of the Snowline at the time of AA

As we have shown in Sections 4.2, UOCs are not dry. The presence of hydration comparable to that of CVs in the matrix of UOCs refutes the previous belief that the inner Solar System must have been dry. Interestingly, the correlation observed between the hydration and the metamorphic grade for UOCs in Section 4.3 seems to extend the correlation previously observed for CV chondrites (Bonal et al., 2020) (Figure 8). This indicates that the snowline must have been positioned inward of the formation reservoirs of both CVs and UOCs at the time of accretion.

Suggestions for possible sources of hydration in the inner Solar System have been given by e.g. McCubbin and Barnes, (2019). Based on constraints of geochronology, isotope anomalies and dynamical models, indications of interstellar H_2O sources were present in inner Solar System during the first 4 m.y. after CAI formation. This time span overlaps with that of the accretion ages of ordinary and carbonaceous chondrites which are estimated to be ~2-4 m.y. after CAI formation (Krot et al., 2015) based on various dating techniques (^{53}Mn-^{53}Cr dating of aqueous alteration products, ^{26}Al-^{26}Mg chondrule formation dating, and peak metamorphic temperature ages). Krot et al., (2015) also argue that ordinary and most carbonaceous chondrite groups show water-ice-to-rock mass ratios consistent with a formation close to the snowline.

If UOC accreted with a significant amount of water ice, and if OCs are derived from UOC precursors, this means that the hydration was lost during thermal metamorphism. The dehydration of UOC upon thermal heating also means that the water may have somehow escaped. It may have diffused toward the

524 asteroidal surface and could have ended forming a transient atmosphere or a frosty surficial layer, for the
525 massive enough asteroids. It may also have been reduced by interaction with metal and sulfides, and
526 escaped in the form of H_2 (Alexander, 2017).

527 Stable isotope anomalies imply that Mars most likely formed from enstatite and ordinary chondrite
528 material (e.g. (Brasser et al., 2017)). Also, the accretion of Mars was fast, with half of its mass accreting
529 within 0.8-2.7 m.y. (Dauphas and Pourmand, 2011). This implies that the OC-like reservoir incorporated
530 in Mars may have preserved its original hydration, if accretion was fast enough that thermal
531 metamorphism did not dehydrate its building blocks. It appears that the martian mantle preserves
532 multiple D/H reservoirs, including one showing a strong deuterium enrichment (Barnes et al., 2020).
533 Measurement of D/H ratio of bulk ordinary chondrites are scarce, but the value obtained by (Alexander
534 et al., 2012) on Sermakona (LL3.0) reveals an elevated D/H (δD=1615.9+/-18.9).

535

536 ## 5. Conclusion

537 In the present work we showed that contrarily to the generally accepted view, UOCs are not dry.
538 Since UOCs experienced some aqueous alteration, their parent bodies must have contained water. At
539 the time the parent bodies of UOCs formed, the temperature must have been low enough to avoid
540 water sublimation and to allow for the planetesimal to accrete water ice. In fact, the hydration of
541 UOCs is comparable to that of CV chondrites once normalized to their matrix abundance. A correlation
542 between the hydration and the peak metamorphic temperature of UOCs could be observed based on
543 the IBD of the FTIR spectra of UOC matrix fragments. This correlation is also observed based on TGA
544 for UOCs with more than 19 % matrix abundance. Interestingly, this correlation extends the one
545 previously observed for CV chondrites (Bonal et al., 2020). We, thus, conclude that the inner Solar

System was not dry and that the snowline at the time of accretion must have been located inward of the UOC parent body formation region.

A subsequent question is whether the water ice accreted by the parent bodies of CVs and UOCs sample the same ice reservoir. Answering this question will have implications on the formation models of the Solar System and, in particular, of the inner planets which so far require CCs as their building blocks.

Acknowledgments

Special thanks go to Van Phan and Rolando Rebois for performing the AFM-IR measurements on matrix fragments and helping with the data treatment of these measurements.

This work has been funded by the Centre National d'Etudes Spatiales (CNES-France) and by the ERC grant SOLARYS ERC-CoG2017-771691.

US Antarctic meteorite samples are recovered by the Antarctic Search for Meteorites (ANSMET) program which has been funded by NSF and NASA, and characterized and curated by the Department of Mineral Sciences of the Smithsonian Institution and Astromaterials Acquisition and Curation Office at NASA Johnson Space Center. We thank the Natural History Museum, Vienna, Department of Mineralogy and Petrography for providing us with a thick section of Mezö-Madaras (Inv-Nr. NHMV-N2140) and bulk samples of Mezö-Madaras (NHMV_ID_#3993_B2), Parnallee (NHMV_ID_#6207_B2) and Tieschitz (NHMV_ID_#7152_A).

We also thank the Museum D'Histoire Naturelle National (MNHN), the Arizona State University (ASU), the Centre de Recherches Pétrographiques et Geochimiques (CRPG) at Nancy and lthe Centre Européen de Recherche et D'Enseignement des Géosciences de l'Environnement (CEREGE), Aix-En-Provence for providing us with the remaining EOC and UOC samples.

6. References

Alexander, C.M.O., 2017. The origin of inner Solar System water. Philos. Trans. R. Soc. Math. Phys. Eng. Sci. 375, 20150384. https://doi.org/10.1098/rsta.2015.0384

Alexander, C.M.O., Barber, D.J., Hutchison, R., 1989. The microstructure of Semarkona and Bishunpur. Geochim. Cosmochim. Acta 53, 3045–3057. https://doi.org/10.1016/0016-7037(89)90180-4

Alexander, C.M.O., Bowden, R., Fogel, M.L., Howard, K.T., Herd, C.D.K., Nittler, L.R., 2012. The Provenances of Asteroids, and Their Contributions to the Volatile Inventories of the Terrestrial Planets. Science 337, 721–723. https://doi.org/10.1126/science.1223474

Alexander, C.M.O., Newsome, S.D., Fogel, M.L., Nittler, L.R., Busemann, H., Cody, G.D., 2010. Deuterium enrichments in chondritic macromolecular material—Implications for the origin and evolution of organics, water and asteroids. Geochim. Cosmochim. Acta 74, 4417–4437. https://doi.org/10.1016/j.gca.2010.05.005

Barnes, J.J., McCubbin, F.M., Santos, A.R., Day, J.M.D., Boyce, J.W., Schwenzer, S.P., Ott, U., Franchi, I.A., Messenger, S., Anand, M., Agee, C.B., 2020. Multiple early-formed water reservoirs in the interior of Mars. Nat. Geosci. 13, 260–264. https://doi.org/10.1038/s41561-020-0552-y

Bennett, M.E., McSween, H.Y., 1996. Shock features in iron-nickel metal and troilite of L-group ordinary chondrites. Meteorit. Planet. Sci. 31, 255–264. https://doi.org/10.1111/j.1945-5100.1996.tb02021.x

Bonal, L., Gattacceca, J., Garenne, A., Eschrig, J., Rochette, P., Krämer Ruggiu, L., 2020. Water and heat: New constraints on the evolution of the CV chondrite parent body. Geochim. Cosmochim. Acta 276, 363–383. https://doi.org/10.1016/j.gca.2020.03.009

Bonal, L., Quirico, E., Flandinet, L., Montagnac, G., 2016. Thermal history of type 3 chondrites from the Antarctic meteorite collection determined by Raman spectroscopy of their polyaromatic carbonaceous matter. Geochim. Cosmochim. Acta 189, 312–337. https://doi.org/10.1016/j.gca.2016.06.017

Brasser, R., Mojzsis, S.J., Matsumura, S., Ida, S., 2017. The cool and distant formation of Mars. Earth Planet. Sci. Lett. 468, 85–93. https://doi.org/10.1016/j.epsl.2017.04.005

Brearley, A.J., 2006. The action of water. Meteor. Early Sol. Syst. II 943, 587--624.

Brearley, A.J., 2003. Nebular versus Parent-body Processing. Treatise Geochem. 1, 711. https://doi.org/10.1016/B0-08-043751-6/01068-9

Dauphas, N., Pourmand, A., 2011. Hf–W–Th evidence for rapid growth of Mars and its status as a planetary embryo. Nature 473, 489–492. https://doi.org/10.1038/nature10077

Dobrică, E., Brearley, A.J., 2014. Widespread hydrothermal alteration minerals in the fine-grained matrices of the Tieschitz unequilibrated ordinary chondrite. Meteorit. Planet. Sci. 49, 1323–1349. https://doi.org/10.1111/maps.12335

Dobrică, E., Le Guillou, C., Brearley, A.J., 2019. Aqueous alteration of porous microchondrules in Semarkona: Implications for hydration, oxidation and elemental exchange processes. Geochim. Cosmochim. Acta 244, 292–307. https://doi.org/10.1016/j.gca.2018.10.002

Doyle, P.M., Jogo, K., Nagashima, K., Krot, A.N., Wakita, S., Ciesla, F.J., Hutcheon, I.D., 2015. Early aqueous activity on the ordinary and carbonaceous chondrite parent bodies recorded by fayalite. Nat. Commun. 6, 7444. https://doi.org/10.1038/ncomms8444

Eschrig, J., Bonal, L., Mahlke, M., Carry, B., Beck, P., Gattacceca, J., 2022. Investigating S-type asteroid surfaces through reflectance spectra of ordinary chondrites. Icarus 381, 115012. https://doi.org/10.1016/j.icarus.2022.115012

Földvári, M., 2011. Handbook of thermogravimetric system of minerals and its use in geological practice. Geological Institute of Hungary, Budapest.

Frost, R.L., Ruan, H., Theo Kloprogge, J., Gates, W.P., 2000. Dehydration and dehydroxylation of nontronites and ferruginous smectite. Thermochim. Acta 346, 63–72. https://doi.org/10.1016/S0040-6031(99)00366-4

Garenne, A., Beck, P., Montes-Hernandez, G., Chiriac, R., Toche, F., Quirico, E., Bonal, L., Schmitt, B., 2014. The abundance and stability of “water” in type 1 and 2 carbonaceous chondrites (CI, CM and CR). Geochim. Cosmochim. Acta 137, 93–112. https://doi.org/10.1016/j.gca.2014.03.034

Howarth, R., 1998. Improved estimators of uncertainty in proportions, point-counting, and pass-fail test results. Am. J. Sci. 298, 594–607. https://doi.org/10.2475/ajs.298.7.594

King, A.J., Solomon, J.R., Schofield, P.F., Russell, S.S., 2015. Characterising the CI and CI-like carbonaceous chondrites using thermogravimetric analysis and infrared spectroscopy. Earth Planets Space 67, 198. https://doi.org/10.1186/s40623-015-0370-4

Krot, A.N., Keil, K., Scott, E.R.D., Goodrich, C.A., Weisberg, M.K., 2014. Classification of meteorites and their genetic relationships, Meteorites and Cosmochemical Processes.

Krot, A.N., Nagashima, K., Alexander, C.M.O., Ciesla, F.J., Fujiya, W., Bonal, L., 2015. Sources of Water and Aqueous Activity on the Chondrite Parent Asteroids, Asteroids IV. https://doi.org/10.2458/azu_uapress_9780816532131-ch033

Kruijer, T.S., Burkhardt, C., Budde, G., Kleine, T., 2017. Age of Jupiter inferred from the distinct genetics and formation times of meteorites. Proc. Natl. Acad. Sci. 114, 6712–6716. https://doi.org/10.1073/pnas.1704461114

McCubbin, F.M., Barnes, J.J., 2019. Origin and abundances of H2O in the terrestrial planets, Moon, and asteroids. Earth Planet. Sci. Lett. 526, 115771. https://doi.org/10.1016/j.epsl.2019.115771

Meteoritical Bulletin Database [WWW Document], 2022. URL https://www.lpi.usra.edu/meteor/metbull.php?sea=O (accessed 12.3.21).

Morbidelli, A., Bitsch, B., Crida, A., Gounelle, M., Guillot, T., Jacobson, S., Johansen, A., Lambrechts, M., Lega, E., 2016. Fossilized condensation lines in the Solar System protoplanetary disk. Icarus 267, 368–376. https://doi.org/10.1016/j.icarus.2015.11.027

642 Potin, S., Manigand, S., Beck, P., Wolters, C., Schmitt, B., 2020. A model of the 3-µm hydration
643 band with Exponentially Modified Gaussian (EMG) profiles: Application to hydrated chondrites and
644 asteroids. Icarus 343, 113686. https://doi.org/10.1016/j.icarus.2020.113686

645 Scott, E.R.D., Keil, K., Stöffler, D., 1992. Shock metamorphism of carbonaceous chondrites.
646 Geochim. Cosmochim. Acta 56, 4281–4293. https://doi.org/10.1016/0016-7037(92)90268-N

647 Scott, E.R.D., Krot, A.N., 2003. Chondrites and their components. Treatise Geochem. 1, 711.
648 https://doi.org/10.1016/B0-08-043751-6/01145-2

649 Stöffler, D., Keil, K., Edward R.D, S., 1991. Shock metamorphism of ordinary chondrites.
650 Geochim. Cosmochim. Acta 55, 3845–3867. https://doi.org/10.1016/0016-7037(91)90078-J

651 Walsh, K.J., Morbidelli, A., Raymond, S.N., O'Brien, D.P., Mandell, A.M., 2011. A low mass for
652 Mars from Jupiter's early gas-driven migration. Nature 475, 206–209.
653 https://doi.org/10.1038/nature10201

654 Warren, P.H., 2011. Stable-isotopic anomalies and the accretionary assemblage of the Earth and
655 Mars: A subordinate role for carbonaceous chondrites. Earth Planet. Sci. Lett. 311, 93–100.
656 https://doi.org/10.1016/j.epsl.2011.08.047

657 Weisberg, M.K., McCoy, T.J., Krot, A.N., 2006. Systematics and Evaluation of Meteorite
658 Classification, Meteorites and the Early Solar System II.

659

Appendix

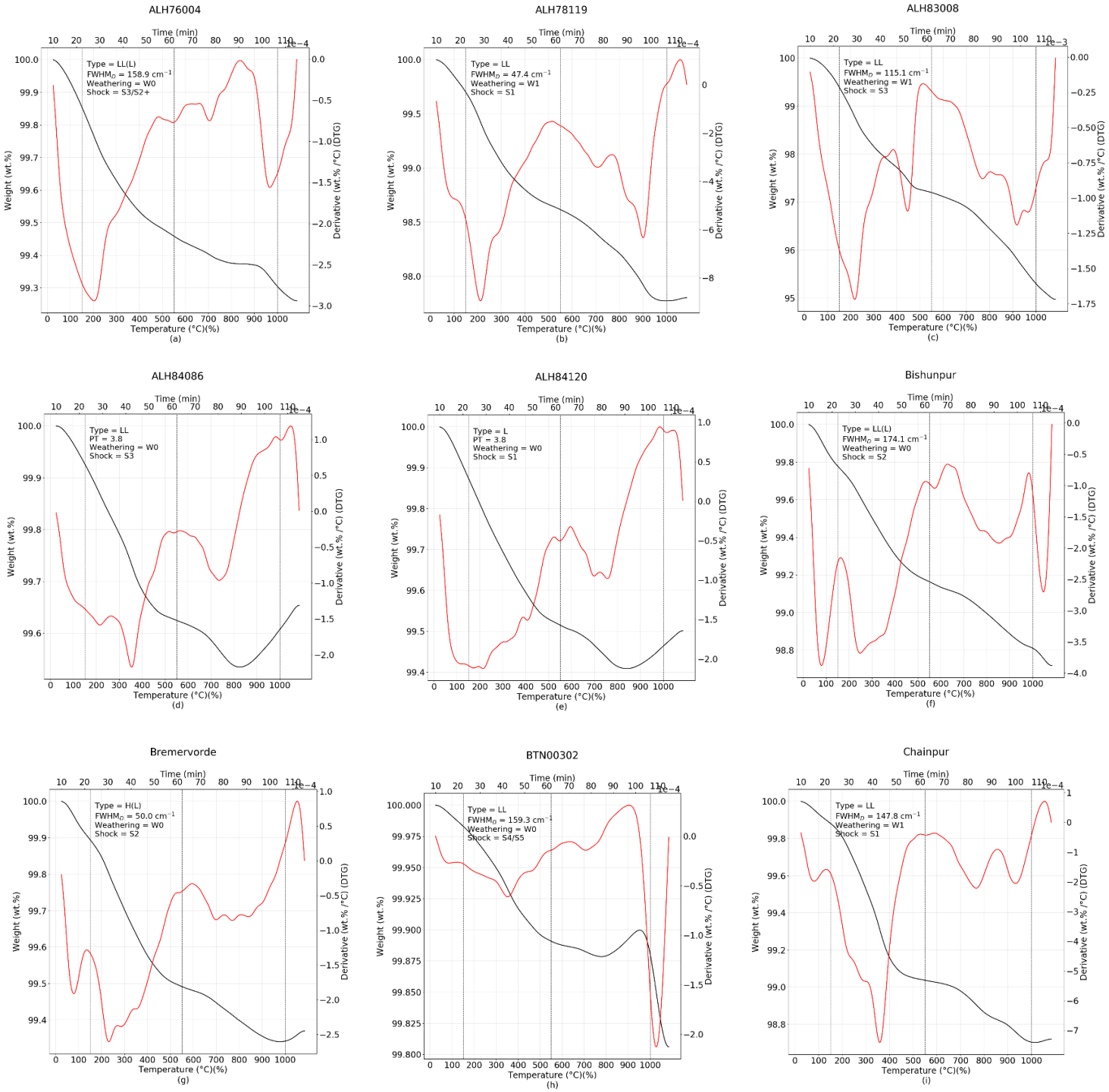

Figure A1: TGA and corresponding DTG curves of all UOCs measured with 35 mg of bulk sample in this present work.

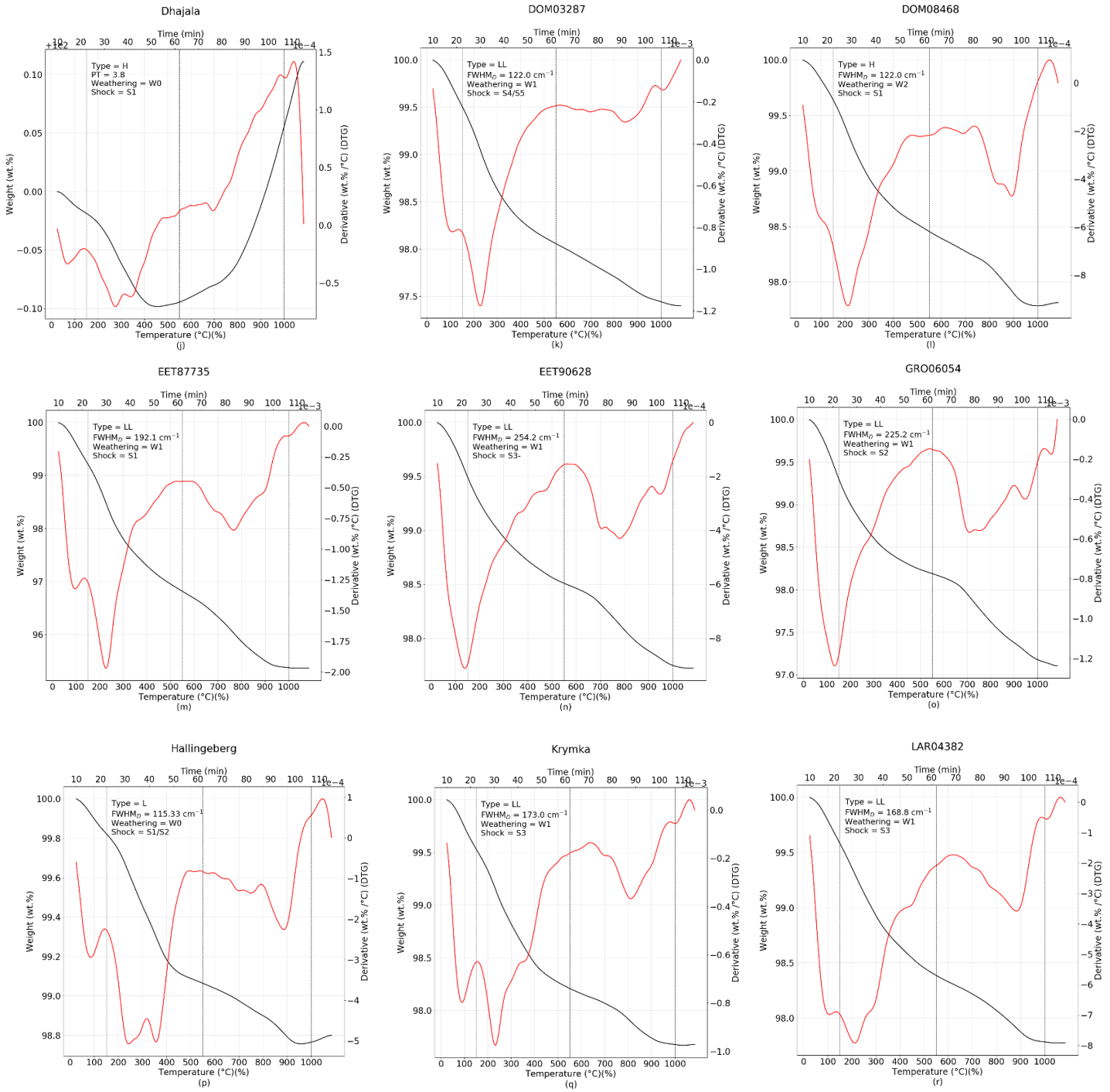

Figure A1: TGA and corresponding DTG curves of all UOCs measured with 35 mg of bulk sample in this present work.

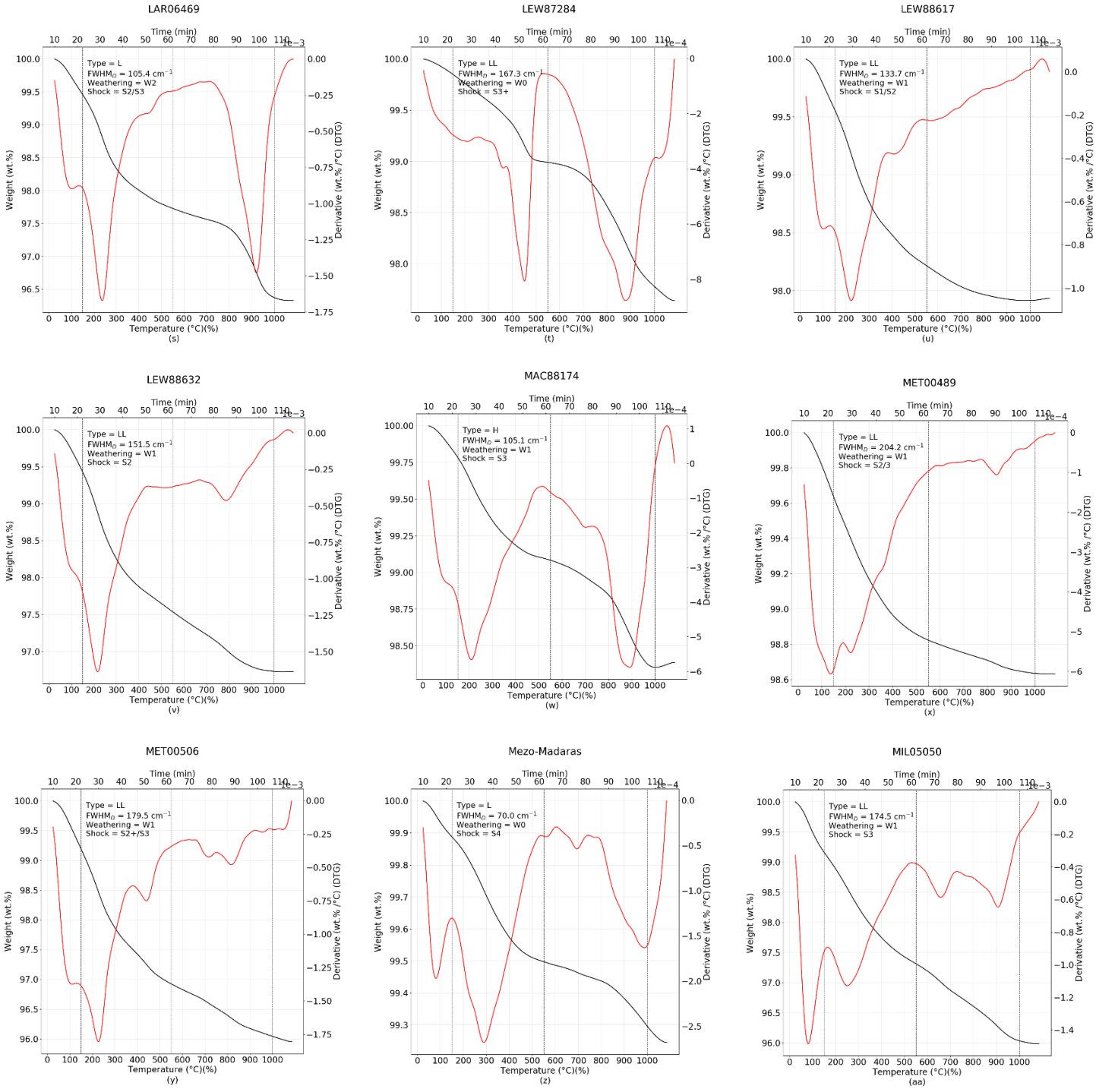

Figure A1: TGA and corresponding DTG curves of all UOCs measured with 35 mg of bulk sample in this present work.

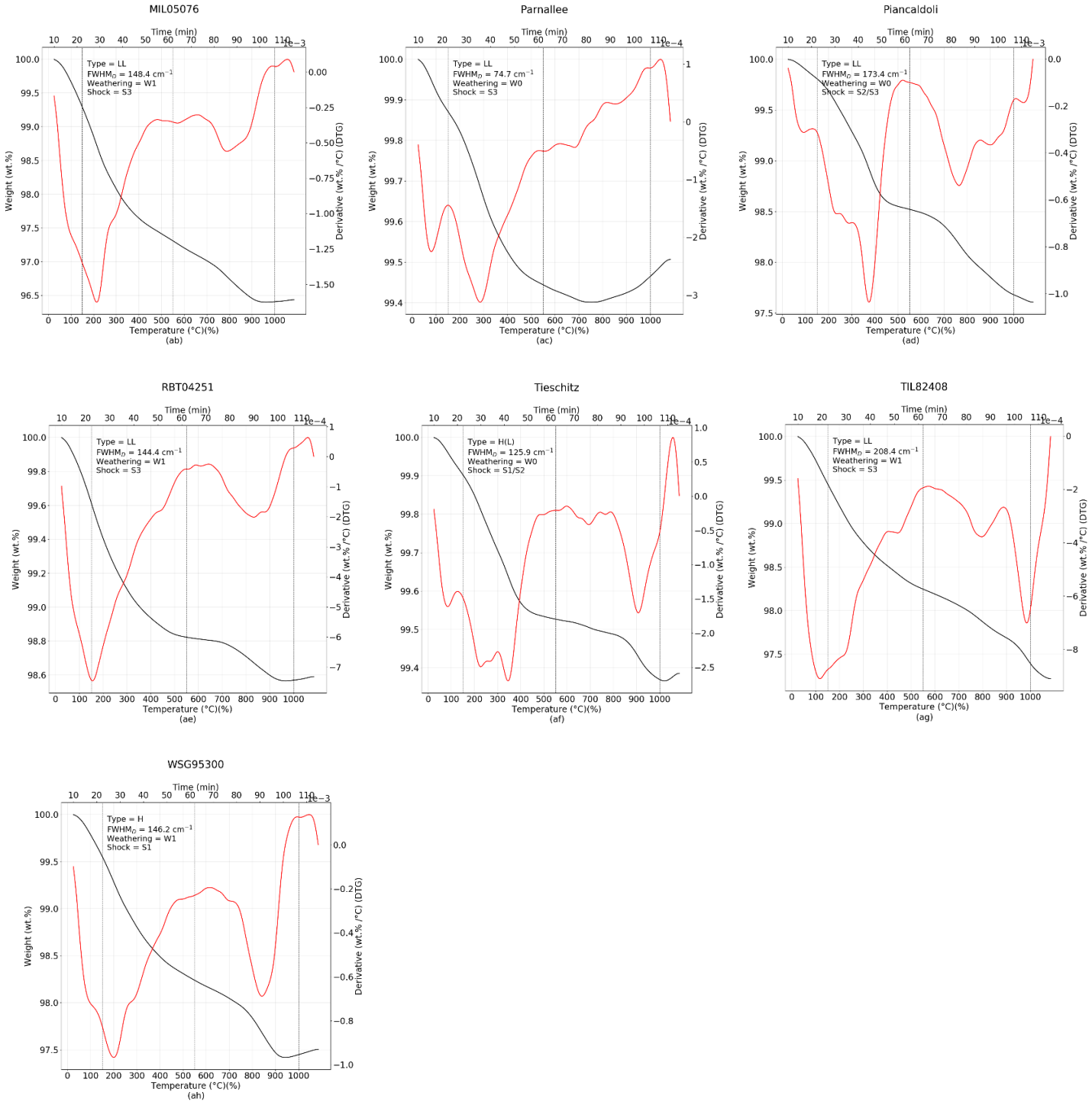

Figure A1: TGA and corresponding DTG curves of all UOCs measured with 35 mg of bulk sample in this present work.

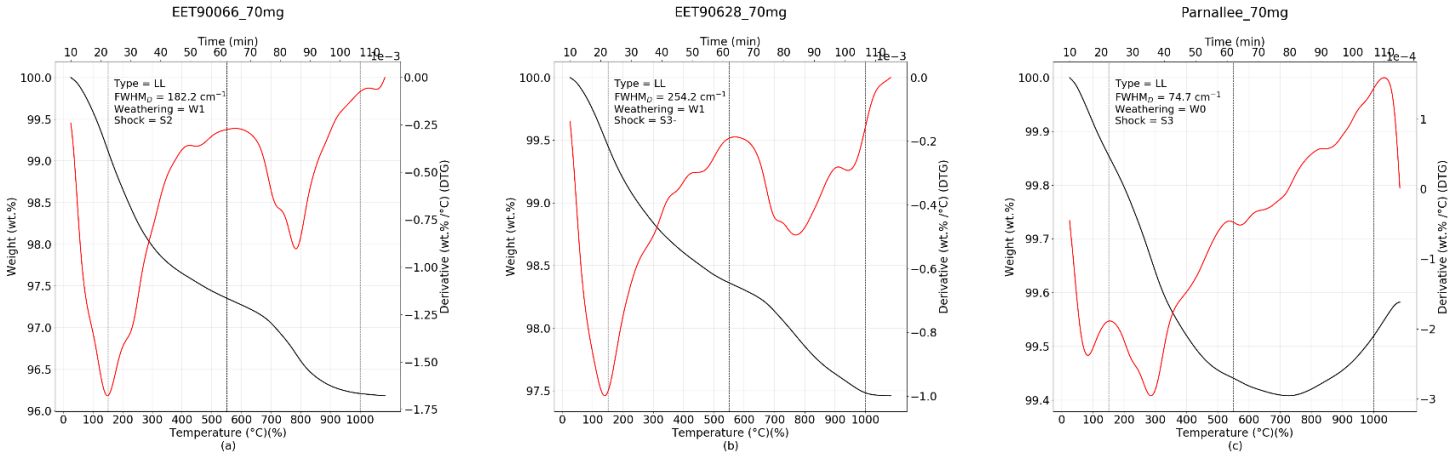

Figure A2: TGA and corresponding DTG curves of the three UOCs measured with 70 mg bulk sample in the present work

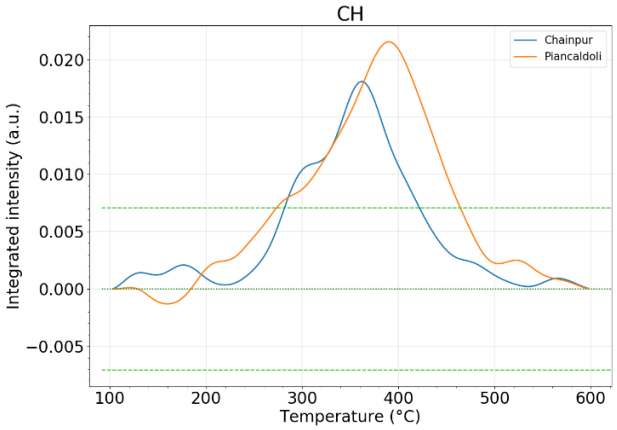

Figure A3: Chemigram of CH for Chainpur and Piancaldoli between 100- 600 °C. The green dotted lines indicate the detection limit based on empty pan measurements.

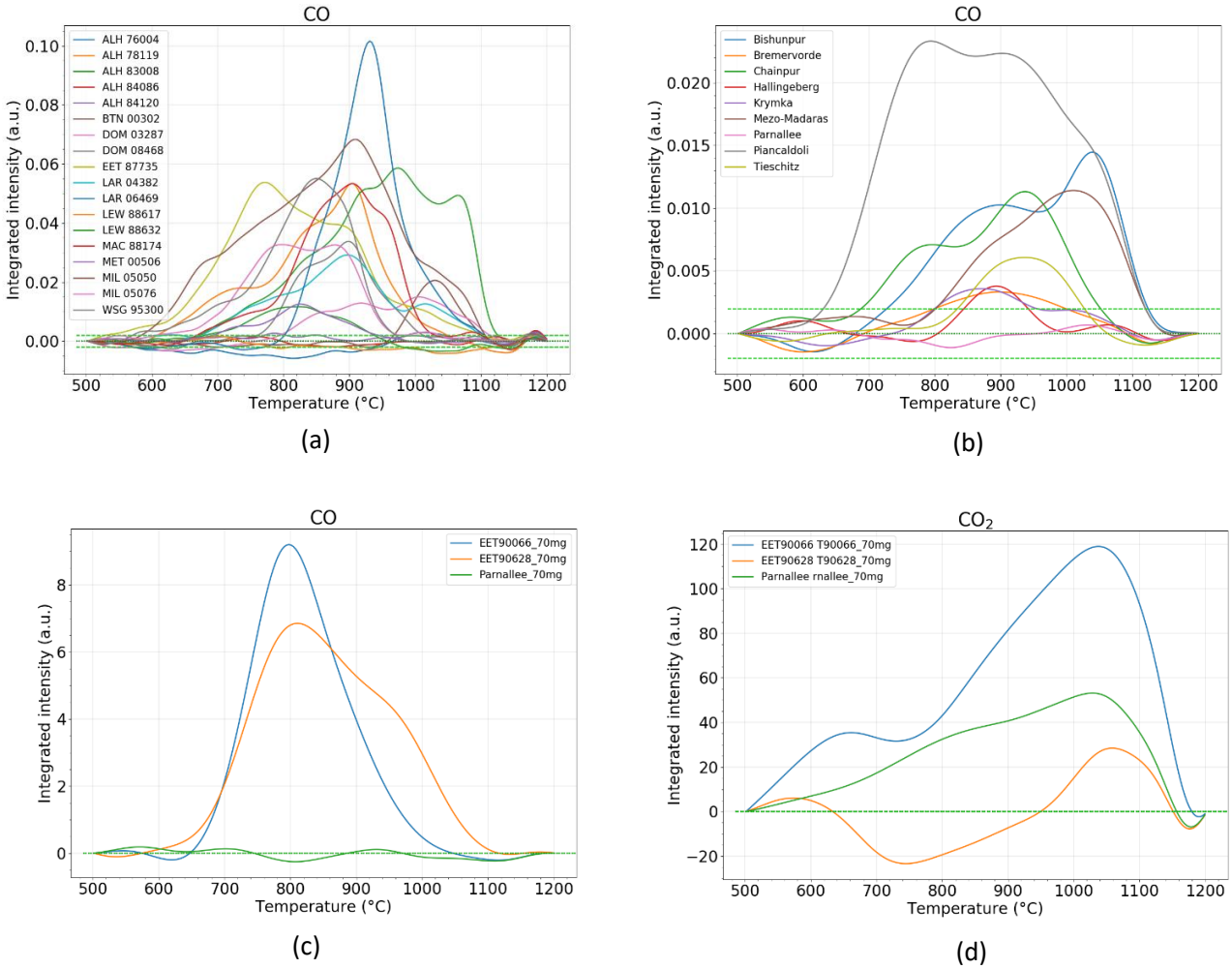

Figure A4: Different chemigrams measured for the UOCs in the present work. (a) and (b) shows the chemigrams of CO of Antarctic and non-Antarctic UOCs, respectively. (c) and (d) show the chemigramms of CO and CO_2 for the three UOCs measured with 70 mg sample mass, respectively. The green dotted lines indicate the detection limit based on empty pan measurements.

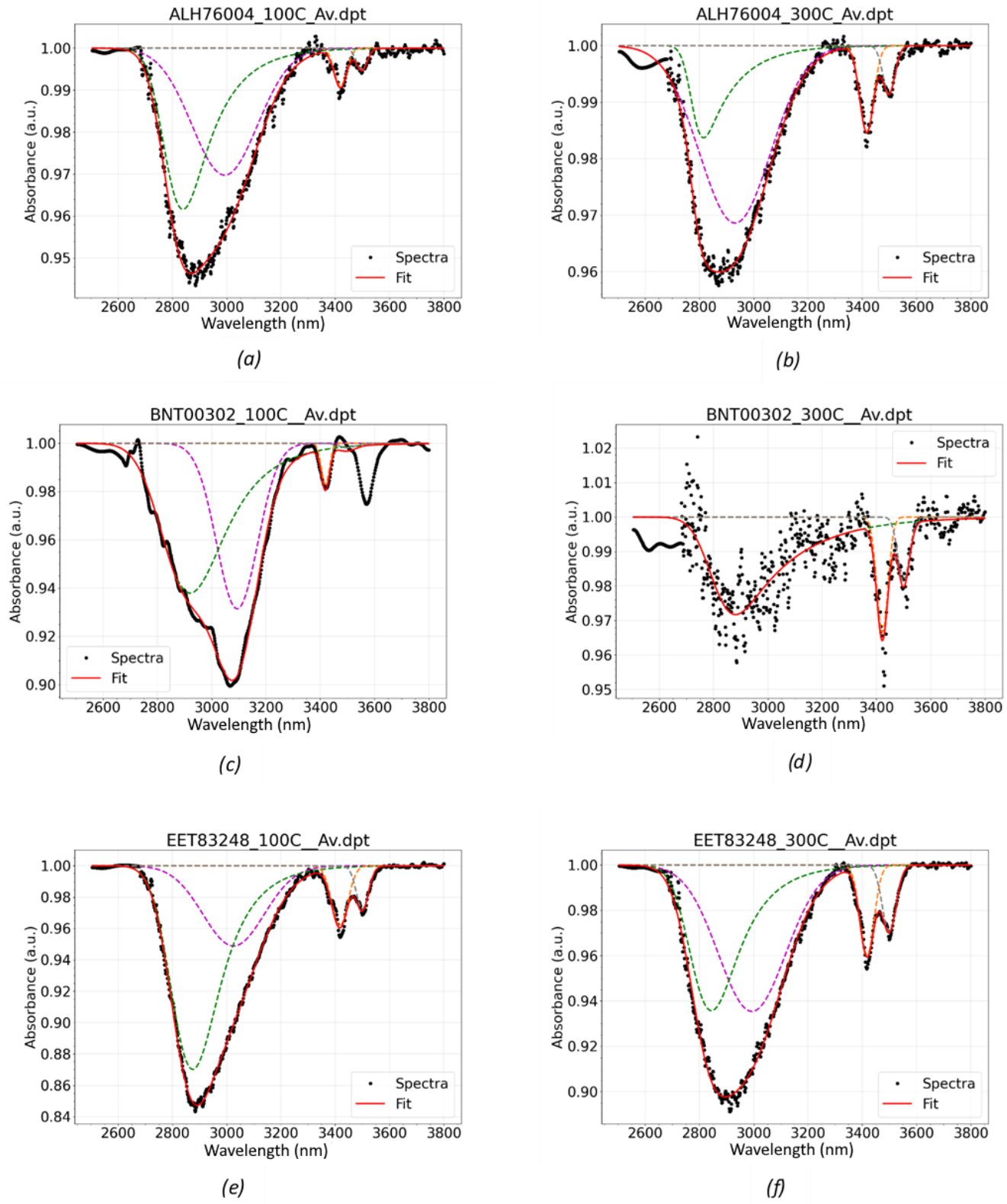

Figure A5: Fit of the 3-micron band for all 14 UOCs measured by FTIR spectroscopy in the present work. Each row shows the fitted 3-micron band of a given sample at 100 °C on the left and at 300 °C on the right.

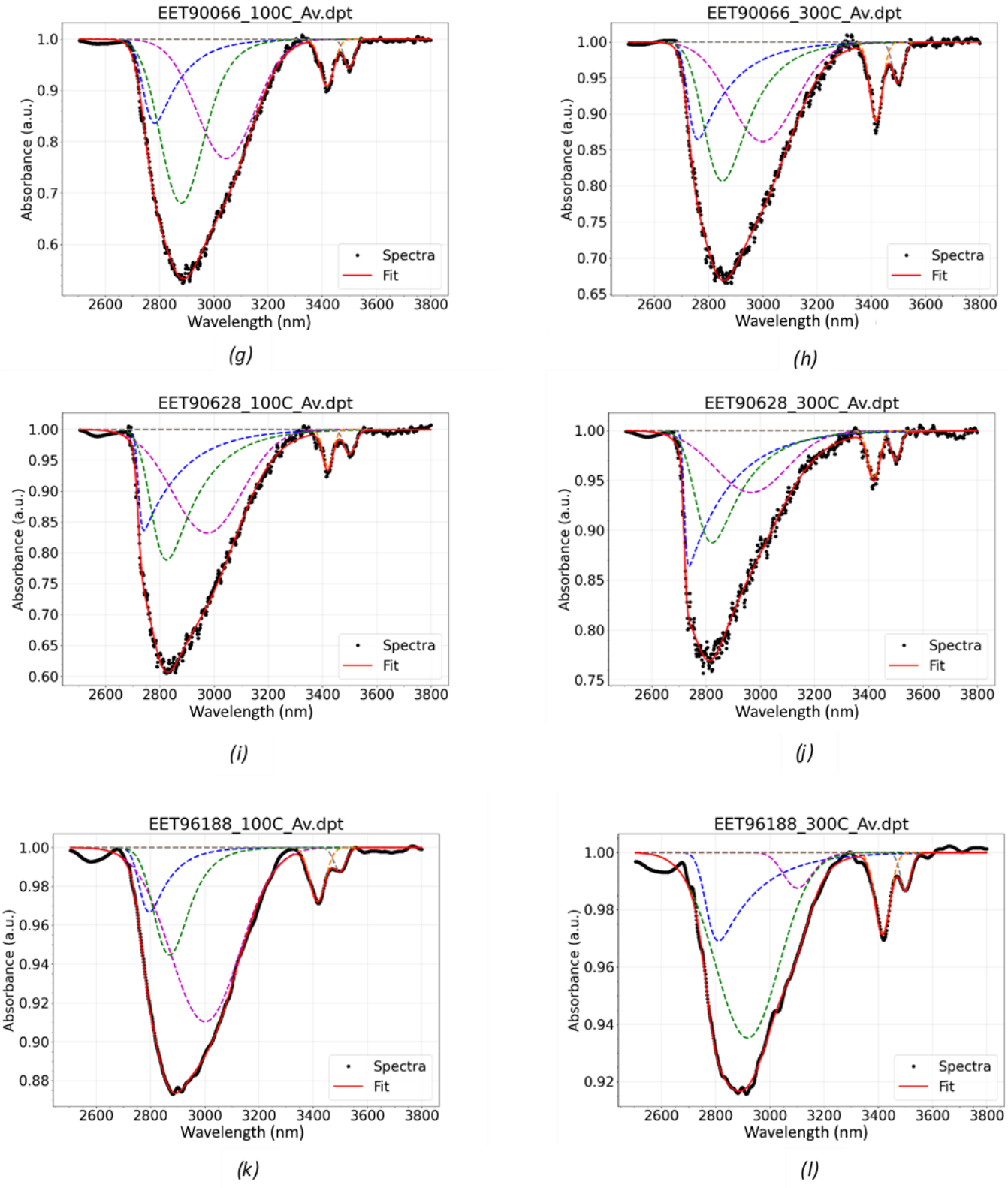

Figure A5: Fit of the 3-micron band for all 14 UOCs measured by FTIR spectroscopy in the present work. Each row shows the fitted 3-micron band of a given sample at 100 °C on the left and at 300 °C on the right.

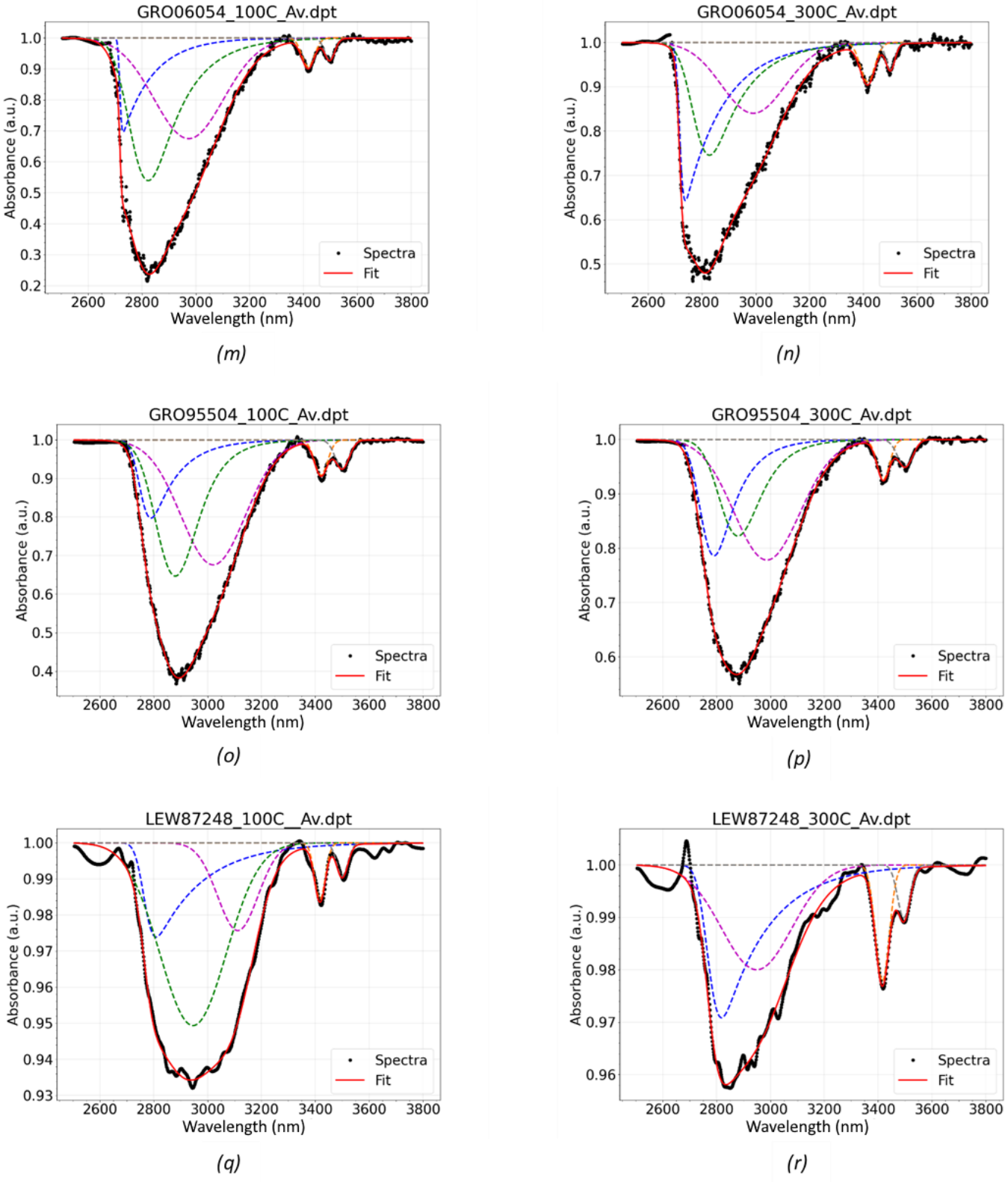

Figure A5: Fit of the 3-micron band for all 14 UOCs measured by FTIR spectroscopy in the present work. Each row shows the fitted 3-micron band of a given sample at 100 °C on the left and at 300 °C on the right.

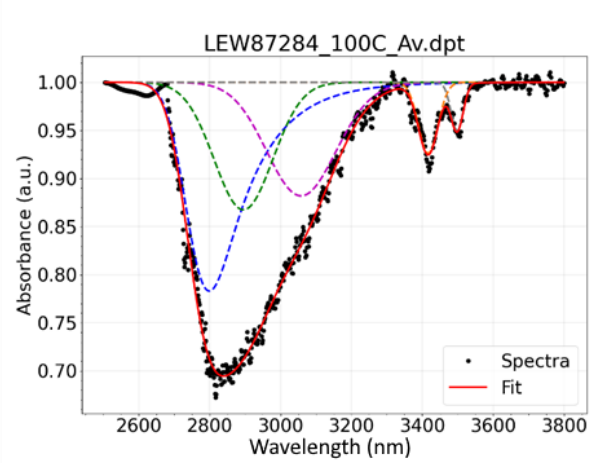

(s)

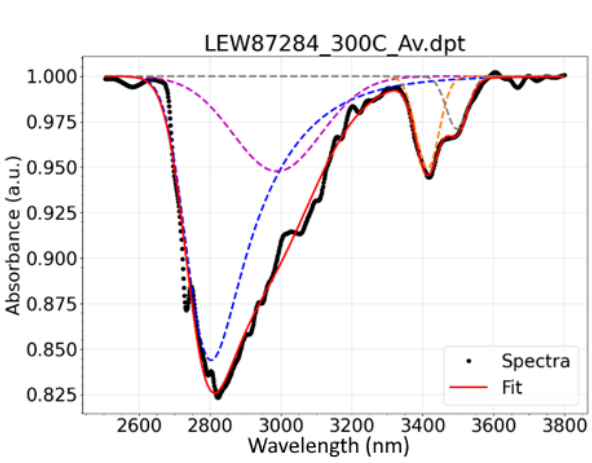

(t)

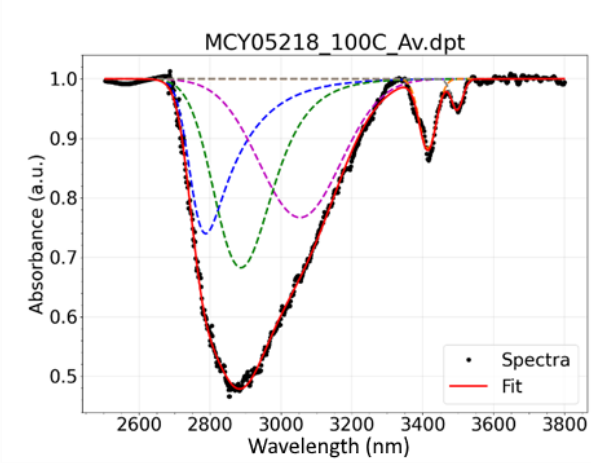

(u)

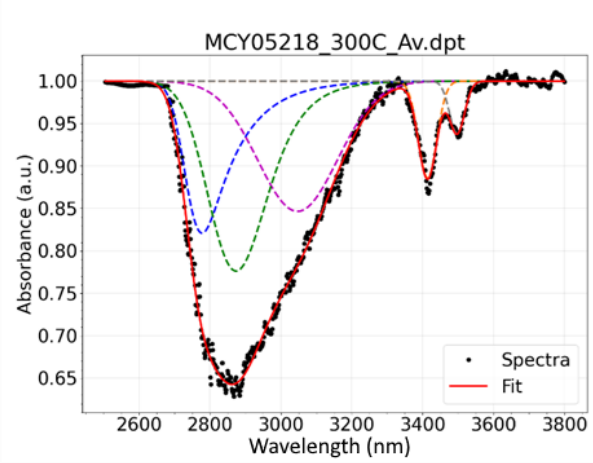

(v)

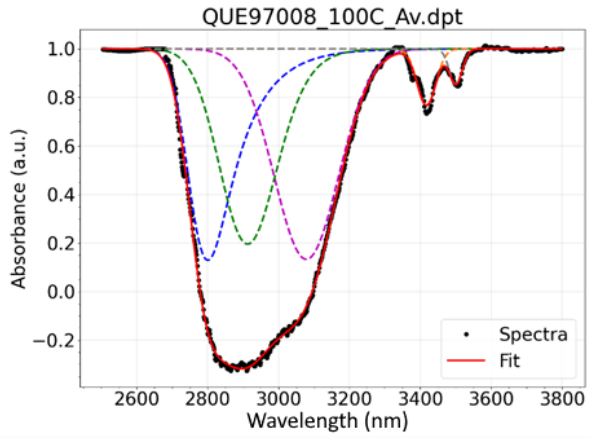

(w)

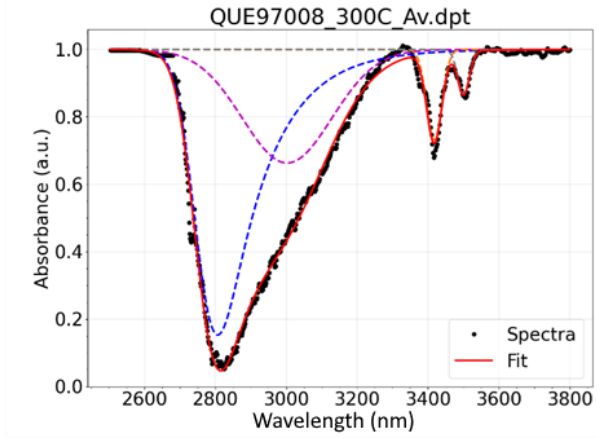

(x)

Figure A5: Fit of the 3-micron band for all 14 UOCs measured by FTIR spectroscopy in the present work. Each row shows the fitted 3-micron band of a given sample at 100 °C on the left and at 300 °C on the right.

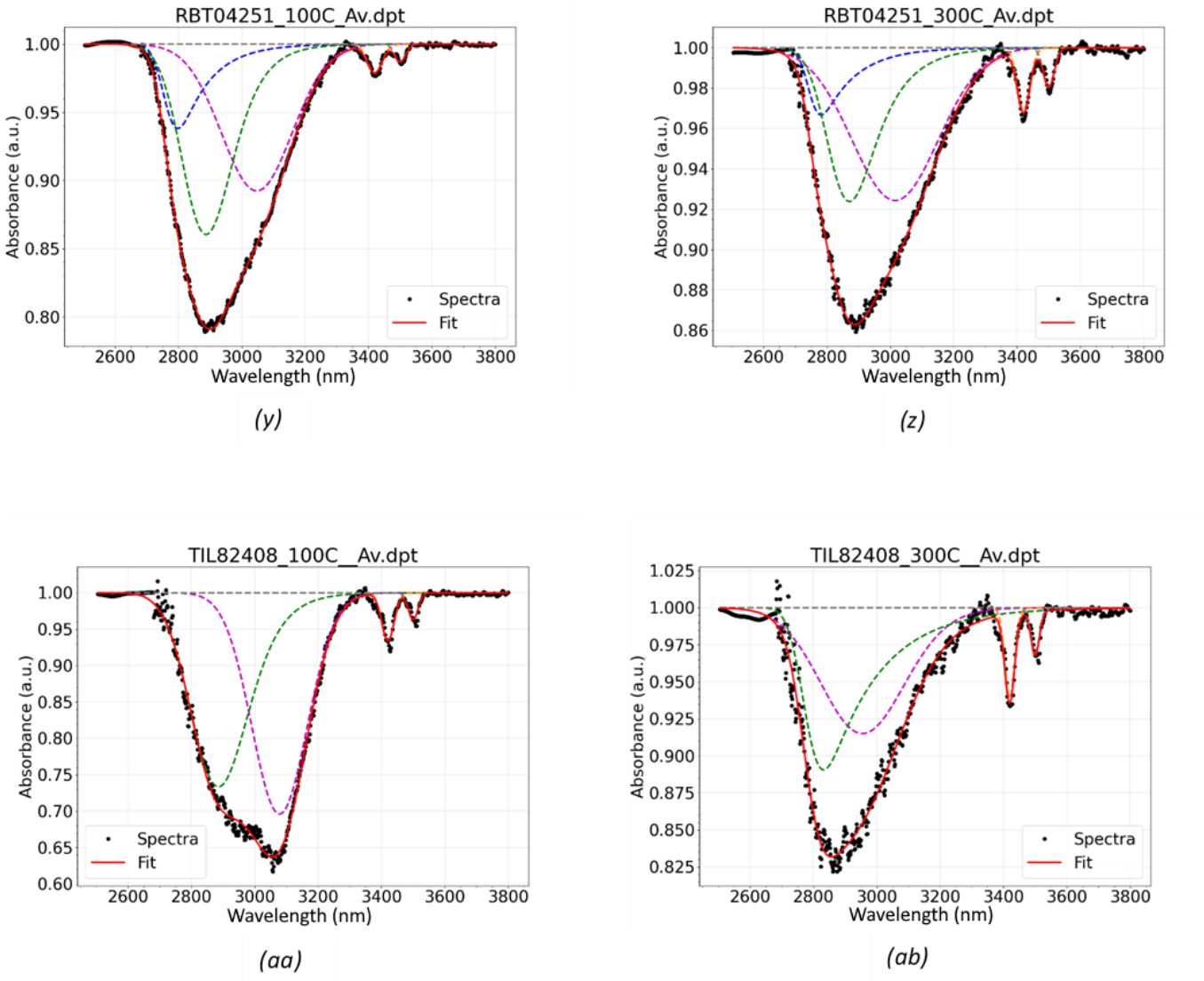

Figure A5: Fit of the 3-micron band for all 14 UOCs measured by FTIR spectroscopy in the present work. Each row shows the fitted 3-micron band of a given sample at 100 °C on the left and at 300 °C on the right.

6 Conclusion and perspectives

The main focus of this three year PhD was on the spectral analysis of varying CC and OC groups. The main objectives can be summarized as follows.

1. Contribute to better our understanding of asteroid reflectance spectra through the in-depth investigation of chondrite spectra.

2. Refine the genetic link between type 3 chondrites and their asteroidal parent bodies.

3. Help constrain the place of formation of different asteroid groups within the protoplanetary disk through the investigation of the post-accretion history in UOCs.

To reach these objectives, a large scale laboratory study of CVs, COs, CRs, UOCs and EOCs was performed. The samples were measured with varying measuring techniques, including reflectance spectroscopy, FTIR spectroscopy of matrix fragments, TGA, petrography and MS measurements. The main results of these studies are summarized below.

6.1 Spectral reflectance analysis of carbonaceous chondrites

During the first part of this thesis, reflectance spectra of 23 CVs, 15 COs, 4 CRs and 31 UOCs were acquired. For each spectrum a number of reflectance spectral features was determined including the 1 µm and 2 µm absorption band depths and positions, the spectral slopes in the 1 µm and 2 µm region, the visual slope at wavelengths lower than 700 nm, the peak reflectance value around 700 nm and the IBD_{Hyd} and position of the 3 µm band.

By comparing these spectral features, clear differences between different chondrite groups as well as a large variability between chondrites of the same group were observed. UOCs show deeper 1 µm and 2 µm absorption features located at lower wavelengths in comparison to CCs. Type 2 CRs exhibit 1 µm and 2 µm absorption features at even lower wavelengths than UOCs, allowing for a clear distinction from type 3 chondrites.

Due to their comparable mineralogy, no clear spectral differences between COs and CVs could be observed.

When investigating the influence that the thermal history of the chondrites has on the reflectance spectra, several spectral features appear to be controlled by the metamorphic grade. For CVs, a correlation between the 1 µm band depth and the metamorphic grade is observed. This correlation is not observed for other chondrite groups including COs. This could be explained by the systematically lower metamorphic grades of the COs versus the CVs considered during this PhD. This would mean that that sufficient chemical modification of olivine resulting in significant spectral changes only occurs above a given metamorphic temperature. For COs, the visual slope is positively correlated with the metamorphic grade indicating an increase in iron silicates and/or iron oxides. Lastly, the 2 µm spectral slope is negatively correlated with the metamorphic grade for all chondrite groups which indicates a decrease in pyroxene content with increasing peak metamorphic temperature (Bonal et al., 2016).

Lastly, the spectral features of the CCs are compared to those of 17 asteroid end member spectra (DeMeo et al., 2009) and 24 Eos family member spectra (RELAB, 2022). Additionally, the spectral features of 9 CKs (taken from the RELAB (2022) database) are compared as well. Firstly, a good match between the 1 µm and 2 µm absorption band depths of UOCs and S-type endmemers is found. This is expected (Nakamura et al., 2011) and validates the approach. CK chondrites show similar 1 µm and 2 µm absorption band depths and positions as the K-type end member. Their 2 µm absorption band depths and 1 µm absorption band position also matches those of Eos family members. This affiliation was previously suggested by Clark et al. (2009) as well. The 1 µm and 2 µm absorption band depths as well as the 1 µm band position of COs and CVs matches well with Eos family members but also with Cb-type and L-type end members. The affiliation of CVs and COs with L-type end members has previously been suggested by Sunshine et al. (2008) and Devogèle et al. (2018) as well. For CR chondrites, the 1 µm band depth and position matches that of X-complex end members as well as some C-complex, T-type and D-type end members. Since only 4 CRs were considered in this study, this result needs to be verified. Important to note is that among a single chondrite group the spectral features seem to match well with several asteroid types. This indicates that a single chondrite group could have several asteroidal parent bodies.

6.2 Spectral reflectance analysis of ordinary chondrites

During the second part of this PhD an in-depth analysis of OCs was performed. Firstly, perographic and magnetic measurements were used to verify the classification into H, L and LL of UOCs. The results show that 74 % of all Antarctic UOCs considerd during this PhD are misclassified in the Meteoritical Bulletin Database (2022). This is attributed to a lack of robust classification data used in the Meteoritical Bulletin Database (2022).

Subsequently, reflectance spectra of a large set of 41 UOCs and 39 EOCs were

obtained and analyzed. No clear dichotomy could be observed between UOC and EOC reflectance spectral values but rather a continuum. Some EOCs show stronger absorption bands than UOCs but for others they are comparable. The Ol/(Ol + Px) ratio of EOCs slightly exceeds that of UOCs for PT $\geq$ 4. The Ol/(Ol + Px) ratio decreases slightly from LL to L to H for PT $\geq$ 4. Furthermore, LLs of PT $\geq$ 5 could be distinguished from H and L based on a shallower 2 µm band depth and a 1 µm band position at longer wavelengths.

When analyzing the influence grain size has on the reflectance spectra of 6 EOCs and 1 UOC, a decrease in the 1 µm and 2 µm band depths as well as in the 700 nm peak reflectance value is observed with decreasing grain size. Furthermore, the 1 µm band position is shifted to shorter wavelengths with smaller gain sizes. Overall, this means EOC spectra become more comparable to UOC spectra the more comparable the grain size of their powders. The larger quantity of porous matrix material in UOCs means that they are ground into fine powders easier by hand than EOCs, making most EOC powders measured during this PhD coarser grained than those of UOCs.

When comparing the spectral features of the UOCs and EOCs with those of a large set of 466 de-space weathered S-type asteroids, the latter seem to cluster in-between UOCs and EOCs when considering the 1 µm and 2 µm band depths. The match between S-type spectral features and those of EOCs or UOCs is dependent on the SW model used. Therefore, it is not possible to identify EOC-like of UOC-like asteroid surfaces based on reflectance spectra alone. A correlation between the 1 µm band depth of S-type asteroid spectra and their diameter was found. When considering the grain size effects observed for UOCs and EOCs earlier, this indicates, that larger S-type bodies have a finer-grained regolith than small ones.

6.3 Chondrites as indicators of the place of formation asteroids

During the last part of this PhD an in-depth study of the hydration history of 41 UOCs was performed. Firstly, petrographic measurements on 39 of the 41 UOCs were used to constrain the modal abundance of the different chondrite components (metal, matrix, sulfides (troilite), magnetite/weathering products, and chondrules/chondrule fragments) and to determine the shock stage and weathering degree. Subsequently, TGA measurements were performed on 39 UOCs and FTIR spectroscopy on 14 UOCs.

The results show that contrarily to the generally accepted view, UOCs are not dry. In fact, once normalized to the matrix abundance the hydration of UOCs is comparable to that of CVs based on TGA. It is also comparable based on the IBD of the 3 µm band of the FTIR spectra. Furthermore, a correlation between the IBD of the 3 µm band of UOCs and their metamorphic grade is observed. This correlation is also observed based on TGA for UOCs with matrix abundances larger than 19 %. Interestingly, this correlation extends the one previously observed for CV chondrites (Bonal et al., 2020).

These results indicate that the asteroidal parent bodies of UOCs must have contained water. Therefore, the temperature in the formation reservoir of UOC parent bodies at the time of accretion must have been low enough to allow water ice accre-

tion. This water was lost during parent body metamorphism, maybe to space or in the form of a transient atmosphere. Planets that accreted fast such as Mars may have thus incorporated an elevated amount of water from the beginning. The location of the snowline at the time of accretion must have been inwards of the UOC parent body formation region. Finally, this shows that the inner Solar System was not dry.

6.4 Perspectives

During this work I have done extensive comparisons between chondrites and asteroids based on the 1 µm and 2 µm reflectance spectral bands. However, as I have shown, finding a definitive link between asteroids and chondrites based on these two features alone is difficult. Therefore, I would like to underline the potential of using the 3 µm hydration band as a further constraint for asteroid-meteorite links.

Preliminary results of the comparison of CCs and C-type asteroids based on the band depth and position of the 3 µm band have been published in Eschrig et al. (2021) (see Chapter 3 and Figure 6.1). They show that spectral variations between and within the different CC groups exist based on the 3 µm band. While the 3 µm band of CMs and Tagish Lake matched well with those of C-type asteroids no matches could be found for type 3 CCs with the limited asteroid spectra available. In order to find a possible match for these chondrites, extending the spectral range of asteroid spectra from the typical 0.45 µm to 2.45 µm range, to the 0.45 µm to 4.0 µm range and, therefore including the 3 µm band, has much potential.

The work done on UOC, EOC and S-type reflectance spectra during this PhD (Chapter 4) as well as the in-depth analysis of the hydration of UOCs (Chapter 5) reveal that the 3 µm band could also have much potential for further constraining the link between S-type asteroids and OCs.

To increase the accuracy of the quantification of hydration based on the 3 µm hydration band (see Section 5.2), IR measurement of matrix fragments with constrained measuring area and known sample thickness are envisaged. This will allow for the normalization of the IR spectra to the thickness of the samples and ease their comparison.

Furthermore, previous works have explored the removal of terrestrial weathering products such as oxy-hydroxides from chondrites through leaching (Krämer Ruggiu et al., 2021). Given that most Antarctic chondrites show terrestrial weathering to various extents, leaching them to help identify the hydrated minerals due to aqueous alteration on the asteroidal parent body sounds promising for the future. To overcome the limitation of low matrix abundance in UOC which significantly increases the difficulty of interpreting the TGA data, additional TGA measurements of matrix-enriched samples are envisaged. Since the separation of a sufficient amount of matrix material in UOCs is extremely difficult and time-consuming (see Section 5.2.1) this will be part of future works and developments.

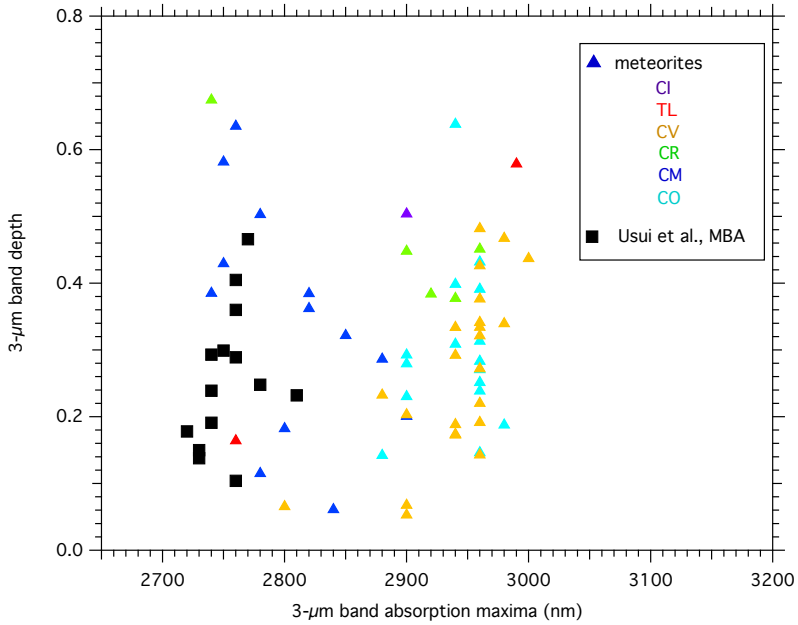

Figure 6.1: Comparison of the 3 µm band depths and positions of CCs with those of C-type asteroids. CIs, CMs and Tagish Lake spectra were taken from Potin et al. (2020a) and the C-type spectra from Usui et al. (2018).

7 Résumé en français

7.1 Introduction

L'étude de la formation du système solaire est une entreprise de longue date. Comprendre son évolution exacte depuis la nébuleuse solaire au disque protoplanétaire puis au système planétaire est un moteur majeur de l'exploration actuelle du système solaire. Ce faisant, nous ouvrons également la porte à un aperçu d'autres systèmes planétaires et éventuellement à la découverte d'autres planètes habitables semblables à la Terre.

Les petits corps du système solaire comprennent les astéroïdes, les comètes, les Troyens, les Centaures et les objets trans-neptuniens. Cependant, au cours de cette thèse, l'accent a été mis uniquement sur les astéroïdes. Les astéroïdes sont parmi les matériaux les plus importants dont nous disposons pour en savoir plus sur l'histoire du système solaire. On pense que la majorité de la population d'astéroïdes d'aujourd'hui sont des "astéroïdes de deuxième génération" qui se seraient formés à partir de quelques grands " corps parents primaires " qui ont été brisés lors de collisions (par exemple Greenwood et al. (2020)). Dans ce qui suit, lorsque l'on se réfère aux "astéroïdes" et au "corps parent astéroïde", on entend les astéroïdes de génération secondaire. Étant de petite taille, certains de ces astéroïdes ont échappé à de grandes quantités de chauffage et de différenciation, ce qui a permis la préservation de matériel primitif, dont certains peuvent remonter à la nébuleuse solaire. Par conséquent, les astéroïdes sont d'un grand intérêt pour répondre à certaines questions fondamentales sur la formation du système solaire. Quels groupes d'astéroïdes auraient pu contribuer aux éléments constitutifs des planètes telluriques ? Auraient-ils pu contribuer à fournir de l'eau et d'autres substances volatiles à la Terre ? Nous savons que la majorité des météorites de notre collection sont d'origine astéroïdale, mais quel groupe de météorites échantillonne quel groupe d'astéroïdes ? Au cours de cette thèse, j'ai essayé de contribuer à répondre à certaines des questions ci-dessus.

La collection de matériaux extraterrestres que nous avons sur Terre comprend des météorites, des particules de poussière interplanétaires (IDP), des micrométéorites antarctiques (AMM) ou des grains cométaires (par exemple Grady and Wright (2006) et ses références). Alors qu'en termes de masse, les météorites ne dominent pas le flux de matière extraterrestre vers la Terre (les micrométéorites livrent $\sim$ 2000 fois plus de matière que les météorites (par exemple, Engrand and Maurette (1998) et

ses références), leurs tailles plus grandes présentent un réel avantage par rapport aux poussières pour les mesures en laboratoire. Au cours de cette thèse, j'ai uniquement travailler sur des météorites.

Les météorites sont des morceaux de matière extraterrestre qui sont éjectés de leur corps parent (par exemple par des processus de collision), trouvent leur chemin vers l'orbite terrestre et survivent au passage à travers l'atmosphère terrestre. Alors que les météorites peuvent provenir de plusieurs types de corps parents différents (y compris les météorites martiennes ou lunaires), la majorité (> 99 % Scott and Krot (2003)) ont une origine astéroïdale. Une fois sur Terre, elles peuvent être trouvées, collectées et analysées en laboratoire. Les météorites pour lesquelles la chute a été observée (chutes) et celles pour lesquelles elle ne l'a pas été (trouvailles) sont distinguées. Outre l'analyse à distance des astéroïdes par spectroscopie de réflectance et les missions de retour d'échantillons, les météorites sont le principal moyen d'enquêter sur les astéroïdes et leur historique de formation.

Généralement, on distingue les météorites différenciées (achondrites, sidérolithe et météorites de fer) et les météorites nondifférenciées (chondrites). Ces derniers contiennent certains des matériaux les plus primitifs de notre système solaire, dont certains peuvent remonter à la nébuleuse solaire. Ainsi, les chondrites sont d'une grande importance pour l'étude de l'origine, la formation et l'évolution du système solaire et sont au centre de cette thèse.

7.1.1 Chondrites

Les chondrites présentent une grande variété de compositions chimiques et minéralogiques permettant l'identification de différentes classes: les chondrites carbonées (CCs), ordinaires (OCs) et enstatites ainsi que les chondrites R (de type Rumuruti) et K (de type Kakangari). Chaque classe a été initialement subdivisée en différents groupes en fonction de leur composition chimique et isotopique stable, de leur pétrographie et de leur minéralogie.

Plus tard, la pétrologie a également été prise en compte pour la classification. Bien que les chondrites soient primitives, elles subissent une gamme de processus secondaires sur leurs corps parents astéroïdes. Cela comprend l'altération aqueuse, le métamorphisme thermique et le métamorphisme de choc. Par conséquent, un modèle de classification supplémentaire a été introduit par Van Schmus and Wood (1967) pour donner une estimation de l'état d'altération de chaque chondrite. Il attribue un type pétrologique (PT), allant du type 1 à 7, à chaque chondrite. Les types 1 et 2 indiquent une altération aqueuse, le type 1 étant le plus altéré par voie aqueuse. Dans certaines études, ces deux groupes sont résumés en 10 sous-catégories allant du type 2.0-2.9 (par exemple Alexander et al. (2013), Harju et al. (2014), Kimura et al. (2020), Rubin et al. (2007) et Prestgard et al. (in prep.)). Les types 4 à 6 (parfois à 7) indiquent une augmentation du degré métamorphique, le type 7 étant le plus métamorphisé. Les chondrites de type 3 sont les plus primitives. Le type 3 est ensuite subdivisé en 10 sous-catégories allant du type 3.0 à 3.9, le grade métamorphique augmentant avec l'augmentation du type (Sears et al., 1995).

L'identification des processus secondaires et la quantification des intensités subies

par chaque chondrite est une tâche importante mais pas facile. Afin d'acquérir la composition originale des corps parents astéroïdaux, il faut comprendre de quelle manière le matériau a été modifié depuis sa formation. En étudiant l'histoire post-accrétion de chaque chondrite, nous pouvons commencer à construire une image des composants originaux de l'astéroïde initial et de ceux qui ont été modifiés.

Une fois sur Terre, les chondrites interagissent avec leurs environnements à des degrés divers, un processus appelé altération terrestre. La quantité d'altération subie dépend du temps et de l'emplacement de conservation ainsi que de la composition et de la texture de la chondrite.

Lorsque l'on compare des anomalies d'isotopes stables (par exemple, ϵ^{50}Ti versus ϵ^{54}Cr) de différents corps du système solaire, deux groupes distincts peuvent être observés (Trinquier et al. (2007), Warren (2011)). Le premier groupe, appelé groupe carboné (C), comprend les CC et présente un pourcentage plus élevé de ϵ^{50}Ti et de ϵ^{54}Cr. Le deuxième groupe, appelé groupe non carboné (NC), comprend les planètes terrestres, les OC et les chondrites à enstatite et plusieurs météorites non chondritiques. Pour ce groupe, les abondances de ϵ^{50}Ti et de ϵ^{54}Cr sont plus faibles. L'existence de deux groupes distincts indique deux réservoirs de formation génétiquement distincts qui étaient spatialement séparés (e.g. Warren (2011)). Contraindre la localisation exacte de ces réservoirs dans le disque ainsi que le début et la durée de leur existence fait l'objet de nombreuses études. Warren (2011) a suggéré que les deux réservoirs auraient pu être initialement séparés par Jupiter, puis mélangés par un processus tel que le modèle du Grand Tack (Walsh et al., 2011). Les objets du groupe NC étant généralement appauvris en matières volatiles, y compris l'eau, par rapport au groupe C (Morbidelli et al. (2015) et ses références), cela suggère que les NC se sont formés dans le système solaire interne à l'intérieur de la ligne des glaces, tandis que les CC se sont formés dans le système solaire externe au-delà de la ligne des glaces.

Par conséquent, au cours de cette thèse de trois ans, j'ai choisi de travailler à la fois sur un grand nombre de CC et sur un grand nombre d'OC. Plus précisément, je me suis concentrée sur les chondrites CV, CO et CR pour les CC. Les spectres de réflectance des CVs, COs et CRs sont assez similaires mais ne semblent pas avoir d'équivalent immédiat parmi les spectres modèles d'astéroïdes extraits de DeMeo et al. (2009). Cela en fait des groupes de chondrites intéressants à étudier. Pour les OC, j'ai travaillé à la fois sur des chondrites ordinaires équilibrées (EOC) et non équilibrées (UOC).

7.1.2 Connexion astéroïde-météorite

La majorité de notre collection de météorites étant d'origine astéroïdale, la question de savoir dans quelle mesure elle échantillonne la ceinture d'astéroïdes se pose. La plupart des informations dont nous disposons sur les astéroïdes se limitent à des observations au sol telles que la spectroscopie de réflectance des surfaces d'astéroïdes. En combinant ces études avec l'analyse des météorites en laboratoire, nous pouvons accroître notre compréhension des astéroïdes, mais est-il possible de trouver un lien génétique entre les météorites et leurs corps parents astéroïdaux ? Alors que de nombreuses correspondances ont été suggérées, seules quelques-unes ont été confirmées

jusqu'à présent.

La spectroscopie de réflectance est un outil-clé pour relier les météorites à leurs corps parents astéroïdaux. Ce n'est pas une tâche facile. Les spectres de réflectance moyens des astéroïdes présentent souvent des caractéristiques spectrales faibles entre 0,45 et 2,45 µm. Les principales caractéristiques spectrales qui peuvent être distinguées entre les différents types sont les bandes d'absorption 1 µm et 2 µm et les pentes spectrales.

De plus, pour les astéroïdes, qui sont exposés à l'environnement spatial, l'altération spatiale (SW) joue un rôle important. SW est le bombardement de la surface de l'astéroïde par des micrométéorites et l'irradiation par les ions de rayons cosmiques et les vents solaires (par exemple Brunetto et al. (2015)). Cela entraîne une modification de leur composition et de leurs propriétés physiques (par exemple Pieters and Noble (2016)) et influence ainsi leurs spectres de réflectance. Étant donné que SW n'affecte que la surface des astéroïdes, toute signature de celui-ci est effacée lors de l'entrée à haute température des météores dans l'atmosphère terrestre. Pour pouvoir comparer les spectres d'astéroïdes et de météorites, les effets de SW sur les spectres d'astéroïdes doivent être pris en compte.

Néanmoins, des tentatives d'identification des corps parents astéroïdaux sur la base des spectres de réflectance ont déjà été faites. En effet, le lien entre les astéroïdes de type S et les OC avait été suggéré sur la base de la spectroscopie de réflectance avant d'être confirmé par les échantillons retournés par la mission spatiale Hayabusa.

7.2 Objectifs de cette thèse

Cette section résume les principaux objectifs de cette thèse. Le premier objectif est de contribuer à une meilleure compréhension des spectres de réflectance des astéroïdes. Comme indiqué, mesurer et analyser les spectres de réflectance des chondrites est un excellent outil pour le faire. Quelles sont les variations spectrales au sein d'un même groupe de chondrites ainsi qu'entre différents groupes de chondrites ? Quelles caractéristiques spectrales pourraient être contrôlées par les processus post-accrétion ? Comment les processus terrestres influencent-ils les spectres de réflectance ? Pour répondre à ces questions, je me suis concentrée sur l'acquisition et l'analyse d'un large ensemble de spectres de réflectance de CC et OC. Contraindre la variation des caractéristiques spectrales des chondrites a alors des implications directes sur les variations des spectres des astéroïdes.

De plus, limiter les caractéristiques spectrales de réflectance des groupes de chondrites et d'astéroïdes permettra une comparaison directe entre les deux. Ce faisant, le second objectif de cette thèse est d'affiner le lien génétique entre les chondrites de type 3 et leurs corps parents astéroïdaux. Comme discuté au paravant ce n'est pas une tâche facile. Je me concentre sur la recherche des corps parents astéroïdes des CC et une tentative est faite pour contraindre davantage le lien déjà établi entre les astéroïdes de type S et les OC.

Le dernier objectif de cette thèse de trois ans est d'aider à contraindre le lieu de formation des différents groupes d'astéroïdes au sein du disque protoplanétaire. Comme

expliqué, nous nous attendons à des réservoirs de formation séparés pour les CC et les OC en fonction des anomalies d'isotopes stables. Cependant, l'emplacement exact de ces réservoirs n'est pas encore bien connu. L'analyse approfondie de l'histoire post-accrétion des chondrites peut aider à contraindre cet emplacement. Par conséquent, je présenterai une étude approfondie de l'histroire d'hydratation d'un ensemble plus large d'UOC. La détection de l'hydratation dans les UOC a des implications sur la position de la ligne des glaces dans le disque protoplanétaire au moment de l'accrétion.

7.3 Analyse en réflectance spectrale des chondrites carbonées de type 3 et recherche de leurs corps parents astéroïdaux

Notre compréhension des spectres de réflectance de différents groupes d'astéroïdes peut être améliorée en augmentant nos connaissances sur les spectres de réflectance de différents groupes de météorites. Les mesures en laboratoire des météorites permettent d'identifier les différences spectrales au sein de différents groupes de météorites ainsi qu'entre eux. Il nous permet d'analyser quelles caractéristiques spectrales sont contrôlées par des processus secondaires tels que le métamorphisme thermique et l'altération aqueuse et permet de rechercher un lien génétique entre les météorites et leurs corps parents astéroïdaux. Alors que les spectres de réflectance des astéroïdes ne peuvent fournir des informations que sur les surfaces d'astéroïdes, établir un lien avec les météorites permet de sonder l'intérieur des astéroïdes. Par exemple, l'analyse des chondrites a montré que les chondres sont un composant principal de l'intérieur de leurs corps parents astéroïdaux. Cependant, trouver un tel lien est une tâche difficile.

L'hypothèse générale est que chaque groupe de météorites échantillonne un corps parent astéroïdal (par exemple Burbine et al. (2002)). Le nombre de tels astéroïdes parents nécessaires pour représenter la collection actuelle de météorites a été estimé entre 95 et 148 (Greenwood et al., 2020). Trouver un lien génétique entre les météorites et les astéroïdes n'a été fait avec succès que dans quelques cas, comme entre l'astéroïde de type S Itokawa et les EOC par la mission de retour d'échantillons Hayabusa (Nakamura et al., 2011). Plusieurs corps parents astéroïdaux ont été suggérés pour les CC sur la base de la spectroscopie de réflectance, mais les liens varient entre les sources (par exemple Bell et al. (1988b), Vernazza et al. (2015), Hiroi et al. (1996) ou Vernazza and Beck (2016)).

Au cours de la première partie de cette thèse, j'ai donc mis l'accent sur l'analyse d'un large ensemble de spectres de réflectance de CC de type 3. J'ai mesuré les spectres de réflectance de 23 CV, 15 CO et 4 CR. 9 spectres CK ont été extraits de la base de données RELAB (2022). De plus, le travail comprenait les spectres de réflectance de 31 UOC que j'ai mesurés. La nouveauté de ce travail était que toutes les chondrites considérées avaient des histoires post-accrétion bien contraintes. Le grade métamorphique de (presque) toutes ces chondrites était auparavant contraint par Bonal et al. (2016). De plus, l'histoire de l'altération aqueuse des CV était auparavant contrainte par Bonal et al. (2020).

Enfin, un total de 24 spectres membres de la famille Eos (RELAB, 2022) et 17 spectres d'astéroïdes modèles (dont C, Cg, Cgh, Ch, B, T, X, Xc, Xe, Xk et D-type) (DeMeo et al., 2009) ont également été inclus.

Un ensemble de caractéristiques spectrales a été déterminé pour chaque spectre de réflectance, y compris les profondeurs de bande, les positions de bande, les pentes spectrales et la valeur de réflectance maximale. En utilisant ces caractéristiques, les différences spectrales entre les groupes de chondrites ont été étudiées. Les principaux résultats sont les suivants : les UOC peuvent être clairement distinguées des CC en montrant des caractéristiques d'absorption beaucoup plus profondes, situées à des longueurs d'onde plus basses. Les chondrites CR de type 2 ont montré des bandes d'absorption à 1 µm à des longueurs d'onde inférieures à celles des CC de type 3. Les CV et les CO, d'autre part, ne pouvaient pas être distinguées sur la base des seules caractéristiques spectrales de réflectance, en raison de leur minéralogie similaire.

J'ai mis en évidence que la bande d'absorptions 1 µm des CV est contrôlée par leur degré métamorphique. Étant donné que la bande à 1 µm est liée à l'olivine, l'augmentation de la profondeur de la bande avec l'augmentation du grade métamorphique indique la modification chimique de l'olivine dans les CV plus la température métamorphique est élevée. Pour les CO, une corrélation entre la pente visuelle et le grade métamorphique a pu être observée. Cela indique une augmentation du fer dans les silicates et/ou du fer oxydé dans les CO avec l'augmentation de la température métamorphique. La corrélation négative de la pente spectrale à 2 µm avec le grade métamorphique observé pour toutes les CC et UOC indique une diminution de la teneur en pyroxène avec l'augmentation de la température métamorphique maximale (Bonal et al., 2016).

Étant donné que les spectres d'astéroïdes modèles sont influencés par SW et que SW influence principalement la pente spectrale, les comparaisons entre les chondrites et les astéroïdes sont effectuées en fonction des profondeurs et des positions du bandes à 1 µm et 2 µm uniquement. En comparant les caractéristiques spectrales des chondrites CV, CO, UOC et CK à celles des astéroïdes modèles et des membres de la famille Eos, certaines caractéristiques spectrales des astéroïdes correspondaient bien à celles de certains groupes de chondrites. Tout d'abord, une bonne correspondance entre les profondeurs de bande d'absorption 1 µm et 2 µm des astéroïdes de type S et des UOC a pu être trouvée, ce qui a légitimé l'approche (Nakamura et al., 2011). Les CK correspondaient bien aux membres de la famille de type K et Eos, comme suggéré par Vernazza et al. (2015). Pour les chondrites CO et CV, une bonne correspondance a pu être trouvée avec les membres de la famille Eos, les astéroïdes de type L et de type Cb. Un lien entre les astéroïdes de type L et les chondrites CV, CO a déjà été suggéré par Sunshine et al. (2008) et Devogèle et al. (2018). Outre les similitudes spectrales, le nombre d'astéroïdes dans une classe donnée, leur distribution dans la ceinture d'astéroïdes et leur appartenance ou non à des familles dynamiques sont également cruciaux pour trouver de bons candidats corps-parents astéroïdaux. Les membres de la famille dynamique sont efficaces pour livrer du matériel météoritique sur Terre. Par conséquent, on s'attend à ce que davantage de fragments de types d'astéroïdes nombreux, répartis dans toute la ceinture d'astéroïdes et faisant partie de familles dynamiques soient livrés sur Terre. Les astéroïdes de type L ne sont pas rares et répartis dans toute la ceinture

d'astéroïdes (entre 2-4 UA) (DeMeo and Carry, 2013) ce qui renforce le lien trouvé.

7.4 Étude des surfaces d'astéroïdes de type S à travers les spectres de réflectance des chondrites ordinaires

Au sein du groupe OC, une large gamme de grades métamorphiques et de variations de minéralogie peuvent être observées. En tant que plus grand groupe de météorites de notre collection actuelle (environ 80 % des trouvailles et des chutes (Meteoritical Bulletin Database, 2022)), elles sont subdivisées en deux groupes principaux basés sur la pétrologie (UOC et EOC, 94 % des OC étant des EOC et seulement 6 % UOC (Meteoritical Bulletin Database, 2022)) et ensuite en trois groupes basés sur la teneur en fer brut et l'état d'oxydation (H, L et LL). Cela suggère que des variations de minéralogie et de pétrologie, telles que des matériaux de type UOC et EOC, devraient également être présentes parmi les astéroïdes de type S. En effet, des variations spectrales peuvent être observées dans un large ensemble de 466 spectres de réflectance d'astéroïdes de type S à notre disposition (Mahlke et al., 2022) mais est-il possible de relier les variations spectrales des astéroïdes à des propriétés spécifiques des OC ?

J'ai obtenu un large ensemble de spectres de réflectance 41 UOC et 39 EOC tout en utilisant des conditions de mesure cohérentes. Le PT de chaque UOC a été préalablement évalué (Bonal et al., 2016). Pour les EOC, les grades métamorphiques sont tirés du Meteoritical Bulletin Database (2022). La classification évaluée en sous-groupes H, L et LL des UOC a été vérifiée par des mesures de susceptibilité magnétique et pétrographiques, y compris la détermination de l'abondance modale du métal par comptage de points et mesures de la taille des chondres sur des sections minces/épaisses. J'ai montré que 74 % des UOC trouvées en Antarctique considérées ici sont mal classées dans le Meteoritical Bulletin Database (2022).

Par la suite, diverses caractéristiques spectrales ont été déterminées pour chaque chondrite pour identifier d'éventuelles différences spectrales entre UOC et EOC ainsi qu'entre H, L et LL. Cette analyse a révélé que les caractéristiques spectrales des UOC et des EOC forment un continuum plus qu'une dichotomie nette. Le rapport Ol/(Ol + Px) des EOC dépasse légèrement celui des UOC, certains affichant également des rapports comparables. Certaines EOC présentent des caractéristiques d'absorption et des valeurs de réflectance maximales plus fortes que pour les UOC, tandis que d'autres sont comparables. Étant donné que la diminution de la taille des grains entraîne une réflectance plus élevée et des profondeurs de bande plus faibles (Mustard and Hays (1997) et Sultana et al. (2021)), les spectres de réflectance d'un total de 6 EOC et d'une UOC ont été mesurés après des temps de broyage variables. Après chaque broyage, la taille approximative des grains a été déterminée au microscope. Comme prévu, l'UOC, qui contient un pourcentage plus élevé de matrice poreuse à grains fins, a été broyée plus facilement que les EOCs. Les résultats ont montré que la différence dans les profondeurs de bande d'absorption et les valeurs de réflectance maximale entre certaines EOC et UOC peut s'expliquer par la taille des grains. La comparaison de

H, L et LL a révélé que les LL de PT ≥ 5 se distinguent de H et L sur la base d'une profondeur de bande 2 µm moins profonde et d'une bande à 1 µ meter à des longueurs d'onde plus longues. Pour PT ≥ 4, le rapport moyen Ol/(Ol + Px) diminue légèrement de LL et L à H.

Au total, 466 spectres d'astéroïdes de type S (Mahlke et al., 2022) ont été traités. L'effet SW a été pris en compte en désaltérant analytiquement les spectres d'astéroïdes suivant Brunetto et al. (2006). Cela permet la comparaison entre les spectres des chondrites et des astéroïdes. De plus, les effets du SW et de la taille des grains sur les différentes caractéristiques spectrales des astéroïdes de type S ont été étudiés par analyse en composantes principales (ACP).

La comparaison avec les caractéristiques spectrales des OC à 1 µm et à 2 µm a révélé que la plupart des spectres d'astéroïdes de type S se regroupent entre les UOC et les EOC. Le rapport moyen Ol/(Ol + Px) des astéroïdes de type S correspond légèrement mieux à celui des EOC qu'aux UOC. Cependant, l'ACP a montré que la qualité d'une correspondance entre les chondrites et les astéroïdes dépend fortement du modèle SW utilisé. L'altération spatiale des spectres d'astéroïdes a entraîné un bleuissement spectral et une augmentation des caractéristiques d'absorption à 1 µm et à 2 µm. En fonction de l'exposition de l'astéroïde de type S à l'espace, les spectres de réflectance passeront de caractéristiques spectrales comparables aux UOC, à comparables aux EOC, à ne pas correspondre du tout.

Enfin, une anti-corrélation entre la profondeur de bande 1 µm des astéroïdes de type S et leur diamètre a été trouvée. Comme l'ont montré les expériences sur la taille des grains au cours de ce travail, nous nous attendons à ce que le contraste de la bande diminue avec la diminution de la taille des grains. Ce résultat pointe donc vers des corps d'astéroïdes plus grands ayant un régolithe à grains fins, tandis que les corps plus petits ont un régolithe à grains plus grossiers. Ce résultat, associé à une meilleure correspondance du rapport Ol/(Ol + Px) des astéroïdes de type S aux EOC, est conforme, mais ne prouve pas définitivement, une structure en oignon pour les astéroïdes de type S.

Le fait qu'aucune différence spectrale claire n'ait pu être trouvée entre les UOC et les EOC basé sur les bandes à 1 µm et à 2 µm seules, souligne le potentiel de l'utilisation des bandes d'hydratation à 3 µm comme contrainte supplémentaire. Les EOC ayant des PT plus élevés, ils devraient être plus secs que les UOC et donc se distinguer des UOC en montrant peu ou pas de bande 3 µm. Pour les UOC, en revanche, des bandes à 3 µm ont clairement été observées. L'extension de la gamme spectrale mesurée sur les astéroïdes de type S à la région 3 µm pourrait aider à contraindre davantage le lien astéroïde-météorite.

7.5 L'histoire de l'hydratation des chondrites ordinaires non équilibrées

Au cours du dernier chapitre de ma thèse, je me suis concentrée sur l'analyse détaillée de l'histoire post-accrétion des UOC. Comme expliqué précédemment, la comparaison des anomalies isotopiques stables de différents petits corps du système solaire

montre deux groupes distincts indiquant deux réservoirs de formation distincts. Le premier groupe, appelé groupe NC, comprend, entre autres, les OC ainsi que les corps internes du système solaire comme la Terre et Mars. Le deuxième groupe appelé groupe C comprend les CC. Les planètes terrestres et les astéroïdes internes du système solaire sont appauvris en matières volatiles, y compris l'eau, par rapport aux corps externes du système solaire tels que les planètes géantes, les comètes et les astéroïdes externes du système solaire (Morbidelli et al., 2015). Cela place les OC dans la catégorie des astéroïdes secs du système solaire interne qui se sont vraisemblablement formés à l'intérieur de la ligne de condensation de l'eau. L'emplacement exact de la ligne de condensation de l'eau au moment de la formation des astéroïde n'est pas encore bien contraint. L'analyse approfondie de l'histoire post-accrétion des chondrites peut apporter des informations importantes pour mieux contraindre cette localisation.

En effet, des minéraux hydratés ont déjà été observés dans quelques UOC les plus primitives telles que Semarkona (LL3.00) et Bishunpur (LL3.15) (par exemple Brearley (2006), Alexander et al. (1989), Dobrică et al. (2019) et Alexander et al. (2010)). L'hydratation actuelle d'une chondrite est contrôlée par une combinaison d'épisodes d'hydratation terrestres et extraterrestres ainsi que par des processus de chauffage. Pour cette raison, j'ai effectué une analyse approfondie de l'histoire de l'altération aqueuse et des chocs d'un grand nombre de 41 UOC. L'histoire thermique des UOC avait été auparavant contrainte par la spectroscopie Raman (Bonal et al., 2016). Des mesures pétrographiques ont été utilisées pour évaluer le degré de choc et le degré d'altération terrestre de chaque UOC. Pour évaluer l'hydratation des UOC, j'ai effectué une analyse thermogravimétrique (TGA) sur 31 des UOC et par spectroscopie FTIR sur 14 d'entre eux.

Ces mesures ont révélé que, contrairement à la croyance commune, les UOC sont hydratées. Par conséquent, leurs corps parents astéroïdaux ne doivent pas avoir été secs. En effet, j'ai montré qu'une fois normalisée à l'abondance de la matrice, l'hydratation des UOC est comparable à celle précédemment observée pour les CV (Bonal et al., 2020). Une corrélation entre l'hydratation et le degré métamorphique a été observée lors de la comparaison de la profondeur de bande intégrée (IBD) de la bande à 3 µm des spectres FTIR aux valeurs $FWHM_D$. Cette corrélation a également été observée pour la perte de masse normalisée à l'abondance de matrice déterminée par TGA, en ne considérant que les UOC avec des abondances matricielles $\geq$ 19 %. Cette corrélation prolonge celle précédemment observée pour les CV. Ces résultats ont indiqué que le système solaire interne n'était pas sec et que l'emplacement de la ligne de condensation de l'eau devait se trouver à l'intérieur de la région de formation des corps-parents des UOCs au moment de l'accrétion.

7.6 Conclusion et perspectives

En comparant ces caractéristiques spectrales des CCs et des OCs, des différences claires entre les différents groupes de chondrites ainsi qu'une grande variabilité entre chondrites d'un même groupe ont été observées. Les CR de type 2 se distinguent des chondrites de type 3. En raison de leur minéralogie comparable, aucune différence

spectrale claire entre les CO et les CV n'a pu être observée. Pour les CV, une corrélation entre la profondeur de la bande à 1 µm et le grade métamorphique est observée. Pour les CO, la pente visuelle est positivement corrélée avec le grade métamorphique.

Une bonne correspondance entre les profondeurs de bande d'absorption des UOC et des spectres modèles d'astéroïdes de type S est trouvée. Ceci est attendu (Nakamura et al., 2011) et valide l'approche. Les chondrites CK s'accordent bien avec les spectres modèles de type K et celles des membres de la famille Eos. Les COs et les CVs correspondent bien aux spectres modèles d'astéroïdes de type Cb et L ainsi qu'aux membres de la famille Eos.

Des mesures pétrographiques et magnétiques ont montré que 74 % de toutes les UOC antarctiques considérées au cours de cette thèse sont mal classées dans la Meteoritical Bulletin Database (2022). Ceci est attribué à un manque de données de classification robustes utilisées dans le Meteoritical Bulletin Database (2022).

Aucune dichotomie claire n'a pu être observée entre les valeurs spectrales de réflectance des UOCs et EOCs, mais plutôt un continuum. Les LL de PT ≥ 5 peuvent être distinguées de H et L en fonction de leurs caractéristiques spectrales de réflectance. L'analyse de l'influence de la taille des grains a montré que les spectres EOC deviennent plus comparables aux spectres UOC plus la taille de leurs grains est comparable.

Lorsque l'on compare les caractéristiques spectrales des UOC et des EOC avec celles d'un grand ensemble de 466 astéroïdes de type S altérés par l'espace, ces derniers semblent se regrouper entre les UOC et les EOC. La correspondance entre les caractéristiques spectrales de type S et celles des EOC ou UOC dépend du modèle de SW utilisé. Une corrélation entre la profondeur de bande à 1 µm des spectres d'astéroïdes de type S et leur diamètre a été trouvée. Lorsque l'on considère les effets de taille de grain observés pour les UOC et les EOC plus tôt, cela indique que les corps de type S plus grands ont un régolithe à grains plus fins que les petits.

Contrairement à l'opinion généralement admise, les UOC ne sont pas sèches. En fait, une fois normalisée à l'abondance de la matrice, l'hydratation des UOC est comparable à celle des CV. De plus, une corrélation entre l'hydratation des UOC et leur grade métamorphique est observée qui prolonge celle précédemment observée pour les chondrites CV.

Ces résultats indiquent que les corps parents astéroïdaux des UOC devaient contenir de l'eau. L'emplacement de la ligne de condensation de l'eau au moment de l'accrétion doit avoir été à l'intérieur de la région de formation du corps parent UOC. Cela montre que le système solaire interne n'était pas sec.

Avec l'acquisition d'un grand nombre de spectres de CV et CO pendant ma thèse et l'acquisition d'un grand nombre de spectres d'astéroïdes de type L, de type K et barbariens pendant la thèse de Max Mahlke (Mahlke et al. (2022)) le lien entre ces groupes de chondrites et d'astéroïdes est revisité. Les résultats préliminaires montrent une bonne correspondance entre les CV et les CO et les astéroïdes de type L sans nécessiter de fortes abondances des CAI (Sunshine et al. (2008) et Devogèle et al. (2018)). Les résultats sont en cours de préparation pour publication.

Pour les perspectives, je voudrais souligner le potentiel d'utilisation de la bande d'hydratation à 3 µm comme contrainte supplémentaire pour les liens astéroïde-météorite. Pour augmenter la précision de la quantification de l'hydratation basée sur la bande d'hydratation à 3 µm, la mesure IR des fragments de matrice avec une zone de mesure contrainte et une épaisseur d'échantillon connue est envisagée. Pour surmonter la limitation de la faible abondance de matrice dans l'UOC qui augmente considérablement la difficulté d'interprétation des données TGA, des mesures TGA supplémentaires d'échantillons enrichis en matrice sont envisagées.

Bibliography

Neyda M. Abreu and Adrian J. Brearley. Early solar system processes recorded in the matrices of two highly pristine cr3 carbonaceous chondrites, met 00426 and que 99177. *Geochimica et Cosmochimica Acta*, 74(3):1146–1171, 2010. ISSN 0016-7037. doi: https://doi.org/10.1016/j.gca.2009.11.009. URL https://www.sciencedirect.com/science/article/pii/S001670370900708X.

C. M. O'D. Alexander, R. Bowden, M. L. Fogel, K. T. Howard, C. D. K. Herd, and L. R. Nittler. The provenances of asteroids, and their contributions to the volatile inventories of the terrestrial planets. *Science*, 337(6095):721–723, 2012. doi: 10.1126/science.1223474. URL https://www.science.org/doi/abs/10.1126/science.1223474.

C. M. O'D. Alexander, K. D. McKeegan, and K. Altwegg. Water reservoirs in small planetary bodies: Meteorites, asteroids, and comets. *Space Science Reviews*, 214:36, 2018. ISSN 1572-9672. doi: https://doi.org/10.1007/s11214-018-0474-9.

C.M.O'D Alexander, D.J Barber, and R Hutchison. The microstructure of semarkona and bishunpur. *Geochimica et Cosmochimica Acta*, 53(11):3045–3057, 1989. ISSN 0016-7037. doi: https://doi.org/10.1016/0016-7037(89)90180-4. URL https://www.sciencedirect.com/science/article/pii/0016703789901804.

C.M.O'D. Alexander, S.D. Newsome, M.L. Fogel, L.R. Nittler, H. Busemann, and G.D. Cody. Deuterium enrichments in chondritic macromolecular material—implications for the origin and evolution of organics, water and asteroids. *Geochimica et Cosmochimica Acta*, 74(15):4417–4437, 2010. ISSN 0016-7037. doi: https://doi.org/10.1016/j.gca.2010.05.005. URL https://www.sciencedirect.com/science/article/pii/S001670371000270X.

Conel M. O'D. Alexander. Quantitative models for the elemental and isotopic fractionations in chondrites: The carbonaceous chondrites. *Geochimica et Cosmochimica Acta*, 254:277–309, 2019. ISSN 0016-7037. doi: https://doi.org/10.1016/j.gca.2019.02.008. URL https://www.sciencedirect.com/science/article/pii/S0016703719300857.

Conel M.O'D. Alexander, Kieren T. Howard, Roxane Bowden, and Marilyn L. Fogel. The classification of cm and cr chondrites using bulk h, c and n abundances and isotopic compositions. *Geochimica et Cosmochimica Acta*, 123:244–260, 2013. ISSN 0016-7037. doi: https://doi.org/10.1016/j.gca.2013.05.019. URL https://www.sciencedirect.com/science/article/pii/S0016703713002986.

Yuri Amelin, Angela Kaltenbach, Tsuyoshi Iizuka, Claudine H. Stirling, Trevor R. Ireland, Michail Petaev, and Stein B. Jacobsen. U–pb chronology of the solar system's oldest solids with variable 238u/235u. *Earth and Planetary Science Letters*, 300(3): 343–350, 2010. ISSN 0012-821X. doi: https://doi.org/10.1016/j.epsl.2010.10.015. URL https://www.sciencedirect.com/science/article/pii/S0012821X10006497.

P. Beck, A. Garenne, E. Quirico, L. Bonal, G. Montes-Hernandez, F. Moynier, and B. Schmitt. Transmission infrared spectra (2–25μm) of carbonaceous chondrites (ci, cm, cv–ck, cr, c2 ungrouped): Mineralogy, water, and asteroidal processes. *Icarus*, 229:263–277, 2014. ISSN 0019-1035. doi: https://doi.org/10.1016/j.icarus.2013.10.019. URL https://www.sciencedirect.com/science/article/pii/S0019103513004387.

J. F. Bell, P. D. Owensby, B. R. Hawke, and M. J. Gaffey. The 52-Color Asteroid Survey: Final Results and Interpretation. In *Lunar and Planetary Science Conference*, volume 19, page 57, Mar 1988a.

J. F. Bell, P. D. Owensby, B. R. Hawke, and M. J. Gaffey. The 52-Color Asteroid Survey: Final Results and Interpretation. In *Lunar and Planetary Science Conference*, volume 19, page 57, Mar 1988b.

J. F. Bell, D. R. Davis, W. K. Hartmann, and M. J. Gaffey. Asteroids: the big picture. *Scanning Electron Microscopy*, pages 921–945, 1989. ISSN 0586-5581. Copyright: Copyright 2018 Elsevier B.V., All rights reserved.

Marvin E. Bennett and Harry Y. McSween. Shock features in iron-nickel metal and troilite of l-group ordinary chondrites. *Meteoritics & Planetary Science*, 31(2):255–264, 1996. doi: https://doi.org/10.1111/j.1945-5100.1996.tb02021.x. URL https://onlinelibrary.wiley.com/doi/abs/10.1111/j.1945-5100.1996.tb02021.x.

Richard P. Binzel, Andrew S. Rivkin, J.Scott Stuart, Alan W. Harris, Schelte J. Bus, and Thomas H. Burbine. Observed spectral properties of near-earth objects: results for population distribution, source regions, and space weathering processes. *Icarus*, 170(2):259–294, 2004. ISSN 0019-1035. doi: https://doi.org/10.1016/j.icarus.2004.04.004. URL https://www.sciencedirect.com/science/article/pii/S0019103504001253.

A. Bischoff. Aqueous alteration of carbonaceous chondrites: Evidence for preaccretionary alteration—a review. *Meteoritics & Planetary Science*, 33(5):1113–1122, 1998. doi: https://doi.org/10.1111/j.1945-5100.1998.tb01716.x. URL https://onlinelibrary.wiley.com/doi/abs/10.1111/j.1945-5100.1998.tb01716.x.

P. A. Bland, M. E. Zolensky, G. K. Benedix, and M. A. Sephton. Weathering of Chondritic Meteorites. In Dante S. Lauretta and Harry Y. McSween, editors, *Meteorites and the Early Solar System II*, page 853. 2006.

Lydie Bonal, Eric Quirico, Michèle Bourot-Denise, and Gilles Montagnac. Determination of the petrologic type of cv3 chondrites by raman spectroscopy of included organic matter. *Geochimica et Cosmochimica Acta*, 70(7):1849–1863, 2006.

ISSN 0016-7037. doi: https://doi.org/10.1016/j.gca.2005.12.004. URL https://www.sciencedirect.com/science/article/pii/S0016703705009415.

Lydie Bonal, Michèle Bourot-Denise, Eric Quirico, Gilles Montagnac, and Eric Lewin. Organic matter and metamorphic history of co chondrites. *Geochimica et Cosmochimica Acta*, 71(6):1605–1623, 2007. ISSN 0016-7037. doi: https://doi.org/10.1016/j.gca.2006.12.014. URL https://www.sciencedirect.com/science/article/pii/S0016703706022617.

Lydie Bonal, Eric Quirico, Laurène Flandinet, and Gilles Montagnac. Thermal history of type 3 chondrites from the antarctic meteorite collection determined by raman spectroscopy of their polyaromatic carbonaceous matter. *Geochimica et Cosmochimica Acta*, 189:312–337, 2016. ISSN 0016-7037. doi: https://doi.org/10.1016/j.gca.2016.06.017. URL https://www.sciencedirect.com/science/article/pii/S0016703716303477.

Lydie Bonal, Jérôme Gattacceca, Alexandre Garenne, Jolantha Eschrig, Pierre Rochette, and Lisa Krämer Ruggiu. Water and heat: New constraints on the evolution of the cv chondrite parent body. *Geochimica et Cosmochimica Acta*, 276:363–383, 2020. ISSN 0016-7037. doi: https://doi.org/10.1016/j.gca.2020.03.009. URL https://www.sciencedirect.com/science/article/pii/S0016703720301708.

Jr. Bottke, W. F., D. Vokrouhlický, D. P. Rubincam, and M. Broz. The Effect of Yarkovsky Thermal Forces on the Dynamical Evolution of Asteroids and Meteoroids. In *Asteroids III*, pages 395–408. 2002.

Jr. Bottke, William F., David Vokrouhlický, David P. Rubincam, and David Nesvorný. The Yarkovsky and Yorp Effects: Implications for Asteroid Dynamics. *Annual Review of Earth and Planetary Sciences*, 34:157–191, May 2006. doi: 10.1146/annurev.earth.34.031405.125154.

A. J. Brearley. Nebular versus Parent-body Processing. *Treatise on Geochemistry*, 1: 711, December 2003. doi: 10.1016/B0-08-043751-6/01068-9.

A. J. Brearley. The Action of Water. In Dante S. Lauretta and Harry Y. McSween, editors, *Meteorites and the Early Solar System II*, page 584. 2006.

R. Brunetto, C. Lantz, D. Ledu, D. Baklouti, M.A. Barucci, P. Beck, L. Delauche, Z. Dionnet, P. Dumas, J. Duprat, C. Engrand, F. Jamme, P. Oudayer, E. Quirico, C. Sandt, and E. Dartois. Ion irradiation of allende meteorite probed by visible, ir, and raman spectroscopies. *Icarus*, 237:278 – 292, 2014. ISSN 0019-1035. doi: https://doi.org/10.1016/j.icarus.2014.04.047. URL http://www.sciencedirect.com/science/article/pii/S0019103514002395.

R. Brunetto, M. J. Loeffler, D. Nesvorný, S. Sasaki, and G. Strazzulla. *Asteroid Surface Alteration by Space Weathering Processes*, pages 597–616. 2015. doi: 10.2458/azu_uapress_9780816532131-ch031.

Rosario Brunetto, Pierre Vernazza, Simone Marchi, Mirel Birlan, Marcello Fulchignoni, Vincenzo Orofino, and Giovanni Strazzulla. Modeling asteroid surfaces from observations and irradiation experiments: The case of 832 karin. *Icarus*, 184(2):327–337, 2006. ISSN 0019-1035. doi: https://doi.org/10.1016/j.icarus.2006.05.019. URL https://www.sciencedirect.com/science/article/pii/S0019103506001862.

T. H. Burbine, T. J. McCoy, A. Meibom, B. Gladman, and K. Keil. *Meteoritic Parent Bodies: Their Number and Identification*, pages 653–667. March 2002.

Thomas H. Burbine, Michael J. Gaffey, and Jeffrey F. Bell. S-asteroids 387 aquitania and 980 anacostia: Possible fragments of the breakup of a spinel-bearing parent body with c03/cv3 affinities. *Meteoritics*, 27(4):424–434, 1992. doi: 10.1111/j.1945-5100.1992.tb00224.x. URL https://onlinelibrary.wiley.com/doi/abs/10.1111/j.1945-5100.1992.tb00224.x.

Schelte J. Bus and Richard P. Binzel. Phase ii of the small main-belt asteroid spectroscopic survey: A feature-based taxonomy. *Icarus*, 158(1):146–177, 2002. ISSN 0019-1035. doi: https://doi.org/10.1006/icar.2002.6856. URL https://www.sciencedirect.com/science/article/pii/S0019103502968569.

A. Cellino, I.N. Belskaya, Ph. Bendjoya, M. Di Martino, R. Gil-Hutton, K. Muinonen, and E.F. Tedesco. The strange polarimetric behavior of asteroid (234) barbara. *Icarus*, 180(2):565–567, 2006. ISSN 0019-1035. doi: https://doi.org/10.1016/j.icarus.2005.09.001. URL https://www.sciencedirect.com/science/article/pii/S0019103505003295.

Clark R. Chapman and John W. Salisbury. Comparisons of meteorite and asteroid spectral reflectivities. *Icarus*, 19(4):507–522, 1973. ISSN 0019-1035. doi: https://doi.org/10.1016/0019-1035(73)90078-X. URL https://www.sciencedirect.com/science/article/pii/001910357390078X.

Christopher R. J. Charles. Disaggregating meteorites by automated freeze thaw. *Review of Scientific Instruments*, 82(6):065102, 2011. doi: 10.1063/1.3597673. URL https://doi.org/10.1063/1.3597673.

Fred J. Ciesla, Dante S. Lauretta, Barbara A. Cohen, and Lon L. Hood. A nebular origin for chondritic fine-grained phyllosilicates. *Science*, 299(5606):549–552, 2003. doi: 10.1126/science.1079427. URL https://www.science.org/doi/abs/10.1126/science.1079427.

Fred J. Ciesla, Thomas M. Davison, Gareth S. Collins, and David P. O'Brien. Thermal consequences of impacts in the early solar system. *Meteoritics & Planetary Science*, 48(12):2559–2576, 2013. doi: https://doi.org/10.1111/maps.12236. URL https://onlinelibrary.wiley.com/doi/abs/10.1111/maps.12236.

Beth Ellen Clark, Maureen E. Ockert-Bell, Ed A. Cloutis, David Nesvorny, Thais Mothé-Diniz, and Schelte J. Bus. Spectroscopy of k-complex asteroids: Parent bodies of carbonaceous meteorites? *Icarus*, 202(1):119–133, 2009. ISSN 0019-1035. doi:

https://doi.org/10.1016/j.icarus.2009.02.027. URL https://www.sciencedirect.com/science/article/pii/S0019103509001067.

Roger N. Clark. Spectroscopy of rocks and minerals and principles of spectroscopy. *Remote Sensing for the Eartb Sciences: Manual of Remote Sensing*, 3, 1999.

R N Clayton. Oxygen isotopes in meteorites. *Annual Review of Earth and Planetary Sciences*, 21(1):115–149, 1993. doi: 10.1146/annurev.ea.21.050193.000555. URL https://doi.org/10.1146/annurev.ea.21.050193.000555.

E.A. Cloutis, P. Hudon, T. Hiroi, and M.J. Gaffey. Spectral reflectance properties of carbonaceous chondrites: 3. cr chondrites. *Icarus*, 217(1):389–407, 2012a. ISSN 0019-1035. doi: https://doi.org/10.1016/j.icarus.2011.11.004. URL https://www.sciencedirect.com/science/article/pii/S0019103511004313.

E.A. Cloutis, P. Hudon, T. Hiroi, M.J. Gaffey, and P. Mann. Spectral reflectance properties of carbonaceous chondrites – 5: Co chondrites. *Icarus*, 220(2):466–486, 2012b. ISSN 0019-1035. doi: https://doi.org/10.1016/j.icarus.2012.05.019. URL https://www.sciencedirect.com/science/article/pii/S0019103512002011.

E.A. Cloutis, P. Hudon, T. Hiroi, M.J. Gaffey, P. Mann, and J.F. Bell. Spectral reflectance properties of carbonaceous chondrites: 6. cv chondrites. *Icarus*, 221(1):328–358, 2012c. ISSN 0019-1035. doi: https://doi.org/10.1016/j.icarus.2012.07.007. URL https://www.sciencedirect.com/science/article/pii/S0019103512002813.

Edward A. Cloutis, Michael J. Gaffey, Timothy L. Jackowski, and Kevin L. Reed. Calibrations of phase abundance, composition, and particle size distribution for olivine-orthopyroxene mixtures from reflectance spectra. *Journal of Geophysical Research: Solid Earth*, 91(B11):11641–11653, 1986. doi: https://doi.org/10.1029/JB091iB11p11641. URL https://agupubs.onlinelibrary.wiley.com/doi/abs/10.1029/JB091iB11p11641.

G.J. Consolmagno, D.T. Britt, and R.J. Macke. The significance of meteorite density and porosity. *Geochemistry*, 68(1):1–29, 2008. ISSN 0009-2819. doi: https://doi.org/10.1016/j.chemer.2008.01.003. URL https://www.sciencedirect.com/science/article/pii/S0009281908000044.

A. Coradini, D. Turrini, C. Federico, et al. Vesta and ceres: Crossing the history of the solar system. *Space Science Reviews*, 163:25–40, 2011. doi: 10.1007/s11214-011-9792-x.

Thomas M. Davison, Fred J. Ciesla, and Gareth S. Collins. Post-impact thermal evolution of porous planetesimals. *Geochimica et Cosmochimica Acta*, 95:252–269, 2012. ISSN 0016-7037. doi: https://doi.org/10.1016/j.gca.2012.08.001. URL https://www.sciencedirect.com/science/article/pii/S0016703712004486.

Rogerio Deienno, Rodney S. Gomes, Kevin J. Walsh, Alessandro Morbidelli, and David Nesvorný. Is the grand tack model compatible with the orbital distribution of main belt asteroids? *Icarus*, 272:114–124, 2016. ISSN 0019-1035. doi: https://doi.org/10.

1016/j.icarus.2016.02.043. URL https://www.sciencedirect.com/science/article/pii/S0019103516001214.

F.E. DeMeo and B. Carry. The taxonomic distribution of asteroids from multi-filter all-sky photometric surveys. *Icarus*, 226(1):723–741, 2013. ISSN 0019-1035. doi: https://doi.org/10.1016/j.icarus.2013.06.027. URL https://www.sciencedirect.com/science/article/pii/S0019103513002923.

FE DeMeo, CMO Alexander, KJ Walsh, CR Chapman, and RP Binzel. The compositional structure of the asteroid belt. *Asteroids iv*, 1:13, 2015.

Francesca E. DeMeo and Benoit Carry. Solar system evolution from compositional mapping of the asteroid belt. *Nature*, 505:629–634, 2014. doi: https://doi.org/10.1038/nature12908.

Francesca E. DeMeo, Richard P. Binzel, Stephen M. Slivan, and Schelte J. Bus. An extension of the bus asteroid taxonomy into the near-infrared. *Icarus*, 202(1):160–180, 2009. ISSN 0019-1035. doi: https://doi.org/10.1016/j.icarus.2009.02.005. URL https://www.sciencedirect.com/science/article/pii/S0019103509000554.

M. Devogèle, P. Tanga, A. Cellino, Ph. Bendjoya, J.-P. Rivet, J. Surdej, D. Vernet, J.M. Sunshine, S.J. Bus, L. Abe, S. Bagnulo, G. Borisov, H. Campins, B. Carry, J. Licandro, W. McLean, and N. Pinilla-Alonso. New polarimetric and spectroscopic evidence of anomalous enrichment in spinel-bearing calcium-aluminium-rich inclusions among l-type asteroids. *Icarus*, 304:31 – 57, 2018. ISSN 0019-1035. doi: https://doi.org/10.1016/j.icarus.2017.12.026. URL http://www.sciencedirect.com/science/article/pii/S0019103517300271. Asteroids and Space Debris.

E. Dobrică and A. J. Brearley. Amorphous silicates in the matrix of semarkona: The first evidence for the localized preservation of pristine matrix materials in the most unequilibrated ordinary chondrites. *Meteoritics & Planetary Science*, 55(3):649–668, 2020. doi: https://doi.org/10.1111/maps.13458. URL https://onlinelibrary.wiley.com/doi/abs/10.1111/maps.13458.

E. Dobrică, C. Le Guillou, and A.J. Brearley. Aqueous alteration of porous microchondrules in semarkona: Implications for hydration, oxidation and elemental exchange processes. *Geochimica et Cosmochimica Acta*, 244:292–307, 2019. ISSN 0016-7037. doi: https://doi.org/10.1016/j.gca.2018.10.002. URL https://www.sciencedirect.com/science/article/pii/S0016703718305763.

Tasha L. Dunn, Timothy J. McCoy, J.M. Sunshine, and Harry Y. McSween. A coordinated spectral, mineralogical, and compositional study of ordinary chondrites. *Icarus*, 208(2):789–797, 2010. ISSN 0019-1035. doi: https://doi.org/10.1016/j.icarus.2010.02.016. URL https://www.sciencedirect.com/science/article/pii/S0019103510000904.

Cécile Engrand and Michel Maurette. Carbonaceous micrometeorites from antarctica. *Meteoritics & Planetary Science*, 33(4):565–580, 1998. doi: https://doi.org/10.1111/

j.1945-5100.1998.tb01665.x. URL https://onlinelibrary.wiley.com/doi/abs/10.1111/j.1945-5100.1998.tb01665.x.

J. Eschrig, L. Bonal, and P. Beck. NIR reflectance spectrum ($i = 0°$, $e = 30°$) of bulk CR chondrites under vacuum at $T = 80°$C, 2019a.

J. Eschrig, L. Bonal, and P. Beck. NIR reflectance spectrum ($i = 0°$, $e = 30°$) of bulk CV chondrites under vacuum at $T = 80°$C, 2019b.

J. Eschrig, L. Bonal, and P. Beck. NIR reflectance spectrum ($i = 0°$, $e = 30°$) of bulk UOC chondrites under vacuum at $T = 80°$C, 2019c.

J. Eschrig, L. Bonal, P. Beck, and T. Prestgard. NIR reflectance spectrum ($i = 0°$, $e = 30°$) of bulk CO chondrites under vacuum at $T = 80°$C, 2019d.

J. Eschrig, L. Bonal, and P. Beck. NIR reflectance spectrum ($i = 0°$, $e = 30°$) of bulk EOC chondrites under vacuum at $T = 80°$C, 2020.

J. Eschrig, L. Bonal, P. Beck, and T.J. Prestgard. Spectral reflectance analysis of type 3 carbonaceous chondrites and search for their asteroidal parent bodies. *Icarus*, 354: 114034, 2021. ISSN 0019-1035. doi: https://doi.org/10.1016/j.icarus.2020.114034. URL https://www.sciencedirect.com/science/article/pii/S0019103520303912.

J. Eschrig, L. Bonal, M. Mahlke, B. Carry, P. Beck, and J. Gattacceca. Investigating s-type asteroid surfaces through reflectance spectra of ordinary chondrites. *Icarus*, 381: 115012, 2022. ISSN 0019-1035. doi: https://doi.org/10.1016/j.icarus.2022.115012. URL https://www.sciencedirect.com/science/article/pii/S0019103522001282.

Mária Földvári. *Handbook of thermogravimetric system of minerals and its use in geological practice*, volume 213. Geological Institute of Hungary Budapest, 2011.

Ray L Frost, Huada Ruan, J Theo Kloprogge, and W.P Gates. Dehydration and dehydroxylation of nontronites and ferruginous smectite. *Thermochimica Acta*, 346(1): 63–72, 2000. ISSN 0040-6031. doi: https://doi.org/10.1016/S0040-6031(99)00366-4. URL https://www.sciencedirect.com/science/article/pii/S0040603199003664.

Michael J. Gaffey and Thomas B. McCord. Asteroid surface materials: Mineralogical characterizations from reflectance spectra. *Space Science Reviews*, 21(5):555–628, Mar 1978.

A. Garenne, P. Beck, G. Montes-Hernandez, R. Chiriac, F. Toche, E. Quirico, L. Bonal, and B. Schmitt. The abundance and stability of "water" in type 1 and 2 carbonaceous chondrites (ci, cm and cr). *Geochimica et Cosmochimica Acta*, 137:93 – 112, 2014. ISSN 0016-7037. doi: https://doi.org/10.1016/j.gca.2014.03.034. URL http://www.sciencedirect.com/science/article/pii/S0016703714002130.

J. Gattacceca, C. Suavet, P. Rochette, B. P. Weiss, M. Winklhofer, M. Uehara, and Jon M. Friedrich. Metal phases in ordinary chondrites: Magnetic hysteresis properties and implications for thermal history. *Meteoritics & Planetary Science*, 49(4):652–676, 2014. doi: https://doi.org/10.1111/maps.12268. URL https://onlinelibrary.wiley.com/doi/abs/10.1111/maps.12268.

Amitabha Ghosh, Stuart J. Weidenschilling, and Harry Y. McSween Jr. Importance of the accretion process in asteroid thermal evolution: 6 hebe as an example. *Meteoritics & Planetary Science*, 38(5):711–724, 2003. doi: https://doi.org/10.1111/j.1945-5100.2003.tb00036.x. URL https://onlinelibrary.wiley.com/doi/abs/10.1111/j.1945-5100.2003.tb00036.x.

J. Gradie and E. Tedesco. Compositional structure of the asteroid belt. *Science*, 216 (4553):1405–1407, 1982. doi: 10.1126/science.216.4553.1405. URL https://www.science.org/doi/abs/10.1126/science.216.4553.1405.

M. M. Grady and I. Wright. Types of extraterrestrial material available for study. In Dante S. Lauretta and Harry Y. McSween, editors, *Meteorites and the Early Solar System II*, page 3. 2006.

Richard C. Greenwood, Thomas H. Burbine, and Ian A. Franchi. Linking asteroids and meteorites to the primordial planetesimal population. *Geochimica et Cosmochimica Acta*, 277:377 – 406, 2020. ISSN 0016-7037. doi: https://doi.org/10.1016/j.gca.2020.02.004. URL http://www.sciencedirect.com/science/article/pii/S0016703720301058.

Jeffrey N. GROSSMAN and Adrian J. BREARLEY. The onset of metamorphism in ordinary and carbonaceous chondrites. *Meteoritics & Planetary Science*, 40(1):87–122, 2005. doi: https://doi.org/10.1111/j.1945-5100.2005.tb00366.x. URL https://onlinelibrary.wiley.com/doi/abs/10.1111/j.1945-5100.2005.tb00366.x.

Jeffrey N. Grossman, Conel M. O'D. Alexander, Jianhua Wang, and Adrian J. Brearley. Bleached chondrules: Evidence for widespread aqueous processes on the parent asteroids of ordinary chondrites. *Meteoritics & Planetary Science*, 35 (3):467–486, 2000. doi: https://doi.org/10.1111/j.1945-5100.2000.tb01429.x. URL https://onlinelibrary.wiley.com/doi/abs/10.1111/j.1945-5100.2000.tb01429.x.

Jeffrey N. Grossman, Conel M. O'D. Alexanders, Jianhua Wang, and Adrian J. Brearley. Zoned chondrules in semarkona: Evidence for high- and low-temperature processing. *Meteoritics & Planetary Science*, 37(1):49–73, 2002. doi: https://doi.org/10.1111/j.1945-5100.2002.tb00795.x. URL https://onlinelibrary.wiley.com/doi/abs/10.1111/j.1945-5100.2002.tb00795.x.

Lawrence Grossmann. Vapor-condensed phase processes in the early solar system. *Meteoritics & Planetary Science*, 45(1):7–20, 2010. doi: https://doi.org/10.1111/j.1945-5100.2009.01010.x. URL https://onlinelibrary.wiley.com/doi/abs/10.1111/j.1945-5100.2009.01010.x.

Bruce Hapke. *Theory of reflectance and emittance spectroscopy*. Cambridge university press, 2012.

Ellen R. Harju, Alan E. Rubin, Insu Ahn, Byeon-Gak Choi, Karen Ziegler, and John T. Wasson. Progressive aqueous alteration of cr carbonaceous chondrites. *Geochimica et Cosmochimica Acta*, 139:267–292, 2014. ISSN 0016-7037. doi: https://doi.org/10.1016/j.gca.2014.04.048. URL https://www.sciencedirect.com/science/article/pii/S0016703714003160.

Carl W. Hergenrother, Michael C. Nolan, Richard P. Binzel, Edward A. Cloutis, Maria Antonietta Barucci, Patrick Michel, Daniel J. Scheeres, Christian Drouet d'Aubigny, Daniela Lazzaro, Noemi Pinilla-Alonso, Humberto Campins, Javier Licandro, Beth E. Clark, Bashar Rizk, Edward C. Beshore, and Dante S. Lauretta. Lightcurve, color and phase function photometry of the osiris-rex target asteroid (101955) bennu. *Icarus*, 226(1):663–670, 2013. ISSN 0019-1035. doi: https://doi.org/10.1016/j.icarus.2013.05.044. URL https://www.sciencedirect.com/science/article/pii/S0019103513002625.

Takahiro Hiroi, Michael E. Zolensky, Carlé M. Pieters, and Michael E. Lipschutz. Thermal metamorphism of the c, g, b, and f asteroids seen from the 0.7 /textmu m, 3 /textmu m, and uv absorption strengths in comparison with carbonaceous chondrites. *Meteoritics & Planetary Science*, 31(3):321–327, 1996. doi: 10.1111/j.1945-5100.1996.tb02068.x. URL https://onlinelibrary.wiley.com/doi/abs/10.1111/j.1945-5100.1996.tb02068.x.

K.T. Howard, C.M.O'D. Alexander, D.L. Schrader, and K.A. Dyl. Classification of hydrous meteorites (cr, cm and c2 ungrouped) by phyllosilicate fraction: Psd-xrd modal mineralogy and planetesimal environments. *Geochimica et Cosmochimica Acta*, 149:206–222, 2015. ISSN 0016-7037. doi: https://doi.org/10.1016/j.gca.2014.10.025. URL https://www.sciencedirect.com/science/article/pii/S0016703714006334.

Richard Howarth. Improved estimators of uncertainty in proportions, point-counting, and pass-fail test results. *American Journal of Science*, 298:594–607, 09 1998. doi: 10.2475/ajs.298.7.594.

G. Huss, Alan Rubin, and Jeffrey Grossman. Thermal metamorphism in chondrites. *Meteorites and the Early Solar System II*, 01 2006.

R. Hutchison, C.M.O. Alexander, and D.J. barber. The semarkona meteorite: First recorded occurrence of smectite in an ordinary chondrite, and its implications. *Geochimica et Cosmochimica Acta*, 51(7):1875–1882, 1987. ISSN 0016-7037. doi: https://doi.org/10.1016/0016-7037(87)90178-5. URL https://www.sciencedirect.com/science/article/pii/0016703787901785.

David Jewitt. The active asteroids. *The Astronomical Journal*, 143(3):66, feb 2012. doi: 10.1088/0004-6256/143/3/66. URL https://doi.org/10.1088%2F0004-6256%2F143%2F3%2F66.

Yoko Kebukawa, Conel M.O'D. Alexander, and George D. Cody. Compositional diversity in insoluble organic matter in type 1, 2 and 3 chondrites as detected by infrared spectroscopy. *Geochimica et Cosmochimica Acta*, 75(12):3530–3541,

2011. ISSN 0016-7037. doi: https://doi.org/10.1016/j.gca.2011.03.037. URL https://www.sciencedirect.com/science/article/pii/S0016703711002043.

M. Kimura, N. Imae, M. Komatsu, J.A. Barrat, R.C. Greenwood, A. Yamaguchi, and T. Noguchi. The most primitive cm chondrites, asuka 12085, 12169, and 12236, of subtypes 3.0–2.8: Their characteristic features and classification. *Polar Science*, 26: 100565, 2020. ISSN 1873-9652. doi: https://doi.org/10.1016/j.polar.2020.100565. URL https://www.sciencedirect.com/science/article/pii/S1873965220300748.

A.J. King, J.R. Solomon, P.F. Schofield, and S. Russell. Characterising the ci and ci-like carbonaceous chondrites using thermogravimetric analysis and infrared spectroscopy. *Earth, Planets and Space*, 67:198, 2015. doi: https://doi.org/10.1186/s40623-015-0370-4.

G.A. Krasinsky, E.V. Pitjeva, M.V. Vasilyev, and E.I. Yagudina. Hidden mass in the asteroid belt. *Icarus*, 158(1):98–105, 2002. ISSN 0019-1035. doi: https://doi.org/10.1006/icar.2002.6837. URL https://www.sciencedirect.com/science/article/pii/S0019103502968375.

A. N. Krot, I. D. Hutcheon, A. J. Brearley, O. V. Pravdivtseva, M. I. Petaev, and C. M. Hohenberg. Timescales and Settings for Alteration of Chondritic Meteorites. In Dante S. Lauretta and Harry Y. McSween, editors, *Meteorites and the Early Solar System II*, page 525. 2006.

A. N. Krot, K. Keil, E. R. D. Scott, C. A. Goodrich, and M. K. Weisberg. Classification of meteorites and their genetic relationships. In Andrew M. Davis, editor, *Meteorites and Cosmochemical Processes*, volume 1, pages 1–63. 2014.

A. N. Krot, K. Nagashima, C. M. O'D. Alexander, F. J. Ciesla, W. Fujiya, and L. Bonal. Sources of Water and Aqueous Activity on the Chondrite Parent Asteroids. In *Asteroids IV*, pages 635–660. 2015. doi: 10.2458/azu_uapress_9780816532131-ch033.

Alexander N. Krot, Michael E. Zolensky, John T. Wasson, Edward R.D. Scott, Klaus Keil, and Kazumasa Ohsumi. Carbide-magnetite assemblages in type-3 ordinary chondrites. *Geochimica et Cosmochimica Acta*, 61(1):219–237, 1997. ISSN 0016-7037. doi: https://doi.org/10.1016/S0016-7037(96)00336-5. URL https://www.sciencedirect.com/science/article/pii/S0016703796003365.

Thomas S. Kruijer, Christoph Burkhardt, Gerrit Budde, and Thorsten Kleine. Age of jupiter inferred from the distinct genetics and formation times of meteorites. *Proceedings of the National Academy of Sciences of the United States of America*, 114(26): 6712–6716, 2017. ISSN 00278424, 10916490. URL https://www.jstor.org/stable/26484974.

L. Krämer Ruggiu, P. Beck, J. Gattacceca, and J. Eschrig. Visible-infrared spectroscopy of ungrouped and rare meteorites brings further constraints on meteorite-asteroid connections. *Icarus*, 362:114393, 2021. ISSN 0019-1035. doi: https://doi.org/10.1016/j.icarus.2021.114393. URL https://www.sciencedirect.com/science/article/pii/S0019103521000828.

Petr Kuchynka and William M. Folkner. A new approach to determining asteroid masses from planetary range measurements. *Icarus*, 222(1):243–253, 2013. ISSN 0019-1035. doi: https://doi.org/10.1016/j.icarus.2012.11.003. URL https://www.sciencedirect.com/science/article/pii/S0019103512004496.

C. Lantz, R. Brunetto, M.A. Barucci, S. Fornasier, D. Baklouti, J. Bourçois, and M. Godard. Ion irradiation of carbonaceous chondrites: A new view of space weathering on primitive asteroids. *Icarus*, 285:43 – 57, 2017. ISSN 0019-1035. doi: https://doi.org/10.1016/j.icarus.2016.12.019. URL http://www.sciencedirect.com/science/article/pii/S0019103516300252.

DS Lauretta, DN DellaGiustina, CA Bennett, DR Golish, KJ Becker, SS Balram-Knutson, OS Barnouin, TL Becker, WF Bottke, WV Boynton, H Campins, BE Clark, HC Connolly, CY Drouet d'Aubigny, JP Dworkin, JP Emery, HL Enos, VE Hamilton, CW Hergenrother, ES Howell, MRM Izawa, HH Kaplan, MC Nolan, B Rizk, HL Roper, DJ Scheeres, PH Smith, KJ Walsh, CWV Wolner, and OSIRIS-REx Team. The unexpected surface of asteroid (101955) bennu. *Nature*, 568(7750): 55—60, April 2019. ISSN 0028-0836. doi: 10.1038/s41586-019-1033-6. URL https://europepmc.org/articles/PMC6557581.

Grossman Lawrence and Larimer John W. Early chemical history of the solar system. *Reviews of Geophysics*, 12(1):71–101, 1974. doi: https://doi.org/10.1029/RG012i001p00071. URL https://agupubs.onlinelibrary.wiley.com/doi/abs/10.1029/RG012i001p00071.

M. Lazzarin, S. Marchi, L.V. Moroz, R. Brunetto, Sara Magrin, P. Paolicchi, and Giovanni Strazzulla. Space weathering in the main asteroid belt: The big picture. volume 647, 08 2006. doi: 10.1086/507448.

Jonathan A. Lewis and Rhian H. Jones. Phosphate and feldspar mineralogy of equilibrated l chondrites: The record of metasomatism during metamorphism in ordinary chondrite parent bodies. *Meteoritics & Planetary Science*, 51(10):1886–1913, 2016. doi: https://doi.org/10.1111/maps.12719. URL https://onlinelibrary.wiley.com/doi/abs/10.1111/maps.12719.

Jonathan A. Lewis and Rhian H. Jones. Primary feldspar in the semarkona ll3.00 chondrite: Constraints on chondrule formation and secondary alteration. *Meteoritics & Planetary Science*, 54(1):72–89, 2019. doi: https://doi.org/10.1111/maps.13194. URL https://onlinelibrary.wiley.com/doi/abs/10.1111/maps.13194.

Jonathan A. Lewis, Rhian H. Jones, and Serafina C. Garcea. Chondrule porosity in the l4 chondrite saratov: Dissolution, chemical transport, and fluid flow. *Geochimica et Cosmochimica Acta*, 240:293–313, 2018. ISSN 0016-7037. doi: https://doi.org/10.1016/j.gca.2018.08.002. URL https://www.sciencedirect.com/science/article/pii/S0016703718304307.

Jonathan A. Lewis, Rhian H. Jones, and Adrian J. Brearley. Plagioclase alteration and equilibration in ordinary chondrites: Metasomatism during thermal metamorphism.

Geochimica et Cosmochimica Acta, 316:201–229, 2022. ISSN 0016-7037. doi: https://doi.org/10.1016/j.gca.2021.10.004. URL https://www.sciencedirect.com/science/article/pii/S0016703721005937.

Y. Lin, M. Kimura, B. Miao, D. Dai, and A. Monoi. Petrographic comparison of refractory inclusions from different chemical groups of chondrites. *Meteoritics & Planetary Science*, 41(1):67–81, 2006. doi: https://doi.org/10.1111/j.1945-5100.2006.tb00193.x. URL https://onlinelibrary.wiley.com/doi/abs/10.1111/j.1945-5100.2006.tb00193.x.

M. Mahlke, Carry B., J. Eschrig, L. Bonal, and P. Beck. Linking cv/co chondrites to l-type asteroids without anomalous enrichment of calcium-aluminum inclusions. *Icarus*, in prep.

Max Mahlke. *Asteroid Taxonomy: A Probabilistic Synthesis of Spectrometry and Albedo from Complete and Partial Observations*. PhD thesis, Observatoire de la Côte d'Azur, 2022.

Max Mahlke, Benoit Carry, and Pierre-Alexandre Mattei. Asteroid taxonomy from cluster analysis of spectrometry and albedo. 2022. doi: 10.48550/ARXIV.2203.11229. URL https://arxiv.org/abs/2203.11229.

S. Marchi, R. Brunetto, S. Magrin, M. Lazzarin, and D. Gandolfi. Space weathering of near-earth and main belt silicate-rich asteroids: observations and ion irradiation experiments. *A&A*, 443(3):769–775, 2005. doi: 10.1051/0004-6361:20053525. URL https://doi.org/10.1051/0004-6361:20053525.

Yves Marrocchi, Lydie Bonal, Jérome Gattacceca, Laurette Piani, Pierre Beck, Richard Greenwood, Jolantha Eschrig, Anne Basque, Pasquale Mario Nuccio, and Franco Foresta Martin. The piancaldoli meteorite: A forgotten primitive ll3.10 ordinary chondrite. *Meteoritics & Planetary Science*, 55(8), 2020. doi: https://doi.org/10.1111/maps.13552. URL https://onlinelibrary.wiley.com/doi/abs/10.1111/maps.13552.

Joseph R Masiero, Francesca E DeMeo, Toshihiro Kasuga, and Alex H Parker. Asteroid family physical properties. *Asteroids IV*, 32:3–340, 2015.

Moe Matsuoka, Tomoki Nakamura, Takahiro Hiroi, Satoshi Okumura, and Sho Sasaki. Space weathering simulation with low-energy laser irradiation of murchison CM chondrite for reproducing micrometeoroid bombardments on c-type asteroids. *The Astrophysical Journal*, 890(2):L23, feb 2020. doi: 10.3847/2041-8213/ab72a4. URL https://doi.org/10.3847%2F2041-8213%2Fab72a4.

Francis M. McCubbin and Jessica J. Barnes. Origin and abundances of h2o in the terrestrial planets, moon, and asteroids. *Earth and Planetary Science Letters*, 526:115771, 2019. ISSN 0012-821X. doi: https://doi.org/10.1016/j.epsl.2019.115771. URL https://www.sciencedirect.com/science/article/pii/S0012821X19304637.

Harry Y. McSween, David W. Mittlefehldt, Andrew W. Beck, Rhiannon G. Mayne, and Timothy J. McCoy. HED Meteorites and Their Relationship to the Geology of Vesta and the Dawn Mission. , 163(1-4):141–174, December 2011. doi: 10.1007/s11214-010-9637-z.

Meteoritical Bulletin Database. The Meteorictical Society - International Society for Metroritics and Planetary Science. https://www.lpi.usra.edu/meteor/metbull.pp, 2022. Accessed: 2022.

Knut Metzler. From 2d to 3d chondrule size data: Some empirical ground truths. *Meteoritics & Planetary Science*, 53(7):1489–1499, 2018. doi: https://doi.org/10.1111/maps.13091. URL https://onlinelibrary.wiley.com/doi/abs/10.1111/maps.13091.

Patrick Michel, Francesca E DeMeo, and William F Bottke. *Asteroids IV*. University of Arizona Press, 2015a.

Patrick Michel, Derek C Richardson, Daniel D Durda, Martin Jutzi, and Erik Asphaug. Collisional formation and modeling of asteroid families. *Asteroids IV*, pages 341–354, 2015b.

Ralph E. Milliken and John F. Mustard. Quantifying absolute water content of minerals using near-infrared reflectance spectroscopy. *Journal of Geophysical Research: Planets*, 110(E12), 2005. doi: 10.1029/2005JE002534. URL https://agupubs.onlinelibrary.wiley.com/doi/abs/10.1029/2005JE002534.

A. Morbidelli, K. J. Walsh, D. P. O'Brien, D. A. Minton, and W. F. Bottke. The dynamical evolution of the asteroid belt. In *Asteroids IV*. University of Arizona Press, 2015. doi: 10.2458/azu_uapress_9780816532131-ch026. URL https://doi.org/10.2458%2Fazu_uapress_9780816532131-ch026.

Alessandro Morbidelli, B Bitsch, A Crida, M Gounelle, T Guillot, S Jacobson, A Johansen, M Lambrechts, and E Lega. Fossilized condensation lines in the solar system protoplanetary disk. *Icarus*, 267:368–376, 2016.

L.V. Moroz, A.V. Fisenko, L.F. Semjonova, C.M. Pieters, and N.N. Korotaeva. Optical effects of regolith processes on s-asteroids as simulated by laser shots on ordinary chondrite and other mafic materials. *Icarus*, 122(2):366 – 382, 1996a. ISSN 0019-1035. doi: https://doi.org/10.1006/icar.1996.0130. URL http://www.sciencedirect.com/science/article/pii/S001910359690130X.

L.V. Moroz, A.V. Fisenko, L.F. Semjonova, C.M. Pieters, and N.N. Korotaeva. Optical effects of regolith processes on s-asteroids as simulated by laser shots on ordinary chondrite and other mafic materials. *Icarus*, 122(2):366–382, 1996b. ISSN 0019-1035. doi: https://doi.org/10.1006/icar.1996.0130. URL https://www.sciencedirect.com/science/article/pii/S001910359690130X.

John F. Mustard and John E. Hays. Effects of hyperfine particles on reflectance spectra from 0.3 to 25 μm. *Icarus*, 125(1):145–163, 1997. ISSN 0019-1035.

doi: https://doi.org/10.1006/icar.1996.5583. URL https://www.sciencedirect.com/science/article/pii/S0019103596955839.

Tomoki Nakamura, Takaaki Noguchi, Masahiko Tanaka, Michael E. Zolensky, Makoto Kimura, Akira Tsuchiyama, Aiko Nakato, Toshihiro Ogami, Hatsumi Ishida, Masayuki Uesugi, Toru Yada, Kei Shirai, Akio Fujimura, Ryuji Okazaki, Scott A. Sandford, Yukihiro Ishibashi, Masanao Abe, Tatsuaki Okada, Munetaka Ueno, Toshifumi Mukai, Makoto Yoshikawa, and Junichiro Kawaguchi. Itokawa dust particles: A direct link between s-type asteroids and ordinary chondrites. *Science*, 333 (6046):1113–1116, 2011. doi: 10.1126/science.1207758. URL https://www.science.org/doi/abs/10.1126/science.1207758.

David Nesvornỳ, Miroslav Brož, Valerio Carruba, et al. Identification and dynamical properties of asteroid families. *Asteroids IV*, 29:7–321, 2015.

David P. O'Brien, Alessandro Morbidelli, and Harold F. Levison. Terrestrial planet formation with strong dynamical friction. *Icarus*, 184(1):39–58, 2006. ISSN 0019-1035. doi: https://doi.org/10.1016/j.icarus.2006.04.005. URL https://www.sciencedirect.com/science/article/pii/S0019103506001278.

David P. O'Brien, Alessandro Morbidelli, and William F. Bottke. The primordial excitation and clearing of the asteroid belt—revisited. *Icarus*, 191(2):434–452, 2007. ISSN 0019-1035. doi: https://doi.org/10.1016/j.icarus.2007.05.005. URL https://www.sciencedirect.com/science/article/pii/S0019103507002230.

Doyle P., Jogo K., Nagashima K., Krot A. N., Wakita S., Ciesla F.J., and Hutcheon J.D. Early aqueous activity on the ordinary and carbonaceous chondrite parent bodies recorded by fayalite. *Nature Communications*, 6(1):7444, 2015. ISSN 2041-1723. doi: https://doi-org.sid2nomade-1.grenet.fr/10.1038/ncomms8444. URL https://doi.org/10.1038/ncomms8444.

J. M. Petit, J. Chambers, F. Franklin, and M. Nagasawa. Primordial Excitation and Depletion of the Main Belt. In *Asteroids III*, pages 711–723. 2002.

Carle M. Pieters and Sarah K. Noble. Space weathering on airless bodies. *Journal of Geophysical Research: Planets*, 121(10):1865–1884, 2016. doi: https://doi.org/10.1002/2016JE005128. URL https://agupubs.onlinelibrary.wiley.com/doi/abs/10.1002/2016JE005128.

S. Potin, P. Beck, F. Usui, L. Bonal, P. Vernazza, and B. Schmitt. Style and intensity of hydration among c-complex asteroids: A comparison to desiccated carbonaceous chondrites. *Icarus*, 348:113826, 2020a. ISSN 0019-1035. doi: https://doi.org/10.1016/j.icarus.2020.113826. URL https://www.sciencedirect.com/science/article/pii/S0019103520302086.

S. Potin, S. Manigand, P. Beck, C. Wolters, and B. Schmitt. A model of the 3-μm hydration band with exponentially modified gaussian (emg) profiles: Application to hydrated chondrites and asteroids. *Icarus*, 343:113686, 2020b. ISSN 0019-1035. doi:

https://doi.org/10.1016/j.icarus.2020.113686. URL https://www.sciencedirect.com/science/article/pii/S0019103520300774.

Sandra Potin, Olivier Brissaud, Pierre Beck, Bernard Schmitt, Yves Magnard, Jean-Jacques Correia, Patrick Rabou, and Laurent Jocou. Shadows: a spectro-gonio radiometer for bidirectional reflectance studies of dark meteorites and terrestrial analogs: design, calibrations, and performances on challenging surfaces. *Appl. Opt.*, 57(28):8279–8296, Oct 2018. doi: 10.1364/AO.57.008279. URL http://opg.optica.org/ao/abstract.cfm?URI=ao-57-28-8279.

Trygve Prestgard, Lydie Bonal, Jolantha Eschrig, Jérôme Gattacceca, Corinne Sonzogni, and Pierre Beck. Miller range 07687 and its place within the cm-co clan. *Meteoritics & Planetary Science*, 56(9):1758–1783, 2021. doi: https://doi.org/10.1111/maps.13736. URL https://onlinelibrary.wiley.com/doi/abs/10.1111/maps.13736.

Trygve Prestgard, Pierre Beck, Lydie Bonal, Jolantha Eschrig, Jérôme Gattacceca, Corinne Sonzogni, and Krämer Ruggiu Lisa. The parent bodies of cr chondrites and their secondary history. *Meteoritics & Planetary Science*, in prep.

Eric Quirico, Pierre-Ivan Raynal, and Michèle Bourot-Denise. Metamorphic grade of organic matter in six unequilibrated ordinary chondrites. *Meteoritics & Planetary Science*, 38(5):795–811, 2003. doi: https://doi.org/10.1111/j.1945-5100.2003.tb00043.x. URL https://onlinelibrary.wiley.com/doi/abs/10.1111/j.1945-5100.2003.tb00043.x.

V. Reddy, T. L. Dunn, C. A. Thomas, N. A. Moskovitz, and T. H. Burbine. *Mineralogy and Surface Composition of Asteroids*, pages 43–63. 2015. doi: 10.2458/azu_uapress_9780816532131-ch003.

RELAB. Reflectance Expperiment Laboratory (RELAB). https://pds-geosciences.wustl.edu/speclib/urn-nasa-pds-relab/data_reflectance/, 2022. Accessed: 2022.

Pierre Rochette, Leonardo Sagnotti, Michèle Bourot-Denise, Guy Consolmagno, Luigi Folco, Jérôme Gattacceca, Maria Luisa Osete, and Lauri Pesonen. Magnetic classification of stony meteorites: 1. ordinary chondrites. *Meteoritics & Planetary Science*, 38(2):251–268, 2003. doi: https://doi.org/10.1111/j.1945-5100.2003.tb00263.x. URL https://onlinelibrary.wiley.com/doi/abs/10.1111/j.1945-5100.2003.tb00263.x.

Alan E. Rubin, Michael E. Zolensky, and Robert J. Bodnar. The halite-bearing zag and monahans (1998) meteorite breccias: Shock metamorphism, thermal metamorphism and aqueous alteration on the h-chondrite parent body. *Meteoritics & Planetary Science*, 37(1):125–141, 2002. doi: https://doi.org/10.1111/j.1945-5100.2002.tb00799.x. URL https://onlinelibrary.wiley.com/doi/abs/10.1111/j.1945-5100.2002.tb00799.x.

Alan E. Rubin, Josep M. Trigo-Rodríguez, Heinz Huber, and John T. Wasson. Progressive aqueous alteration of cm carbonaceous chondrites. *Geochimica et Cosmochimica Acta*, 71(9):2361–2382, 2007. ISSN 0016-7037. doi: https://doi.org/10.1016/j.gca.2007.02.008. URL https://www.sciencedirect.com/science/article/pii/S001670370700083X.

Alex Ruzicka, Christine Floss, and Melinda Hutson. Amoeboid olivine aggregates (aoas) in the efremovka, leoville and vigarano (cv3) chondrites: A record of condensate evolution in the solar nebula. *Geochimica et Cosmochimica Acta*, 79:79–105, 2012. ISSN 0016-7037. doi: https://doi.org/10.1016/j.gca.2011.11.043. URL https://www.sciencedirect.com/science/article/pii/S0016703711007186.

J. W. Salisbury. Infrared(2.1-25μm)spectra of minerals. *The Johns Hopkins University Press*, 267, 1991. URL https://cir.nii.ac.jp/crid/1570854174138195840.

D. Schwander, T. Berg, G. Schönhense, U. Ott, and H. Palme. Refractory Metal Nuggets in Carbonaceous Chondrites are Early Solar Nebula Condensates. In *Workshop on Formation of the First Solids in the Solar System*, volume 1639 of *LPI Contributions*, page 9070, November 2011.

E. R. D. Scott and A. N. Krot. Chondrites and their Components. *Treatise on Geochemistry*, 1:711, December 2003. doi: 10.1016/B0-08-043751-6/01145-2.

Edward R D Scott, Alexander N Krot, and Ian S Sanders. Isotopic dichotomy among meteorites and its bearing on the protoplanetary disk. *The Astrophysical journal*, 854(2):164, February 2018. ISSN 0004-637X. doi: 10.3847/1538-4357/aaa5a5. URL https://europepmc.org/articles/PMC6398615.

Edward R.D. Scott, Klaus Keil, and Dieter Stöffler. Shock metamorphism of carbonaceous chondrites. *Geochimica et Cosmochimica Acta*, 56(12):4281–4293, 1992. ISSN 0016-7037. doi: https://doi.org/10.1016/0016-7037(92)90268-N. URL https://www.sciencedirect.com/science/article/pii/001670379290268N.

D. W. Sears, J. N. Grossman, C. L. Melcher, L. M. Ross, and A. A. Mills. Measuring metamorphic history of unequilibrated ordinary chondrites. , 287:791–795, October 1980. doi: 10.1038/287791a0.

Derek WG Sears, Andrew D Morse, Robert Hutchison, R Kyle Guimon, Lu Jie, CM O'D Alexander, Paul H Benoit, Ian Wright, Colin Pillinger, Tian Xie, et al. Metamorphism and aqueous alteration in low petrographic type ordinary chondrites. *Meteoritics*, 30(2):169–181, 1995.

L. Somenzi, A. Fienga, J. Laskar, and P. Kuchynka. Determination of asteroid masses from their close encounters with mars. *Planetary and Space Science*, 58(5):858–863, 2010. ISSN 0032-0633. doi: https://doi.org/10.1016/j.pss.2010.01.010. URL https://www.sciencedirect.com/science/article/pii/S0032063310000383.

C. Sonett, D. Colburn, and K. Schwartz. Electrical heating of meteorite parent bodies and planets by dynamo induction from a pre-main sequence t tauri "solar wind". *Nature*, 219:924–926, 1968. doi: https://doi-org.sid2nomade-1.grenet.fr/10.1038/219924a0.

Fridolin Spitzer, Christoph Burkhardt, Francis Nimmo, and Thorsten Kleine. Nucleosynthetic pt isotope anomalies and the hf-w chronology of core formation in inner and outer solar system planetesimals. *Earth and Planetary Science Letters*, 576:

117211, 2021. ISSN 0012-821X. doi: https://doi.org/10.1016/j.epsl.2021.117211. URL https://www.sciencedirect.com/science/article/pii/S0012821X21004660.

Dieter Stöffler, Klaus Keil, and Scott Edward R.D. Shock metamorphism of ordinary chondrites. *Geochimica et Cosmochimica Acta*, 55(12):3845–3867, 1991. ISSN 0016-7037. doi: https://doi.org/10.1016/0016-7037(91)90078-J. URL https://www.sciencedirect.com/science/article/pii/001670379190078J.

R. Sultana, O. Poch, P. Beck, B. Schmitt, and E. Quirico. Visible and near-infrared reflectance of hyperfine and hyperporous particulate surfaces. *Icarus*, 357:114141, 2021. ISSN 0019-1035. doi: https://doi.org/10.1016/j.icarus.2020.114141. URL https://www.sciencedirect.com/science/article/pii/S0019103520304814.

J. M. Sunshine, H. C. Connolly, T. J. McCoy, S. J. Bus, and L. M. La Croix. Ancient asteroids enriched in refractory inclusions. *Science*, 320(5875):514–517, 2008. doi: 10.1126/science.1154340. URL https://www.science.org/doi/abs/10.1126/science.1154340.

S. Sutton, C.M.O'D. Alexander, A. Bryant, A. Lanzirotti, M. Newville, and E.A. Cloutis. The bulk valence state of fe and the origin of water in chondrites. *Geochimica et Cosmochimica Acta*, 211:115–132, 2017. ISSN 0016-7037. doi: https://doi.org/10.1016/j.gca.2017.05.021. URL https://www.sciencedirect.com/science/article/pii/S001670371730296X.

David J. Tholen and M. Antonietta Barucci. Asteroid taxonomy. In Richard P. Binzel, Tom Gehrels, and Mildred Shapley Matthews, editors, *Asteroids II*, pages 298–315, January 1989.

Graf Thomas and Marti Kurt. Collisional history of h chondrites. *Journal of Geophysical Research: Planets*, 100(E10):21247–21263, 1995. doi: https://doi.org/10.1029/95JE01903. URL https://agupubs.onlinelibrary.wiley.com/doi/abs/10.1029/95JE01903.

Kazushige Tomeoka, Jr. McSween, Harry Y., and Peter R. Buseck. Mineralogical alteration of cm carbonaceous chondrites: A review. *Antarctic Meteorite Research*, 2:221, October 1989.

Anne Trinquier, Jean-Louis Birck, and Claude J. Allegre. Widespreadsup54/supcr heterogeneity in the inner solar system. *The Astrophysical Journal*, 655(2):1179–1185, feb 2007. doi: 10.1086/510360. URL https://doi.org/10.1086/510360.

J. I. Trombka, S. W. Squyres, J. Brückner, W. V. Boynton, R. C. Reedy, T. J. McCoy, P. Gorenstein, L. G. Evans, J. R. Arnold, R. D. Starr, L. R. Nittler, M. E. Murphy, I. Mikheeva, R. L. McNutt, T. P. McClanahan, E. McCartney, J. O. Goldsten, R. E. Gold, S. R. Floyd, P. E. Clark, T. H. Burbine, J. S. Bhangoo, S. H. Bailey, and M. Petaev. The elemental composition of asteroid 433 eros: Results of the near-shoemaker x-ray spectrometer. *Science*, 289(5487):2101–2105, 2000. doi: 10.1126/science.289.5487.2101. URL https://www.science.org/doi/abs/10.1126/science.289.5487.2101.

Harold C. Urey. The cosmic abundances of potassium, uranium, and thorium and the heat balances of the earth, the moon, and mars. *Proceedings of the National Academy of Sciences*, 41.3:127–144, 1955.

Fumihiko Usui, Sunao Hasegawa, Takafumi Ootsubo, and Takashi Onaka. AKARI/IRC near-infrared asteroid spectroscopic survey: AcuA-spec. *Publications of the Astronomical Society of Japan*, 71(1), 12 2018. ISSN 0004-6264. doi: 10.1093/pasj/psy125. URL https://doi.org/10.1093/pasj/psy125. 1.

W.R. Van Schmus and J.A. Wood. A chemical-petrologic classification for the chondritic meteorites. *Geochimica et Cosmochimica Acta*, 31(5):747–765, 1967. ISSN 0016-7037. doi: https://doi.org/10.1016/S0016-7037(67)80030-9. URL https://www.sciencedirect.com/science/article/pii/S0016703767800309.

P. Vernazza, D. Fulvio, R. Brunetto, J.P. Emery, C.A. Dukes, F. Cipriani, O. Witasse, M.J. Schaible, B. Zanda, G. Strazzulla, and R.A. Baragiola. Paucity of tagish lake-like parent bodies in the asteroid belt and among jupiter trojans. *Icarus*, 225(1): 517 – 525, 2013. ISSN 0019-1035. doi: https://doi.org/10.1016/j.icarus.2013.04.019. URL http://www.sciencedirect.com/science/article/pii/S001910351300184X.

P. Vernazza, B. Zanda, R. P. Binzel, T. Hiroi, F. E. DeMeo, M. Birlan, R. Hewins, L. Ricci, P. Barge, and M. Lockhart. MULTIPLE AND FAST: THE ACCRETION OF ORDINARY CHONDRITE PARENT BODIES. *The Astrophysical Journal*, 791 (2):120, aug 2014. doi: 10.1088/0004-637x/791/2/120. URL https://doi.org/10.1088/0004-637x/791/2/120.

P. Vernazza, M. Marsset, P. Beck, R. P. Binzel, M. Birlan, R. Brunetto, F. E. Demeo, Z. Djouadi, C. Dumas, S. Merouane, O. Mousis, and B. Zanda. Interplanetary dust particles as samples of icy asteroids. *The Astrophysical Journal*, 806(2):204, jun 2015. doi: 10.1088/0004-637x/806/2/204. URL https://doi.org/10.1088%2F0004-637x%2F806%2F2%2F204.

Pierre Vernazza and Pierre Beck. Composition of solar system small bodies, 2016. URL https://arxiv.org/abs/1611.08731.

Kevin J Walsh, Alessandro Morbidelli, Sean N Raymond, David P O'Brien, and Avi M Mandell. A low mass for mars from jupiter's early gas-driven migration. *Nature*, 475 (7355):206–209, 2011.

Paul H. Warren. Stable-isotopic anomalies and the accretionary assemblage of the earth and mars: A subordinate role for carbonaceous chondrites. *Earth and Planetary Science Letters*, 311(1):93–100, 2011. ISSN 0012-821X. doi: https://doi.org/10.1016/j.epsl.2011.08.047. URL https://www.sciencedirect.com/science/article/pii/S0012821X11005115.

S.J. Weidenschilling. The distribution of mass in the planetary system and solar nebula. *Astrophysics and Space Science*, 51:153–158, 1977. doi: https://doi-org.sid2nomade-1.grenet.fr/10.1007/BF00642464.

George W. Wetherill. An alternative model for the formation of the asteroids. *Icarus*, 100(2):307–325, 1992. ISSN 0019-1035. doi: https://doi.org/10.1016/0019-1035(92)90103-E. URL https://www.sciencedirect.com/science/article/pii/001910359290103E.

F. Wlotzka. A Weathering Scale for the Ordinary Chondrites. *Meteoritics*, 28(3): 460–460, July 1993.

Toru Yada, Masanao Abe, Tatsuaki Okada, et al. Preliminary analysis of the hayabusa2 samples returned from c-type asteroid ryugu. *Nature Astronomy*, 6: 214–220, 2022. doi: 10.1038/s41550-021-01550-6. URL http://www.nature.com/articles/s41550-021-01550-6.

Tetsuya Yokoyama, Kazuhide Nagashima, Izumi Nakai, et al. Samples returned from the asteroid ryugu are similar to ivuna-type carbonaceous meteorites. *Science*, 0(0): eabn7850, 2022. doi: 10.1126/science.abn7850. URL https://www.science.org/doi/abs/10.1126/science.abn7850.

Kiyoshi Yomogida and Takafumi Matsui. Multiple parent bodies of ordinary chondrites. *Earth and Planetary Science Letters*, 68(1):34–42, 1984. ISSN 0012-821X. doi: https://doi.org/10.1016/0012-821X(84)90138-9. URL https://www.sciencedirect.com/science/article/pii/0012821X84901389.